Collaborative Mobile Cable-Driven Parallel Robots

Tahir Rasheed

THESE DE DOCTORAT DE

L'ÉCOLE CENTRALE DE NANTES
COMUE UNIVERSITE BRETAGNE LOIRE

ECOLE DOCTORALE N° 602
Sciences pour l'Ingénieur
Spécialité : *Robotique - Mécanique*

Par

Tahir RASHEED

Collaborative Mobile Cable-Driven Parallel Robots

Thèse présentée et soutenue à Nantes, le 9 décembre 2019
Unité de recherche : UMR 6004, Laboratoire des Sciences du Numérique de Nantes

Rapporteurs :

Jean-Pierre MERLET	Directeur de recherche, INRIA
Hélène CHANAL	Maître de conférence, HDR, Institut Pascal, Sigma-Clermont

Composition du Jury :

Président :	Jean-Pierre MERLET	Directeur de recherche, INRIA
Examinateurs :	Philippe CARDOU	Professeur des Universités, Université Laval, Québec, QC, Canada
	Philip LONG	Chercheur, Irish Manufacturing Research
Invité :	Adolfo SUAREZ ROOS	Equipe ROC, IRT Jules Verne, Nantes
Dir. de thèse :	Stéphane CARO	Directeur de recherche, CNRS, LS2N, Nantes
Co-dir. de thèse :	David MARQUEZ-GAMEZ	Chercheur, Université de Liverpool

Abstract

Cable-Driven Parallel Robots (CDPRs) are parallel manipulators whose rigid links are replaced by cables. CDPRs combine the advantages of parallel robots with the properties of cables, leading to potentially very effective mechanisms. The particular property of cables provide CDPRs several advantages, including larger workspaces, higher payload-to-weight ratio and lower manufacturing costs. However, when the working environment is cluttered, CDPRs cannot be used to accomplish complicated tasks. Under these circumstances, it may be necessary to use Reconfigurable Cable-Driven Parallel Robots (RCDPRs), whose geometric parameters can be modified in order to avoid the obstacles contained in the working environment and improve the RCDPR performances, for instance, higher stiffness, higher payload capability, lower cable tensions and lower energy consumption. However, for most existing RCDPRs, the reconfigurability is performed either discrete and manually or continuously, but with bulky reconfigurable systems.

This doctoral thesis presents a novel concept of Mobile Cable-Driven Parallel Robots (MCDPRs) as a new robotic system, which uses a combination of mobile robots and a CDPR. The goal of MCDPRs is to overcome the manual and discrete reconfigurability of RCDPRs and to develop a mobile, deployable and autonomous CDPR, which can be configured based on the desired task. Moreover, MCDPRs present a new technical innovation that could help to bring more flexibility and versatility with respect to existing industrial robotic solutions. Two MCDPR prototypes have been developed during the course of this thesis. The first MCDPR prototype is named FASTKIT, whose goal is to provide a low cost and versatile robotic solution for logistics. The second prototype is named MoPICK, whose targeted applications are mobile tasks in a constrained environment, for example, a workshop or logistic operations in a warehouse.

The thesis manuscript is composed of five chapters. The first chapter presents the state of the art related to cable-driven mechanisms. It also details the two MCDPR prototypes developed during the course of this thesis.

The second chapter starts by deriving all the necessary conditions that should be satisfied in order to achieve the static equilibrium of a MCDPR. These equilibrium conditions are exploited to develop a Tension Distribution Algorithm for the real time control of a MCDPR. Similarly, the equilibrium conditions are also used in the third chapter, which analyzes the Wrench-Feasible-Workspace of MCDPRs. Multiple case studies are investigated in both the chapters to show that the approach is applicable to both planar and spatial MCDPRs.

The fourth chapter deals with the kinematic performance and twist capabilities of MCDPRs. The kinematic performance of a MCDPR is analyzed by deriving its

first-order kinematic model, where each cable of the manipulator is modeled as a Universal-Prismatic-Spherical kinematic chain. Each mobile base is modeled as a Revolute-Prismatic-Prismatic kinematic chain. A general kinematic architecture is also developed for MCDPRs using the aforementioned kinematic chains.

The last chapter of the thesis presents multiple path planning strategies for MCDPRs, in order to reconfigure the CDPR's geometric architecture and to perform the desired task.

Key words: Collaborative Robotics, Mobile Cable Robots, Path Planning, Workspace analysis, Tension Distribution Algorithm.

Résumé

Les robots parallèles à câble (RPC) sont un type de manipulateurs parallèles dont les liens rigides sont remplacés par des câbles. Les RPC combinent les avantages des robots parallèles avec les propriétés des câbles, ce qui conduit à des mécanismes potentiellement très efficaces. La propriété particulière des câbles offre plusieurs avantages aux RPCs, tels que un grand espace de travail, un rapport charge utile/poids plus élevé et des coûts de fabrication plus faible. Cependant, lorsque l'environnement de travail est encombré, le RPC ne peut pas être utilisé pour accomplir des tâches complexes. Dans ces circonstances, il peut être nécessaire d'utiliser des robots parallèles à câble reconfigurables (RPCRs), dont les paramètres géométriques peuvent être modifiés afin d'éviter les obstacles contenus dans l'environnement de travail et d'améliorer les performances du RPCR, par exemple, une plus grande raideur, une capacité de charge utile supérieure, des tensions dans les câble inférieures et une consommation énergétique moindre. Cependant, pour la plupart des RPCRs existants, la reconfigurabilité s'effectue soit de manière discrète, soit manuellement. Elle peut également s'effectuer de manière continue mais généralement avec des systèmes reconfigurables complexes et volumineux.

Cette thèse de doctorat présente un nouveau concept de robots parallèle à câble mobile (RPCMs) comme un nouveau système robotique, qui utilise une combinaison de robots mobiles et un RPC. L'objectif des RPCMs est de surmonter la reconfigurabilité manuelle et discrète des RPCRs et de développer un RPC mobile, déployable et autonome, qui peut être adapté en fonction de la tâche à réaliser. De plus, les RPCMs présentent une nouvelle innovation technique qui pourrait contribuer à apporter plus de flexibilité et de polyvalence par rapport aux solutions robotiques industrielles existantes. Deux prototypes de RPCMs ont été développés au cours de cette thèse. Le premier prototype RPCM s'appelle FASTKIT, dont l'objectif est de fournir une solution robotique peu coûteuse et polyvalente pour la logistique. Le deuxième prototype s'appelle MoPICK, dont les applications ciblées sont des tâches mobiles dans un environnement contraint, par exemple, un atelier ou des opérations logistiques dans un entrepôt.

Le manuscrit de thèse est composé de cinq chapitres. Le premier chapitre présente l'état de l'art sur les robots parallèles entraînés par câbles. Il détaille également les deux prototypes RPCM développés au cours de cette thèse.

Le deuxième chapitre commence par déterminer toutes les conditions à respecter pour atteindre l'équilibre statique d'un RPCM. Ces conditions d'équilibre sont exploitées pour développer un algorithme de distribution des tensions pour le contrôle en temps réel du RPCM. De même, les conditions d'équilibre sont également utilisées dans le troisième chapitre, qui analyse l'espace de travail des RPCM. Plusieurs

études de cas sont examinées dans les deux chapitres pour montrer que l'approche est applicable aux RPCM planaires et spatiaux.

Le quatrième chapitre traite des performances cinématiques des RPCM. La performance cinématique d'un RPCM est analysée en dérivant son modèle cinématique de premier ordre, où chaque câble du manipulateur est modélisé comme une chaîne cinématique sphérique-cardan-prismatique. Alors que chaque base mobile est modélisée comme une chaîne cinématique pivot-glissière-glissière. Un modèle cinématique globale des RPCM est ensuite obtenu.

Le dernier chapitre de la thèse présente des stratégies de planification de trajectoires multiples pour les RPCM, afin de reconfigurer l'architecture géométrique du RPC et d'effectuer la tâche souhaitée.

Mots clés : Robotique collaborative, robots mobiles à câbles, planification des trajectoires, analyse de l'espace de travail, algorithme de distribution des tensions.

Contents

List of Figures

List of Tables

1

Introduction

Contents

Science and technology have a major role in the evolution of our present society by influencing our daily life. Whether it is the means of transportation, entertainment, sports or communication, even the most minor aspects of our daily life has been completely changed by the technology. One emerging field through which science

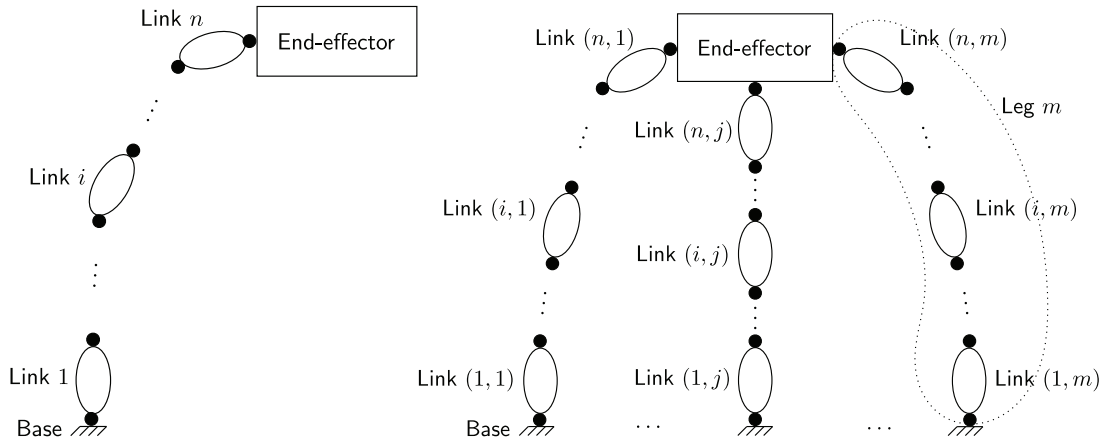

(a) n-links serial mechanism (b) m-legs parallel mechanism with n-links per leg

Figure 1.1: Serial and parallel mechanisms

has made a considerable impact on our society is robotics. Over the past 50 years, robotics have improved our society immensely. With the advancement of technology, robots are being exploited in almost all the research fields such as civil, engineering, medicine, agriculture and energy. One of the widely used area of research regarding the robots are serial and parallel manipulators.

Serial robots are designed as a series of links connected by motor-actuated joints that extend from a base to an end-effector, typically having an anthropomorphic architecture described as a "shoulder", an "elbow", and a "wrist". While parallel robots are closed-loop mechanisms, composed of several independent serial chains, defined as legs or limbs, connecting the moving-platform to a fixed base [Mer06]. Figure 1.1 illustrates the difference between the serial and parallel mechanisms.

Parallel robots have been part of the robotics landscape for several years. Their mechanical properties make them most appropriate for tasks that require large payload to weight ratios, high stiffness, precision, repeatability, high payload capabilities and large dynamic trajectories. One typical parallel robot is the Gough-Stewart platform, composed of six Universal-Prismatic-Spherical limbs, as shown in Fig. 1.2. The concept of Gough-Stewart platform has been applied for various applications such as AMiBA telescope [HAC+09] for motion simulators.

Parallel robots have also been widely used in several industrial applications, most commonly for manufacturing [CW03, WS02] and pick-and-place operations. The Delta robot [PRF90, Cla90] is an example of an extensively used parallel robot in the food and electronic industries for fast pick-and-place operations.

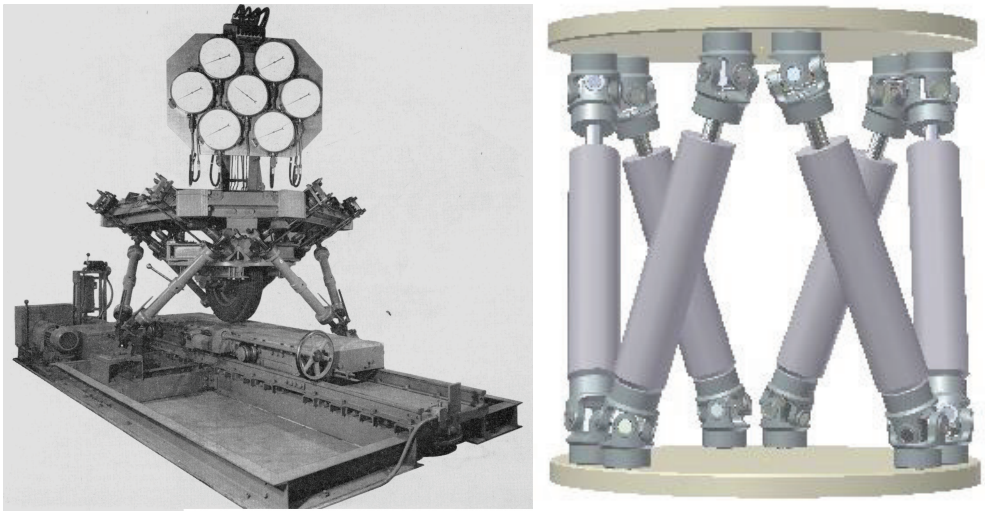

(a) (b)

Figure 1.2: (a) Original Gough-Stewart platform and its (b) $3D$ model

1.1 Cable-Driven Parallel Robots (CDPRs)

Cable-driven parallel robots (CDPRs) combine the principles of parallel robots with the properties of cables, leading to potentially very effective mechanisms. Thus, CDPRs form a particular class of parallel robots whose moving platform is connected to a fixed base frame by cables. The connection points between the cables and the base frame are referred to as *exit points*. Similarly, the cable attachment points on the moving-platform are denoted as *anchor points*. The cables may be coiled/uncoiled by motorized winches allowing a control system to adjust the cable lengths between the winch exit points and the anchor points. Appropriate length adjustment of cables allows one to control the degrees-of-freedom (DoF) of the moving-platform.

CDPRs are said to be advantageous in terms of workspace size, being easy to reconfigure, having low inertia, high speed motion, high payload to weight ratio (as cables are flexible members that can support very large tensile loads per mass unit), having simpler structure and being safer for cooperative tasks. Cables are much lighter than rigid links of a serial or parallel robot, and very long cables can be used. As a result, the end-effector of a cable robot can achieve high accelerations and velocities and work in a very large workspace (*e.g.*, a stadium). The main advantages of CDPRs over conventional robots are:

Large Workspace: Thanks to the potential high cable lengths, the CDPRs moving-platform can have larger translational workspace than those parallel robots composed of rigid links.

High dynamics: CDPRs are capable of generating high speeds and accelerations, thanks to their lightweight characteristics. For example, the FALCON manipu-

lator [KCTK97] can achieve a velocity up to 13 m/s, and a peak acceleration of 43 G.

Large payload capacity: Cable properties provide CDPRs with a high payload capability. For example, the payload capability of the CoGiRo manipulator [CoG08] is up to 500 kg, while the total mass of the moving components of the prototype is about 100 kg.

Highly energy efficient: In the case of serial robots, the actuators also have to bear the weight of the preceding links and actuators in addition to the payload. This results in high energy consumption. For conventional parallel robots, the fact that the actuator payload can be shared between their limbs means they are more energy efficient than serial robots [LB01]. Consequently, the energy consumption of CDPRs is focused on the motion of the moving-platform and the payload. It is shared by the number of the lightweight cables, leading to very low energy consumption and high payload-to-weight ratio.

Low cost: CDPR has usually a simple architecture, mainly composed of cheap and simple mechanical components. These components are usually standard and thus having a low manufacturing and maintenance cost.

Modular and reconfigurable: CDPRs have a relatively simple structure. The assembly and disassembly of these manipulators are easy. Moreover, CDPRs can easily be made to be modular and reconfigurable.

Classification of CDPRs

CDPRs are generally classified in two categories, *i.e,* fully suspended and fully constrained configurations. Both these configurations have their own advantages and drawbacks.

In fully suspended configuration (see Fig. 1.3a), the cables are usually located on the top of the structure and the space below the moving-platform is free of cables. The static equilibrium of the moving-platform is assured by the gravity force generated by the payload of the moving-platform. The gravity force acts as a virtual cable pulling the moving platform with a constant force along the gravity direction and is shared among all the cables. Consequently, suspended CDPRs usually offer higher payload capabilities and lower energy consumption. Fully suspended configuration also minimizes the risks of collision between the cables and elements in the workspace. However, performances of suspended CDPRs are directly related to the payload of the moving platform. When the payload is low, the stiffness of the CDPR is reduced and hence, such CDPRs are prone to low platform positioning accuracy, vibrations and instability.

In fully-constrained configuration (see Fig. 1.3b), cables are coming from both the top and the bottom of the fixed structure. Since cables cannot push the moving

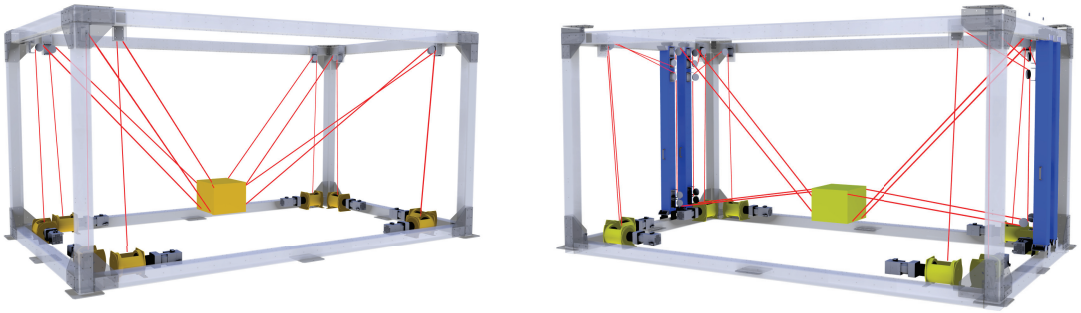

(a) (b)

Figure 1.3: (a) Suspended configuration (b) Fully-constrained configuration

platform, redundant cables are usually used to achieve the equilibrium of the fully constrained CDPRs moving-platform [RGL98], assuming that external wrenches can be exerted along any direction. Fully-constrained CDPRs are preferred for applications requiring high stiffness and positioning accuracy and good dynamic performance. However, they can be problematic in a cluttered environment due to risk of cable/cable collisions.

1.2 Reconfigurable Cable-Driven Parallel Robots (RCDPRs)

In spite of several advantages of CDPRs, several challenges remain. For example, CDPRs impose a strong requirement regarding the free circulation of the cables without interference with the environment. Indeed, collision free trajectory generation must consider all types of collisions, namely, cable/cable, cable/moving-platform, cable/environment and moving-platform/environment collision type [MTT+99, WSS08]. However, in a cluttered environment, cable collisions with objects cannot be completely avoided within the CDPR workspace.

In most applications discussed in Sec.2.1, the CDPR has a fixed cable layout which is determined during its design. In the following, a CDPR cable layout refers to the positions of the cable exit points and the positions of the connection points between the cables and the moving-platform. Thus, the aforementioned collisions can significantly reduce the workspace of a classical CDPR having a fixed cable layout. Hence, the location of the CDPR's cable attachment points must be carefully chosen in order to maximize the manipulator's workspace. It is therefore reasonable to adjust their geometry (which has a large influence on the performances) according to the task requirements and the robot's environment. Such solutions are named as Reconfigurable Cable-Driven Parallel Robots (RCDPRs).

RCDPRs are a class of CDPRs whose geometric parameters, such as the locations of the exit points and the cable connection points on the moving platform, can

be modified. By changing the manipulator configuration, its workspace may be enlarged and collisions between the cables and the environment can be avoided. At the same time, some robot performances may be improved, for instance, higher stiffness, higher payload capability, larger workspace, lower cable tensions and lower energy consumption. Classical CDPRs having a fixed cable layout are mostly proven successful if the tasks to be fulfilled will be simple and the working environment will not be cluttered. When those assumptions are not satisfied, RCDPRs may be a good alternative to achieve the prescribed goal.

1.3 Mobile Cable-Driven Parallel Robots (MCDPRs)

To the best of our knowledge, for most existing RCDPRs, the reconfigurability is performed either discrete and manually or continuously, but with bulky reconfigurable systems. Moreover, the reconfiguration is usually a costly and time consuming task. This thesis introduces Mobile Cable-Driven Parallel Robots (MCDPRs) that can be seen as new types of RCDPRs. The idea for introducing MCDPRs is to overcome the manual and discrete reconfigurability of RCDPRs such that an autonomous reconfiguration can be achieved. The goal of MCDPRs is to develop a mobile, deployable and autonomous CDPRs, that can be adapted based on the desired task. Section 1.3.1 presents the architecture and parameterization of MCDPRs.

Two MCDPRs prototypes have been developed during the course of this thesis. The first prototype is named FASTKIT, which is composed of an active and a passive mobile bases carrying a six DoF moving-platform, pulled by eight cables. The goal of the FASTKIT project is to provide a low cost and versatile robotic solution for logistics using a combination of mobile robots and a CDPR. The second prototype is named MoPICK, composed of a three DoF point mass moving-platform pulled by four cables mounted on four mobile bases. The targeted applications of MoPICK are mobile tasks in a constrained environment, for example, a workshop or logistic operations in a warehouse. Both these MCDPRs prototypes are described in Secs. 1.3.2 and 1.3.3.

1.3.1 MCDPR Parameterization

A MCDPR is composed of a classical CDPR with m cables and a n DoF moving-platform mounted on p mobile bases. A concept idea of a MCDPR is illustrated in Fig. 1.4a with $p = 4$ mobile bases and $n = 6$ DoF moving-platform displaced by $m = 8$ cables. The cable exit points are a function of the mobile base position and orientation. Each mobile base can navigate in the environment thus allowing the system to autonomously alter the geometry of the CDPR. It must be noted that the mobile bases are planar robots, *i.e.,* they can only navigate in a plane parallel to

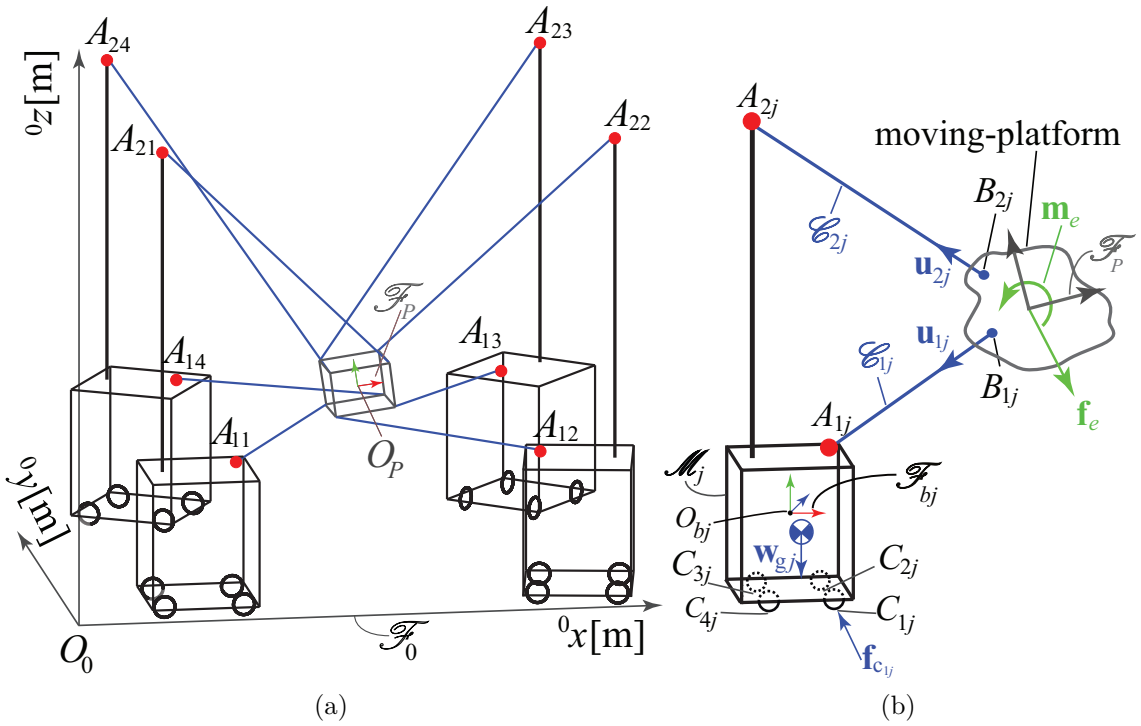

Figure 1.4: (a) A MCDPR with eight cables ($m = 8$) and four mobile bases ($p = 4$). Its moving-platform has six degree-of-freedom (n = 6) (b) jth mobile base with four wheels ($c_j = 4$)

the ground, thus, accordingly the CDPR carried by the mobile bases can only be reconfigured in the aforementioned plane. Consequently, the height of the cable exit points remains constant.

Let m_j be the number cables connected to the jth mobile base denoted as $\mathscr{M}_j$, $j = 1, \ldots, p$. The ith cable attached to $\mathscr{M}_j$ is named as $\mathscr{C}_{ij}$, $i = 1, \ldots, m_j$. As a result, m cables are attached to the moving-platform.

$$m = \sum_{j=1}^{p} m_j. \tag{1.1}$$

Let $\mathbf{u}_{ij}$ be the unit vector pointing from the anchor point B_{ij} to the exit point A_{ij} of cable $\mathscr{C}_{ij}$. $\mathbf{t}_{ij}$ is the $\mathscr{C}_{ij}$ cable tension vector expressed as:

$$\mathbf{t}_{ij} = \mathbf{u}_{ij} t_{ij}, \tag{1.2}$$

where t_{ij} denotes the tension in the cable $\mathscr{C}_{ij}$. The jth mobile base is assumed to have c_j wheels. C_{kj}, $k = 1, \ldots, c_j$ are the contact points between the jth mobile base $\mathscr{M}_j$ and the ground. Figure 1.4b illustrates $\mathscr{M}_j$ with four wheels ($c_j = 4$).

Let $\mathscr{F}_0$ be the base frame of origin O_0 and axes ^0x, ^0y and ^0z while $\mathscr{F}_{bj}$ denotes the frame attached to $\mathscr{M}_j$ with origin O_{bj} and axes ^{bj}x, ^{bj}y and ^{bj}z, illustrated in

Figure 1.5: FASTKIT concept: A cable-driven parallel robot mounted on two mobile platforms [PRMG+20]

Fig. 1.4. Mobile bases are assumed to be capable of performing two-DoF translational motions along x_0 and y_0 and one-DoF rotational motion about an axis parallel to z_0.

1.3.2 FASTKIT

The FASTKIT concept shown in Fig. 1.5, is a MCDPR prototype developed in the framework of ECHORD++ FASTKIT project[1]. Figure 1.6 shows the FASTKIT protoype composed of a $n = 6$-DoF moving-platform equipped with a gripper, an active and a passive $p = 2$ mobile bases connected to each other through $m = 8$ cables. FASTKIT project addresses an industrial need for fast picking and kitting operations in existing storage facilities while being easy to install, keeping existing infrastructures and covering large areas. Nowadays, there exist several robotic solutions for logistic applications. One of the most popular automatic storage systems is the multi-shuttle system described in [LŠP11, YMQ11], which guarantees high performance in terms of working rate. The main drawbacks of such systems are the high investment cost,

[1]FASTKIT Videos: https://www.youtube.com/channel/UCJ8QRs818MBc8YSbn-bZVjA

the long installation time and the lack of flexibility.

Such systems are usually installed over large warehouses presenting a high entry and exit flow of storage boxes. In such conditions, an acceptable *Return On Investment* is usually guaranteed. On the other hand, this solution is no longer possible or profitable for small warehouses, where there is no room for the installation of a large multi-shuttle system, or for warehouses characterized by a very low entry and exit flow of storage units, for which the high investment cost of a multi-shuttle solution is not justified.

On the contrary, FASTKIT is made up of CDPR mounted on two mobile bases. As a result, it combines the autonomy of mobile robots with the advantages of CDPR, namely, large workspace, high payload-to-weight ratio, low end-effector inertia, deployability and reconfigurability. Moreover, CDPRs lead generally to low cost and easy maintenance solutions. Thanks to their characteristics, CDPRs can be used for different tasks such as the manipulation of heavy payloads or fast pick-and-place operations. Indeed, logistics is a very interesting field of application for CDPRs. Accordingly, FASTKIT aims at providing the user with a flexible and low cost logistic solution to equip small warehouses.

Therefore, the novelty of FASTKIT lies in the combination of autonomous mobile platforms and a CDPR. The main challenge in FASTKIT dealt with the design, modeling, workspace analysis and the synchronization between the CDPR and the two mobile bases while performing a desired task.

1.3.2.1 Main Components

The main components of FASTKIT are: (*i*) the main structure, (*ii*) the actuation system, (*iii*) its pulleys, (*iv*) its moving-platform equipped with a gripper, and (*v*) two electrical cabinets. Here are the FASTKIT specifications:

- a desired workspace of 5 meters long by 2 meters high,
- a linear velocity of the moving-plaform equal to 1 m/s,
- a maximum of 12 kg payload.

The 2.4 m high main structure is made up of aluminum profile bars, directly fixed on the top of the two mobile bases.

Actuation and Transmission System

The actuation system consists of eight identical modules, each module being composed a motor, a gearbox, an elastic coupling, a transmission shaft, two bearings and a winch, as shown in Fig. 1.7.

Based on the foregoing specifications, the required maximum cable tension and maximum cable velocity are equal to 45 N and 2 m/s, respectively. As a result, 8LVA23 B&R motors coupled with 8GP30 B&R gearboxes were selected. Table 1.1

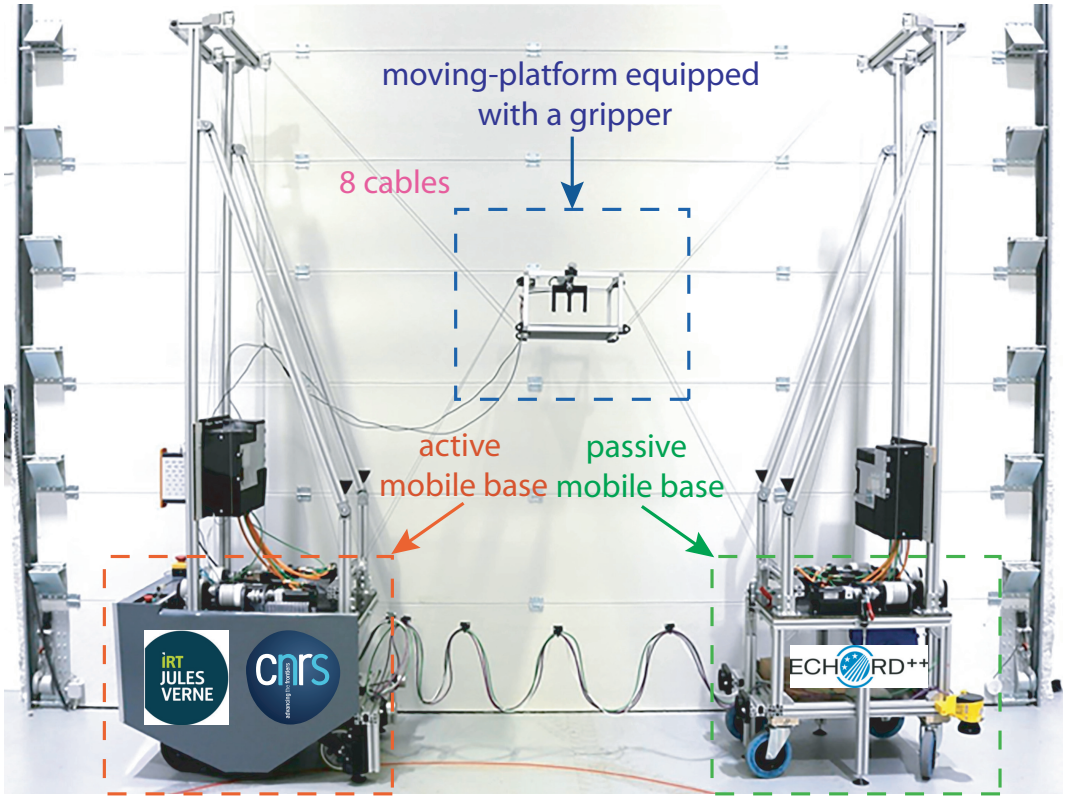

Figure 1.6: FASTKIT prototype

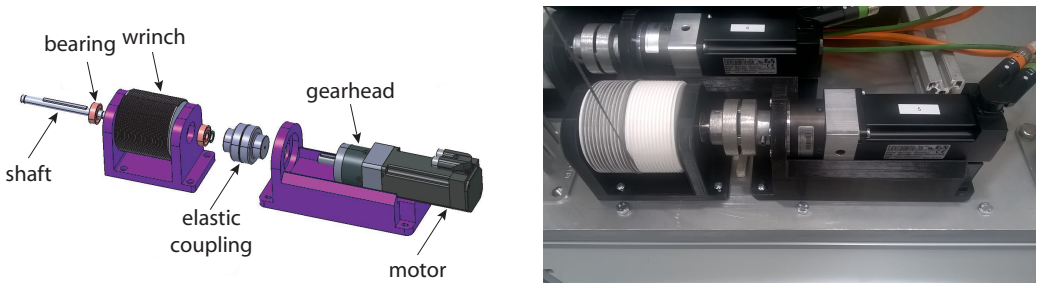

(a) CAD modeling (b) Implemented system

Figure 1.7: FASTKIT actuation and transmission system

gives the characteristics of the selected motors.

Pulleys

The pulleys have been designed to minimize friction, allowing the cable to easily roll around the sheave and that the sheave itself can rotate freely around its vertical axis. The sheave is equipped with a ball bearing whereas two angular contact ball bearings are used to free the sheave rotation around the vertical axis.

Figure 1.8a shows the CAD model of the eight pulleys used for the assembly of the CDPR in a suspended configuration. Figure 1.8b shows the CAD model of the additional four pulleys that have been designed for the CDPR in a fully constrained

Requirements	
Maximum cable tension	45 N
Maximum cable velocity	2 m/s
Actuators	
Actuation system efficiency	70%
Gearhead ratio	5:1
Wrinches	
Drum diameter	0.08 m
Motors (working point)	
Torque	0.6 Nm
Angular velocity	1600 rpm

Table 1.1: Characteristics of the selected motors

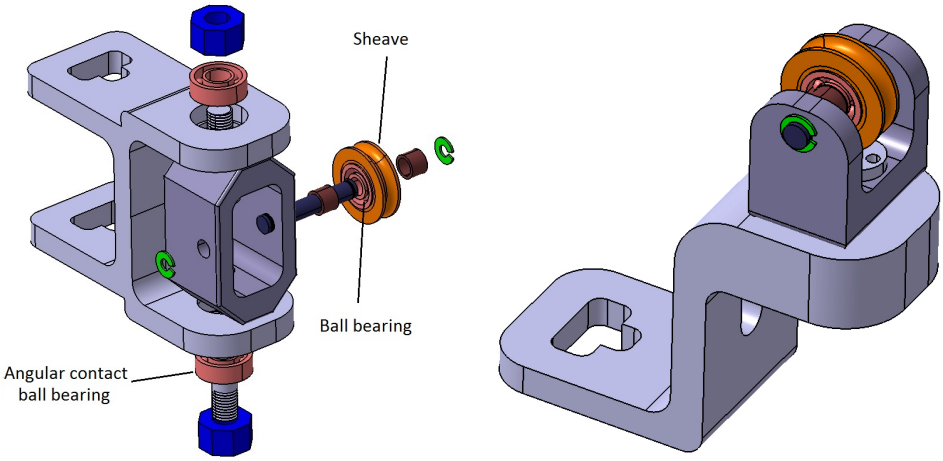

(a) CAD model of the first pulley type (b) CAD model of the second pulley type

Figure 1.8: FASTKIT pulleys

configuration.

Moving-Platform and Gripper

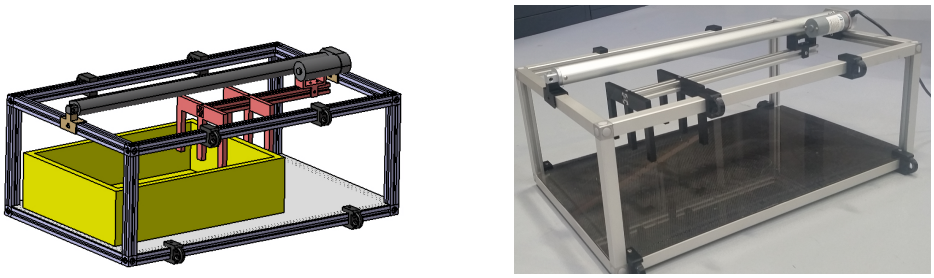

(a) CAD modeling (b) Final assembly

Figure 1.9: Moving-platform with its gripper grabbing a storage unit box

The moving-platform has been designed to be capable of grasping, carrying and dropping a box of size 0.4 m × 0.3 m × 0.15 m, which is representative of the storage units used in logistics. Inner dimensions of the platform are 0.6 m × 0.36 m × 0.2 m. Figure 1.9a depicts the CAD model of the moving-platform equipped with its gripper. In this case, the mass of the moving-platform should be a minimum. The actual moving-platform, shown in Fig. 1.9, weighs 5 Kg. A Firgelli linear motor[2] was used to construct the moving-platform gripper. It should be noted that the moving-platform tilt, required to grab and release boxes, is also controlled through the cable lengths.

Sick Laser Scanners

Each mobile base is equipped with a s300 sick laser scanner as shown in Fig. 1.5. It has 3 m field range and 270 degree scanning angle. This kind of scanner is used for the motion planning and obstacle avoidance during the navigation mode, discussed in Sec. 1.3.2.3.

Electrical Cabinets

The actuation system of the CDPR is controlled and powered by means of two electrical cabinets, one installed onto each mobile base. Those two cabinets are slightly different. Both electrical cabinets are composed of: (*i*) two variable speed drives; (*ii*) two 80V power supplies for the synchronous motors; (*iii*) one 24V power supply for the drives and (*iv*) one safety relay. In addition, the electrical cabinet embedded in the active mobile base is equipped with an industrial PC that controls the whole robot. Figure 1.10 shows the main electrical cabinet with the industrial PC. For the sake of compatibility, the speed drives, the power supplies and the industrial PC have been provided by the motor supplier, namely, B&R Automation™.

Figure 1.10: The FASTKIT electrical cabinet mounted onto the active mobile base

[2] https://www.firgelliauto.com/products/mini-track-actuator#ptab-specifications

1.3.2.2 Working modes of FASTKIT

FASTKIT is capable of autonomously navigating in its environment to reach the task location, this action is referred to as a navigation mode. During this mode, the two mobile bases are coupled together and act as a single working unit while the moving-platform is fixed on the two mobile bases (see Fig. 1.11a). The twist of the moving-platform and the passive mobile base is equal to the twist generated by the active mobile base. No cable motion is generated during the navigation mode. In short, FASTKIT acts as a classical mobile robot during the navigation mode. Navigation mode ends once the desired position, *i.e.,* task location, is attained.

Afterwards, the second working mode, referred to as the task mode, deploys the system in such a way that its workspace corresponds to the current task specification. The system calculates the required mobile base position from the desired workspace and ensures the controllability of the platform during the deployment. Once the system is successfully deployed, a set of stabilizers is used to ensure the stability of the prototype. During this mode, the passive mobile base is static while the motion of the cables and the active mobile base is used to deploy the complete system. Finally, the moving-platform is moved accurately by the CDPR at high velocity over a large area by controlling the either the cable tensions or cable velocities. (see Figs. 1.11b and 1.11c)[3].

The major challenges faced during the task mode of FASTKIT occur when the system has reached the task location and needs to be deployed in order to perform the desired pick and place operation. The first challenge is to determine if the desired task is feasible and/or within the reachable workspace. Secondly, the deployment strategy, *i.e.,* the transition between stowed CDPR and active CDPR, must be developed. It should be noted that during the task mode, FASTKIT is kinematically redundant due to the additional mobility of the active mobile base. Thus, the issue of kinematic redundancy was also required to be addressed during the deployment of FASTKIT. Although, FASTKIT acts as a classical mobile base during the navigation, in general, it may not be the case for classical MCDPRs. Hence, a generic planning approach is required for MCDPRs to perform the desired task. Moreover, the control laws are also required. The first control law tested on the FASTKIT CDPR is a velocity control law. However, in order to implement it, its kinematic model must be derived. While straightforward to implement, a significant difficulty associated with the velocity controller is the feasible distribution of the tensions among the cables. Hence, during the task execution and due to model errors, cables may become slack or conversely, stretched. In order to cope with this undesired behavior, a torque control can be applied. However, this necessitates a feasible cable tension distribution

[3]Demonstration of FASTKIT: https://youtu.be/TJSsfjNlvZ4

(a) navigation mode

(b) undeployed configuration at the task location

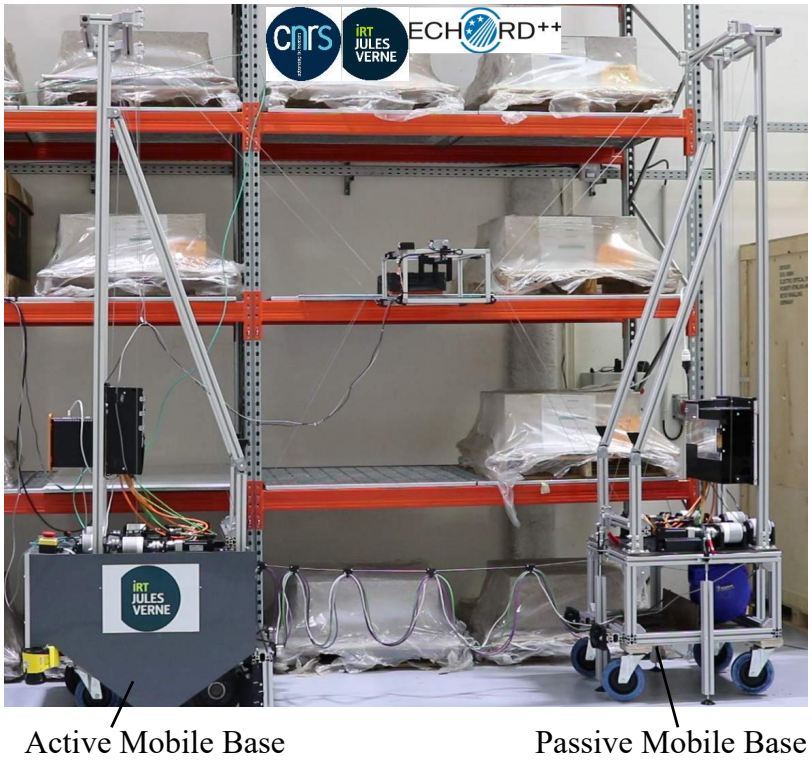

(c) deployed configuration at the task location

Figure 1.11: FASTKIT working modes

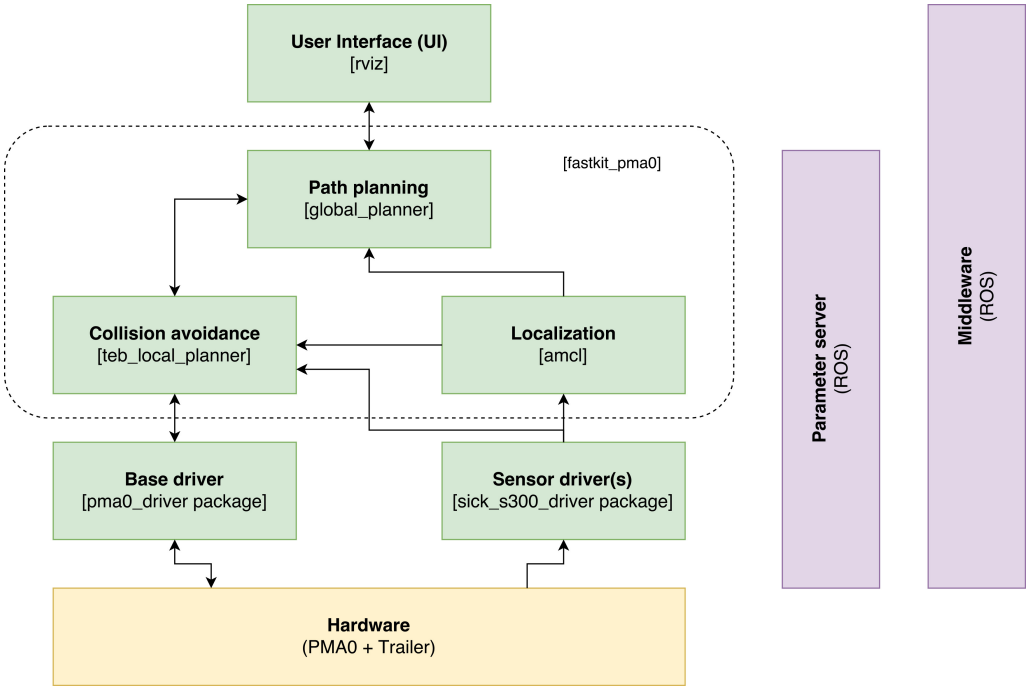

Figure 1.12: Architecture of the Fastkit navigation stack. Green boxes represents software packages, names of packages are in brackets

to effectively move the robot within its workspace.

1.3.2.3 FASTKIT Navigation

As discussed earlier, during the navigation mode, FASTKIT act as a single working unit, *i.e.,* a single mobile robot. Several approaches exist in the literature for the motion planning and control of mobile robots [Esk12, PJS06, BHJ+82, CHL+05, LaV06]. Based on aforementioned techniques, a two dimensional navigation stack[4] has been developed by researchers using the Robot Operating System (*ROS*)[5] framework [QCG+09] and used extensively for autonomous navigation of mobile robots. It is extremely useful for the navigation and path planning of mobile robots. The job of navigation stack is to produce a safe path for the robot to execute, by processing data from odometry, *i.e.,* wheels encoders, sensor streams *i.e.,* laser scanners, and environment map. It is implemented by means a set of interconnected algorithms. As shown in Fig. 1.12, those algorithms create altogether a complex decision making process:

Base driver: low-level software to control the velocity of the mobile robot;

Sensor driver: low-level software to get sensor information, in this case scanner distance readings;

Localization: software to localize the robot in the environment;

[4]Ros navigation stack [online]. http://wiki.ros.org/navigation
[5]http://www.ros.org/

Collision avoidance: software, with high priority, to compute collision free-path for the robot w.r.t. environment dynamics ;

Path planning: global planner to compute shortest path to goal;

User Interface: visualization tool to control robot behavior, here we have used RVIZ, a built-in software in *ROS*.

Therefore, the robot is able to model its environment, plan and move to a specific goal while avoiding obstacles. The core of the framework is to provide a set of standards, namely, sensors information, actuators control and transmission protocols, to allow users to share work and generic algorithms for multiple and various robotic systems. The reader is referred to [QCG+09] for further details about the *ROS* framework.

The key challenge for an autonomous mobile robot relies on the *perception* of its environment and the *decision* it makes accordingly. This means, from the robot point of view answering questions like: Where am I? Where am I going? How should I get there? Navigation can therefore be separated in three problematics:

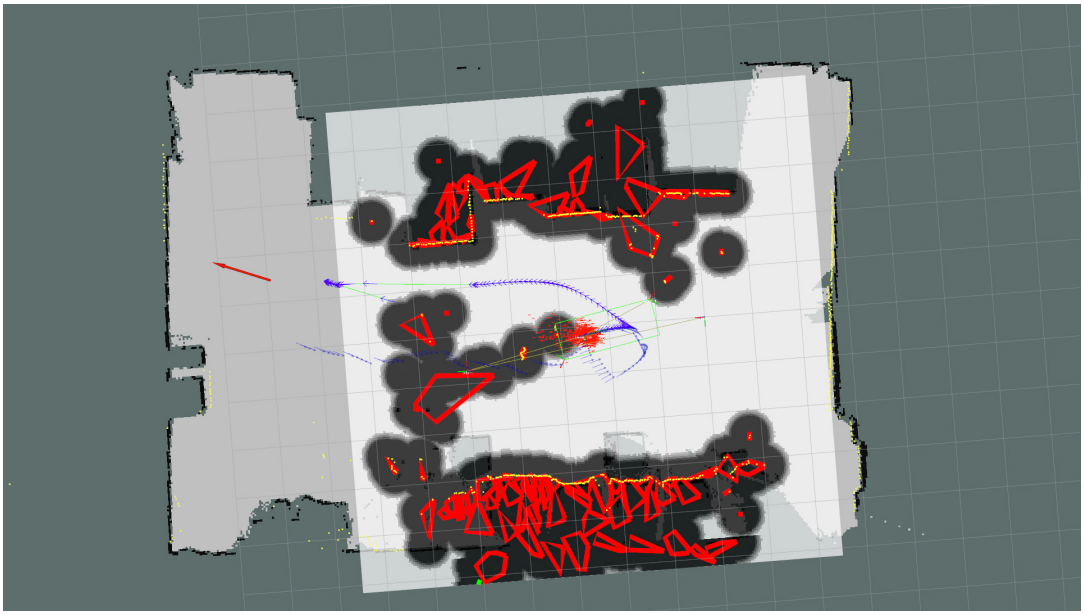

Figure 1.13: Visualization of the planned trajectory towards a goal. The robot is represented by the green box. The planned trajectory is represented by the blue arrow, red polygons represent obstacles and red arrow shows the position objective. Black areas represent the inflation around obstacles for the cost function to guarantee collision avoidance.

1. *Mapping*:

   In order to autonomously navigate, the first step is to generate a map (see Fig. 1.13), that is readable by the robot. The map generated by the navigation stack contains the location of the obstacles, in Fig. 1.13 represented by Red polygons. The obstacles are projected in to a two dimensional plane (the

floor), then inflated to create an area around the obstacles (in black) that guarantee that the robot will not collide with any objects, no matter what is its orientation. In the navigation stack, the map of the environment is represented in the form of a cost map. It is a grid map where each cell is assigned a specific value or cost. Higher costs indicate a smaller distance between the robot and an obstacle. The inflated obstacles contain maximum cost. Accordingly, obstacle free regions carry minimum cost.

The navigation stack uses Simultaneous Localization and Mapping (SLAM), a technique that consists in mapping an environment at the same time that the robot is moving. In other words, while the robot navigates through an environment, it gathers information from the environment through its sensors (for FASKIT sick lasers) and generate and/or update the map. Generally, the initial map is generated by manually moving the robot in the environment while running SLAM on it.

Two types of maps are generated by the navigation stack defined as local and global cost-maps. The global cost-map represents the whole environment(or a huge portion of it), and is only generated once for a constant environment. However, the local cost-map moves in the global cost-map in relation to the robot current position and, in general, formed when moving towards the goal.

2. *Localization*: The navigation stack uses Adaptive Monte Carlo Localization, which is a tool that allows to localize the robot in an environment with a known map. This localization system is based on the Monte Carlo localization approach which randomly distributes the particles in a known map, representing the possible robot locations, and then uses a particle filter to determine the actual robot pose.
3. *Planning motion*: At the final step, the robot plans and follows a path towards the goal while it deviates from the obstacles that appear on its path throughout the course. Path-finding is done by a planner which uses a series of different algorithms to find the shortest path while avoiding obstacles. Two path planners are used known as local and global planners. At first, the full path is optimized by the global planner over the global cost-map. It takes the current robot position and the goal and traces the trajectory of minimum cost with respect to the global cost-map. After a path has been obtained, the robot starts following the path generated by the global planner. During the execution, optimization of autonomous driving at close proximity is carried out by the local planner over the local cost-map. The local system detects the nearby obstacles (either static or dynamic), and is responsible for creating a trajectory roll-out over the global trajectory, that is able to return to the original trajectory with an optimal cost. Thus, together both planners find an optimal path given a

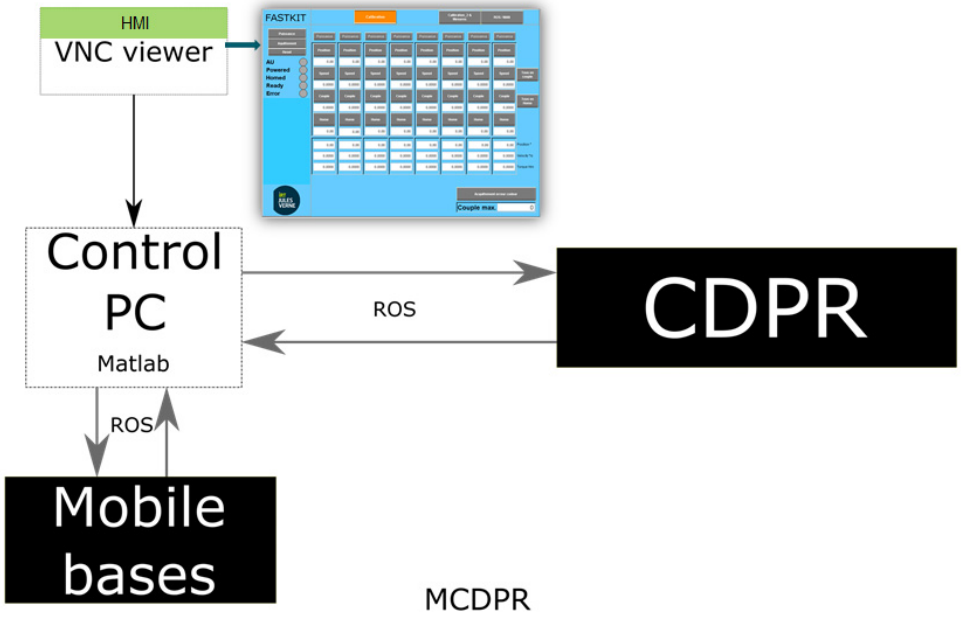

Figure 1.14: FASTKIT control architecture

navigational goal in the real world.

Figure 1.13 shows a result of planned trajectory for FASTKIT in a dynamic environment using *ROS* navigation stack. The computed polygons can be seen in red. Note that if no polygon can be found, a single point still represents the obstacle. As the environment also contain some dynamic obstacles, hence, the trajectory generated by the global planner toward the red arrow, *i.e.*, objective, was modified by the local planner as soon a dynamic obstacle is approached towards the robot. A simulation video showing the implementation of *ROS* navigation stack on FASTKIT can be seen at[6].

1.3.2.4 FASTKIT control architecture

The control architecture adopted in the scope of FASTKIT is described in Fig. 1.14. The control algorithms are written in Matlab and then sent to the industrial PC through *ROS*. A *ROS* package for communicating with the B&R™ motors had previously been developed. However, it should be noted that *ROS* cannot run as fast as the B&R™ industrial PC. Hence, some data might get lost during the communication and the system no longer conforms to an industrial standards in terms of robustness and response time.

[6] https://www.youtube.com/watch?v=VzfasvIjD1w

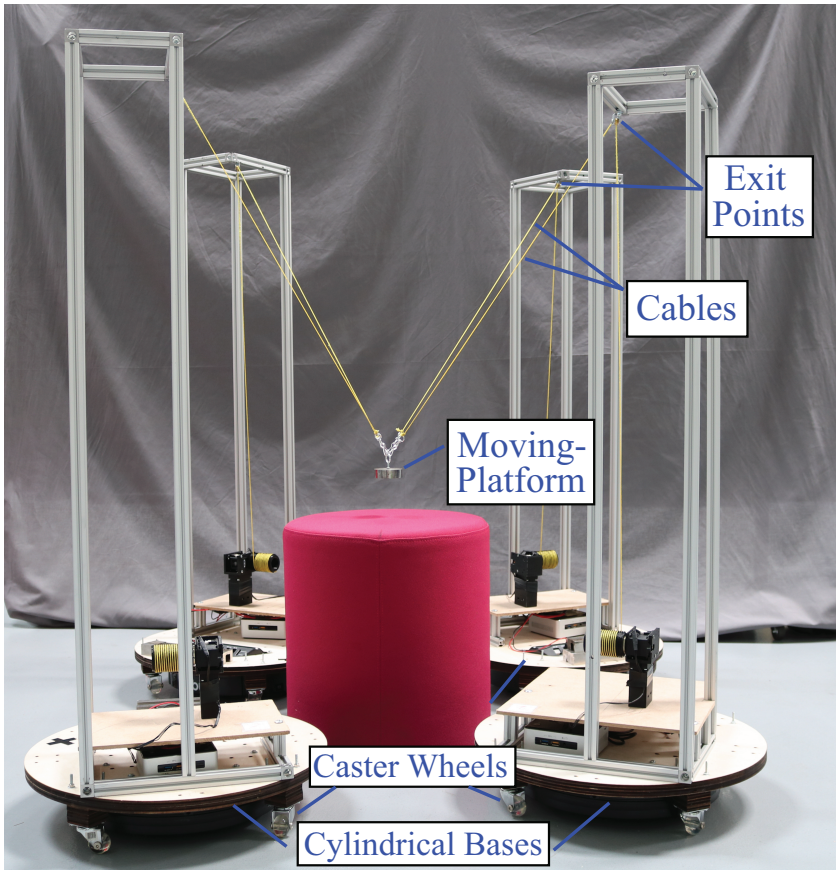

Figure 1.15: MoPICK a MCDPR prototype. MoPICK is capable of performing multiple manipulation tasks in a constrained environment, for example, a workshop.

1.3.3 Mobile Pick-and-Place (MoPICK)

A second MCDPR prototype developed in the course of this thesis is named MoPICK[7] shown in Fig.1.15. MoPICK is composed of a three DoF point mass moving-platform pulled by four cables mounted on four mobile bases. MoPICK uses four Turtlebots [KSJ+16], each with two motorized wheels and two supporting wheels at the front and rear, as its mobile bases. A cylindrical shaped structure of radius 0.25 m is added to support the aluminum frame which holds the pulleys of the CDPR. To improve the stability of the mobile bases, four additional caster wheels are added. Thus, each mobile base has eight wheels in total and the design ensures that at least five wheels are always in contact with the ground. Indeed, by construction, either the three rear passive wheels or the three front passive wheels are in contact. The motorized wheels have individual spring suspensions, which permit ground contact and thus the ability to drive the base at all times.

MoPICK mobile bases displace via a non-holonomic differential drive mechanism [BL89, MM14]. It means that each mobile base can generate a pure rotational

[7]Demonstration of MoPICK: https://youtu.be/_zfqtNsrpHI

motion about a vertical axis passing through its geometric center (${}^{bj}z$) and a translational motion in the direction perpendicular to the axle of the motorized wheels ${}^{bj}x$. The CDPR carried by MoPICK is designed such that the exit points A_{ij} lie on the aforementioned vertical axis (${}^{bj}z$), preventing changes in the directional vector $\mathbf{u}_{ij}$ of the cable $\mathscr{C}_{ij}$ due to rotational motion of $\mathscr{M}_j$. Thus, for a given pose of the moving platform, cable configurations are determined by only localizing the mobile bases in ${}^0x{}^0y$ plane. The mobile bases are displaced by sending velocity commands to the motorized wheels while the CDPR is controlled either by defining its cable tensions or cable velocities.

To avoid slack, the cable tension lower bound is null. The cable tension upper bound depends on the actuation system used to actuate the cables of the MCDPR, *i.e.,* motors, winches etc. In MoPICK prototype, Dynamixel MX-64AT actuators and winches whose drum diameter is equal to 0.2 m, are used, to pull the cables. Based on the hardware specification and safety issues, the cable tension upper bound is set to 15 N.

V-REP model of MoPICK:

A dynamic model of the MoPick system is developed using the simulation environment V-REP [RSF13], shown in Fig. 1.16. The implemented solution enables us to use the same software in order to control the real or the virtual hardware. As a result we can test and debug new algorithms in simulation (with a perfectly known ground truth) before using them on the real team of robots for final tuning and verification, thus speeding up the development time and easing the debugging process.

The pulleys and cables are modeled as a sequence of joints and mass objects, as shown in Fig. 1.17. The pulleys are represented as a vertical revolute passive joint followed by a small spherical mass and a horizontal revolute passive joint. The cables are modelled as a sequence of prismatic joint, cylindrical mass, prismatic joint, cylindrical mass and a final spherical joint attaches the cable to the common platform. The model does not take into account the pulley diameter and the cable sag. The first prismatic joint allows to control the cable length, while the second prismatic joint is responsible for the cable behaviour through a specific call-back script that allows to model the cable elasticity and damping but also the fact that cables transmit the tension forces but no compression forces. To have a stable simulation, some model design rules need to be considered [VRE]. In particular the cable masses are slightly augmented in order to reduce bad conditioning on the solver. In our tests, the Vortex physical engine gave best results.

The model of the mobile bases is based on an existing TurtleBot model [Veg16]. However, based on the design of MoPICK, a cylinder and four caster wheels are added to each mobile bases for additional stability (see Fig. 1.16).

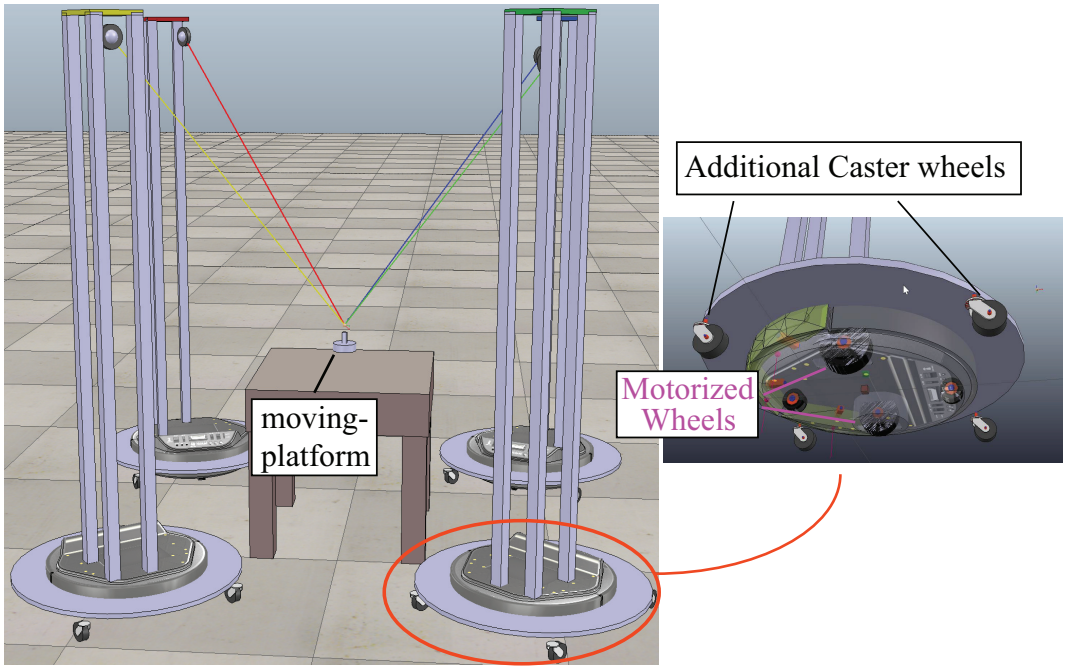

Figure 1.16: V-REP model of MoPICK

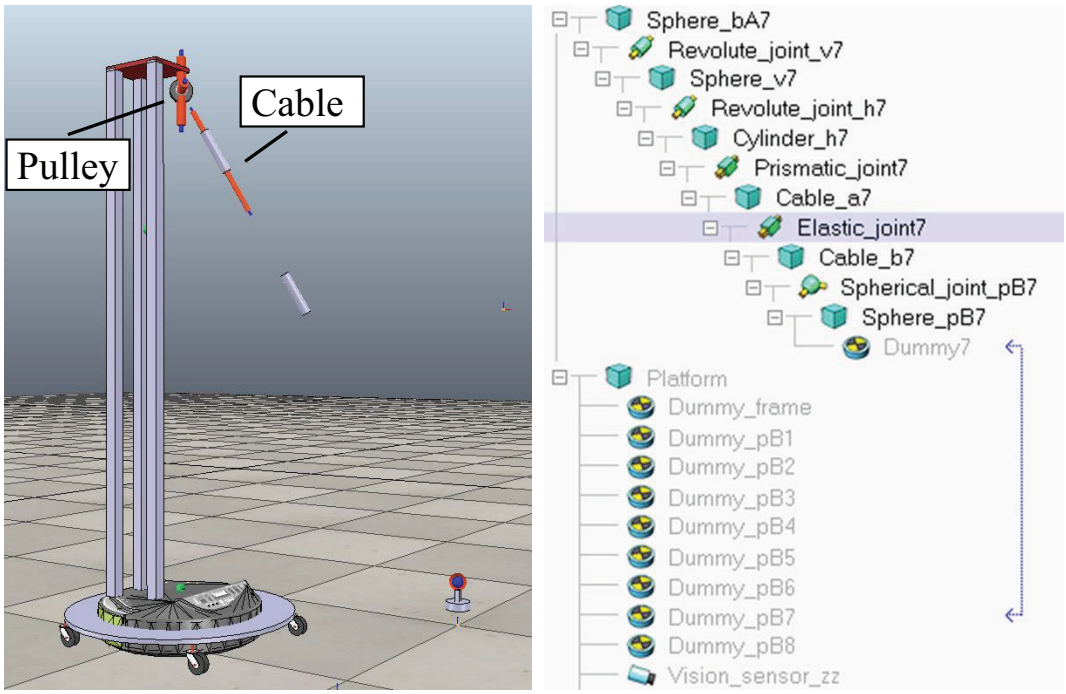

Figure 1.17: The representation of a cable and its pulley in V-REP

1.4 Challenges and Open Issues

As discussed earlier, MCDPRs combine the autonomy of mobile robots with the advantages of CDPRs; however, the combination of these two types of manipulators make them more complex. Moreover, their combination also adds constraints to the

individual sub-systems. In this section, we outline the main aspects of theoretical and technical issues and challenges raised by the peculiarities of MCDPRs as a new robotic system arrangement. These issues and challenges were mainly faced while designing FASTKIT and MoPICK. In the light of these aspects, the main contributions of this thesis will be defined.

1.4.1 MCDPR Equilibrium

The first step is to investigate the conditions that must be respected in order to keep the MCDPR in the state of equilibrium. In case of classical CDPRs, the cable exit points are mounted on a fixed base. As a result, its equilibrium solely depends on the equilibrium of its moving-platform, which is achieved by balancing the required set of wrenches with the wrenches generated the cables on the moving-platform, given the tensions in the cables are within their respective bounds. In contrast, non-fixed bases may become unstable due to the reaction forces and moments generated by the tensions in the CDPR cables mounted on it. As a consequence, for MCDRPs, the stability of their mobile bases must be defined as a function of the cable tensions. Afterwards, for the analysis of MCDPRs, the stability conditions associated with the equilibrium of the mobile bases must be taken into account in addition to the equilibrium of their moving-platform.

1.4.2 Workspace

One of the major challenges during the task mode of FASTKIT, *i.e.*, when the system reaches at the task location and needs to be deployed in order to perform the desired pick and place operation, is to determine if the desired task is feasible and within the reachable workspace. Moreover, from the design point of view, is it important to investigate to what extent these robots are capable of generating forces and moments at their moving-platform, while respecting all the equilibrium conditions associated with the CDPR and the mobile bases. As a result, a methodology to trace the workspace of MCDPRs is required.

1.4.3 Kinematics

From the design point of view of MCDPRs, in addition to their wrench capabilities, it is also essential to develop a methodology that can evaluate their kinematic performance. The kinematic performance of any robotic system can be analyzed from its first-order kinematic model. Accordingly, to analyze the twist capabilities of MCDPRs, it is also essential to derive its first-order kinematic model.

Each manipulator type in a MCDPR has its individual kinematic ability, *i.e.,* in general, a cable robot has a parallel kinematic architecture while a mobile base has a serial kinematic architecture. With the integration of these two individual

architectures, a general kinematic architecture for MCDPRs can be developed, which can be helpful to derive their first-order kinematic model. The model can be later exploited to acquire the MCDPR twist capabilities. Furthermore, the aforementioned model can also be useful for constructing the velocity control law for MCDPRs, which is quite easy to implement and apply.

1.4.4 MCDPR Redundancy

There are two different types of redundancies in robotic systems. The first type is actuation redundancy, in which the system possess more number of actuators than the DoFs of its moving-platform. The second type is kinematic redundancy, in which the system contains more DoFs compared to the DoFs of the moving-platform, *i.e.,* kinematically redundant manipulators posses more controlling variables than needed for a set of specified tasks. For MCDPRs, we may encounter both of these types of redundancies. Both of them can be advantageous; however, this comes usually at the expense of complex analysis of the system.

Actuation redundancy

As detailed earlier, to compensate the uni-directional force constraints in classical CDPRs, more than n number of cables are used, which generates $(m - n)$ degrees of actuation redundancy. As a result, an infinite number of possible sets of cable tensions exists that can keep the moving-platform in a desired pose. However, finding a feasible distribution of forces among the cables can be quite challenging. The classical approaches used to determine the feasible distribution of the cable tensions only take into account the equilibrium of the moving-platform while respecting the constraints associated to the cable tension limits. However, for MCDPRs, the stability of the mobile bases must be considered in addition to the cable tension limits for computing the feasible distribution of the cable tensions. The force distribution can be later used to develop the torque control laws for MCDPRs.

Kinematic redundancy

One of the objectives of introducing MCDPRs is to achieve a continuous and autonomous reconfiguration of RCDPRs. However, as a result of the additional mobility, MCDPRs are kinematically redundant. This is an issue of major relevance for motion planning and control purposes. This type of redundancy can be exploited to re-configure the CDPR's geometric architecture. Thus, motion planning of such systems should exploit the kinematic redundancy in order to find the feasible configurations of the system with respect to the desired task.

For FASTKIT, one of the major challenges concerned the deployment strategies for performing a task safely and reliably. It should be noted that during the task

mode, FASTKIT is kinematically redundant due to the additional mobility of the active mobile base. Thus, the issue of kinematic redundancy must also be considered. Although, FASTKIT acts as a classical mobile base during the navigation, in general, it may not be the case for classical MCDPRs. For example, in case of MoPICK, all the mobile bases are active and can move independently. Hence, more generic planning strategies are required for MCDPRs. This includes redundancy resolution schemes to avoid collisions with the obstacles in the surrounding environment.

1.5 Thesis Contributions and Organization

In the light of the detailed discussion in Sec. 1.4, the scientific challenges associated to MCDPRs are grouped into five categories:

1. **MCDPR Equilibrium:** We began our research by deriving MCDPR's static equilibrium conditions. As explained earlier, a classical CDPR connected to fixed base considers only the static equilibrium of its moving-platform while respecting the bounds on the cable tensions. In contrast, as a MCDPR possesses moving bases, additional constraints are generated, which are associated with stability of the mobile bases. Thus, these stability conditions must be taken into consideration to ensure the complete equilibrium of a MCDPR. The stability of a mobile base is characterized by its tipping and sliding conditions. The tipping conditions depend on the moment generated at the boundaries of the mobile base footprint. These tipping conditions depend uniquely on the weight of the mobile base and the tension in the cables mounted on it. Likewise, the sliding conditions also depend on the weight of the mobile base and the tension in the cables carried by it. However, the sliding conditions are represented in the form of a friction cone. For ease of analysis, the non-linear sliding conditions are linearized and the friction cone is transformed into a four-sided friction pyramid.
2. **Tension Distribution Algorithm for MCDPRs:** The control of cable-driven manipulators with actuation redundancy requires a real-time algorithm that can compute continuous distribution of the cable tensions. For classical CDPRs, a geometric approach known as Barycenter/Centroid is frequently used to acquire a real time, continuous and feasible solution of the cable tensions, which only considers its lower and uppers bounds imposed by the actuators and the transmission systems. However, this approach is not directly applicable on MCDPRs due to the additional conditions associated with the static equilibrium of the mobile bases.

   We have developed a real time Tension Distribution Algorithm (TDA) by extending the classical Barycenter/Centroid method to MCDPRs. The algo-

rithm forms a Feasible Cable Tension Domain (FCDT) representing the set of feasible tensions based on the cable tension limits and the conditions associated with the static equilibrium of the mobile bases. This FCTD takes the form of a $(m-n)$-dimensional convex polytope. The presented TDA finds the vertices of the feasible polygon or proves that it is null. If the feasible polygon exists and is determined, then the centroid of the polygon is calculated which is a solution furthest from all the constraints. The coordinates of the centroid are used to compute the feasible distribution of the cable tensions. The proposed algorithm is investigated on multiple case studies including FASTKIT and MoPICK. The obtained results show that the new set of constraints developed for MCDPRs are sufficient to compute feasible cable tensions such that they stay within the required set of limits while ensuring the stability of all the mobile bases. The algorithm is relevant for real-time implementations, however, it is only applicable and validated for MCDPRs up to two degrees of actuation redundancy.

3. **Workspace Analysis of MCDPRs:** For the desired task to be feasible, it must be within the region where robot can exert the required set of wrenches in order to accomplish the task. For this purpose, we have developed a methodology to determine the Wrench-Feasible Workspace (WFW) of MCDPRs. Similar to the TDA, the proposed workspace also depends, not only on the static equilibrium of the moving-platform, but on the static equilibrium of the mobile bases as well. WFW is traced using Available Wrench Set (AWS) which defines the set of wrenches the moving-platform can generate. AWS of MCDPRs takes the form of a n-dimensional convex polytope. The AWS is constructed using two different approaches, *i.e.*, convex hull and the Hyperplane Shifting Method (HSM). The convex-hull approach uses the vertices of the cable tension space to determine the vertices of AWS and forms the boundary of the convex polytope. HSM allows us to determine the AWS geometrically by characterizing the facets of the polytope. The equivalence between both the approaches is also presented. Multiple case studies are investigated in order to show that the approach is applicable to both planar and spatial MCDPRs. The approach is experimentally validated on a MCDPR with a point-mass end-effector and two mobile bases.
4. **Kinematic Performances of MCDPRs:** To derive the MCDPRs first-order kinematic model, each cable of the manipulator is modeled as a Universal-Prismatic-Spherical kinematic chain. Furthermore, as mobile bases are only capable of generating two-DoF translational motions and one-DoF rotational motion in a plane, they are modeled as a Revolute-Prismatic-Prismatic kinematic chains. By integrating the aforementioned chains, a general kinematic

architecture is developed for MCDPRs, where the cables carried by the jth mobile base are connected in parallel with each other, while the jth mobile base is linked in series with the aforementioned parallel architecture of the cables mounted on it. The first-order kinematic model is used to determine the Available Twist Set (ATS) of MCDPRs by considering both the joint velocity limits for the cables and the mobile bases. If $m = n$, ATS will correspond to a single convex polytope. However, if $m > n$, ATS will be the region bounded by C_m^n convex polytopes. Finally, ATS will be used to determine the twist capacities of the moving-platform.

5. **MCDPR Path Planning:** The last contribution of the thesis focuses on the utilization of kinematic redundancy in MCDPRs to find system configurations that can make the desired tasks feasible while respecting the set of constraints. Hence, the final chapter of the thesis presents the redundancy planning schemes for MCDPRs.

   Redundancy planning of MCDPRs is presented in two parts. At first, the problem of determining an optimal path for MCDPRs with one degree of kinematic redundancy is addressed. The problem to the path planning is formulated as a bi-objective optimization problem that corresponds to the minimization of the total trajectory time and maximization of the robot wrench feasibility throughout the trajectory. FASTKIT is used as a case study with a desired pick-and-place operation.

   The second half of the chapter presents two different path planning strategies for highly redundant manipulators. The first approach is a sampling based iterative path planning algorithm which plans the manipulator's path in two subsequent stages. In the first stage, the algorithm searches for a feasible and collision free path of mobile bases. The second stage generates an optimal path of the moving-platform to reach at the desired pose. The second approach deals with the path planning of highly redundant MCDPRs using direct transcription optimization method. It is an optimization based approach where the continuous path planning problem is transcribed into a discrete optimization problem of N steps, with the goal to maximize the wrench capability of the robot at each step while minimizing the total path length. The desired moving-platform poses are enforced using a set of equality constraints. In the direct method, rather than simulating the continuous evolution of the system, the states at all way-points are optimized simultaneously. The resulting discrete path is transformed into a continuous motion profile in time using cubic splines. The proposed approach is validated through simulation and experimentally on MoPICK.

Thesis Organization

This manuscript is organized as follows. Chapter 2 presents the current state-of-the-art on the most relevant issues to the subject related to this thesis. Chapter 3 starts by expressing the static equilibrium conditions of the moving-platform and mobile bases. The chapter uses these conditions to develop a real-time and continuous Tension Distribution Algorithm for MCDPRs. Similarly, the equilibrium conditions are also used in Chapter 4, which analyzes the Wrench-Feasible-Workspace of MCDPRs. Chapter 5 presents the first order kinematic model of MCDPRs. Moreover, based on the aforementioned model, it investigates the twist capabilities of the manipulator. Chapter 6 focuses on the redundancy resolution schemes for the reconfiguration planning of the MCDPR cable layout in order to accomplish the desired task. Finally, Chapter 7 concludes this manuscript by summarizing the main contributions of this doctoral thesis and by discussing future research perspectives.

2

State of the art

Contents

The aim of this chapter is to review the most relevant issues to the subject related to this thesis. The first part of the chapter provides an overview on the state of the art on CDPRs and RCDPRs. This review covers their wide range of applications. The variety of prototypes developed in the literature reflects the large number of possibilities offered by cable-driven mechanisms.

One of the fundamental problem in cable-driven mechanisms is the unilateral actuation constraints of cables. Thus, the review also covers different approaches used to deal with fundamental problem on finding the suitable cable tension distribution. This problem arises when the number of actuators is higher than the number of degrees of freedom of the moving-platform. It becomes much more challenging when cables are additionally mounted onto the moving bases.

Afterwards, the review covers multiple approaches for the workspace analysis of CDPRs in order to characterize their wrench capabilities. Finally, the review is completed by presenting different path planning strategies.

2.1 Existing CDPRs and their Applications

CDPRs are being used in multiple applications. Research on CDPRs originates from America in 1984. A cable-controlled parallel manipulator is designed for underwater operation. In 1989, the RoboCrane project was started in America by the National Institute of Standards and Technology (NIST), which stand out for simplicity and extensive use especially in processing machinery, port cargo handling, bridge construction, welding, airplane paintings and other areas, as shown in Fig 2.1.

Another CDPR prototype, named FALCON [KCTK97], was developed at the end of the 90s by Kawamura *et al* from Ritsumeikan University. Falcon is six DoF cable robot and uses seven cables with an emphasis on achieving high speed for assembly operations. This CDPR has the ability to reach the linear velocity up to 13 m/s and linear accelerations of 43 G.

In the last decades, research on CDPRs gains wide attention and is highly motivated by the modern engineering demand for large payload capacity and workspace. CDPRs have been increasingly and widely applied in relevant tasks, but mainly in tasks which require a large workspace, *e.g.*, support structures for giant telescopes [YTWH09], cargo handling [HC04], large-scale assembly and handling operations [PMV10]. Other applications include the broadcasting of sporting events, cargo handling [HC04], warehouse applications [BLS+13], haptic devices [GRR01, FCCG14], motion simulators [MLB+16], and search and rescue deployable platforms [MD10] (see Fig .2.2). In 2013, Pott *et al.* designed another family of CDPRs, the IPAnema series [PMK+13], for fast pick-and-place and other industrial operations (see Fig. 2.6). Some of the world's well-known CDPR prototypes and their applications are detailed below.

The Skycam is the most commercially used CDPR, shown in Fig. 2.3. The Skycam uses a suspended cable configuration with four cables and three degrees of freedom moving-platform equipped with a camera system. The aim of skycam is to maneuver the onboard camera in translation in the open space over a playing area of a stadium or arena. The camera package weighs less than 14 kilograms and can achieve a velocity up to 13 m/s.

CDPRs have also proven successful for handling heavy payloads in large areas. Recent studies have been performed in the framework of the CoGiRo (Control of Giant Robot) ANR project [CoG08]. Its main goal is to propose and validate innovative methodologies and means to design, calibrate and control CDPRs having

Figure 2.1: NIST RoboCrane painting an aeroplane

Figure 2.2: MARIONET-CRANE, CDPR for search and rescue operations

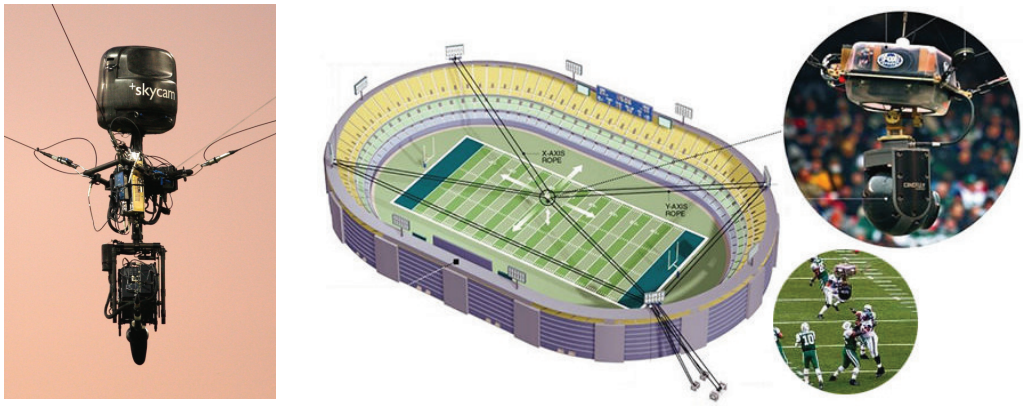

Figure 2.3: Skycam, a CDPR for broadcasting sport events

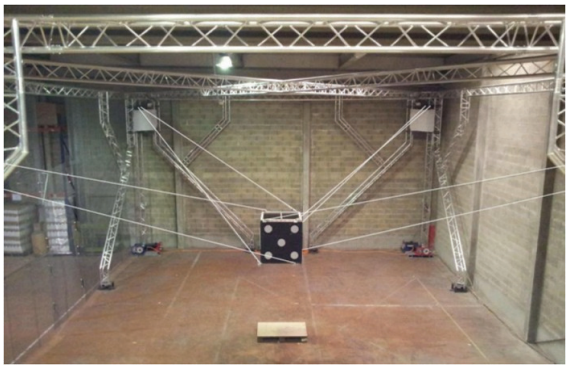

Figure 2.4: CoGiRo prototype, developed by the LIRMM and Tecnalia

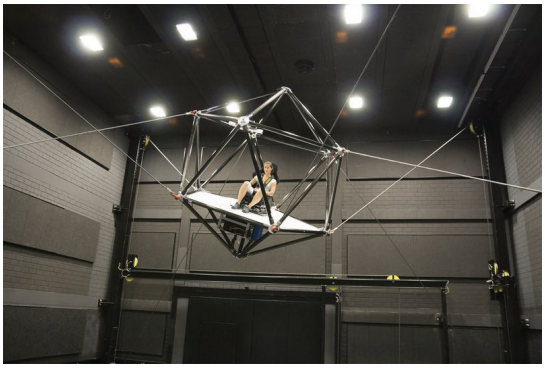

Figure 2.5: MPI CableRobot Simulator

a very large workspace and handling heavy payloads. Multiple contributions have been carried out in the framework of the CoGiRo project. [LGCH13] estimates the weight of the moving-platform and actuator dynamic parameters which resulted in better tracking performances. [GCRB12] introduce a new simplified static analysis of CDPRs by inextensible cables of non-negligible mass. [GCRB15] propose tools to

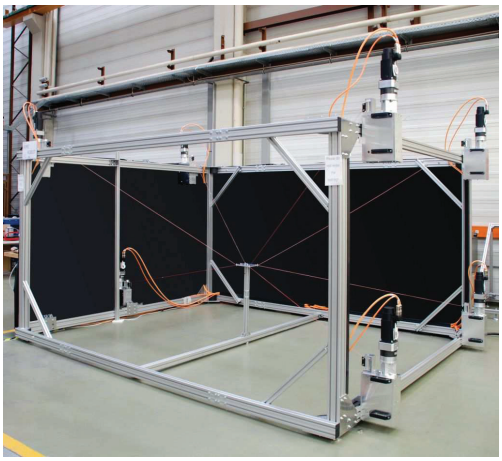

Figure 2.6: IPAnema prototype developed by Fraunhofer IPA

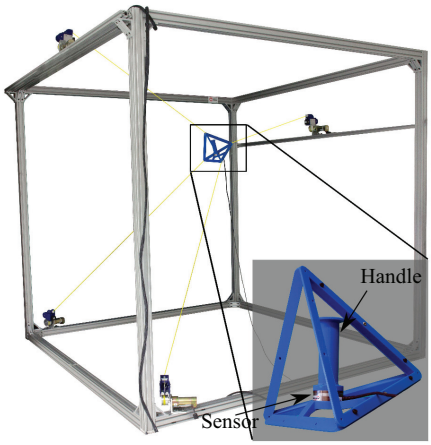

Figure 2.7: CDPR based haptic interface developed at Université Laval

Figure 2.8: CABLAR CDPR protoype developed by University of Duisburg-Essen

develop an efficient cable layout. The CoGiRo CDPR prototype is shown in Fig. 2.4.

CDPRs have also been used for developing motion simulators. Figure 2.5 shows a CDPR prototype for motion simulation [MLB+16] developed at the Max Planck Institute for Biological Cybernetics in cooperation with the Fraunhofer Institute for Manufacturing Engineering and Automation IPA. This is the first CDPR capable of transporting humans while at the same time setting new standards in terms of workspace, acceleration and payload for a motion simulators.

CDPRs can also be used as haptic devices allowing the user to move in large spaces. The low inertia of CDPRs over a comparatively big workspace makes them appropriate for large workspace haptic interfaces [GASM08, HKMP15]. One of the

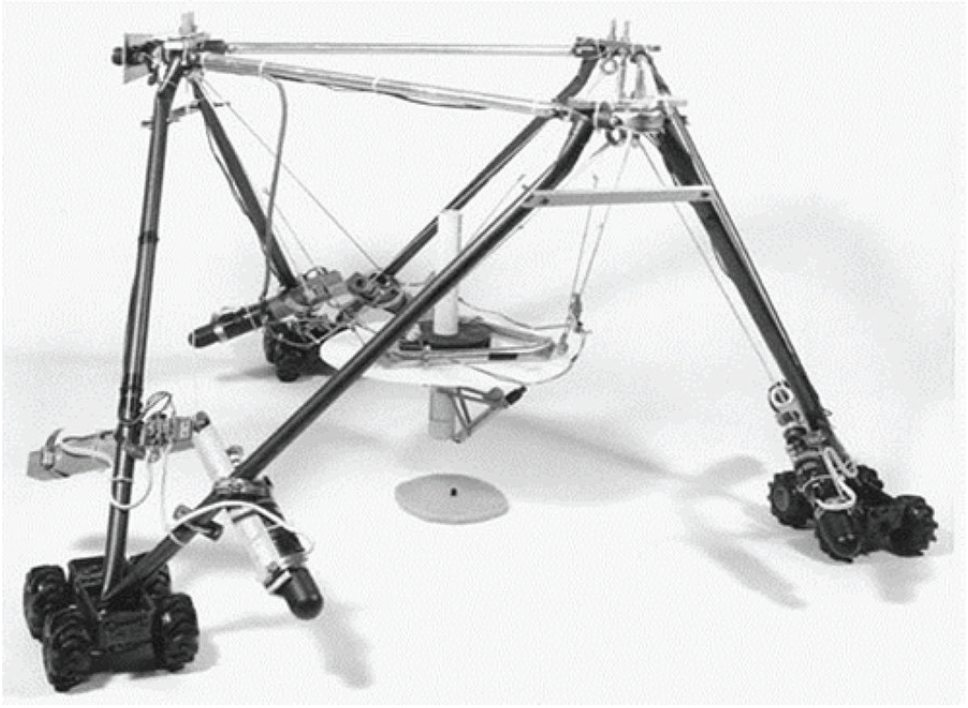

Figure 2.9: NIST Mobile RoboCrane

CDPR-based prototypes used as a haptic device is named SPIDAR, designed for complex hand physical interactions [Sat02]. Another CDPR based haptic prototype, developed at Université Laval, Québec, Canada [FCCG14], is shown in Fig. 2.7.

CABLAR shown in Fig. 2.8 is a fully-constrained CDPR prototype driven by eight cables and is mainly designed for warehousing and storage retrieval tasks. CABLAR is capable of generating fast motions while consuming comparably low energy. [BLNS12] shows that by using by a CDPR based prototype for the transportation of the goods in logistic applications can drastically reduce the cycle time, which is crucial in such applications.

2.2 Reconfigurable CDPRs

Several research studies have been performed in the field of Reconfigurable CDPRs. Preliminary studies on Reconfigurable CDPRs were performed in the context of the NIST RoboCrane project [BADJ96, BJP+00], as shown in Fig. 2.9. Izard et al [IGM+13] also studied a family of RCDPRs for industrial applications. Some interesting tools for the design and control of Reconfigurable Cable-Driven Parallel Robots were developed in [Bla15] while considering cable sagging and dealing with uncertainties. Some of the RCDPR prototypes and their applications are detailed below.

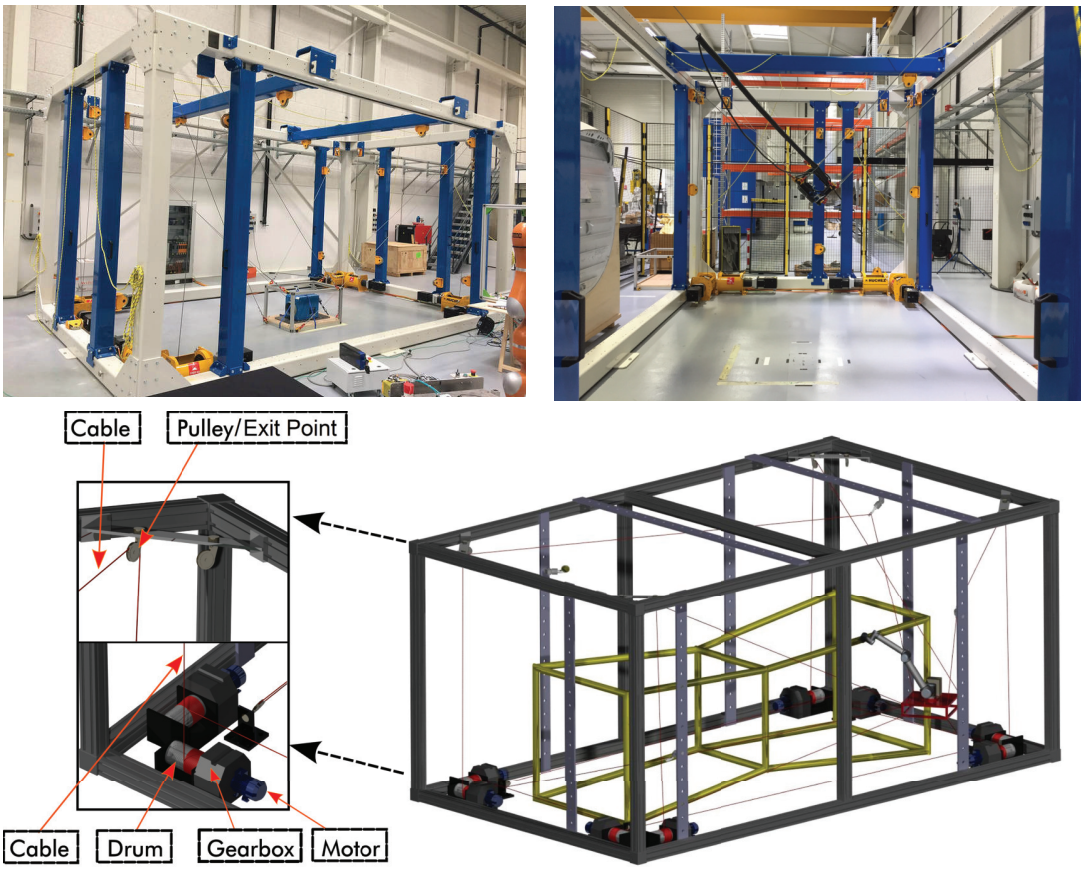

Figure 2.10: CAROCA prototype located at IRT Jules Verne (Technocampus Ocean)

IRT Jules Verne CAROCA Project

From a mechanical point of view, changing the geometry of CDPR is relatively easy by modifying the location of the cable exit points. Thus, discrete reconfigurations where the locations of the cable exit points are selected from a finite set of possible values were studied in [GCGG15, GCGG16]. Those papers proposed different strategies to determine an optimized robot architecture based on the required task and the robot's environment.

A RCDPR with discrete reconfigurations capabilities is developed at IRT Jules Verne in the framework of the CAROCA project[1], is shown in Fig. 2.10 . CAROCA project aimed at investigating the performance of CDPRs and RCDPRs for large scale industrial applications in cluttered industrial environments. The targeted industrial applications for CAROCA are (*i*) assembling, sandblasting and painting of big structures, (*ii*) inspection and photogrammetry measurement of large parts and (*iii*) pick-and-place operations of various parts in terms of mass and shape. CAROCA prototype is 7 m long, 4 m wide and 3 m high. It is composed of eight cables coiled around 120 mm diameter Huchez^{TM} winches, which are pulling a moving-platform.

[1]Evaluation des CApacités de la RObotique à CÂbles dans un contexte industriel

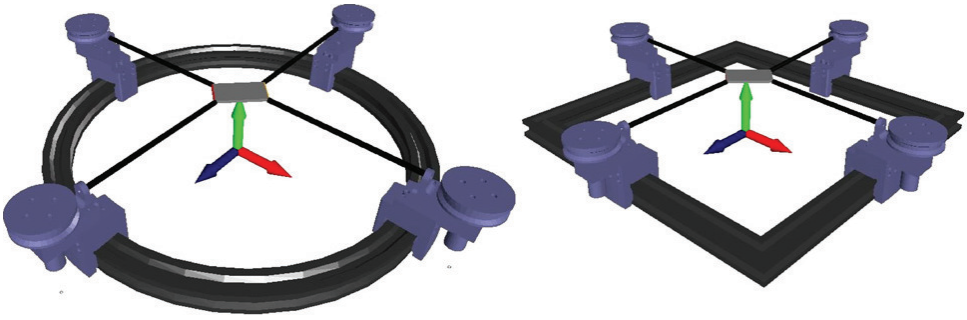

Figure 2.11: CDPRs with base mobility in multi-domain modeling and simulation tools [AAK17]

The winches are actuated by synchronous motors having a nominal speed of 2200 rpm and a nominal torque equal to 15.34 Nm. A two-stage gearbox of reduction ratio equal to 40 is mounted between each motor and its winch. As a consequence, the prototype is capable of lifting up to one ton. The prototype has pulleys of radius 150 mm with two degrees of freedom all of which can be remounted to a multitude of different positions on the frame. Thanks to its reconfigurability, the robot can be configured in a both suspended or fully-constrained configurations depending on the application at hand.

CDPRs with base mobility

CDPRs with moving bases have also been investigated in the past. [AAK17] presents a study on planar CDPR with a base mobility for optimizing the orientation workspace and stiffness of the moving-platform. Mainly, two different configurations were analyzed and compared to the traditional fixed-base CDPRs as shown in Fig 2.11. It has been shown that the rectangular configuration improves the orientation workspace in one direction, however, it is limited by the nature of the base setup. The circular configuration exhibited vast improvements both in terms of translational and rotational workspace. A similar system for optimizing the robot configuration in order to increase the position accuracy of the moving-platform is presented in [SRK18].

Another example of a variable structure and reconfigurable CDPR carried by multiple moving bases for agricultural applications is shown in Fig. 2.12. To meet higher system flexibility and application requirements in various agricultural plants, it is convenient to implement these systems by means of mobile pillars that transport winches and platform, and can be fixed on stand-on legs at some locations to provide stable CDPR structure [SRB15].

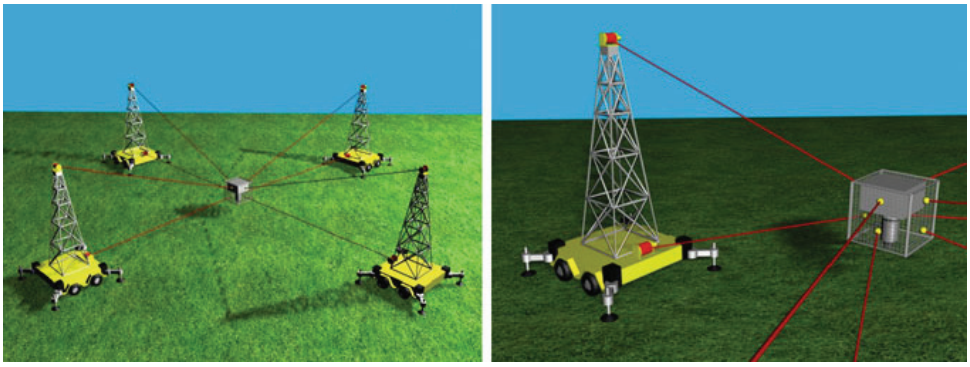

Figure 2.12: CDPR with mobile pillars for agricultural applications

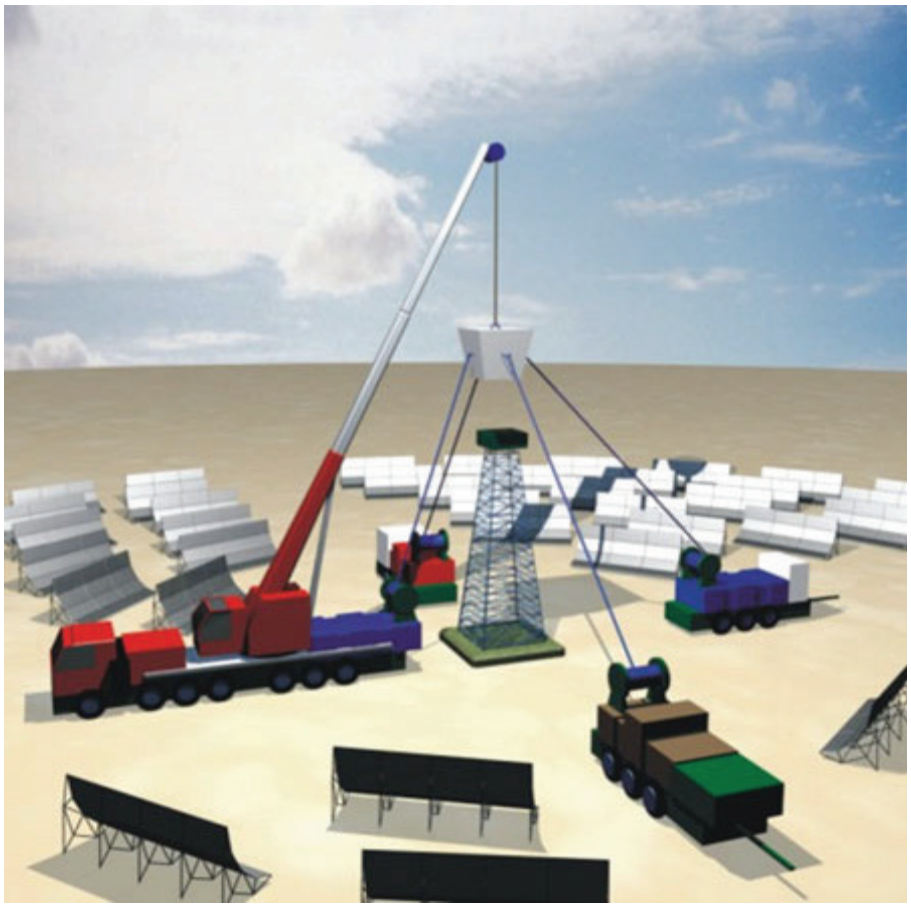

Figure 2.13: Concept idea of an Extended-crane system

Extended-crane system

Another concept idea of a reconfigurable CDPR is shown in Fig 2.13 represented as extended-crane system. It represents a combination between a CDPR, multiple moving units and a conventional crane. The robot configuration is created to support task decomposition between the overhead crane (mainly performs the weight balancing and gross motion) and the side cable system (mainly responsible for fine lateral positioning and orientation). The extended crane can considerably improve

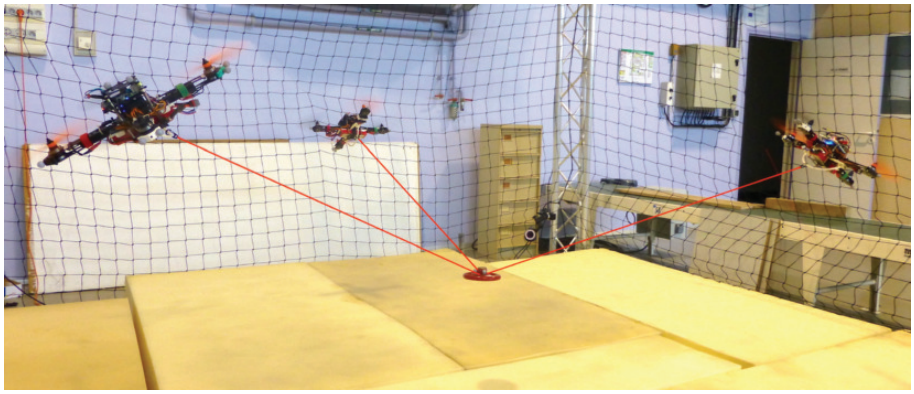

Figure 2.14: Aerial cable towed prototype developed at LS2N [ECC19]

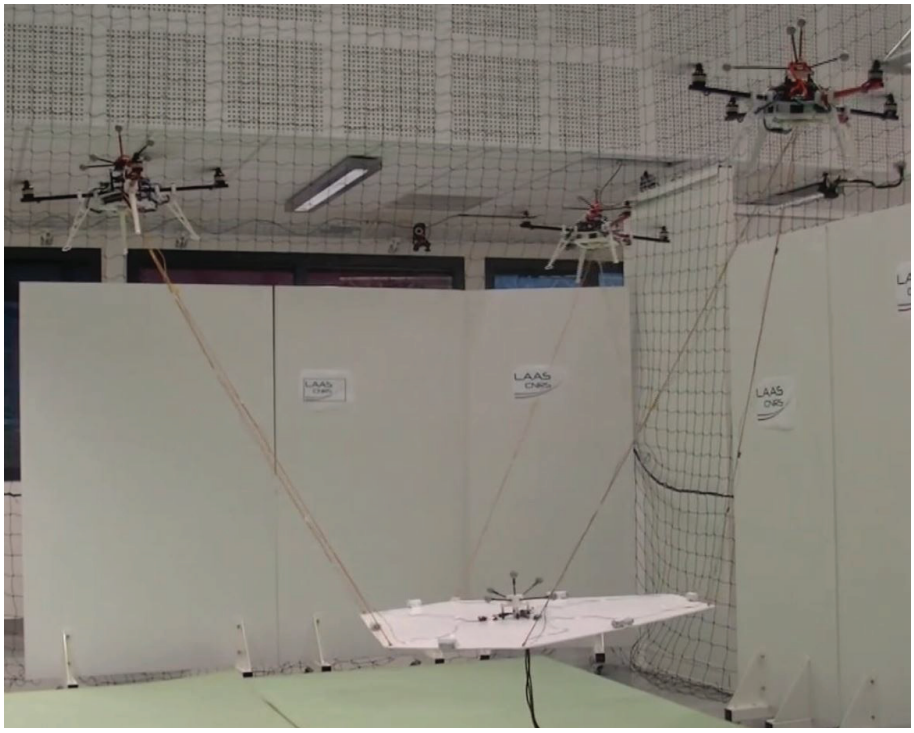

Figure 2.15: Octahedral version of the FlyCrane system [MFDRGC13]

flexibility and efficiency of assembly of heavy parts with complex irregular geometry.

Aerial cable towed systems

Aerial cable towed systems can also be seen as reconfigurable CDRPs that are composed of multiple aerial vehicles connected to a rigid body payload or to a point mass moving-platform through cables as shown in Figs. 2.14 [ECC19] and 2.15 [MFDRGC13]. Aerial cable towed systems have proved to be useful in contexts, such as supply delivery missions and rescue operations [BKMO11], as well as environmental monitoring and surveillance [Wil06]. Compared to classical CDPRs, the motion planning and control of aerial cable towed systems is much more

challenging. Moreover, the payload capability of aerial cable towed system largely depends on the maximum thrust of the aerial vehicles.

2.3 Relevant research issues

This section aims at providing an overview of the current state of the art related to the subject of this thesis. One of the most challenging issues in cable driven mechanisms is the unilateral actuation constraints of cables. Indeed, cables can pull, but not push an object. This issue is also true for MCDPRs. As a consequence, existing works on tension distribution strategies, wrench capability analysis of CDPRs and path planning approaches are described thereafter.

2.3.1 Tension Distribution

The static or the dynamic equilibrium of a CDPR is assured by its cable tensions. Most cable robot systems where solely cables are used to displace the end-effector require more than n number of cables to compensate their uni-directional force constraints. Hence, CDPRs contain $m - n$ degrees of actuation redundancy. While controlling such redundantly actuated manipulators, the distribution of forces among its cables can be quite challenging. Indeed, at any point along a trajectory, there exists an infinite number of possible sets of cable tensions that can keep the moving-platform in equilibrium. If cable tensions are not distributed homogeneously, they may approach their lower or upper limits. In case of reaching their minimum limit, cables may become slack, which can lead to lack of stiffness and hence a loss of control. Therefore, it is important to find a continuous and acceptable distribution of tensions in the cables to perform a desired task. Non-continuous cable tensions could be considered as solutions; however, since they are needed for control, such tensions would cause steps in motor torques, which in turn leads to vibrations and high mechanical loads.

For classical CDPRs, different approaches were proposed in the literature to calculate the force distribution among its cables known as Tension Distribution Algorithms (TDAs). Most of these TDAs optimize the cable tensions based on a given criterion, while taking into account the constraints on the cable tension limits. The following section provides a brief overview on the existing TDAs.

The most commonly used TDAs for calculating the force distribution among the cables of classical CDPRs are the following:

– Gradient-based optimization approach (Verhoeven's method): [Ver04] addresses the problem of finding acceptable solutions by transforming it into a nonlinear optimization problem on a convex polyhedron. The solution of the optimization problem is unique and continuous in most of the cases. However, due to the

Method	Real-Time Capable	Continuity	Redundancy	Computational speed
Gradient-based optimization	no	yes	any	medium
Quadratic programming	yes	yes	any	medium
Linear programming	no	no	any	fast
Minimizing norm solution with Dykstra	no	no	any	slow
Centroid/Barycentric	yes	yes	1, 2	fast

Table 2.1: Comparison between different Tension Distribution Algorithms [Pot14]

nature of the formulated problem, the approach is not suitable for a real time implementation.

- Quadratic programming: [BPH06] formulates an optimization problem with a quadratic cost function and with linear constraints on the cable tension limits. The algorithm is found to be faster in certain examples if a good initial solution is provided.
- Linear programming Methods: [BJS+09] presents a novel linear program formulation that yields optimally safe tension distributions in classical CDPRs by the introduction of a slack variable. The slack variable also enables explicit computation of a near-optimal, feasible starting point. This, in turn, enables rapid computation of the optimally safe tension distributions. The formulation also contains a parameter that can be used to steer cable tensions towards desired regions of operation. [OA05] proposes a method to find a feasible space for tension distribution described by a set of linear inequalities and to plan the trajectory of the robot by staying within this feasible space. In general, linear programming methods cannot guarantee a continuous solution nor suitable for the real-time control purposes.
- Minimizing norm solution with Dykstra method: [HK07] presents a numerical procedure based on convex analysis and optimization to calculate the minimum-norm solution that minimizes the two norm of the cable tension vector. The procedure is based on convex optimization that utilizes the Dykstra's alternating projection algorithm to reach an optimum solution. The algorithm is neither real-time capable nor can guarantee the continuity of the solutions.

– Centroid/Barycentric approach: [LG13a, GLRB15] propose a TDA for n-DoF CDPRs driven by $n+2$ cables. The set of feasible cable tensions of n-DoF $(n+2)$-cable CDPRs is a 2-D convex polygon. The algorithm computes the vertices of the convex polygon of feasible cable tension distributions by following the polygon edges in a clockwise or counterclockwise order, or it proves that this polygon is empty. Once all the polygon vertices are determined, centroid and/or weighted barycenter tension distributions can be determined directly. The computation time is driven by triangulations in the r-dimensional space which become more complex for higher dimensions. Currently, the barycentric algorithm has been shown for redundancies up to $r = m - n = 2$. Due to its geometric nature, the algorithm is efficient and appropriate for real-time applications.

A summary of the TDA's mentioned above is given in Table 2.1.

It must be noted that the cable tension distribution is largely influenced by the cable model. For example, in case of fully suspended CDPRs, the cable tension distribution makes sense as long as cables are elastic.

2.3.2 Workspace

Substantial work has been reported in the literature on the determination of the reachable workspaces and equilibrium conditions of CDPRs [Ver04, GG06, VH00, BEU04, REU04, EUV04, PFAM04]. Generally the workspace of a cable-driven parallel robot can be defined as the set of its moving-platform poses for which a particular wrench is feasible, *i.e.*, for which a particular wrench can be generated at the moving-platform by pulling on it with the cables having positive tensions [GG06, VH00].

Several workspaces and equilibrium conditions have been defined in the literature for CDPRs. The two most significant and commonly used definitions of CDPR workspaces based on the desired task and the wrench requirements of its moving-platform are the Wrench Feasible Workspace (WFW) and the Wrench Closure Workspace (WCW) detailed as follows.

Wrench Feasible Workspace

In several applications, it is essential to know, given the limits on the actuation forces in the cables, whether the robot has ability to generate the required set of wrenches to perform a desired task, which can be, for example, the displacement of a sensor mounted on the moving-platform [BRO85] or payload handling [Mer08, ABD93]. These requirements lead to the concept of force feasibility, which verifies if the desired task can be performed at any chosen configuration. A pose of a CDPR is said to be wrench-feasible in a particular configuration and for a specified set of wrenches if

the tension forces in the cables can counteract any external wrench of the specified set applied to the end-effector [EUV04]. A region is wrench feasible if the robot can exert the desired set of wrenches at any point within it. This region, referred to as Wrench Feasible Workspace, constitutes the workspace which is wrench-feasible for a particular application. It is formally defined as the set of platform poses for which any wrench of a given set of wrenches can be balanced with wrenches generated by the cables such that the tension in each cable remains within the lower and upper bounds [BEU04, REU04, GDM, BREU06].

For any given CDPR configuration, the set of wrenches that can be generated by the cables on the moving-platform is defined as the Available Wrench Set (AWS). For classical CDPRs, AWS depends on the robot geometric architecture, *i.e.*, fixed exit points and cable anchor points on the moving-platform. It also depends on the configuration as well as on the minimum and maximum acceptable tensions in the cables. Once the AWS is determined, the robot's ability to generate the required set of wrenches to perform a task can be predicted. The set of wrenches required to complete the desired task, referred to as the Required Wrench Set (RWS), can only be generated by the robot if and only if it is fully included in AWS. Hence, a necessary condition to complete the desired task is expressed as:

$$\text{RWS} \subseteq \text{AWS}. \tag{2.1}$$

Thus, if RWS is a subset of the AWS, then all the required wrenches in the task wrench set can be generated by the robot.

WFW has been extensively used by the researchers. [GKP+08] presents numerical methods that can be used to determine solutions to the design problem of finding geometries of fully constrained CDPRs for which a prescribed workspace is fully inscribed in the WFW. [HFM+05a] presents an approach for the time-optimal trajectory planning of CDPRs using WFW based on the actuator and cable tension limits. [LCC18] introduces the concept of a new Cable-Driven Parallel Crane whose usable workspace is determined with the approach of WFW. [OS14] presents an optimization based strategy to find an optimal CDPR cable layout, *i.e.,* fixed exit points and anchor points on the moving-platform, with the objective to maximize the total orientation of the moving platform determined using WFW.

Wrench Closure Workspace

From a general design point of view, it is of great interest to determine the workspace that contains the set of moving-platform poses for which any wrench is feasible. Thus the concept of wrench-closure is introduced that analyzes the ability of the CDPR moving-platform to support any arbitrary required wrenches. WCW is defined as the

set of poses of the platform for which any wrench can be generated at the platform by tightening the cables [GG06, GG05]. A pose of the moving-platform belongs to the WCW if and only if the static equilibrium of the moving platform is assured by any non-negative cables tensions.

The WCW is a particular instance of the WFW in which both the required set of wrenches and the tensions in the cables are not bounded. Hence, unlike the WFW, the WCW does not depend on the choice of a particular set of wrenches. For CDPRs having more cables than DoFs, the WCW depends only on the CDPR architecture, *i.e.,* on the locations of the cable exit points and the positions of the attachment points of the cables on the moving-platform.

Two necessary conditions must be fulfilled in order to determine the wrench closure of a given moving-platform pose. Firstly, the wrench matrix defined by Eq. (3.4) must be full-rank. Secondly, WCW is only applicable on CDPRs with more cables than DoFs, *i.e.,* WCW can only be traced for the CDPRs whose n-DoF moving-platform is displaced by at least $n + 1$ cables.

WCW has been widely used in grasping problems in order to verify if the gripper can achieve a stable static equilibrium of the grasped object. A strong similarity exists between CDPRs and multifinger grasping systems where the wrenches applied by the cables and fingers have both a unidirectional nature. The connection between wrench-closure in CDPRs and force-closure grasp (a grasp in which the fingers can attain a static equilibrium against any arbitrary external wrench applied to the grasped object) has been presented in [EUV04]. The tools presented in the latter has been exploited to study the wrench closure in CDPRs. WCW has been studied for planar CDPRs in [GG06] and for spatial CDPRs in [GMD06].

Other Worksaces for CDPRs

In several applications, the moving-platform may simply have to transport a payload. This is a particular case of the WFW in which only the gravity wrench due to the weight of the moving platform is considered. A set of moving-platform poses where the cables can compensate for its weight are known as Static Feasible Workspace.

Generally, collision free motion is required from the CDPR to prevent any damage to the CDPR structure and to the objects in the surrounding environment. Therefore, some other workspaces has been also defined known as Interference Free Workspace [PCGO10] and Collision Free Workspace [LOZ+09]. Interference Free Workspace consists of the set of moving platform poses where the cables do not have any interference with each other. Similarly, the Collision Free Workspace is compromised of the set of accessible poses of the moving platform where no collision between the cables and the surrounding environment is guaranteed.

The dynamic equilibrium of the moving platform is investigated using the Dynamic

Feasible Workspace. By definition, the Dynamic Feasible Workspace is the set of dynamic feasible moving platform poses. A pose is dynamic feasible if a prescribed set of moving platform accelerations is feasible, with cable tensions lying in between given lower and upper bounds. Dynamic workspace has been studied for planar CDPRs in [BG05] and for spatial CDPRs in [GGC].

2.3.3 Path Planning strategies

Several path planning strategies have been investigated in the literature. Global search methods such A* and *Dijkstra* [Dij59], are guaranteed to find optimal trajectories in a discretized workspace. These algorithms are an ideal choice however they perform poorly in high dimensions [LaV06] and are seldom used for complex robotic problems without facilitating search operations by including a heuristic of some kind, for instance first planning on a lower dimensional manifold [CCL10].

On the other hand, stochastic sampling based motion planning algorithms overcome the requirement of complete space discretization, by randomly sampling the state space. The two most popular sampling based planning algorithms are Rapidly-exploring Random Trees (RRT) [LaV06] and Probalistic Roadmaps [KSLO96]. RRT grows a tree from an initial configuration in state space to a desired configuration by generating random control inputs, however a drawback is the requirement to grow a new tree for any changes in the initial configuration. PRM overcomes this limitation by simply building a re-usable road-map that covers the region, after which a search method can be used to rapidly find the shortest path on this road-map. However, this is no longer valid for dynamic environments. Neither algorithm has optimally guarantees, and hence a major improvement is given in [KF11] where two new algorithms denoted RRT* PRM*, which are provably asymptotically optimal, are proposed. Nevertheless, in spite of the practical benefit of sampling based algorithms and their relative ease of implementation there are a number limitations. Convergence in complex environments requires a large computational time and their finite time solutions are often of poor quality, indeed the creation of executable trajectories often necessitates the inclusion of an additional smoothing step, which may affect the feasibility of the solution. Hence, a popular technique is to initialize a trajectory optimization algorithm using sampling based methods for instance [KBA17]. Additionally, it is difficult to embed large number kinodynamic constraints, crucial for CDPRs, in such algorithms. In particular such constraints may lead to unintuitive trajectory selections [MSJ+11, AGV+14]. Sampling based methods must be tuned in order to overcome the well-known *narrow passage problem*[VS18]. Finally, these methods are unsuitable for systems where the planning problem changes with discrete events for instance for locomotion or pushing tasks, where intermediate contact is made with the environment [OLP19, OLP18].

In contrast, trajectory optimization methods can take into account complex state and environmental constraints. The simplest trajectory optimization approach, known as the shooting method, selects control inputs and simulates the resulting motion [Bet98, DBDW06]. The inputs are tuned using the error between the actual final state and a desired final state. The main advantage of shooting methods is the guarantee that if a resulting solution is obtained, this solution is continuously feasible. However, single shooting methods require a very good initial guess or have trouble finding solutions, often leading to a locally optimal solution in the neighborhood of the initial guess. This problem may be alleviated by breaking the trajectory into segments and solving a shooting problem at each segment, known as multi-shooting [Kel17]. Furthermore, both sampling based methods and direct transcription methods may be used to obtain an initial guess before using the shooting method.

On the contrary, direct transcription or collocation methods [PMN+16, WFP+17], discretize the trajectory into node points. The states and control variables at each node form the decision variables, while the system evolution i.e, the dynamics between each node, must be defined in the constraint equations. Often the formulation of the direct transcription method leads to complexities [PMN+16] while also increasing the overall problem dimension and therefore the overall computational overhead. Indeed specialist software (SNOPT) [GMS05] is often required to aid the implementation. However, direct transcription methods are sparse and the smoothness of the resulting equations increases computational efficiency [Hub14]. Direct transcription methods have been successfully applied to robotic system and scenarios with highly non-linear properties [PCT14, OLP19, LKOP19]. However, unlike shooting method since dynamics are approximated between each node the results may not be executable on hardware and thus require post processing.

2.4 Conclusion

This chapter starts by giving a detailed review on classical Cable-Driven Parallel Robots (CDPRs) and Reconfigurable Cable-Driven Parallel Robots (RCDPRs). It presents a wide range of their diverse applications. The variety of prototypes developed in the literature reflects the large number of possibilities offered by the cable-driven mechanisms. However, it was discussed in Chapter 1 that the classical CDPRs face several limitations mainly with its fixed cable layout.

The goal of this thesis is to study and develop a robotic system that is capable of generating all the six degrees-of-freedom of the end-effector while being capable of applying the wrenches in a large and cluttered environment. In order to develop such a system, we came up with the idea of Mobile Cable-Driven Parallel Robots (MCDPRs)

which has the ability to fulfill this requirement. To develop such a hybrid manipulator, we need to answer several research issues. Firstly, in order to design MCDPRs, we require appropriate tools to trace their workspaces. Secondly, for the control purposes, we require a feasible Tension Distribution Algorithm for the MCDPR cables. Moreover, in order to perform the desired tasks, we also need the trajectory planning algorithm for MCDPRs.

Section 2.3 briefly presented the state of the art on the aforementioned research issues associated to cable driven mechanisms. Firstly, different existing methodologies to calculate the force distribution among the cables of a CDPR were presented. Later on, a detailed review was presented on the existing methodologies used for the workspace analysis of CDPRs. Finally, a detailed study was presented on existing path planning strategies.

To the best of our knowledge, those research issues have not been tackled for MCDPRs in the literature yet. Therefore, in this thesis, we have done extensive studies on MCDPRs. Chapter 3 presents a real-time Tension Distribution Algorithm for MCDPRs. Chapter 4 describes a strategy to trace the workspace of MCDPRs. Finally, the task-based trajectory planning strategies are presented in 6.

3

Tension Distribution Algorithm for MCDPRs

Contents

A real-time control of a MCDPR demands for a real-time cable tension distribution. To avoid steps in the motor torques, the calculated tension distribution among the cables also has to be continuous along the trajectory. Consequently, a good TDA is expected to provide a real-time and continuous solution for the cable tensions. An algorithm is said to be real-time capable if the computation time is reasonably short, the worst-case computation time can be strictly bounded and a real-time implementation was reported in the literature [Pot14]. For most of the TDAs presented in Sec. 2.3.1, finding a suitable distribution of cable tensions is formulated as an optimization problem, which generally expensive in terms of computation time because of their iterative nature. Consequently, for real-time applications, a non-iterative approach is preferred. Therefore, a geometric algorithm, such as Centroid/Barycentric approach is also required for determining the feasible distribution of the cable tensions for a MCDPR.

The following sections are focused on extending the aforementioned geometric TDA developed for classical CDPRs in [LG13a, GLRB15] to MCDPRs, while maintaining the ability to compute a continuous solution of the cable tensions in real-time. The presented algorithm is applicable up to two degrees of actuation redundancy. In case of CDPRs, the algorithm forms a Feasible Cable Tension Domain (FCTD) representing the set of feasible tensions based on their lower and upper bounds. In contrast to classical CDPRs, FCTD for MCDPRs must take into account the conditions associated with the static equilibrium of the mobile bases derived in Sec. 3.1. The aforementioned FCTD is discussed in Sec. 3.2. Accordingly, a new TDA aiming at obtaining the centroid/barycenter of the modified FCTD is presented in Sec. 3.3. Three case studies are discussed in Sec. 3.4 to evaluate the output of the presented TDA. Finally, Sec. 3.5 concludes this chapter.

3.1 Static Equilibrium of MCDPRs

A MCDPR is in static equilibrium if and only if (iff) its moving-platform and mobile bases are all in static equilibrium. Therefore, the static equilibrium conditions of the moving-platform and the mobile bases of MCDPRs are formulated in this section.

3.1.1 Static Equilibrium of the Moving Platform

The static equilibrium equations of the moving-platform are expressed as [KI93, HFM+05b]:

$$\sum_{j=1}^{p}\sum_{i=1}^{m_j}\mathbf{u}_{ij}t_{ij} = \mathbf{f}, \tag{3.1a}$$

$$\sum_{j=1}^{p}\sum_{i=1}^{m_j}\mathbf{c}_{rij}t_{ij} = \mathbf{m}, \tag{3.1b}$$

where $\mathbf{f} = [f^x, f^y, f^z]^T$ and $\mathbf{m} = [m^x, m^y, m^z]^T$ denote the forces and moments applied by the cables onto the moving platform. $\mathbf{c}_{rij}$ gives the direction of the actuation moment applied by the cable $\mathscr{C}_{ij}$ onto the moving-platform expressed as:

$$\mathbf{c}_{rij} = \mathbf{r}_{ij} \times \mathbf{u}_{ij}, \tag{3.2}$$

where $\mathbf{r}_{ij}$ is a vector pointing from the origin O_P of the moving-platform frame $\mathscr{F}_P$ to the cable anchor point B_{ij}. The static equilibrium of the moving-platform is expressed in a matrix form as:

$$\mathbf{W}\mathbf{t} = \mathbf{w}, \tag{3.3}$$

where $\mathbf{W}$ is a $(n \times m)$ wrench matrix mapping the cable tension vector $\mathbf{t} \in \mathbb{R}^m$ onto the wrenches $\mathbf{w} \in \mathbb{R}^n$ applied by the cables onto the moving-platform.

$$\mathbf{W} = \begin{bmatrix}\mathbf{W}_1 & \dots & \mathbf{W}_j & \dots & \mathbf{W}_p\end{bmatrix}, \tag{3.4}$$

$$\mathbf{w} = \begin{bmatrix}\mathbf{f}\\ \mathbf{m}\end{bmatrix}, \tag{3.5}$$

$$\mathbf{t} = \begin{bmatrix}\mathbf{t}_1 & \dots & \mathbf{t}_j & \dots & \mathbf{t}_p\end{bmatrix}^T. \tag{3.6}$$

$\mathbf{W}_j$ is a $(n \times m_j)$-dimensional matrix whose columns are the actuation wrenches exerted by the cables attached to $\mathscr{M}_j$. $\mathbf{t}_j$ is a m_j-dimensional cable tension vector corresponding to the cables connected to $\mathscr{M}_j$.

$$\mathbf{t}_j = \begin{bmatrix}t_{1j} & \dots & t_{ij} & \dots & t_{m_j j}\end{bmatrix}^T, \tag{3.7a}$$

$$\mathbf{W}_j = \begin{bmatrix} \mathbf{w}_{1j} & \dots & \mathbf{w}_{ij} & \dots & \mathbf{w}_{m_j j} \end{bmatrix}. \tag{3.7b}$$

$\mathbf{w}_{ij}$ is the actuation wrench generated by the cable $\mathscr{C}_{ij}$ and is expressed as:

$$\mathbf{w}_{ij} = \begin{bmatrix} \mathbf{u}_{ij} \\ \mathbf{c}_{rij} \end{bmatrix}. \tag{3.8}$$

The cable tension are all bounded between a minimum and positive tension $\underline{t}_{ij}$ and a maximum tension $\bar{t}_{ij}$

$$\underline{\mathbf{t}} \leq \mathbf{t} \leq \bar{\mathbf{t}}, \tag{3.9}$$

where

$$\underline{\mathbf{t}} = \begin{bmatrix} \underline{t}_{11} & \underline{t}_{21} & \dots & \underline{t}_{m_1 1} & \underline{t}_{12} & \dots & \underline{t}_{m_2 2} & \underline{t}_{13} & \dots & \underline{t}_{m_p p} \end{bmatrix}^T, \tag{3.10a}$$

$$\bar{\mathbf{t}} = \begin{bmatrix} \bar{t}_{11} & \bar{t}_{21} & \dots & \bar{t}_{m_1 1} & \bar{t}_{12} & \dots & \bar{t}_{m_2 2} & \bar{t}_{13} & \dots & \bar{t}_{m_p p} \end{bmatrix}^T. \tag{3.10b}$$

3.1.2 Static Equilibrium of Mobile Bases

The static equilibrium of a wheeled mobile base can be characterized by its tipping and sliding conditions. To obtain the effect of these conditions on the wrench abilities of the moving platform, the latter must be first expressed in terms of the cable tensions. From Fig. 1.4b, equilibrium conditions of $\mathscr{M}_j$ can be expressed as [RLMGC18d]:

$$\mathbf{w}_{gj} + \sum_{k=1}^{c_j} \mathbf{f}_{c_{kj}} - \sum_{i=1}^{m_j} \mathbf{t}_{ij} = \mathbf{0} \tag{3.11a}$$

$$\mathbf{g}_j \times \mathbf{w}_{gj} + \sum_{k=1}^{c_j} \mathbf{c}_{kj} \times \mathbf{f}_{c_{kj}} - \sum_{i=1}^{m_j} \mathbf{b}_{ij} \times \mathbf{t}_{ij} = \mathbf{0} \tag{3.11b}$$

where $\mathbf{f}_{c_{kj}} = [f^x_{c_{kj}}, f^y_{c_{kj}}, f^z_{c_{kj}}]$ denotes the ground contact force at C_{kj}. $\mathbf{g}_j$ denotes the Cartesian coordinate vector of the center of gravity G_j. $\mathbf{c}_{kj}$ denotes the Cartesian coordinate vector of the wheel contact point C_{kj}. $\mathbf{b}_{ij}$ denotes the Cartesian coordinate vector of the platform attachment points B_{ij}. $\mathbf{w}_{gj}$ is the weight vector of $\mathscr{M}_j$. The aforementioned vectors are all expressed in the base frame $\mathscr{F}_0$.

Equations (3.11a) and (3.11b) represent the classical static equilibrium conditions of $\mathscr{M}_j$ in terms of the cable tensions. From those equations, Secs. 3.1.2.1 and 3.1.2.2 formulate the static equilibrium conditions corresponding to the tipping and sliding conditions of mobile bases in terms of cable tensions.

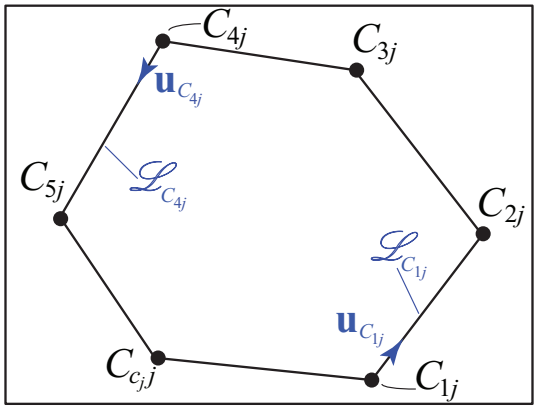

Figure 3.1: Footprint of $\mathscr{M}_j$ with $c_j = 6$ wheels

3.1.2.1 Tipping conditions of the Mobile Bases

The equilibrium towards the tipping of a wheeled robot is defined by an index named Zero-Moment Point (ZMP) [LGW14, SB04, VB04]. It is the point where the moment of ground contact forces is reduced to the pivoting moment of friction forces about an axis normal to the ground. It amounts to the point where the sum of the moments due to planar ground reaction forces is null. The ZMP of $\mathscr{M}_j$, denoted by C_{zj}, can be calculated from the wheel contact points $C_{kj},\ k = 1, \ldots, c_j$ as [Rud14]

$$\mathbf{c}_{zj} = \frac{\sum_{k=1}^{c_j} \mathbf{c}_{kj} f^z_{c_{kj}}}{\sum_{k=1}^{c_j} f^z_{c_{kj}}}, \tag{3.12}$$

where $\mathbf{c}_{zj}$ denotes the Cartesian coordinate vector of C_{zj}. The tipping conditions depend on the moments generated at the boundaries of the mobile base footprint. The footprint is formed by joining the contact points $C_{kj}, k = \{1, \ldots, c_j\}$, selected counter-clockwise (See Fig. 3.1). The boundary between the two consecutive contact points C_{kj} and C_{k+1j} of $\mathscr{M}_j$ is denoted as $\mathscr{L}_{C_{kj}}$ of unit vector $\mathbf{u}_{C_{kj}}$. Let $m_{C_{kj}}$ be the moment generated about $\mathscr{L}_{C_{kj}}$ at the instant when $\mathscr{M}_j$ loses contact with the ground at the points which do not form the boundary $\mathscr{L}_{C_{kj}}$,

$$m_{C_{kj}} = \mathbf{u}^T_{C_{kj}}((\mathbf{g}_j - \mathbf{c}_{kj}) \times \mathbf{w}_{gj}) + \sum_{i=1}^{m_j} \mathbf{u}^T_{C_{kj}}((\mathbf{c}_{kj} - \mathbf{b}_{ij}) \times \mathbf{u}_{ij}) t_{ij}, \quad k = 1, \ldots, c_j. \tag{3.13}$$

For $\mathscr{M}_j$ to be in static equilibrium, $m_{C_{kj}},\ k = 1, \ldots, c_j$, should be negative, namely,

$$m_{C_{kj}} \ \leq \ 0, \quad k = 1, \ldots, c_j. \tag{3.14}$$

Equation (3.14) defines the tipping conditions of $\mathscr{M}_j$ expressed in terms of the cable tensions $t_{ij},\ i = 1, \ldots, m_j$. Each kth boundary $\mathscr{L}_{C_{kj}}$ is associated with a single tipping condition. It means that the total number of tipping conditions to be satisfied

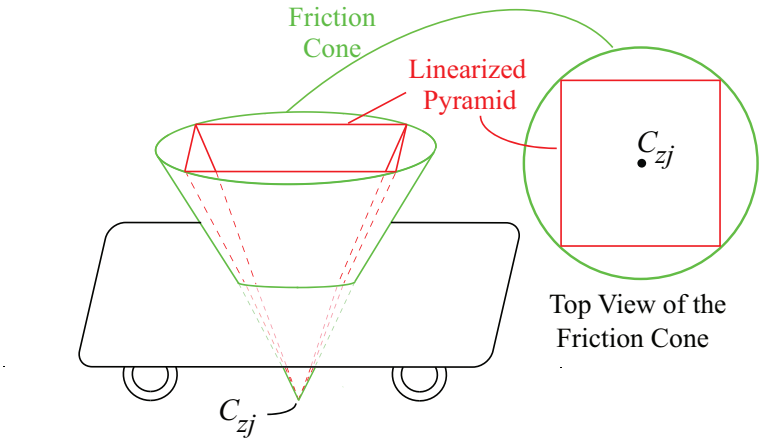

Figure 3.2: Linearized friction pyramid at ZMP (C_{zj})

for $\mathscr{M}_j$ to be in static equilibrium is equal to the number of wheels c_j.

3.1.2.2 Sliding conditions of the Mobile Bases

A commonly used model of friction in robotic manipulation is Coulomb law. The law states that the friction force magnitude in the tangent plane at the contact interface is related to the normal force magnitude by the friction coefficient μ. Two friction coefficients are usually defined, a static friction coefficient and a kinetic (or sliding) friction coefficient. For simplicity, we will assume the simplest Coulomb friction model with a single friction coefficient which is reasonable for hard and dry materials.

The friction laws can be interpreted in terms of a friction cone where the contact forces must stay within the cone in order to avoid relative sliding between the contacting bodies. Hence, the sliding conditions are defined by a friction cone at each wheel of the mobile base. For the mobile base to be in static equilibrium, the ground contact force $\mathbf{f}_{c_{kj}}$ at C_{kj} must be within the corresponding kth friction cone. The frictional effects due to the wheel contact points can be represented as a single friction cone located at the ZMP expressed as,

$$\sqrt{{}^{bj}f_{c_{zj}}^{x\ 2} + {}^{bj}f_{c_{zj}}^{y\ 2}} \leq \mu\ {}^{bj}f_{c_{zj}}^{z}, \tag{3.15}$$

where ${}^{bj}\mathbf{f}_{c_{zj}} = [{}^{bj}f_{c_{zj}}^{x}\ {}^{bj}f_{c_{zj}}^{y}\ {}^{bj}f_{c_{zj}}^{z}]^T$ represents the ground contact force at ZMP expressed in frame $\mathscr{F}_{bj}$. For sake of simplicity and ease of analysis, the sliding condition is linearized and the friction cone becomes a four-sided friction pyramid [SCBK17, CPN17] as shown in Fig. 3.2. Consequently, Eq. (3.15) is simplified as

follows:

$$\begin{bmatrix} 1 & 0 & -\mu \\ -1 & 0 & -\mu \\ 0 & 1 & -\mu \\ 0 & -1 & -\mu \end{bmatrix} {}^{bj}\mathbf{f}_{c_{zj}} \leq \mathbf{0}_4, \tag{3.16}$$

where μ denotes the friction coefficient between the ground and the wheels of $\mathscr{M}_j$. Equation (3.16) can be represented in the base frame $\mathscr{F}_0$ as

$$\mathbf{E}_F \, {}^0\mathbf{f}_{c_{zj}} \leq \mathbf{0}_4, \tag{3.17}$$

where

$${}^0\mathbf{f}_{c_{zj}} = {}^0\mathbf{R}_{bj} \, {}^{bj}\mathbf{f}_{c_{zj}}, \tag{3.18}$$

$$\mathbf{E}_F = \begin{bmatrix} 1 & 0 & -\mu \\ -1 & 0 & -\mu \\ 0 & 1 & -\mu \\ 0 & -1 & -\mu \end{bmatrix} {}^{bj}\mathbf{R}_0, \tag{3.19}$$

$$\mathbf{0}_4 = \begin{bmatrix} 0 & 0 & 0 & 0 \end{bmatrix}^T. \tag{3.20}$$

${}^0\mathbf{R}_{bj}$ denotes the rotation matrix from $\mathscr{F}_0$ to $\mathscr{F}_{bj}$. Accordingly, ${}^{bj}\mathbf{R}_0$ is the inverse of ${}^0\mathbf{R}_{bj}$. ${}^0\mathbf{f}_{c_{zj}} = [{}^0f^x_{c_{zj}} \; {}^0f^y_{c_{zj}} \; {}^0f^z_{c_{zj}}]^T$ denotes the ground contact forces at ZMP expressed in $\mathscr{F}_0$:

$${}^0\mathbf{f}_{c_{zj}} = \sum_{k=1}^{c_j} \mathbf{f}_{c_{kj}} = -\mathbf{w}_{gj} + \sum_{i=1}^{m_j} \mathbf{u}_{ij} t_{ij}. \tag{3.21}$$

Let $\mathbf{E}_F^g$ denotes the gth row of $\mathbf{E}_F$, $g = 1, \ldots, 4$. Substituting Eq. (3.21) in Eq. (3.17), the sliding condition associated to the gth boundary of the friction pyramid can be expressed as:

$$\sum_{i=1}^{m_j} \mathbf{E}_F^g \mathbf{u}_{ij} t_{ij} - \mathbf{E}_F^g \mathbf{w}_{gj} \leq 0, \quad g = 1, \ldots, 4 \tag{3.22}$$

As a result, Eq. (3.22) defines the sliding conditions associated with $\mathscr{M}_j$ formulated in the form of a linearized friction pyramid in terms of the cable tensions t_{ij}, $i = 1, \ldots, m_j$.

3.2 Feasible Cable Tension Domain of MCDPRs

For classical CDPRs, the FCTD takes the shape of a $(m-n)$-dimensional convex polytope. It is formed by mapping the constraints associated to the cable tension limits into the nullspace of the wrench matrix $\mathbf{W}$. However, due to the additional static equilibrium conditions discussed in Sec. 3.1.2, the classical approach is not sufficient to fully characterize the FCTD of MCDPRs [RLMGC18d]. As a consequence, this section presents FCTD for MCDPRs which takes into account the static equilibrium conditions of the MCDPR mobile bases in addition to the cable tension limits.

3.2.1 FCTD based on cable tension limits

The FCTD for classical CDPRs is formed by mapping the cable tension limit constraints into the null space of the wrench matrix $\mathbf{W}$. If the wrench matrix is full rank, the particular solution of Eq. (3.3), denoted by $\mathbf{t}_P$ is expressed as,

$$\mathbf{t}_P = \mathbf{W}^{+}\mathbf{w}, \tag{3.23}$$

where $\mathbf{W}^{+}$ is the Moore Penrose pseudo inverse of the wrench matrix $\mathbf{W}$. A homogeneous solution $\mathbf{t}_N$ can be added to the particular solution $\mathbf{t}_P$ such that:

$$\mathbf{t} = \mathbf{t}_P + \mathbf{t}_N \implies \mathbf{t} = \mathbf{W}^{+}\mathbf{w} + \mathbf{N}\boldsymbol{\lambda} \tag{3.24}$$

where $\mathbf{N}$ is the $m \times (m-n)$ null space projector of the wrench matrix $\mathbf{W}$, defined as:

$$\mathbf{N} = \begin{bmatrix} \mathbf{n}_{11} \\ \mathbf{n}_{21} \\ \vdots \\ \mathbf{n}_{m_1 1} \\ \mathbf{n}_{12} \\ \vdots \\ \mathbf{n}_{m_p p} \end{bmatrix} \tag{3.25}$$

where each component $\mathbf{n}_{ij}$ of $\mathbf{N}$ in Eq. (3.25) is a $(1 \times (m-n))$ row vector. $\boldsymbol{\lambda}$ is a $(m-n)$ dimensional arbitrary vector that moves the particular solution into the feasible range of cable tensions. The columns of $\mathbf{N}$ form a basis of the nullspace of $\mathbf{W}$. $\mathbf{t}_P$ is the minimum-norm solution of Eq. (3.3) and $\mathbf{t}_N$ is the homogeneous solution that maps $\boldsymbol{\lambda}$ in to the nullspace of $\mathbf{W}$. According to [LG13a, GLRB15], there exists a $(m-n)$-dimensional affine space Σ defined by the solution of Eq. (3.23)

and another m-dimensional hypercube Ω defined by the feasible cable tensions:

$$\Sigma = \{\mathbf{t} \mid \mathbf{W}\mathbf{t} = \mathbf{w}\} \tag{3.26}$$

$$\Omega = \{\mathbf{t} \mid \underline{\mathbf{t}} \ \leq \ \mathbf{t} \ \leq \ \overline{\mathbf{t}}\} \tag{3.27}$$

The intersection between these two spaces ($\Sigma \cap \Omega$) amounts to a $(m-n)$-dimensional convex polytope. Such a polytope exists if and only if the tension distribution admits at least one solution that satisfies the cable tension limits as well as the equilibrium of the moving-platform. The $(m-n)$-dimensional convex polytope is formulated by the linear inequalities that can be acquired by substituting Eq. (3.24) in Eq. (3.9):

$$\underline{\mathbf{t}} \ \leq \ \mathbf{t}_P + \mathbf{N}\boldsymbol{\lambda} \tag{3.28a}$$

$$\mathbf{t}_P + \mathbf{N}\boldsymbol{\lambda} \ \leq \ \overline{\mathbf{t}} \tag{3.28b}$$

Combining the above equations yield:

$$\underline{\mathbf{t}} - \mathbf{t}_P \ \leq \ \mathbf{N}\boldsymbol{\lambda} \ \leq \ \overline{\mathbf{t}} - \mathbf{t}_P. \tag{3.29}$$

The above mentioned linear inequalities form a $(m-n)$-dimensional convex polytope in the $\boldsymbol{\lambda}$-space associated with the constraints on the cable tension limits. Thus, for a given moving-platform pose of a CDPR, its FCTD corresponds to the $(m-n)$-dimensional convex polytope, denoted as $\mathcal{A}_{CDPR}$, can be expressed as:

$$\mathcal{A}_{CDPR} = \ \{\boldsymbol{\lambda} \ \in \ \mathbb{R}^{m-n} \mid \underline{\mathbf{t}} - \mathbf{t}_P \ \leq \ \mathbf{N}\boldsymbol{\lambda} \ \leq \ \overline{\mathbf{t}} - \mathbf{t}_P\}. \tag{3.30}$$

It should be noted that in case of one degree of actuation redundancy, *i.e.* a CDPR with $n+1$ cables, the feasible polytope is one dimensional space, *i.e.*, a line.

3.2.2 FCTD based on the tipping conditions of the mobile bases

This section aims at defining the FCTD of MCDPRs by considering the additional static equilibrium conditions associated with the tipping condition of the mobile bases presented in Sec. 3.1.2.1. To include the aforementioned conditions of the mobile bases into the FCTD of CDPRs, they must be first expressed in the $\boldsymbol{\lambda}$-space by substituting the cable tension t_{ij} into the tipping conditions (Eq. (3.14)). From Eq. (3.24), the cable tension t_{ij} can be expressed as:

$$t_{ij} = t_{Pij} + \mathbf{n}_{ij}\boldsymbol{\lambda}, \tag{3.31}$$

where t_{Pij} represents the particular (minimum-norm) solution of the cable $\mathscr{C}_{ij}$. By substituting Eq. (3.31) into Eq. (3.13), the tipping conditions of $\mathscr{M}_j$ takes the form:

$$\begin{aligned}\sum_{i=1}^{m_j} \mathbf{u}_{C_{kj}}^T((\mathbf{c}_{kj}-\mathbf{b}_{ij})\times\mathbf{u}_{ij})\ \mathbf{n}_{ij}\boldsymbol{\lambda} \ &\leq\ -\mathbf{u}_{C_{kj}}^T((\mathbf{g}_j-\mathbf{c}_{kj})\times\mathbf{w}_{gj}) \\ -\sum_{i=1}^{m_j} \mathbf{u}_{C_{kj}}^T((\mathbf{c}_{kj}-\mathbf{b}_{ij})\times\mathbf{u}_{ij})\ t_{Pij}, \quad & k=1,\ldots,c_j.\end{aligned} \tag{3.32}$$

For simplification, Eq. (3.32) can also be expressed in the following form:

$$\mathbf{n}_{C_{kj}}\boldsymbol{\lambda} \ \leq\ -\overline{M}_{C_{kj}},\ k=1,\ldots,c_j. \tag{3.33}$$

where

$$\overline{M}_{C_{kj}} = \mathbf{u}_{C_{kj}}^T((\mathbf{g}_j-\mathbf{c}_{kj})\times\mathbf{w}_{gj}) + \sum_{i=1}^{m_j} \mathbf{u}_{C_{kj}}^T((\mathbf{c}_{kj}-\mathbf{b}_{ij})\times\mathbf{u}_{ij})\ t_{Pij} \tag{3.34}$$

$$\mathbf{n}_{C_{kj}} = \sum_{i=1}^{m_j} \mathbf{u}_{C_{kj}}^T((\mathbf{c}_{kj}-\mathbf{b}_{ij})\times\mathbf{u}_{ij})\ \mathbf{n}_{ij} \tag{3.35}$$

$\overline{M}_{C_{kj}}$ represents the tipping moment of $\mathscr{M}_j$ about $\mathscr{L}_{C_{kj}}$ due to its weight and the particular solution of the cable tensions $t_{ij},\ i=1,\ldots,m_j$. Equation (3.33) defines the tipping condition for the mobile bases expressed in Eq. (3.14) in the $\boldsymbol{\lambda}$-space. Similarly, the complete system of tipping conditions for a MCDPR can be expressed in the $\boldsymbol{\lambda}$-space as:

$$\underline{\mathbf{m}} \ \leq\ \mathbf{N}_C\ \boldsymbol{\lambda} \ \leq\ \overline{\mathbf{m}} \tag{3.36}$$

where

$$\mathbf{N}_C = \begin{bmatrix} \mathbf{n}_{C_{11}} \\ \mathbf{n}_{C_{21}} \\ \vdots \\ \mathbf{n}_{C_{c_1 1}} \\ \vdots \\ \mathbf{n}_{C_{c_p p}} \end{bmatrix},\quad \underline{\mathbf{m}} = \begin{bmatrix} -\infty \\ -\infty \\ \vdots \\ -\infty \\ \vdots \\ -\infty \end{bmatrix},\quad \overline{\mathbf{m}} = \begin{bmatrix} -\overline{M}_{C_{11}} \\ -\overline{M}_{C_{21}} \\ \vdots \\ -\overline{M}_{C_{c_1 1}} \\ \vdots \\ -\overline{M}_{C_{c_p p}} \end{bmatrix}. \tag{3.37}$$

The term $-\infty$ are added for the sake of algorithm [GLRB15] as the latter requires both lower and upper bounds. Equation (3.36) defines FCTD associated to the tipping conditions of the MCDPR mobile bases.

3.2.3 FCTD based on the sliding conditions of the mobile bases

Similar to the previous section, the FCTD associated with the sliding conditions can be defined by mapping the latter into the $\boldsymbol{\lambda}$-space. It can be acquired by substituting the cable tension t_{ij} from Eq. (3.31) expressed as a function of $\boldsymbol{\lambda}$ in the sliding conditions of $\mathscr{M}_j$ define in Eq. (3.22).

$$\sum_{i=1}^{m_j} \mathbf{E}_F^g \mathbf{u}_{ij} \mathbf{n}_{ij} \boldsymbol{\lambda} \;\leq\; \mathbf{E}_F^g \; w_{gj} - \sum_{i=1}^{m_j} \mathbf{E}_F^g \mathbf{u}_{ij} t_{Pij}, \quad g = 1, \ldots, 4. \tag{3.38}$$

Equation (3.38) can also be expressed in simplified form as:

$$\mathbf{n}_{Fgj} \boldsymbol{\lambda} \;\leq\; \overline{F}_{gj}, \quad g = 1, \ldots, 4, \tag{3.39}$$

where

$$\mathbf{n}_{Fgj} = \sum_{i=1}^{m_j} \mathbf{E}_F^g \mathbf{u}_{ij} \mathbf{n}_{ij}, \tag{3.40}$$

$$\overline{F}_{gj} = \mathbf{E}_F^g \; w_{gj} - \sum_{i=1}^{m_j} \mathbf{E}_F^g \mathbf{u}_{ij} t_{Pij}. \tag{3.41}$$

Equation (3.39) defines the sliding conditions of $\mathscr{M}_j$ into the $\boldsymbol{\lambda}$-space. Similarly, the complete system of sliding conditions for a MCDPR can be expressed in the $\boldsymbol{\lambda}$-space as:

$$\underline{\mathbf{f}} \;\leq\; \mathbf{N}_f \; \boldsymbol{\lambda} \;\leq\; \overline{\mathbf{f}}, \tag{3.42}$$

where

$$\mathbf{N}_f = \begin{bmatrix} \mathbf{n}_{F11} \\ \vdots \\ \mathbf{n}_{F41} \\ \mathbf{n}_{F12} \\ \vdots \\ \mathbf{n}_{F4p} \end{bmatrix}, \qquad \underline{\mathbf{f}} = \begin{bmatrix} -\infty \\ \vdots \\ -\infty \\ -\infty \\ \vdots \\ -\infty \end{bmatrix}, \qquad \overline{\mathbf{f}} = \begin{bmatrix} \overline{F}_{11} \\ \vdots \\ \overline{F}_{41} \\ \overline{F}_{12} \\ \vdots \\ \overline{F}_{4p} \end{bmatrix}. \tag{3.43}$$

3.2.4 FCTD of MCDPRs

Let $\mathcal{A}$ denote the FCTD of MCDPRs. It is formed by mapping the static equilibrium conditions expressed in $\boldsymbol{\lambda}$-space (Eqs. (3.36 and (3.42)) onto the $(m-n)$-dimensional

FCTD, $\mathcal{A}_{CDPR}$, formed by the cable tension limits defined by Eq. (3.29).

$$\mathcal{A} = \left\{ \boldsymbol{\lambda} \in \mathbb{R}^{m-n} \mid \begin{bmatrix} \underline{\mathbf{t}} - \mathbf{t}_P \\ \underline{\mathbf{m}} \\ \underline{\mathbf{f}} \end{bmatrix} \leq \begin{bmatrix} \mathbf{N} \\ \mathbf{N}_C \\ \mathbf{N}_F \end{bmatrix} \boldsymbol{\lambda} \leq \begin{bmatrix} \overline{\mathbf{t}} - \mathbf{t}_P \\ \overline{\mathbf{m}} \\ \overline{\mathbf{f}} \end{bmatrix} \right\}. \tag{3.44}$$

In the following sections, $\mathcal{A}$ will be referred to as the feasible polytope.

3.3 Real-time and continuous TDA for MCDPRs

The inequality constraints from Eq. (3.44) are used to compute the feasible distribution of tensions among the cables using a TDA. As discussed earlier, in this section an existing geometric TDA defined for classical CDPRs is extended to MCDPRs. The proposed algorithm only deals with MCDPRs having up to two degrees of actuation redundancy. Section 3.3.1 presents a TDA for MCDPRs with two degrees of actuation redundancy. Accordingly, Sec. 3.3.2 discusses a TDA for MCDPRs with one degree of actuation redundancy.

3.3.1 MCDPRs with two degrees of actuation redundancy

For the MCDPRs with n-DoF moving-platform pulled by $n+2$ cables, $\mathcal{A}$ takes the form of a two-dimensional convex polygon. Each inequality constraint from Eq. (3.44) defines a two-dimensional line in the $\boldsymbol{\lambda} = [\lambda_1 \ \lambda_2]$ space, where the coefficients of $\boldsymbol{\lambda}$ define the slope of the corresponding lines. The intersections between these lines form a feasible polygon. The presented TDA aims to find the vertices of the feasible polygon or prove that the $\mathcal{A}$ is null. If the feasible polygon exists and is determined, then the centroid of the polygon is calculated. This is the solution that is furthest from all inequality constraints. Finally, the $\boldsymbol{\lambda}$ coordinates of the centroid are used to compute the feasible distribution of tension among the cables using Eq. (3.24). The algorithm is briefly explained below.

The algorithm starts with the intersection point w_{ij} between any two inequality lines L_i and L_j, where each intersection point w_{ij} corresponds to a specific value of $\boldsymbol{\lambda}$. After reaching the intersection point w_{ij}, the algorithm leaves the current line L_j and follows the next line L_i in order to find the next intersection point w_{ki} with line L_k.

The feasible polygon $\mathcal{A}$ is associated with the feasible index set I. The feasible index set at a given point $\boldsymbol{\lambda}$ is the set consisting of the indices of the rows of Eq. (3.44) satisfied at $\boldsymbol{\lambda}$, *e.g.*, if the rows $1, 5, 7$, and 9 are satisfied, the corresponding feasible index set is $I = \{1, 5, 7, 9\}$. At each intersection point, the feasible index set is unchanged or modified by adding the corresponding row index of Eq. (3.44). It means that for each intersection point, the number of rows from Eq. (3.44) satisfied

at current intersection point should be greater than or equal to the number of rows satisfied at previous visited points. Accordingly, the algorithm makes sure to converge toward the solution. The algorithm keeps track of the intersection points and updates the first vertex of the feasible polytope, denoted as w_f, which depends on the update of feasible index set I. If the feasible index set is updated at intersection point w, the first vertex of the polytope is updated as $w_f = w$.

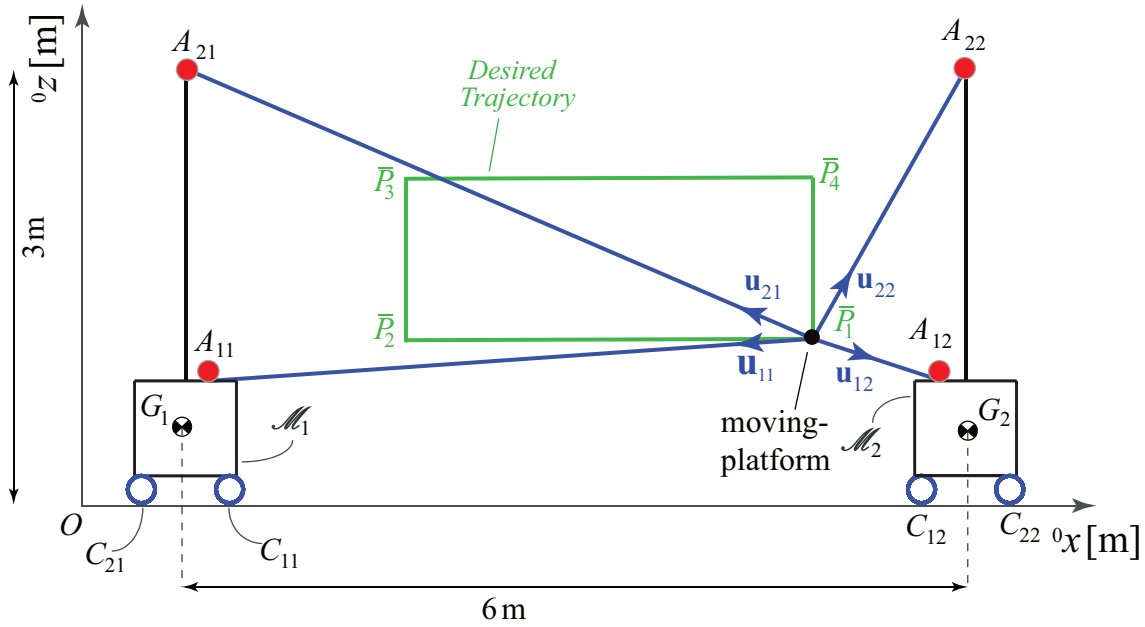

Figure 3.3: MoPICK configuration and Desired Trajectory

Let's consider that the algorithm has reached a point w_{cb} by first following line L_a, then following L_b intersecting with line L_c. The feasible index set I_{cb} at w_{cb} should be such that $I_{ba} \subseteq I_{cb}$. If index c is not available in I_{ba}, then $I_{cb} = I_{ba} \cup\ c$ as the row c is now satisfied. Accordingly $w_f = w_{cb}$ will become the first vertex of the polytope. At each update of the feasible index set I, a new feasible polytope is achieved and the first vertex w_f of the polytope is replaced by the current intersection point. This procedure is repeated until a feasible polytope (if it exists) is found, which is determined by visiting w_f more than once. After computing the feasible polytope, its centroid, namely the solution furthest away from all the constraints is calculated. The $\boldsymbol{\lambda}$ coordinates of the centroid is used to calculate the feasible tension distribution using Eq. (3.24). The evolution of the algorithm and the resulting feasible polygon is presented for two different case studies in the following sections.

3.3.1.1 Case Study: Planar MCDPR with two mobile bases and four cables connected to a point mass moving-platform

The first case study is a planar MCDPR with $p = 2$ mobile bases carrying $m = 4$ cables and an $n = 2$-DoF point mass moving-platform shown in Fig. 3.3. The feasible

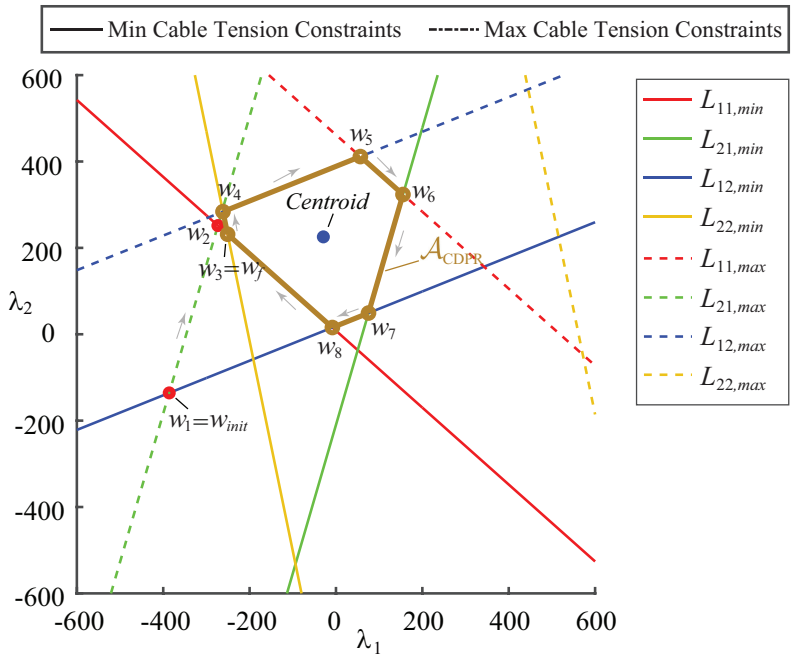

Figure 3.4: Feasible Polygon considering only cable tension limits of a 2-DoF point mass MCDPR case study

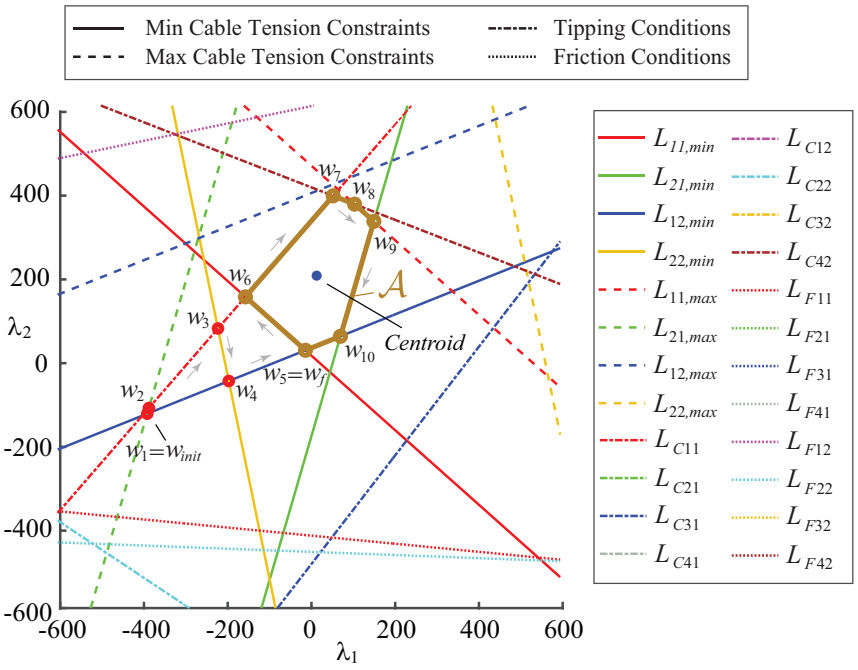

Figure 3.5: Feasible Polygon considering both cable tension limits and the static equilibrium conditions of a 2-DoF point mass MCDPR case study

polygon $\mathcal{A}_{CDPR}$ based only on the cable tension limits is illustrated in Fig. 3.4, while the feasible polygon $\mathcal{A}$ based on the cable tension limits and the static equilibrium of the mobile bases is illustrated in Fig. 3.5.

The algorithm starts at an initial intersection point $w_1 = w_{init}$. The arrows indi-

cate the evolution of the algorithm. For determining $\mathcal{A}_{CDPR}$, the algorithm proceeds as follows $w_1, w_2, w_3, w_4, w_5, w_6, w_7, w_8$ and terminates at $w_f = w_3$ as this intersection point was already visited before. For the determination of $\mathcal{A}$, the algorithm proceeds as follows $w_1, w_2, w_3, w_4, w_5, w_6, w_7, w_8, w_9, , w_{10}$ and finally terminates at $w_5 = w_f$. It can be observed that $\mathcal{A}$ is smaller than $\mathcal{A}_{CDPR}$ and, as a consequence, their centroids are different. The $\boldsymbol{\lambda}$ coordinates of $\mathcal{A}_{CDPR}$ ($\mathcal{A}$, resp.) centroid is $[-32.3,\ 228.5]$ ($[3.1481,\ 213.6]$, resp.).

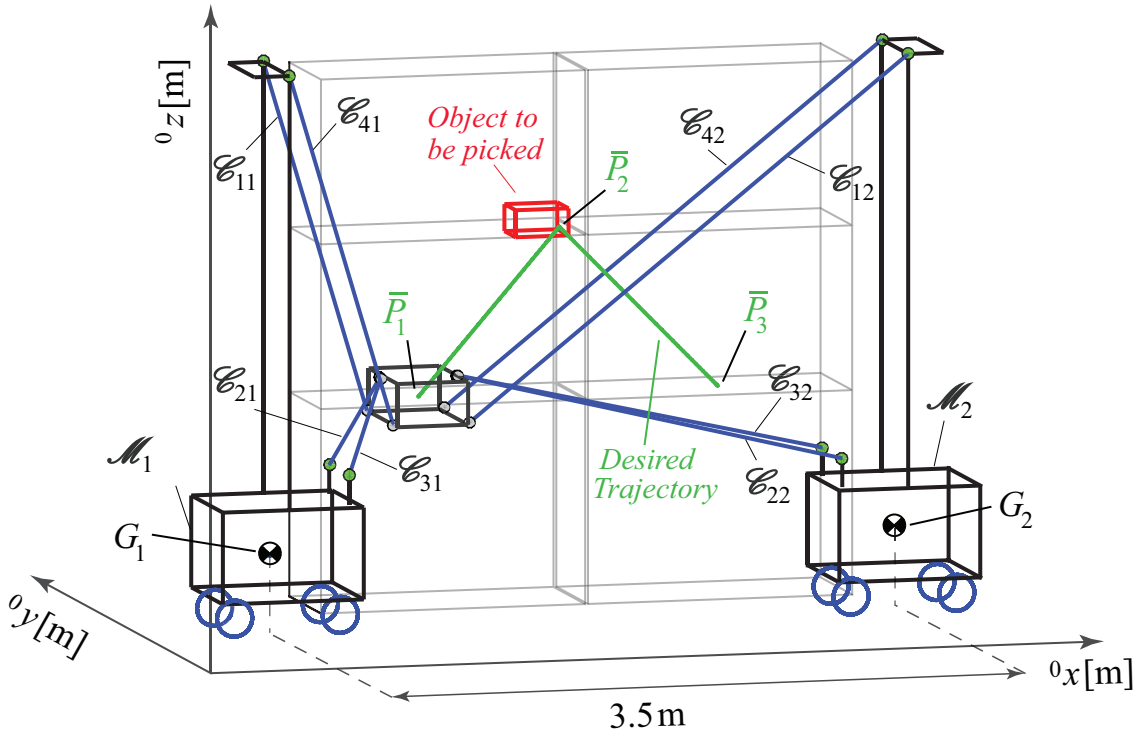

Figure 3.6: FASTKIT configuration and desired pick-and-place task

3.3.1.2 Case Study: FASTKIT

The second case study is a MCDPR prototype FASTKIT. It consists of two mobile bases carrying a CDPR with two degrees of actuation reduncancy. The studied configuration of the FASTKIT is shown in Fig. 3.6. Accordingly, for the moving-platform to be in static equilibrium, the polygons $\mathcal{A}_{CDPR}$ and $\mathcal{A}$ are illustrated in Figs. 3.7 and 3.8, respectively. Similar to the previous case study, the algorithm starts at initial intersection point $w_1 = w_{init}$ and evolves as indicated by the arrows. $\mathcal{A}_{CDPR}$ is determined by following order of the intersection points $w_1, w_2, \ldots, w_{14}$ and finally terminates at $w_9 = w_f$. Similarly, $\mathcal{A}$ is determined by following order of the intersection points $w_1, w_2, \ldots, w_{13}$ and terminates at $w_9 = w_f$. Similarly as in previous case study, it can be observed that the additional constraints reduce the size of the feasible polygon $\mathcal{A}$ when compared to $\mathcal{A}_{CDPR}$. The $\boldsymbol{\lambda}$ coordinates of the

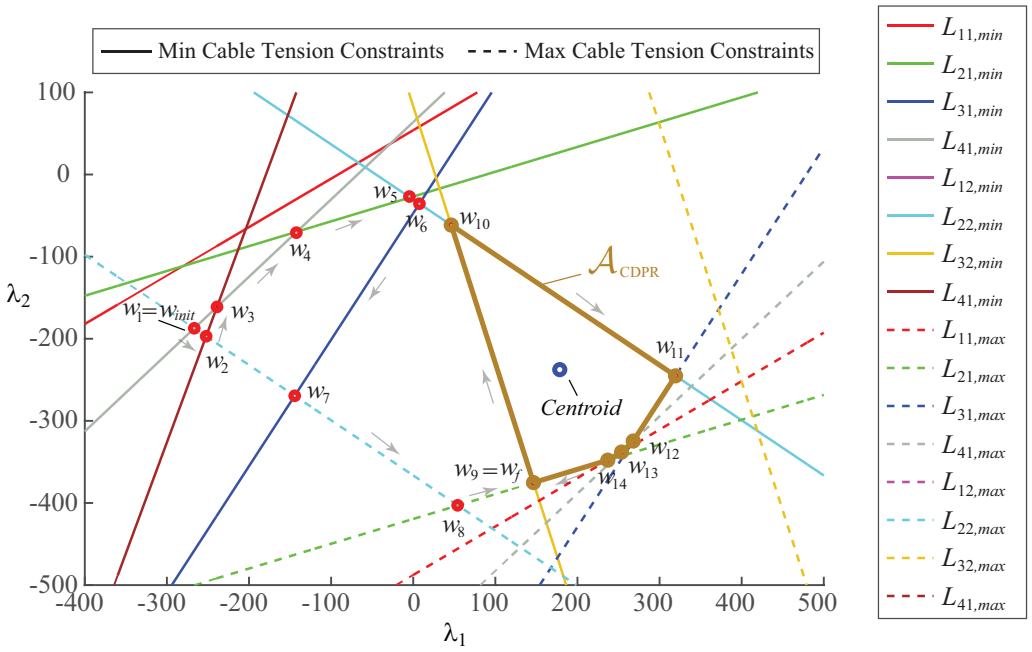

Figure 3.7: Feasible Polygon considering only cable tension limits of FASTKIT

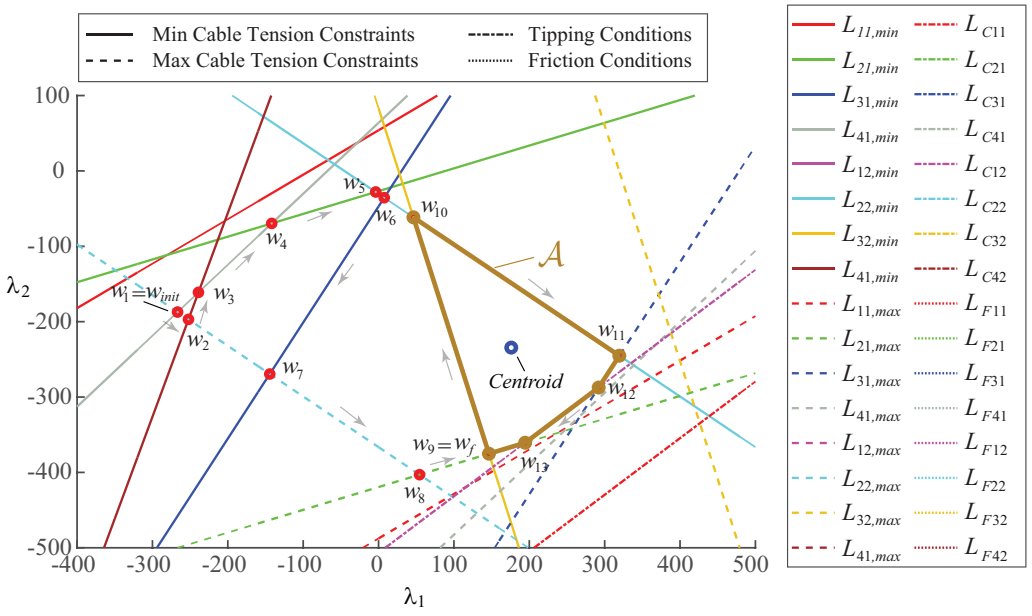

Figure 3.8: Feasible Polygon considering both cable tension limits and static equilibrium conditions of FASTKIT

centroids of $\mathcal{A}_{CDPR}$ and $\mathcal{A}$ are $[178.4619, \ -237.6105]$ and $[176.0786, \ -234.4328]$, respectively.

3.3.2 MCDPRs with one degree of actuation redundancy

For MCDPRs with n-DoF moving-platform pulled by $n+1$ cables, $\mathcal{A}$ takes the form of a one dimensional space, *i.e.,* a single dimensional line. Thus, each inequality

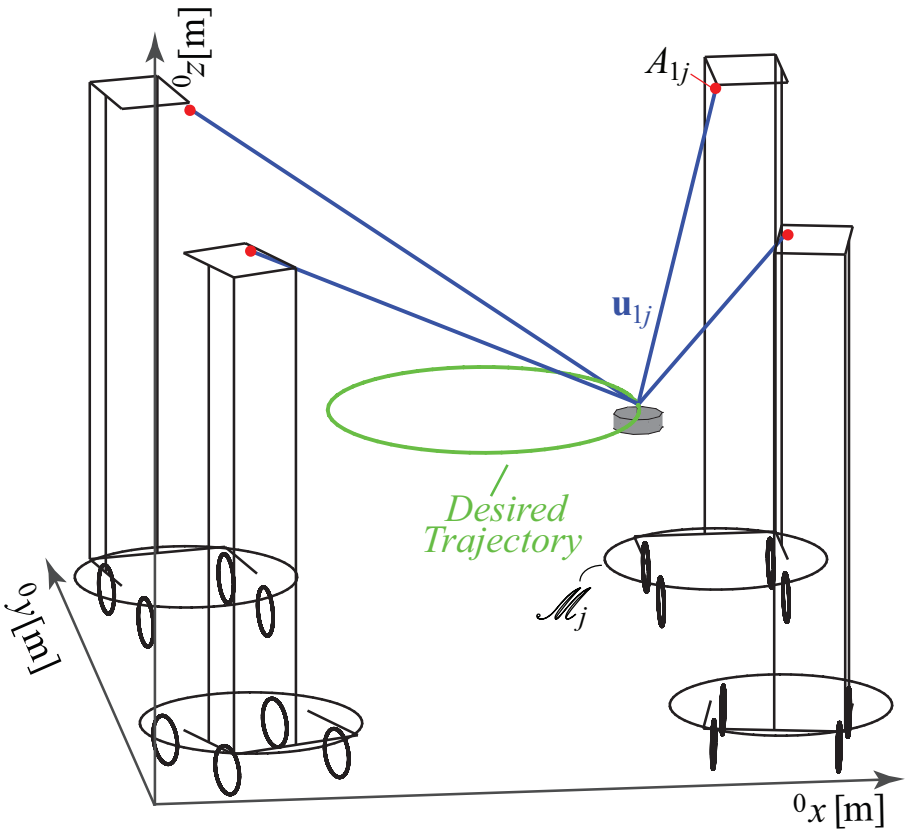

Figure 3.9: MoPICK configuration and Desired Trajectory

constraint from Eq. (3.44) is reduced to an intersection point on a single dimensional λ-axis. As a consequence, to find the acceptable distribution of the cable tensions, we have only one DoF to move on a straight line via choosing a suitable λ. In such a scenario, the feasible polygon will be composed of only two vertices, which are defined by the two inequality constraints from Eq. (3.44), whose intersection on the λ-axis satisfy all the rows of Eq. (3.44). Finally, the centroid of the feasible polygon is used to compute the feasible distribution of tension among the cables using Eq. (3.24). Based on the above discussion, a simple TDA for MCDPRs with one degree of actuation redundancy can be provided as:

- Compute the λ-intersections for each inequality constraint from Eq. (3.44).
- For each λ-intersection, compute the corresponding feasible index set I.
- If the feasible polygon exists, there must be two λ-intersections that satisfy all the inequalities of Eq. (3.44), *i.e.,* the feasible index set I contains the indices of all the rows of Eq. (3.44).
- Finally, the centroid of the feasible polygon is computed and is used to calculate the feasible cable tension distribution.

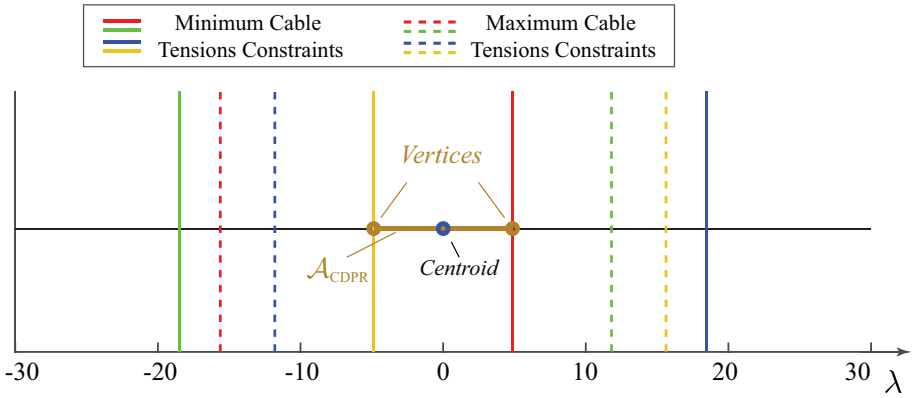

Figure 3.10: Feasible Polygon considering only tension limit constraints of MoPICK

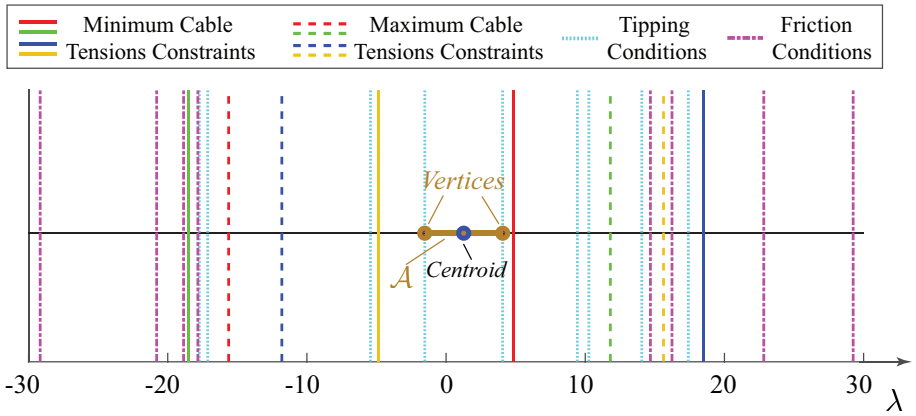

Figure 3.11: Feasible Polygon considering both cable tension limits and the static equilibrium conditions of MoPICK

3.3.2.1 Case Study: MoPICK

To examine the FCTD of a MCDPR with one degree of actuation redundancy, we have considered MoPICK with the configuration understudy shown in Fig. 3.9. For the moving-platform position to be in static equilibrium, the feasible polygons $\mathcal{A}_{CDPR}$ and $\mathcal{A}$ are illustrated in Figs. 3.10 and 3.11, respectively. Similar to the earlier case studies, it is evident that the additional static equilibrium conditions of the mobile bases reduce the space of feasible cable tension solutions which satisfy all the constraints of Eq. (3.44). The $\boldsymbol{\lambda}$ coordinate of $\mathcal{A}_{CDPR}$ centroid is 0, while of $\mathcal{A}$ is 1.29, respectively.

3.4 Results of TDA for a desired trajectory

For each MCDPR case study presented in the previous section, the proposed TDA is validated through simulation on a prescribed test trajectory. The algorithm is assessed based on the continuity of the solution for the cable tensions, while respecting the

constraints associated to the cable tension limits and the static equilibrium conditions of the mobile bases.

The constraints associated to the cable tension limits are simply evaluated by verifying the solution of cable tension lies within its lower and upper bounds $\underline{t}$ and $\bar{t}$. The tipping conditions are evaluated based on the evolution of the ZMP. For a concise comparison, the ZMP of each mobile base is normalized between 0 and 1, and is referred to as normalized ZMP, *i.e.*, if normalized ZMP stays within the defined limits of 0 and 1, C_{zj} stays within the boundaries of the wheels footprint and all the tipping conditions associated with $\mathscr{M}_j$ are satisfied.

3.4.1 Case Study: Planar MCDPR with two mobile bases and four cables connected to a point mass moving-platform

For the case study of a MCDPR with a two DoF point mass moving-platform, the proposed TDA is validated on a test trajectory depicted in Fig. 3.3. It is rectangular test trajectory designed to displace the point mass moving-platform by sequentially passing through the points $\overline{P}_1$ to $\overline{P}_4$. Each corner of the rectangular test trajectory is a zero velocity point. Total trajectory time is 10 s having 3 s for $\overline{P}_1\overline{P}_2$ and $\overline{P}_3\overline{P}_4$ path while 2 s for $\overline{P}_2\overline{P}_3$ and $\overline{P}_4\overline{P}_1$ path. The moving platform has a mass of 8 kg while each mobile bases is 150 kg. Dimension of each mobile base is $0.75 \times 0.64 \times 0.7$ m^3. The distance between the two mobile bases is 6 m while the exit points A_{2j} are located at the height of 3 m. Lower and upper bounds on the cable tension are set to 0 N and 280 N, respectively.

The evolution of normalized ZMP is illustrated in Fig. 3.12. As mentioned earlier, the normalized ZMP must lie in between 0 and 1 for the mobile bases to be in the state of static equilibrium with respect to the tipping conditions. If only the constraints associated to the cable tension limits are considered, the mobile bases will tip over during the path $2-3$ and $4-1$ as ZMP exits the support polygon. While considering both cable tension limits and the static equilibrium conditions associated to the mobile bases, the desired trajectory is completed with the ZMP remaining within the support polygon. Fig. 3.13 depicts the cable tensions computed using the FCTD for MCDPRs. The cable tensions are within their respective bounds throughout the trajectory.

A video showing the evolution of the feasible polygon as a function of time considering only tension limit constraints and both tension limits and static equilibrium conditions of the mobile bases can be seen at[1]. This video also shows the location the mobile base ZMP as well as some example tipping configurations of the mobile cable-driven parallel robot under study.

[1] https://drive.google.com/open?id=1q9GT4hBtZjcmbamsCNy5UIeoGviN8NG0

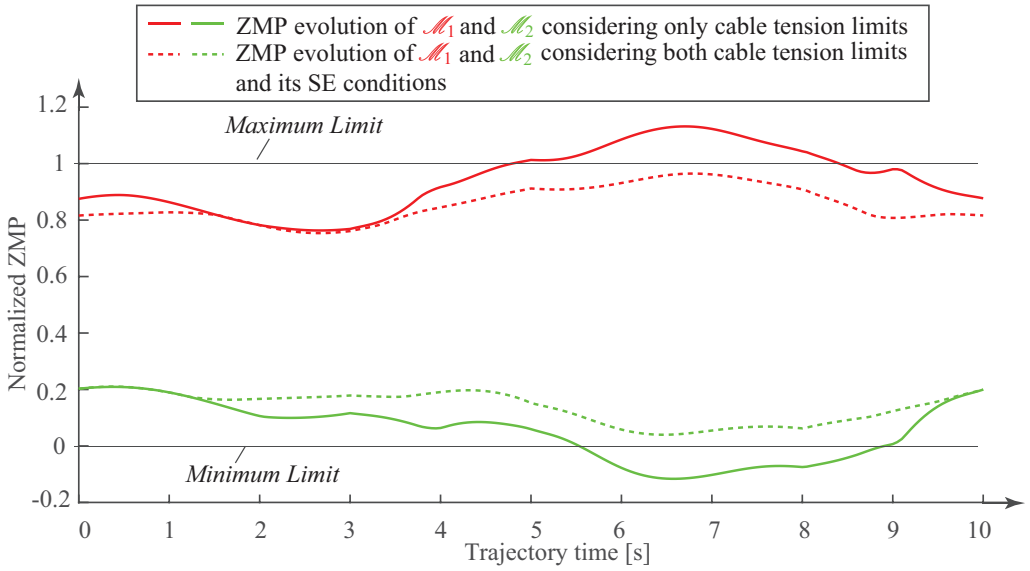

Figure 3.12: Evolution of normalized ZMP of a two DoF point mass MCDPR case study

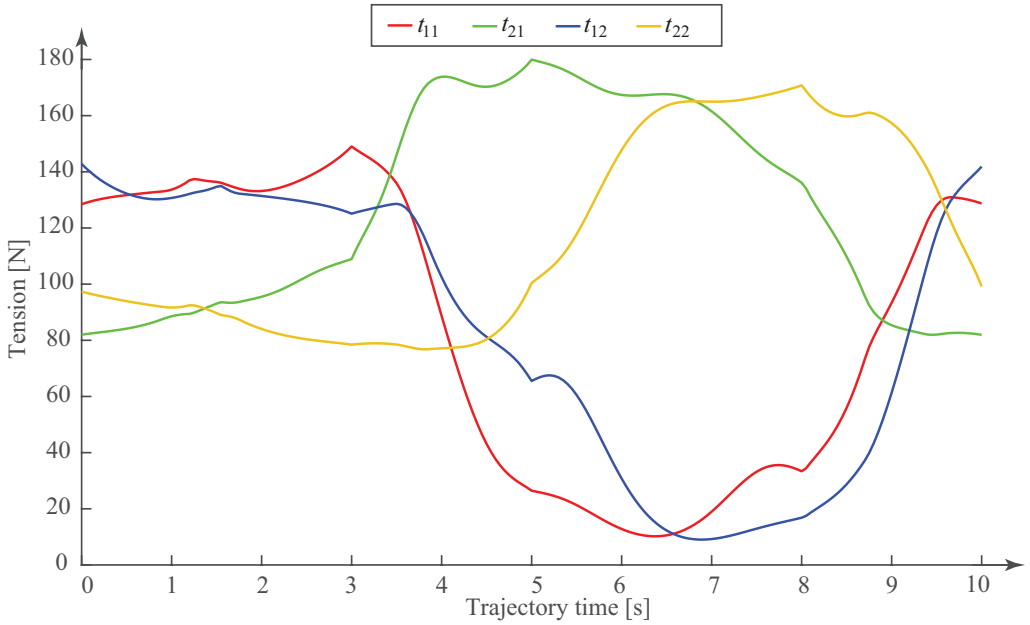

Figure 3.13: Cable tension profile of a two DoF point mass MCDPR case study

3.4.2 FASTKIT

To study the results of the proposed TDA on FASTKIT, a pick-and-place trajectory is designed depicted in green in Fig. 3.6. The total trajectory time is set to 10 s and is composed of two distinct paths, *i.e.,* $\overline{P}_1\overline{P}_2$ and $\overline{P}_2\overline{P}_3$, each with maximum duration of 5 s. The mass of the moving-platform is set to 10 kg and each mobile base is 150 kg. The trajectory is started with the moving-platform is at $\overline{P}_1$ followed by $\overline{P}_2$. An object of 5 kg must be picked at $\overline{P}_2$ from the shelf increasing the total

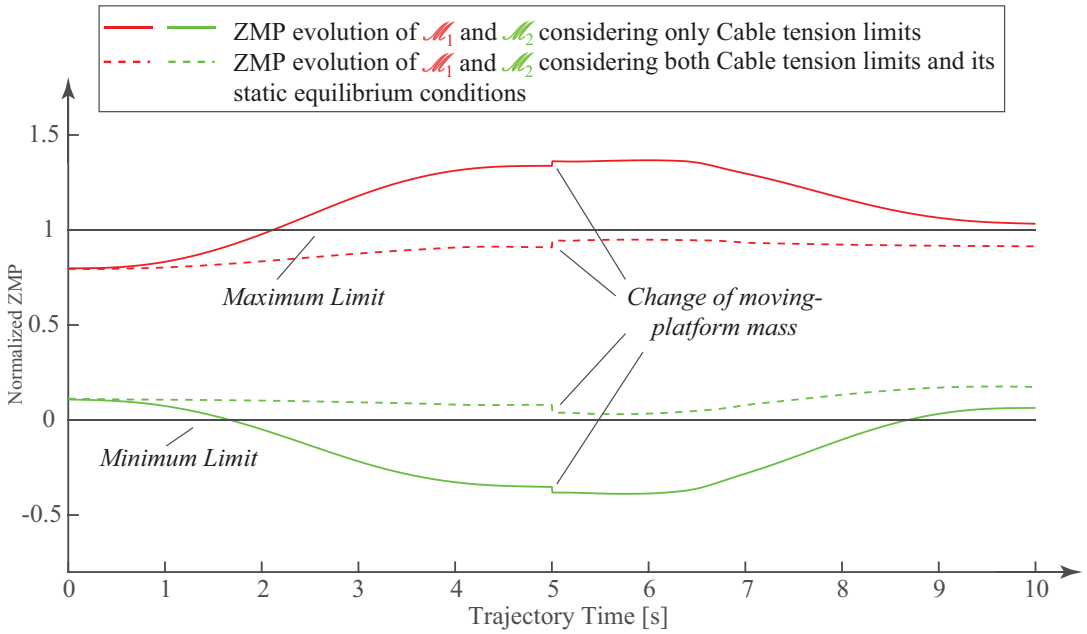

Figure 3.14: Evolution of normalized ZMP of FASTKIT

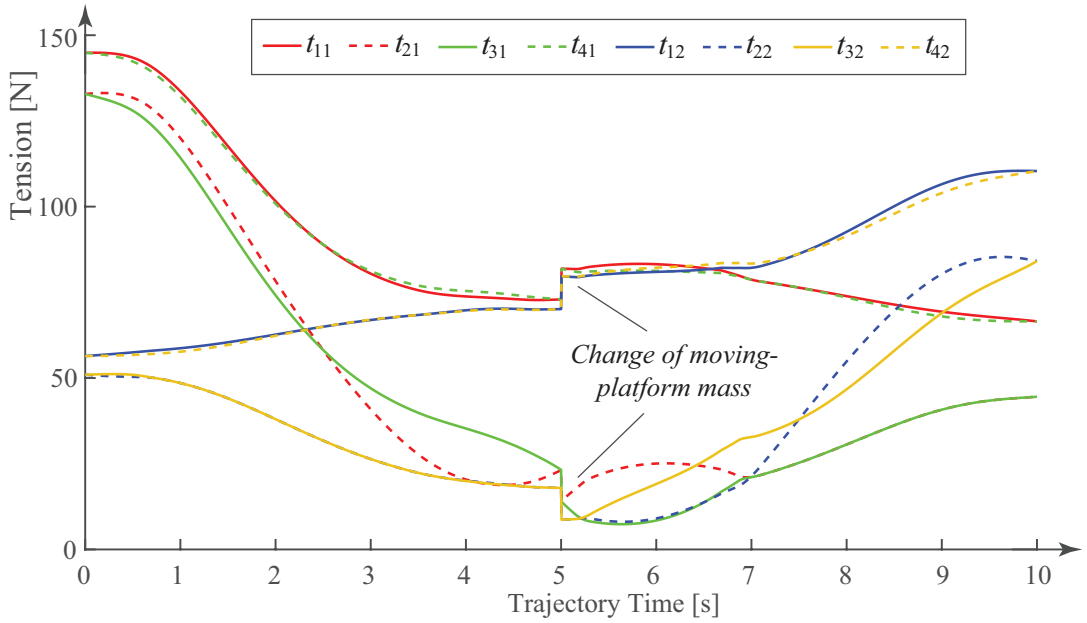

Figure 3.15: Cable tension profile of FASTKIT

weight of the moving-platform to 15 kg during the path $\overline{P}_2\overline{P}_3$.

Lower and upper bounds on the cable tension are set to 0 N and 200 N, respectively. The evolution of normalized ZMP for the desired trajectory is illustrated in Fig. 3.14. It can be observed that by considering only the constraints associated to the cable tension limits, both the mobile bases tip over as ZMP exits the support polygon. While taking into account both the cable tension limits and the static equilibrium conditions associated to the mobile bases, the desired trajectory is completed

with the ZMP remaining within the support polygon. The evolution of the cable tensions computed by the modified TDA is shown in Fig. 3.15. It is evident that the modified TDA generates a continuous profile of the cable tensions, which are kept within their respective bounds throughout the trajectory. A discontinuity at time equals to 5 s is due to the change in the moving-platform weight, when the object is picked from the shelf.

3.4.3 MoPICK

A circular trajectory designed to study the proposed TDA on MoPICK and is depicted in green in Fig. 3.9. The total time to complete the circular trajectory is set to 10 s. The weight of the point mass moving-platform is 1 kg, while the weight of each mobile base is 5 kg. The cable tension lower bound is null while the cable tension upper bound is set to 15 N.

The evolution of normalized ZMP for the desired circular trajectory is illustrated in Fig. 3.16. It can be observed that by considering only the constraints associated to the cable tension limits, the mobile base $\mathscr{M}_1$ tips over as its ZMP goes out of the footprint boundary. While taking into account both the cable tension limits and the static equilibrium conditions associated to the mobile bases, the desired trajectory is completed with the ZMP of all the mobile bases remaining within the support polygon. The evolution of the cable tensions computed by the modified TDA to generate the desired wrenches on the moving-platform is shown in Fig. 3.17. Similar to the previous case studies, the modified TDA generated a continuous profile of the cable tensions, which are within their respective bounds throughout the trajectory.

A simulation video illustrating the evolution of the feasible polygon as a function of time for the desired circular trajectory considering both cable tension limits and the static equilibrium conditions of the mobile bases can be seen at[2].

3.5 Conclusion

Due to the uni-directional nature of cables, over-constrained CDPRs, *i.e.,* CDPRs with more cables than the DoF of their moving-platform, are preferred in numerous applications. However, this leads to actuation redundancy. The control of such redundantly actuated manipulators requires a real-time algorithm that can compute continuous distribution of the cable tensions by considering its lower and uppers bounds imposed by the actuators and the transmission systems. For classical CDPRs, a geometric approach known as Barycenter/Centroid is frequently used to acquire a real-time, continuous feasible solution of the cable tensions. However, the approach is not directly applicable to MCDPRs due to the additional conditions associated with

[2] https://drive.google.com/open?id=1pmtTmMpQrLgu_vogtv2183HFOAXGpSE8

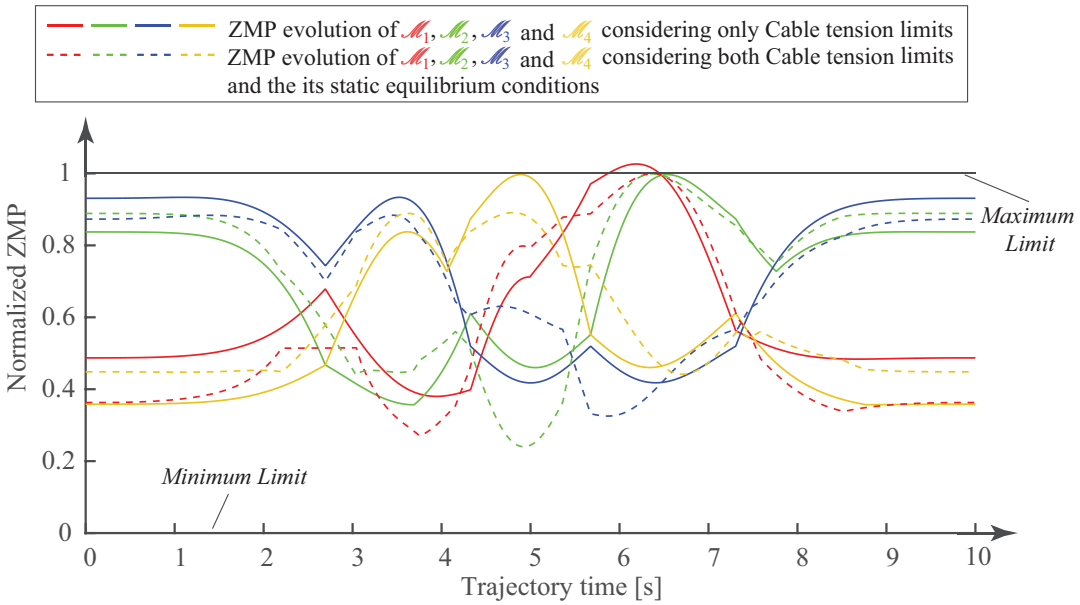

Figure 3.16: Evolution of normalized ZMP of MoPICK

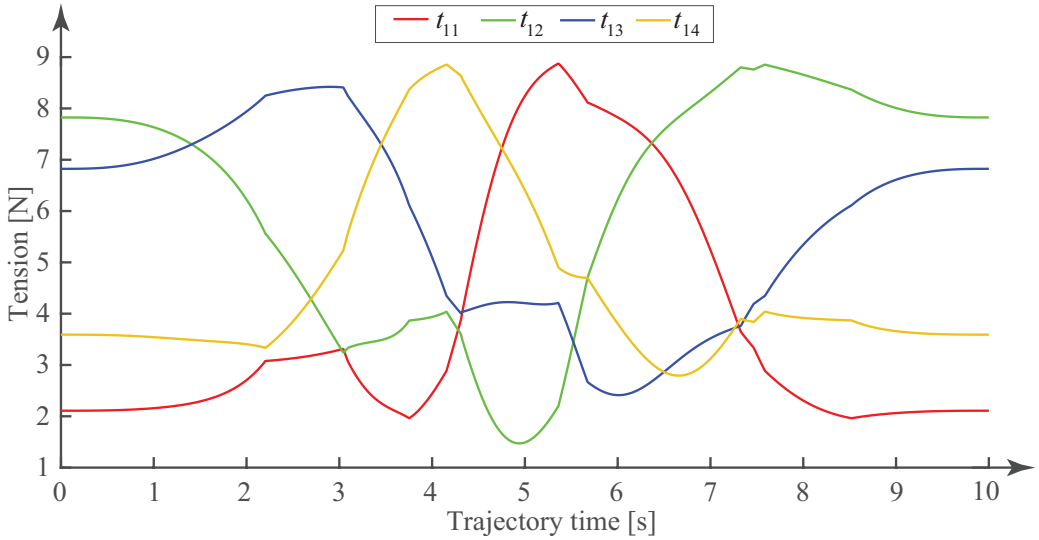

Figure 3.17: Cable tension profile of MoPICK

the static equilibrium of the mobile bases. Therefore, this chapter has introduced a real-time TDA by extending the classical Barycenter/Centroid method to MCDPRs.

Initially, the static equilibrium conditions of MCDPRs are studied. In contrast to a classical CDPR, which only considers the static equilibrium of the moving-platform, for MCDPRs the additional conditions associated with the mobile bases must be taken into account. The equilibrium of the mobile bases is characterized by their

tipping and sliding conditions. The tipping conditions depends on the moment generated at the boundaries of the mobile base footprint. This moment uniquely depends on the weight of the mobile base and the tension in the cables attached to it. Likewise, the sliding conditions also depend on the weight of the mobile base and those cable tensions. However, the sliding conditions are represented in the form of a friction cone. For ease of analysis, the non-linear sliding conditions are linearized and the friction cone becomes a four-sided friction pyramid.

Using the aforementioned static equilibrium conditions, a real-time TDA is developed for MCDPRs. The proposed algorithm forms a FCTD representing the set of feasible tensions based on the cable tension limits and the conditions associated with the static equilibrium of the mobile bases. This FCTD takes the form of a $(m - n)$-dimensional convex polytope. The presented TDA finds the vertices of the feasible polygon or proves that it is null. If the feasible polygon exists and is determined, then the centroid of the polygon will be calculated, which amounts somehow the solution as far as possible from the constraints. The coordinates of the centroid are used to compute the feasible distribution of the cable tensions. The obtained results show that the new set of constraints developed for MCDPRs (Eq. (3.44)) are sufficient to compute feasible cable tensions such that they stay within the required set of limits while ensuring the stability of all the mobile bases. The proposed algorithm was investigated on multiple case studies including FASTKIT and MoPICK. The algorithm is relevant for real-time implementations, however, it has only been validated up to two degrees of actuation redundancy.

4

Wrench-Feasible Workspace of MCDPRs

Contents

In many applications, it is required that the end-effector operates in a particular workspace with the ability to exert a set of wrenches. In this case, it is appropriate to consider the Wrench feasible workspace. Moreover, WFW is more relevant from a practical viewpoint. Despite the fact that much work has been done in the area of generating WFW workspace of classical CDPRs, however, these techniques cannot be directly used for MCDPRs due to the additional conditions associated with the static equilibrium of the mobile bases derived in Chapter 3. Hence, this chapter presents a methodology to determine the Wrench-Feasible Workspace of MCDPRs.

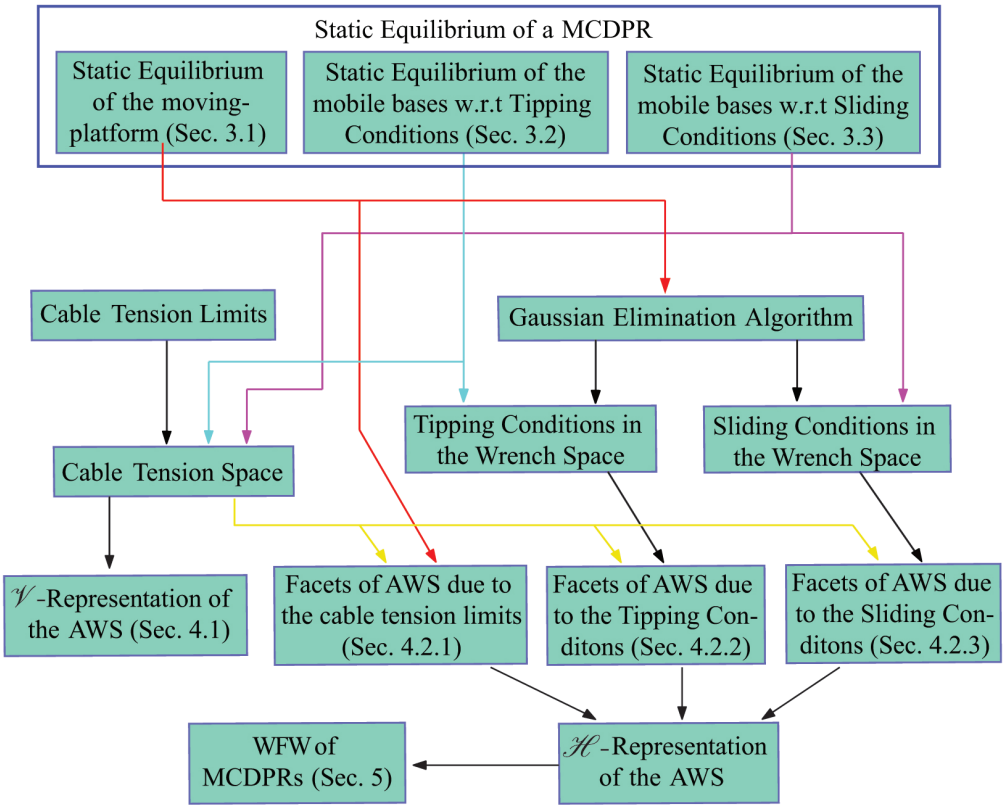

Figure 4.1: Methodology used to determine the WFW of a MCDPR

As mentioned earlier, WFW is defined as the set of moving-platform poses for which the required set of wrenches can be balanced by the AWS, *i.e.*, the wrenches generated by the cables on the moving-platform. It is shown in [BGM10, GK10] that the AWS of a classical CDPR takes the form of a n-dimensional zonotope which is a special class of convex polytope. A zonotope is a type of polytope that is centrally symmetric. Each face of a zonotope has another face that is parallel to it [Grü03]. The two widely used approaches to construct convex polytopes are $\mathscr{V}$-representation, known as the Convex Hull approach, and $\mathscr{H}$-representation, known as the Hyperplane Shifting Method (HSM).

Determination of the AWS requires a cable tension space. The cable tension space illustrates the region of acceptable tensions in the cables that can keep the robot in equilibrium. The cable tension space of classical CDPRs is formed only by the cable tension limits $\underline{t}_{ij}$ and $\bar{t}_{ij}$. Contrary to classical CDPRs, the static equilibrium of the mobile bases, characterized by its tipping and sliding conditions, should be taken into account in addition to the cable tension limits to determine the cable tension space of MCDPRs. This cable tension space is exploited to determine the $\mathscr{V}$-representation of the AWS.

For classical CDPRs, the $\mathscr{H}$-representation of the AWS is defined by constructing the facets of the polytope and depends on the robot geometric architecture and the

cable tension limits. However, due to the additional static equilibrium conditions of the mobile bases, the AWS is no longer a zonotope, but a convex polytope. Therefore, the $\mathscr{H}$-representation of the AWS for MCDPRs is defined by constructing its facets using both the cable tension limits and the static equilibrium conditions of the mobile bases expressed in the wrench space. The aforementioned conditions are originally derived in the tension space (Eqs. (3.14) and (3.22)) that can be mapped into the wrench space by solving the static equilibrium of the moving-platform defined by Eq. (3.3) using Gaussian Elimination Algorithm. Finally, the $\mathscr{H}$-representation of the AWS is exploited to trace the WFW workspace of MCDPRs. This methodology is illustrated by the flowchart shown in Fig. 4.1

The rest of the chapter aims at presenting the approach to determine the WFW for MCDPRs. The cable tension space of MCDPRs is detailed in Sec. 4.1.1. A methodology to map the static equilibrium conditions of the mobile bases into the wrench space of the moving-platform is described in Sec. 4.1.2.2. Accordingly, the AWS of MCDPRs is calculated using both the $\mathscr{V}$-representation and the $\mathscr{H}$-representation as explained in Sec. 4.1. Section 4.2 explains how the WFW is traced using H-representation of the AWS. Additionally, three case studies are investigated in Sec. 4.2 along with the experimental validation of the concept.

4.1 Available Wrench Set for MCDPRs

As mentioned earlier, the AWS of a classical CDPR, denoted as $\mathscr{A}_{CDPR}$, depends uniquely on the robot's geometric architecture and the cable tension limits [BGM10, GK10], expressed as:

$$\mathscr{A}_{CDPR} = \left\{ \begin{bmatrix} \mathbf{f} \\ \mathbf{m} \end{bmatrix} \in \mathbb{R}^n \mid \begin{bmatrix} \mathbf{f} \\ \mathbf{m} \end{bmatrix} = \mathbf{W}\boldsymbol{t},\ \underline{t}_{ij} \leq t_{ij} \leq \bar{t}_{ij},\ i = 1, \ldots, m_j,\ j = 1, \ldots, p \right\}. \tag{4.1}$$

In contrast, the AWS of MCDPRs cannot be fully characterized by the cable tension limits as the mobile bases static equilibrium conditions must be considered. Hence, the AWS of a MCDPR, denoted as $\mathscr{A}$ is defined as:

$$\begin{aligned} \mathscr{A} = \Bigg\{ \begin{bmatrix} \mathbf{f} \\ \mathbf{m} \end{bmatrix} \in \mathbb{R}^n \mid \begin{bmatrix} \mathbf{f} \\ \mathbf{m} \end{bmatrix} = \mathbf{W}\boldsymbol{t},\ \underline{t}_{ij} \leq t_{ij} \leq \bar{t}_{ij},\ m_{C_{kj}} \leq 0, \\ \mathbf{E}_F\ {}^0\mathbf{f}_{c_{zj}} \leq \mathbf{0}_4,\ i = 1, \ldots, m_j,\ k = 1, \ldots, c_j,\ j = 1, \ldots, p \Bigg\}. \end{aligned} \tag{4.2}$$

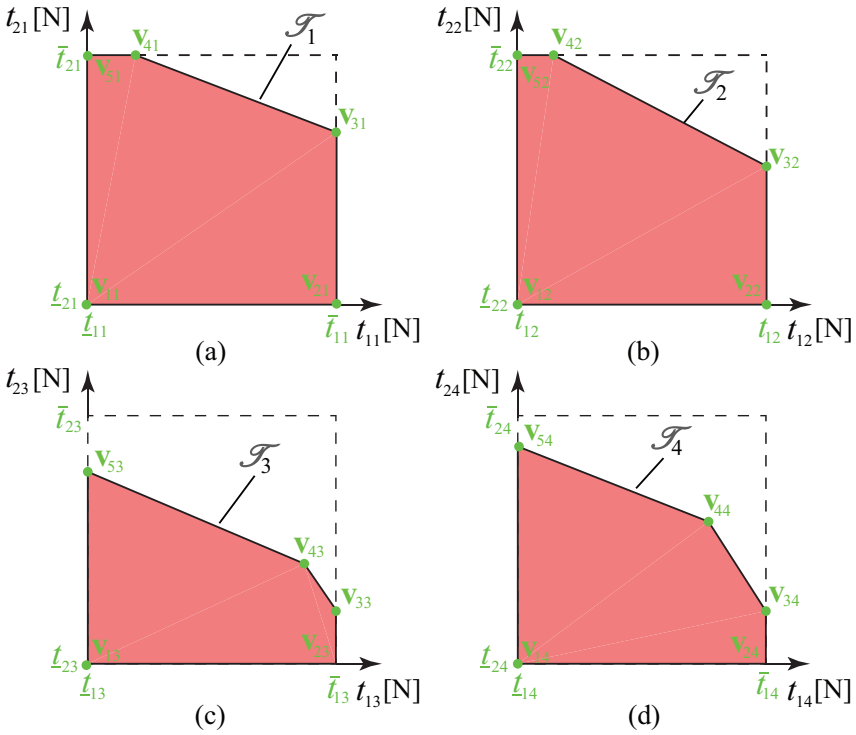

Figure 4.2: Tension space associated to (a) $\mathscr{M}_1$, (b) $\mathscr{M}_2$,(c) $\mathscr{M}_3$,(d) $\mathscr{M}_4$ considering both the cable tension limits and the static equilibrium of the mobile bases

The expression of the AWS for MCDPRs corresponds to the definition of a convex polytope. Both the above mentioned approaches, *i.e.*, $\mathscr{V}$-representation and $\mathscr{H}$-representation will be exploited to characterize such convex polytopes. $\mathscr{V}$-representation is preferred for visualizing the AWS but is computationally more expensive than $\mathscr{H}$-representation, which is used to determine the relation between the AWS and the required wrenches to perform a task. The convex-hull approach uses the vertices of the cable tension space to determine the vertices of AWS and forms the boundary of the convex polytope, detailed in Sec. 4.1.1. HSM allows us to determine the AWS geometrically by characterizing the facets of the polytope, explained in Sec. 4.1.2.

4.1.1 Convex Hull Method

For MCDPRs, AWS takes the form of a convex polytope and is the image of the tension space under the linear mapping of the wrench matrix $\mathbf{W}$ [BGM10, GK10, RLMGC18a]. Thus $\mathscr{V}$-representation defines the AWS of MCDPRs by finding the set of vertices forming the boundary of the convex polytope. The vertices of the AWS are obtained by mapping the tension space vertices into the wrench space under $\mathbf{W}$. Thus the tension space vertices of a MCDPR should first be defined.

The cable tension space defines the region of acceptable cable tensions which

maintains the static equilibrium of a MCDPR. As discussed earlier, the tension space of classical CDPRs is only formed by the cable tension limits and takes the form of a m-dimensional hypercube [BGM10]. For MCDPRs, the jth mobile base has its own independent m_j-dimensional tension space associated only with its attached cables of tensions $t_{ij},\ i = 1,\dots,m_j$. Therefore, the cable tension space of $\mathscr{M}_j$, denoted as $\mathscr{T}_j$, is formed by mapping the static equilibrium conditions of the latter defined by Eqs. (3.14) and (3.22) on the m_j-dimensional tension space formed by the cable tension limits $\underline{t}_{ij}$ and $\bar{t}_{ij},\ i = 1,\dots,m_j$. As an example, Fig. 4.2 illustrates the tension space associated with each mobile base of a MCDPR shown in Fig 1.4a

Without loss of generality, let's assume that $\mathscr{T}_j$ is composed of v_j vertices. Let the m_j-dimensional coordinate vector of the dth vertex of $\mathscr{T}_j$, $d = 1,\dots,v_j$ be denoted as $\mathbf{v}_{dj}$. The vertices of $\mathscr{T}_j$ and their coordinates can be obtained using the Double Description Method [Mot53], which exploits the static equilibrium conditions of $\mathscr{M}_j$ and the bounds on the cable tensions $t_{ij},\ i = 1,\dots,m_j$. Let $\mathscr{V}_j$ be the set of vertices of $\mathscr{T}_j$,

$$\mathscr{V}_j = \{\mathbf{v}_{dj}\}, \qquad d = 1,\dots,v_j. \tag{4.3}$$

The coordinates of the vertices for $\mathscr{T}_j$ can be expressed in a matrix form as:

$$\mathbf{V}_j = [\mathbf{v}_{1j}\ \mathbf{v}_{2j}\ \dots\ \mathbf{v}_{dj}\ \dots \mathbf{v}_{v_j j}], \tag{4.4}$$

where $\mathbf{V}_j$ is a $(m_j \times v_j)$ matrix containing the coordinates of the vertices of $\mathscr{T}_j$. Let v be the total number of vertices formed by the m cables, which is defined by the product of the number of vertices of the tension space associated to each mobile base, namely,

$$v = \prod_{j=1}^{p} v_j. \tag{4.5}$$

The vertices of the tension space of a MCDPR can be obtained by taking the Cartesian product between the vertices of $\mathscr{V}_j$, $j = 1,\dots,p$. Let $\mathscr{V}$ denote the set of all vertices of the tension space for a given MCDPR. Let $\mathbf{V}$ be a $(m \times v)$-matrix denoting the coordinates of the vertices in $\mathscr{V}$ expressed as:

$$\mathbf{V} = [\mathbf{v}_1\ \mathbf{v}_2\ \dots\ \mathbf{v}_l\ \dots\ \mathbf{v}_v], \tag{4.6}$$

where $l = 1,\dots,v$. $\mathbf{v}_l$ is a m-dimensional vector representing the coordinates of the lth vertex of the MCDPR cable tension space noted as $\mathscr{T}$. The image of AWS is constructed from $\mathbf{V}$ under the linear mapping of the wrench matrix $\mathbf{W}$ expressed as:

$$\mathbf{W}_A = \mathbf{W}\mathbf{V}, \tag{4.7}$$

where $\mathbf{W}_A$ is a $(n \times v)$-matrix representing the image of the vertices of the MCDPR tension space into the wrench space. The convex hull of the points whose coordinate vectors are the columns of $\mathbf{W}_A$ leads to the AWS of the MCDPR using a numerical procedure known as *quickhull* [BDH96].

4.1.2 Hyperplane Shifting Method

Hyperplane Shifting Method is a geometric approach, which defines a convex polytope as the intersection of the half-spaces bounded by its hyperplanes [GK10]. The classical HSM used to characterize the AWS of the CDPRs is explained in [BGM10, GK10], however, this is only applicable if the tension space is a hypercube, *i.e.,* when the facets of the AWS only comprises the constraints associated with the cable tension limits. Due to the additional static equilibrium conditions, the classical HSM is therefore not sufficient to fully characterize the AWS of MCDPRs [RLMGC18a]. Thus, for MCDPRs, the additional facets of the AWS associated with the static equilibrium of the mobile bases must be determined. As a consequence, this section introduces an improved version of HSM while taking into account the static equilibrium conditions of the MCDPR mobile bases in addition to the cable tension limits.

Section 4.1.2.1 characterizes the facets of the AWS denoted as $\mathscr{H}_q^+$, $\mathscr{H}_q^-$, associated with the cable tension limits of MCDPRs, where $q = 1, \ldots, C_{n-1}^m = \frac{m!}{(m-n+1)!(n-1)!}$. To express the facets of the AWS associated with the static equilibrium conditions of $\mathscr{M}_j$, it is required to map the latter into the wrench space. Therefore, Sec. 4.1.2.2 presents the adopted methodology to map the static equilibrium conditions of $\mathscr{M}_j$ into the wrench space. Eventually, Secs. 4.1.2.3 and 4.1.2.4 present the hyperplanes associated with both the tipping and sliding conditions of $\mathscr{M}_j$.

4.1.2.1 Hyperplanes associated with Cable Tension Limits

For classical CDPRs, AWS takes the form of a zonotope by considering only the constraints associated with the cable tension limits [BGM10, GK10]. The facets of the zonotope are formed by the set of vectors $\beta_{ij}\mathbf{u}_{ij}\Delta t_{ij}$, $0 \leq \beta_{ij} \leq 1$. Δt_{ij} represents the difference between the maximum and minimum cable tension limits of cable $\mathscr{C}_{ij}$, expressed as:

$$\Delta t_{ij} = \bar{t}_{ij} - \underline{t}_{ij}. \tag{4.8}$$

The shape of the zonotope is formed by the directions of the cable unit vectors $\mathbf{u}_{ij}$ while the size of the zonotope depends on Δt_{ij}. However, Δt_{ij} is no longer a

constant for MCDPRs as illustrated in Fig. 4.2. The property of a zonotope having parallel facets still holds as the shape of the facets are defined by the cable unit vectors $\mathbf{u}_{ij}$. However the location of the hyperplanes forming the facets of the AWS is modified leading to a convex polytope with parallel facets. Thus, the hyperplanes associated with the cable tension limits for MCDPRs are determined using classical HSM detailed in [BGM10, GK10] and by considering the modified tension space.

The pairs of parallel hyperplanes are determined by the sets of $(n-1)$ column vectors of $\mathbf{W}$ [BGM10, GK10]. As a consequence, the cable tension limits leads to C_{n-1}^{m} hyperplanes $(\mathscr{H}_q^+, \mathscr{H}_q^-,\ q = 1, \ldots, C_{n-1}^{m})$. The first step is to obtain the orientation of those hyperplanes by taking $n-1$ linear combinations out of m columns of $\mathbf{W}$. The qth combination, ${}^{c}\mathbf{W}^{q}$ is a $(n \times n-1)$-matrix containing $(n-1)$ columns of $\mathbf{W}$. The remaining $m-n+1$ columns of $\mathbf{W}$ are denoted as ${}^{d}\mathbf{W}^{q}$ such that,

$$\mathbf{W} = \left[{}^{c}\mathbf{W}^{q} \quad {}^{d}\mathbf{W}^{q} \right], \qquad q = 1, \ldots, C_{n-1}^{m}. \tag{4.9}$$

The orientation of $\mathscr{H}_q^+, \mathscr{H}_q^-$ is defined by the n-dimensional unit vector $\mathbf{e}_q$ orthogonal to its facets, expressed as

$$\mathbf{e}_q = \frac{\mathbf{r}_q}{||\mathbf{r}_q||}, \tag{4.10}$$

where $\mathbf{r}_q$ is a n-dimension vector expressed as the linear combination of the columns of ${}^{c}\mathbf{W}^{q}$. The position of $\mathscr{H}_q^+, \mathscr{H}_q^-$ is given by the projection of the MCDPR tension space vertices on $\mathbf{e}_q$. Let $\mathbf{l}_q$ be a m-dimensional vector representing the projection of $\mathbf{W}$ on $\mathbf{e}_q$,

$$\mathbf{l}_q = \mathbf{W}^T \mathbf{e}_q. \tag{4.11}$$

It is noteworthy that the projection of the actuation wrenches in ${}^{c}\mathbf{W}$ is null as they are orthogonal to $\mathbf{e}_q$. Let h_q^+, h_q^- be the maximum and minimum combinations of $\mathbf{l}_q$ with the coordinates of the MCDPR tension space vertices, namely,

$$h_q^+ = \max\left(\mathbf{v}_l^T\ \mathbf{l}_q, \quad l = 1, \ldots, v \right); \quad h_q^- = \min\left(\mathbf{v}_l^T\ \mathbf{l}_q, \quad l = 1, \ldots, v \right). \tag{4.12}$$

To completely characterize the location of the hyperplanes, a point p_q^+ (p_q^-, resp.) must be defined on $\mathscr{H}_q^+$ ($\mathscr{H}_q^-$, resp.), expressed as:

$$\mathbf{p}_q^+ = h_q^+ \mathbf{e}_q + \mathbf{W}\underline{\mathbf{t}}; \qquad \mathbf{p}_q^- = h_q^- \mathbf{e}_q + \mathbf{W}\underline{\mathbf{t}}, \tag{4.13}$$

where $\underline{\mathbf{t}} = [\underline{t}_{11}, \ldots, \underline{t}_{ij}, \ldots, \underline{t}_{m_p p}]^T$ is a m-dimensional vector containing the cable tension lower bounds. $\mathbf{W}\underline{\mathbf{t}}$ defines the wrench generated by the minimum cable

tensions. The position of $\mathscr{H}_q^+$ ($\mathscr{H}_q^-$, resp.) is determined by a shifting distance d_q^+ (d_q^-, resp.) along $\mathbf{e}_q$ from the origin, expressed as:

$$d_q^+ = \mathbf{e}_q^T \mathbf{p}_q^+; \qquad d_q^- = \mathbf{e}_q^T \mathbf{p}_q^-. \tag{4.14}$$

Finally, the respective pairs of hyperplanes $\mathscr{H}_q^+$, $\mathscr{H}_q^-$ are expressed as:

$$\mathscr{H}_q^+ : \ \mathbf{e}_q^T \begin{bmatrix} \mathbf{f} \\ \mathbf{m} \end{bmatrix} \ \leq \ d_q^+; \qquad \mathscr{H}_q^- : \ -\mathbf{e}_q^T \begin{bmatrix} \mathbf{f} \\ \mathbf{m} \end{bmatrix} \ \leq \ d_q^-. \tag{4.15}$$

The above procedure is repeated to determine the C_{n-1}^m pairs of hyperplanes associated with the m cables of a MCDPR.

4.1.2.2 Static Equilibrium of $\mathscr{M}_j$ in Wrench Space

To map the static equilibrium conditions associated with $\mathscr{M}_j$ into the wrench space, the system of linear equations defined in Eq. (3.3) should be solved. In case $m = n$ and $\mathbf{W}$ is full rank, the cable tensions $t_{ij}, i = 1, \ldots, m_j$ are expressed as,

$$\mathbf{t} \ = \mathbf{W}^{-1}\mathbf{w}. \tag{4.16}$$

The solutions of the cable tensions $t_{ij}, \ i = 1, \ldots, m_j$ extracted from Eq. (4.16) are substituted in static equilibrium the conditions of $\mathscr{M}_j$ defined in Eqs. (3.14) and (3.22) to map the latter into the wrench space. Thus, if $m = n$, each static equilibrium condition in the tension space will also generate a single condition into the wrench space.

On the contrary, if $m > n$, there will exist $C_n^m = \frac{m!}{(m-n)!n!}$ number of possible solutions for t_{ij} to map the static equilibrium conditions associated with $\mathscr{M}_j$ into the wrench space. As a consequence, there exists C_n^m number of $(n \times n)$ square sub-matrices of the wrench matrix $\mathbf{W}$ denoted as ${}^a\mathbf{W}^s, s = 1, \ldots, C_n^m$ containing n columns of $\mathbf{W}$. Let ${}^a\mathbf{t}^s$ be a n-dimensional vector containing the cable tensions associated with the actuation wrenches of ${}^a\mathbf{W}^s$. Let ${}^a\mathbf{V}^s$ be a $(n \times v)$ matrix denoting the coordinates of the tension space vertices of ${}^a\mathbf{t}^s$. ${}^a\mathbf{V}^s$ is defined by extracting the corresponding rows of $\mathbf{V}$ from Eq. (4.6) associated with the cable tensions included in ${}^a\mathbf{t}^s$. The remaining $m - n$ columns of $\mathbf{W}$ and the corresponding cable tension vector along with the coordinates of the tension space vertices are denoted as ${}^b\mathbf{W}^s$, ${}^b\mathbf{t}^s$ and ${}^b\mathbf{V}^s$ respectively. Thus for the sth combination, the static equilibrium of the moving platform defined in Eq. (3.3) can be expressed by splitting the Wrench matrix into its square sub matrix ${}^a\mathbf{W}^s$ and the remaining columns ${}^b\mathbf{W}^s$ as

$${}^a\mathbf{W}^s \ {}^a\mathbf{t}^s + {}^b\mathbf{W}^s \ {}^b\mathbf{t}^s = \mathbf{w} \implies {}^a\mathbf{W}^s \ {}^a\mathbf{t}^s = \mathbf{w} - {}^b\mathbf{W}^s \ {}^b\mathbf{t}^s \qquad s = 1, \ldots, C_n^m. \tag{4.17}$$

Therefore, the coordinates of the MCDPR tension space vertices in Eq. (4.6) can be expressed for the sth combination as,

$$\mathbf{V}^s = \begin{bmatrix} {}^a\mathbf{V}^s \\ {}^b\mathbf{V}^s \end{bmatrix} = \begin{bmatrix} {}^a\mathbf{v}_1^s & \dots & {}^a\mathbf{v}_l^s & \dots & {}^a\mathbf{v}_v^s \\ {}^b\mathbf{v}_1^s & \dots & {}^b\mathbf{v}_l^s & \dots & {}^b\mathbf{v}_v^s \end{bmatrix}, \tag{4.18}$$

where ${}^a\mathbf{v}_l^s$ and ${}^b\mathbf{v}_l^s$ denote the lth column of ${}^a\mathbf{V}^s$ and ${}^b\mathbf{V}^s$, respectively. Equation (4.17) amounts to a linear system of equations having n number of equations with n unknowns (${}^a\mathbf{t}^s$). The Gaussian Elimination Algorithm [Poo14] is used to solve such linear system of equations presented in Appendix A. The Algorithm determines the components of a cable tension vector ${}^a\mathbf{t}^s$. The meaningful solutions *i.e.* the solutions for the cable tensions t_{ij} included in ${}^a\mathbf{t}^s$ only are extracted and used to map the static equilibrium conditions of $\mathscr{M}_j$ into the wrench space explained as follows.

Amongst the m_j cables attached to $\mathscr{M}_j$, let m_{ja} be the number of cables whose tensions are components of vector ${}^a\mathbf{t}_j^s$. The tensions of the remaining $m_{jb} = m_j - m_{ja}$ cables are the components of vector ${}^b\mathbf{t}_j^s$. As a consequence, the cable tension vector $\mathbf{t}_j$ and its associated actuation wrench matrix $\mathbf{W}_j$ defined in Eq. (3.7) can also be expressed as:

$$\mathbf{t}_j^s = \begin{bmatrix} {}^a\mathbf{t}_j^{sT} & {}^b\mathbf{t}_j^{sT} \end{bmatrix}^T = \begin{bmatrix} {}^at_{1j}^s & \dots & {}^at_{oj}^s & \dots & {}^at_{m_{ja}j}^s & {}^bt_{1j}^s & \dots & {}^bt_{rj}^s & \dots & {}^bt_{m_{jb}j}^s \end{bmatrix}^T, \tag{4.19a}$$

$$\mathbf{W}_j^s = \begin{bmatrix} {}^a\mathbf{w}_{1j}^s & \dots & {}^a\mathbf{w}_{oj}^s & \dots & {}^a\mathbf{w}_{m_{ja}j}^s & {}^b\mathbf{w}_{1j}^s & \dots & {}^b\mathbf{w}_{rj}^s & \dots & {}^b\mathbf{w}_{m_{jb}j}^s \end{bmatrix}, \tag{4.19b}$$

where $s = 1, \dots, C_n^m$. ${}^at_{oj}^s$, $o = 1, \dots, m_{ja}$ and ${}^bt_{rj}^s$, $r = 1, \dots, m_{jb}$ are the oth and rth components of ${}^a\mathbf{t}_j^s$ and ${}^b\mathbf{t}_j^s$, respectively. ${}^a\mathbf{w}_{oj}^s$ (${}^b\mathbf{w}_{rj}^s$, resp.) is the actuation wrench associated with the cable tension ${}^at_{oj}^s$ (${}^bt_{rj}^s$, resp.). Using Gaussian Elimination Algorithm, the cable tension ${}^at_{oj}^s$, $o = 1, \dots, m_{ja}$ is obtained as:

$${}^at_{oj}^s = \frac{\alpha_{oj}^s \ (\mathbf{w} - {}^b\mathbf{W}^s \ {}^b\mathbf{t}^s)}{\alpha_{oj}^s \ {}^a\mathbf{w}_{oj}^s}, \qquad o = 1, \dots, m_{ja}, \ s = 1, \dots, C_n^m \tag{4.20}$$

where α_{oj}^s is a n-dimensional row vector acquired from Gaussian Elimination Algorithm. As an example, the output of algorithm for the MCDPR in Fig. 1.4a is presented in Appendix B. From Eq. (4.20), the tensions in the cables attached to $\mathscr{M}_j$ are substituted in the corresponding static equilibrium condition to map it into the wrench space presented in the following sections.

4.1.2.3 Hyperplanes associated with the tipping conditions

This section presents the hyperplanes of the AWS associated with the tipping conditions of $\mathscr{M}_j$ about the footprint boundary $\mathscr{L}_{C_{kj}}$, noted as $\mathscr{H}^s_{Ckj},\ k=1,\ldots,c_j,\ s=1,\ldots,C^m_n$. Using Eq. (4.19a), the tipping conditions of $\mathscr{M}_j$ defined by Eq. (3.13) about $\mathscr{L}_{C_{kj}}$ is expressed as:

$$\begin{aligned}&\mathbf{u}^T_{C_{kj}}((\mathbf{g}_j-\mathbf{c}_{kj})\times\mathbf{w}_{gj})\ +\ \sum_{o=1}^{m_{ja}}\mathbf{u}^T_{C_{kj}}((\mathbf{c}_{kj}-{}^a\mathbf{b}^s_{oj})\times{}^a\mathbf{u}^s_{oj})\ {}^at^s_{oj}\\&+\sum_{r=1}^{m_{jb}}\mathbf{u}^T_{C_{kj}}((\mathbf{c}_{kj}-{}^b\mathbf{b}^s_{rj})\times{}^b\mathbf{u}^s_{rj})\ {}^bt^s_{rj}\ \le 0,\quad k=1,\ldots,c_j,\ s=1,\ldots,C^m_n.\end{aligned}\tag{4.21}$$

where ${}^a\mathbf{b}^s_{oj}$ and ${}^b\mathbf{b}^s_{rj}$ are the coordinate vectors of the anchor points to which the cables of tension vectors ${}^a\mathbf{t}^s_{oj}$ and ${}^b\mathbf{t}^s_{rj}$ are attached. ${}^a\mathbf{u}^s_{oj}$ and ${}^b\mathbf{u}^s_{rj}$ are the directional vector of those cables. Substituting Eq. (4.20) in Eq. (4.21) yields,

$$\begin{aligned}&\sum_{o=1}^{m_{ja}}\frac{\mathbf{u}^T_{C_{kj}}((\mathbf{c}_{kj}-{}^a\mathbf{b}^s_{oj})\times{}^a\mathbf{u}^s_{oj})\alpha^s_{oj}}{\alpha^s_{oj}{}^a\mathbf{w}^s_{oj}}\begin{bmatrix}\mathbf{f}\\\mathbf{m}\end{bmatrix}+\sum_{r=1}^{m_{jb}}\mathbf{u}^T_{C_{kj}}((\mathbf{c}_{kj}-{}^b\mathbf{b}^s_{rj})\times{}^b\mathbf{u}^s_{rj})\ {}^bt^s_{rj}\\&-\sum_{o=1}^{m_{ja}}\frac{\mathbf{u}^T_{C_{kj}}((\mathbf{c}_{kj}-{}^a\mathbf{b}^s_{oj})\times{}^a\mathbf{u}^s_{oj})\alpha^s_{oj}}{\alpha^s_{oj}{}^a\mathbf{w}^s_{oj}}\ {}^b\mathbf{W}^s\ {}^b\mathbf{t}^s+\mathbf{u}^T_{C_{kj}}((\mathbf{g}_j-\mathbf{c}_{kj})\times\mathbf{w}_{gj})\le 0,\\&k=1,\ldots,c_j,\ s=1,\ldots,C^m_n.\end{aligned}\tag{4.22}$$

Equation. (4.22) gives the tipping conditions for $\mathscr{M}_j$ expressed in the wrench space. Eq. (4.22) characterizes a hyperplane $\mathscr{H}^s_{Ckj}$:

$$\mathscr{H}^s_{Ckj}\ :\ (\mathbf{e}^s_{Ckj})^T\begin{bmatrix}\mathbf{f}\\\mathbf{m}\end{bmatrix}\ \le\ d^s_{Ckj},\ k=1,\ldots,c_j,\ s=1,\ldots,C^m_n,\tag{4.23}$$

where $\mathbf{e}^s_{Ckj}$ is a n-dimensional unit vector orthogonal to $\mathscr{H}^s_{Ckj}$ expressed as:

$$\mathbf{e}^s_{Ckj}=\sum_{o=1}^{m_{ja}}\frac{\mathbf{u}^T_{C_{kj}}((\mathbf{c}_{kj}-{}^a\mathbf{b}^s_{oj})\times{}^a\mathbf{u}^s_{oj})}{\alpha^s_{oj}{}^a\mathbf{w}^s_{oj}}\alpha^s_{oj},\ k=1,\ldots,c_j,\ s=1,\ldots,C^m_n.\tag{4.24}$$

The distance from the origin of the wrench set to hyperplane $\mathscr{H}^s_{Ckj}$ along $\mathbf{e}^s_{Ckj}$ is defined by d^s_{Ckj}. This distance is a function of the weight of $\mathscr{M}_j$ and the cable

tensions included in ${}^{b}\mathbf{t}^{s}$, namely,

$$\begin{aligned} d^{s}_{Ckj} = \max\left(\sum_{o=1}^{m_{ja}} \frac{\mathbf{u}^{T}_{C_{kj}}((\mathbf{c}_{kj} - {}^{a}\mathbf{b}^{s}_{oj}) \times {}^{a}\mathbf{u}^{s}_{oj})\alpha^{s}_{oj}}{\alpha^{s}_{oj}\,{}^{a}\mathbf{w}^{s}_{oj}}\ {}^{b}\mathbf{W}^{s}\ {}^{b}\mathbf{v}^{s}_{l},\ l = \{1,\ldots,v\} \right) \\ - \min\left(\sum_{r=1}^{m_{jb}} \mathbf{u}^{T}_{C_{kj}}((\mathbf{c}_{kj} - {}^{b}\mathbf{b}^{s}_{rj}) \times {}^{b}\mathbf{u}^{s}_{rj})\ {}^{b}v^{s}_{rdj},\ d = \{1,\ldots,v_j\} \right) \\ - \mathbf{u}^{T}_{C_{kj}}((\mathbf{g}_{j} - \mathbf{c}_{kj}) \times \mathbf{w}_{gj}) \leq 0,\ k = 1,\ldots,c_j,\ s = 1,\ldots,C^{m}_{n}. \end{aligned} \tag{4.25}$$

where ${}^{b}v^{s}_{rdj}$ is the rth component of the tension space generated by cable tensions ${}^{b}t^{s}_{rj},\ r = 1,\ldots,m_{jb}$. The shifting distance d^{s}_{Ckj} represents the wrench capabilities of the moving platform against the corresponding tipping conditions about $\mathscr{L}_{C_{kj}}$ for sth combination. ${}^{b}\mathbf{W}^{s}\ {}^{b}\mathbf{v}^{s}_{l}$ represents the wrenches applied by tension space vertices in ${}^{b}\mathbf{V}^{s}$ along $\mathbf{e}^{s}_{Ckj}$. This must be maximized to acquire the maximum wrench capabilities of the moving platform. On the contrary, the term $\mathbf{u}^{T}_{C_{kj}}((\mathbf{c}_{kj} - {}^{b}\mathbf{b}^{s}_{rj}) \times {}^{b}\mathbf{u}^{s}_{rj})^{b}t^{s}_{rj}$ contributes to the tipping of $\mathscr{M}_j$ due to the cable tensions ${}^{b}t^{s}_{rj},\ r = 1,\ldots,m_{jb}$, and thus should be minimized. Each mobile base generates up to $c_j \times C^{m}_{n}$ possible hyperplanes corresponding to its tipping conditions.

4.1.2.4 Hyperplanes associated with the sliding conditions

This section describes the hyperplanes of the AWS associated with sliding conditions of mobile base $\mathscr{M}_j$, noted as $\mathscr{H}^{s}_{Fgj}, g = 1,\ldots,4, s = 1,\ldots,C^{m}_{n}$, respectively. The sliding conditions defined by Eq. (3.22) can be expressed using Eq. (4.19a) as,

$$\sum_{o=1}^{m_{ja}} \mathbf{E}_{F}\,{}^{a}\mathbf{u}^{s}_{oj}\,{}^{a}t^{s}_{oj} + \sum_{r=1}^{m_{jb}} \mathbf{E}_{F}\,{}^{b}\mathbf{u}^{s}_{rj}\,{}^{b}t^{s}_{rj} - \mathbf{E}_{F}\mathbf{w}_{gj} \leq \mathbf{0}_4,\quad s = 1,\ldots,C^{m}_{n}. \tag{4.26}$$

Substituting Eq. (4.20) in Eq. (4.26) yields:

$$\begin{aligned} \sum_{o=1}^{m_{ja}} \frac{\mathbf{E}_{F}\,{}^{a}\mathbf{u}^{s}_{oj}\alpha^{s}_{oj}}{\alpha^{s}_{oj}\,{}^{a}\mathbf{w}^{s}_{oj}} \begin{bmatrix} \mathbf{f} \\ \mathbf{m} \end{bmatrix} - \sum_{o=1}^{m_{ja}} \frac{\mathbf{E}_{F}\,{}^{a}\mathbf{u}^{s}_{oj}\alpha^{s}_{oj}}{\alpha^{s}_{oj}\,{}^{a}\mathbf{w}^{s}_{oj}}\ {}^{b}\mathbf{W}^{s}\ {}^{b}\mathbf{t}^{s} + \sum_{r=1}^{m_{jb}} \mathbf{E}_{F}\,{}^{b}\mathbf{u}^{s}_{rj}\,{}^{b}t^{s}_{rj} \\ - \mathbf{E}_{F}\ \mathbf{w}_{gj} \leq \mathbf{0}_4,\quad s = 1,\ldots,C^{m}_{n}. \end{aligned} \tag{4.27}$$

Equation (4.27) expresses the sliding conditions of $\mathscr{M}_j$ into the wrench space. The latter can be directly expressed in the form of a hyperplane $\mathscr{H}^{s}_{Fgj}$ as,

$$\mathscr{H}^{s}_{Fgj} \ :\ (\mathbf{E}^{s}_{Fgj})^{T} \begin{bmatrix} \mathbf{f} \\ \mathbf{m} \end{bmatrix} \leq d^{s}_{Fgj},\ s = 1,\ldots,C^{m}_{n},\ g = 1,\ldots,4. \tag{4.28}$$

where $\mathbf{E}^s_{Fgj}$ is a n-dimensional unit vector orthogonal to $\mathscr{H}^s_{Fgj}$ expressed as:

$$\mathbf{E}^s_{Fgj} = \sum_{o=1}^{m_{ja}} \frac{\mathbf{E}^g_F \ {}^a\mathbf{u}^s_{oj} \ \alpha^s_{oj}}{\alpha^s_{oj} \ {}^a\mathbf{w}^s_{oj}}, \ s = 1, \ldots, C^m_n, \ g = 1, \ldots, 4. \tag{4.29}$$

$\mathbf{E}^g_F$ denotes the gth row of $\mathbf{E}_F$. The shifted distance of $\mathscr{H}^s_{Fgj}$ is denoted as d^s_{Fgj}:

$$\begin{aligned} d^s_{Fgj} = \max\left(\sum_{o=1}^{m_{ja}} \frac{\mathbf{E}_F \, {}^a\mathbf{u}^s_{oj} \alpha^s_{oj}}{\alpha^s_{oj} \ {}^a\mathbf{w}^s_{oj}} \ {}^b\mathbf{W}^s \ {}^b\mathbf{v}^s_l, \ l = \{1, \ldots, v\} \right) \mathbf{E}^g_F \ \mathbf{w}_{gj} \\ + \ \mathbf{E}^g_F \ \mathbf{w}_{gj} - \min\left(\sum_{r=1}^{m_{jb}} \mathbf{E}^g_F \ {}^b\mathbf{u}^s_{rj} \ {}^b v^s_{rdj}, \ d = \{1, \ldots, v_j\} \right), \\ s = 1, \ldots, C^m_n, \ g = 1, \ldots, 4. \end{aligned} \tag{4.30}$$

The shifting distance d^s_{Fgj} represents the wrench capabilities of the moving platform with respect to the corresponding sliding conditions associated with the gth boundary of the linearized friction pyramid of $\mathscr{M}_j$. It should be noted that each mobile base can generates up to $4 \times C^m_n$ possible hyperplanes corresponding to its sliding conditions.

4.2 Wrench Feasible Workspace of MCDPRs

The capacity margin index μ defined in [GCCRC14, RCCG15] can be used to calculate if a moving-platform pose is wrench-feasible. It is also known as a measure of the robustness of the equilibrium of the robot, expressed as,

$$\mu = \min \ (\ \min \ \mu_{xy}), \tag{4.31}$$

where μ_{xy} is the signed distance from the xth vertex of $\mathscr{R}$ to the yth facet of $\mathscr{A}$. μ is positive if and only if all the vertices of RWS are inscribed by $\mathscr{A}$, *i.e.* the moving platform has the ability to generate RWS while respecting all the equilibrium conditions of a MCDPR.

In the following sections the wrench capabilities of three MCDPRs are outlined. The results are compared with the wrench capabilities of the classical CDPRs which only considers the constraints associated with the cable tension limits.

4.2.1 Case study: $p = 2$, $m = 4$ and $n = 2$ DoF MCDPR

The first case study is a planar MCDPR with a 1.5kg point mass end-effector shown in Fig. 4.3a. The corresponding cable tension space is illustrated in Figs. 4.3c and 4.3d. The AWS defined by the Convex Hull approach is illustrated in Fig. 4.3e. It can be observed that by considering only the cable tension limit constraints, the AWS in

black corresponds to the wrench capabilities of a classical CDPR in the form of a zonotope. On the contrary, by taking into account the additional static equilibrium conditions associated with the mobile bases, the MCDPR AWS in green is no longer a zonotope, but a convex polytope.

Figure 4.3f depicts the AWS for the MCDPR configuration shown in Fig. 4.3a, obtained by the HSM detailed in Sec. 4.1.2. The AWS due to cable tension limits is split by four additional hyperplanes due to the tipping and friction constraints named as $\mathscr{H}^1_{t21}$, $\mathscr{H}^1_{f21}$, $\mathscr{H}^6_{t12}$ and $\mathscr{H}^6_{f12}$ respectively. The hyperplane $\mathscr{H}^1_{t21}$ ($\mathscr{H}^6_{t12}$, resp.) is associated with the tipping of $\mathscr{M}_1$ ($\mathscr{M}_2$, resp.) at C_{21} (C_{12}, resp.) for $s = 1$ ($s = 6$, resp.), respectively. Similarly, the hyperplane $\mathscr{H}^1_{f21}$ ($\mathscr{H}^6_{f12}$, resp.) is associated with the sliding of $\mathscr{M}_1$ ($\mathscr{M}_2$, resp.). The aforementioned hyperplanes are computed using ${}^a\mathbf{t}^s$ and ${}^b\mathbf{t}^s$ for $s = 1$ and $s = 6$, defined as:

$$ {}^a\mathbf{t}^1 = \begin{bmatrix} {}^at^1_{11} \\ {}^at^1_{21} \end{bmatrix}, \quad {}^a\mathbf{t}^6 = \begin{bmatrix} {}^at^1_{12} \\ {}^at^1_{22} \end{bmatrix}, \quad {}^b\mathbf{t}^1 = \begin{bmatrix} {}^bt^1_{12} \\ {}^bt^1_{22} \end{bmatrix}, \quad {}^b\mathbf{t}^6 = \begin{bmatrix} {}^bt^1_{11} \\ {}^bt^1_{21} \end{bmatrix}. \tag{4.32} $$

The static workspace of the planar MCDPR is shown in Fig. 4.3b. The green region corresponds to the static workspace of the manipulator computed based on the cable tension limits, the mobile base tipping and sliding conditions. The gray region shows the area that cannot be reached by the point-mass end-effector because of mobile base tipping and/or sliding. The simulation and the experimental validations of this case study can be seen in video[1].

4.2.2 Case study: $p = 4$, $m = 8$ and $n = 3$ DoF Planar MCDPR

The second case study is a planar MCDPR with $n = 3$ DoF moving-platform illustrated in Fig. 4.4a. The modified tension space is computed for a given moving-platform pose based on the cable tension limits, mobile base tipping and sliding conditions illustrated in Fig. 4.5. Based on the vertices of the tension space, the $\mathscr{V}-$representation of the AWS is shown in Fig. 4.4b. The green area depicts the AWS of the manipulator characterized by the cable tension limits, the mobile base tipping and sliding conditions. The wrenches that cannot be generated by the end-effector due to the tipping and/or sliding of mobile bases are illustrated in gray.

Figure 4.6 depicts the hyperplanes associated with the static equilibrium of the MCDPR under study. The AWS due to cable tension limits is split by additional four hyperplanes due to the tipping and friction constraints named as $\mathscr{H}^1_{t21}$, $\mathscr{H}^2_{t21}$, $\mathscr{H}^1_{f21}$ and $\mathscr{H}^2_{f21}$ respectively. From Fig. 4.5, it appears that only the hyperplanes associated with the cable tension limits and the static equilibrium conditions of $\mathscr{M}_1$ define the facets of the AWS. The static equilibrium conditions of $\mathscr{M}_2$ do not affect

[1] https://youtu.be/UsvBnJ8q2v4

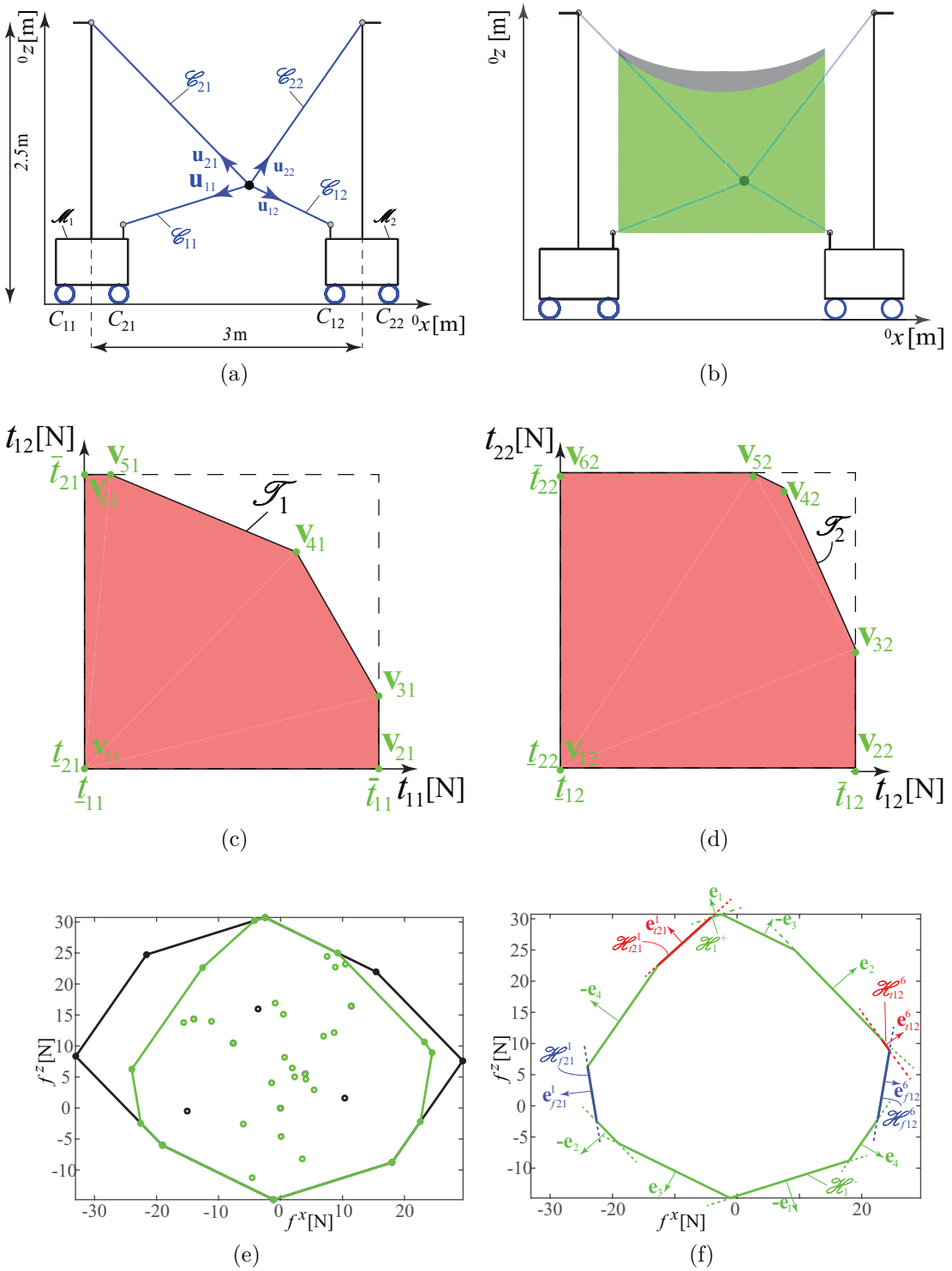

Figure 4.3: (a) Planar MCDPR with one point-mass end-effector, two mobile bases and four cables (b) Static workspace (c,d) Modified cable tension space (e) $\mathscr{V}-$Representation of AWS of a CDPR (in black) and MCDPR (in green) (f) $\mathscr{H}-$Representation of the AWS formed by the intersection of the hyperplanes

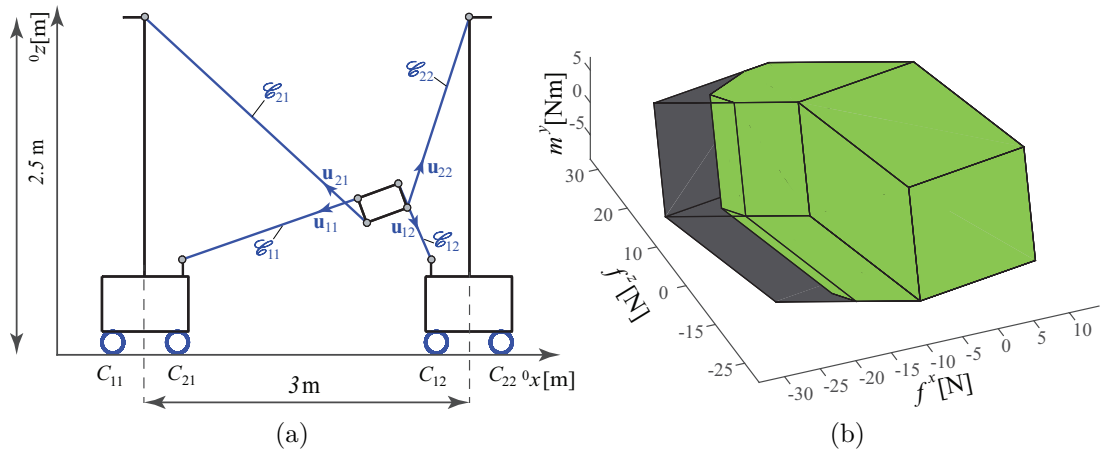

Figure 4.4: (a) Configuration under study of $p = 2$, $m = 4$ and $n = 3$ MCDPR (b) Comparison of AWS between CDPR (in black + green) and MCDPR (in green)

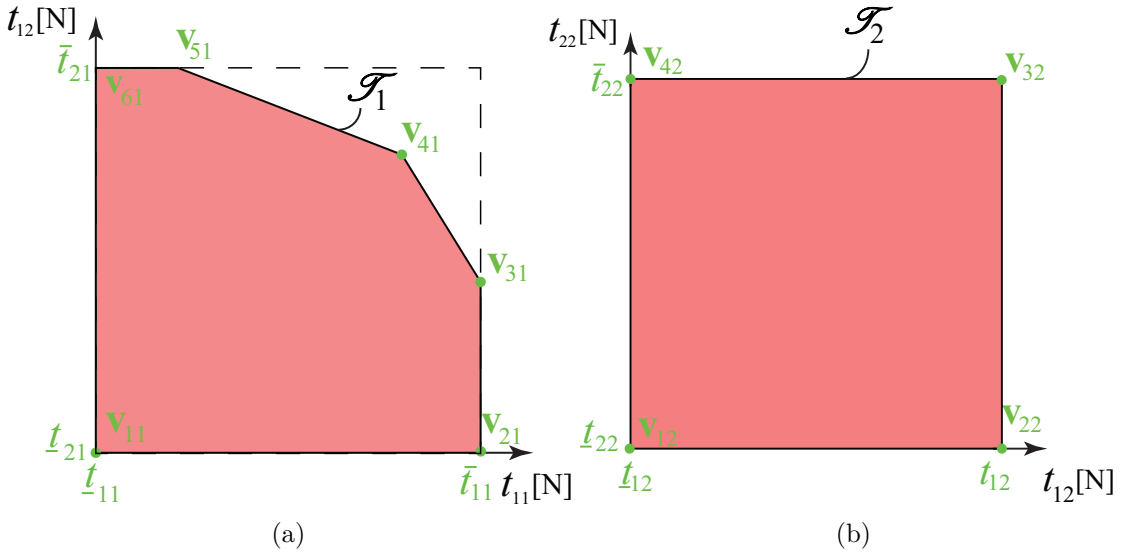

Figure 4.5: (a) $\mathscr{T}_1$ and $\mathscr{T}_2$ for MCDPR configuration in Fig. 4.4a

$\mathscr{T}_2$, and thus do not affect the AWS.

4.2.3 Case study: $p = 2$, $m = 8$ and $n = 6$ DoF Spatial MCDPR

The methodology described in Fig. 4.1 is used to trace the WFW of FASTKIT shown in Figs. 4.7a and 4.7c for different locations of the mobile bases. The green region corresponds to the static workspace of FASTKIT determined using the cable tension limits, the mobile base tipping and sliding conditions. The gray region illustrates the area that cannot be reached by the end-effector due to the tipping and/or sliding of the FASTKIT mobile bases. It should be noted that the higher the relative distance between the mobile bases, the smaller the wrench capability of FASTKIT along the vertical direction. The evolution of FASTKIT WFW as a function of the relative

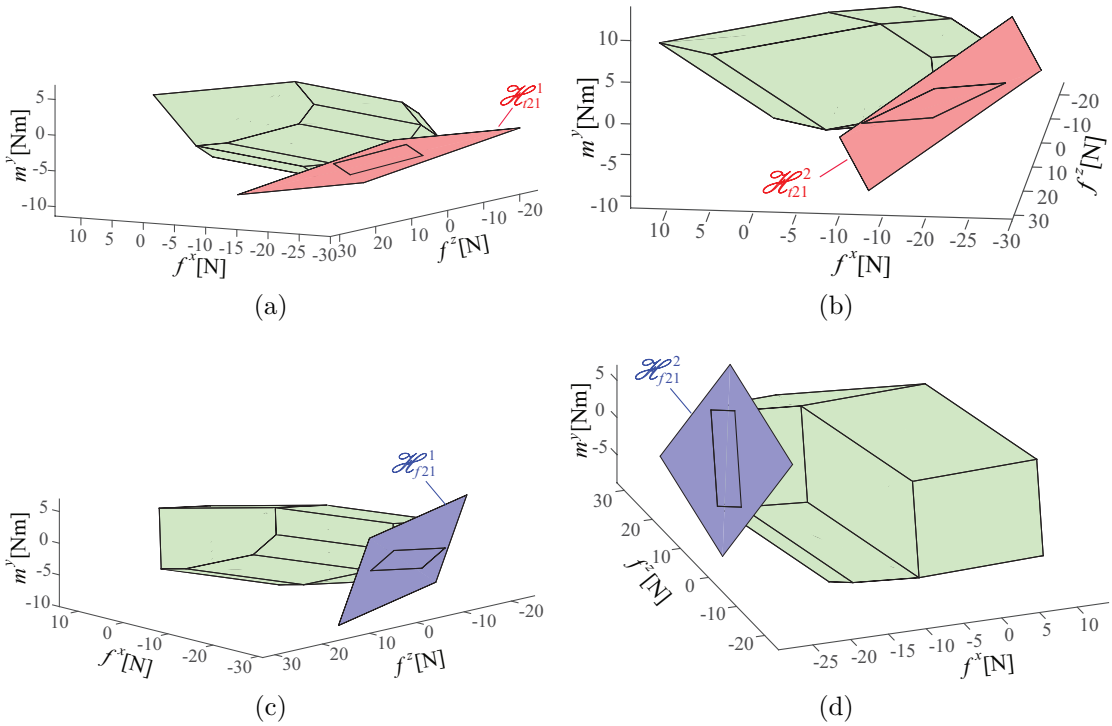

Figure 4.6: Correspondence between the WFW facets obtained with the Convex Hull approach (in green) and those obtained with HSM (a,b) Mobile Base tipping; (c,d) Mobile Base sliding for the moving-platform pose shown in Fig. 4.4a

distance between the two mobile bases can be seen in video[2].

From the AWS of FASTKIT in the configuration shown in Fig. 4.7a, the maximum absolute moments (forces, resp.) that the platform can support about (along, resp.) ${}^0x$, ${}^0y$ and ${}^0z$ axes are illustrated in Fig. 4.8. It can be seen that the wrench capability of the moving-platform is lower when the mobile bases are moving than when the the latter are fixed.

4.3 Conclusion

This chapter introduced a methodology to determine the Available Wrench Set of Mobile Cable-Driven Parallel Robots. The Available Wrench Set is required to trace the Wrench-Feasible Workspace of Mobile Cable-Driven Parallel Robots. The workspace depends, not only on the static equilibrium of the moving-platform, but on the static equilibrium of the mobile bases as well. The Available Wrench Set takes the form of a convex polytope and is defined using two different approaches, *i.e.*, Convex Hull and the Hyperplane Shifting Method. Convex Hull is preferred for visualizing the AWS but is computationally more expensive than Hyperplane Shifting Method,

[2]https://youtu.be/EXbp1Bb7OCo

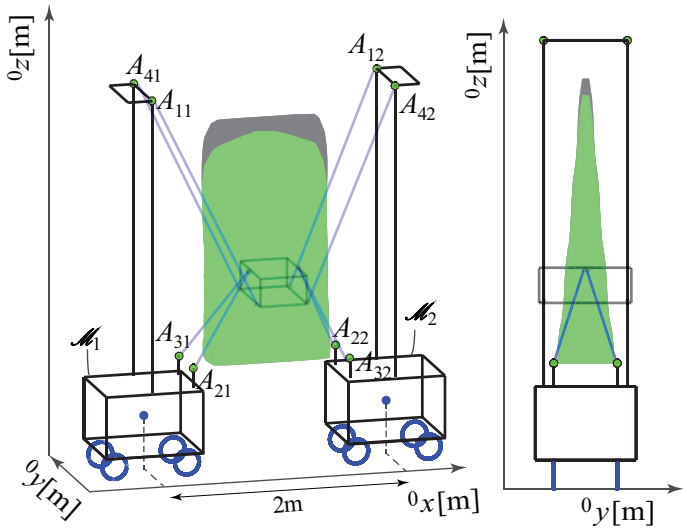

(a)

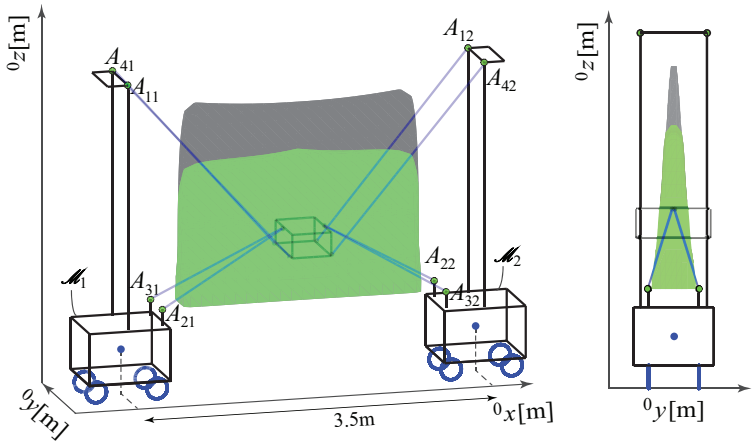

(b)

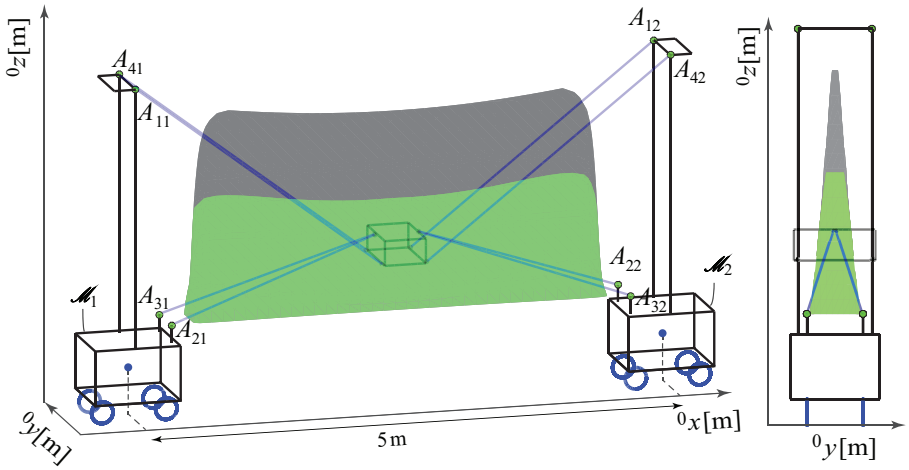

(c)

Figure 4.7: WFW of FASTKIT at different configuration of mobile bases with a constant moving-platform orientation

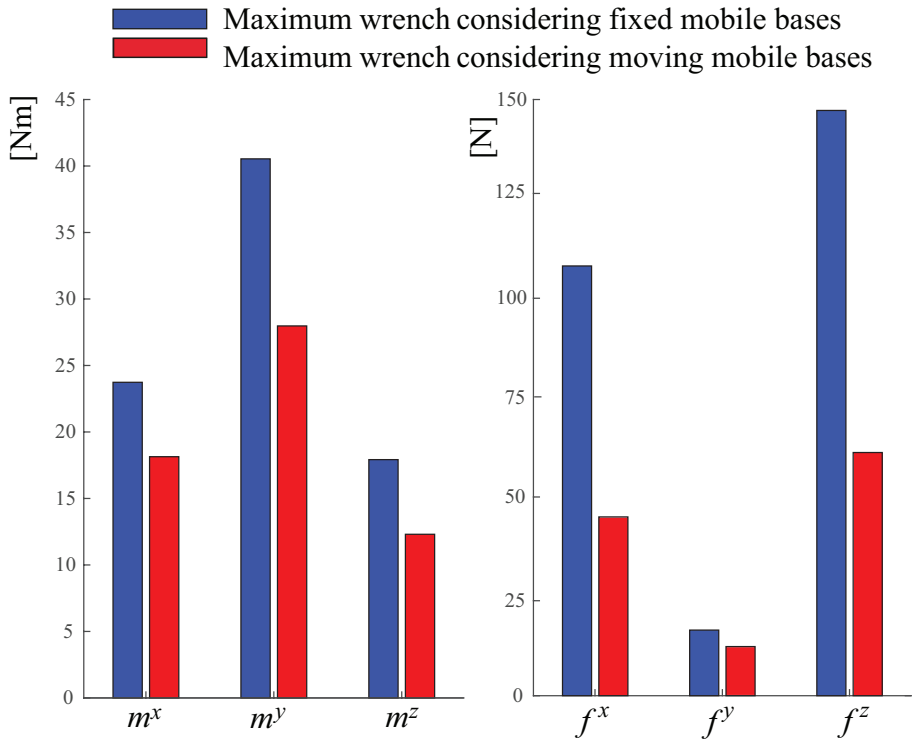

Figure 4.8: Wrench capability of FASTKIT

which is used to determine the relation between the AWS and the required wrenches to perform a task. The former method defines the AWS of MCDPRs by finding the set of vertices forming the boundary of the convex polytope. The latter method is a geometric approach, which defines a convex polytope as the intersection of the half-spaces bounded by its hyperplanes. The equivalence of both approaches are shown. Compared to the classical Cable-Driven Parallel Robots, the additional static equilibrium conditions associated with the Mobile Bases may affect the Available Wrench Set. Multiple case studies are carried out in order to show that the approach is applicable to both planar and spatial Mobile Cable-Driven Parallel Robots. The approach was experimentally validated on a Mobile Cable-Driven Parallel Robot with a point-mass moving-platform and two active mobile bases.

5

Kinematic Modeling and Twist Feasibility of MCDPRs

Contents

Both the static and the kinematic aspects should be taken into account during robot design in order to select the right hardware, *e.g.*, actuators, gearboxes, building materials etc. Similarly for cable-driven mechanisms, in addition to moving-platform wrench capabilities, the design of the winches requires knowledge of cable and moving-platform velocities as their characteristics (motors, gearboxes and drums) are based on motor torque and velocity. Therefore, during the design of a CDPR, both the wrench and the kinematic performances are taken into considerations. Multiple papers deals with the kinematic analysis of parallel manipulators [Mer96, Mer98],

however, few focus on the twist analysis of CDPRs. [GCG15] extended the approach of wrench feasibility to evaluate the twist capabilities of CDPRs by introducing the concept of twist feasibility. A pose of a CDPR moving-platform is said to be twist-feasible if all the twists (linear velocity and angular velocity combinations), within a specified set, referred to as Required Twist Set (RTS), can be generated by the cables on the moving-platform while satisfying the cable speed limits imposed by the actuators and the transmission systems [LGCC18].

Similarly, from the design point of view of MCDPRs, in addition to their wrench capabilities, it is essential to develop a methodology that can evaluate their kinematic performances. The wrench capabilities of MCDPRs are presented in Chapter 4, while this chapter outlines their kinematic modeling and twist capabilities. Section 5.1 presents the kinematic model of MCDPRs which is derived by modeling cables as a Universal-Prismatic-Spherical kinematic chains and mobile bases as four-wheeled planar robots with two-DoF translational motions and one-DoF rotational motion. Section 5.2 determines the Available Twist Set (ATS) for MCDPRs. The ATS can be used to obtain the twist capacities of the moving-platform. Section 5.3 presents the twist capacities of the moving-platform for two different MCDPRs case studies. Finally, Sec. 5.4 concludes this chapter.

5.1 Kinematic modeling

To analyze the twist capabilities of MCDPRs, it is necessary to derive its first-order kinematic model. As MCDPRs are composed of two different robotic systems, *i.e.*, a cable robot and a mobile base, with each one having its own kinematic abilities; thus, initially each system is modeled independently. The jth mobile base and its m_j number of cables is denoted as jth PD module, denoted as pd_j. Each pd_j consists of a proximal ($prox_j$) and a distal ($dist_j$) module. $prox_j$ represents jth mobile base while $dist_j$ consists of m_j number of cables between $\mathscr{M}_j$ and the moving-platform.

In this thesis, cables are assumed to be straight and massless, thus can be modeled as a Universal-Prismatic-Spherical (UPS) kinematic chain where the prismatic joint is active while the universal and spherical joints are passive. Consequently, $\mathscr{M}_j$ is carrying m_j number of Universal-Prismatic-Spherical kinematic chains. On the other hand, the mobile bases are planar robots with two-DoF translational motions and one-DoF rotational motion, thus, $prox_j$ can be modeled as a virtual Revolute-Prismatic-Prismatic (RPP) kinematic chain between the base frame $\mathscr{F}_0$ and the frame $\mathscr{F}_{bj}$ attached to $\mathscr{M}_j$. All the joints of the RPP kinematic chain of the $prox_j$ module are set to be active.

Figure. 5.1a shows the MCDPR parameterization with the aforementioned modules shown for an illustrative example with $p = 4$ mobile bases and $n = 6$-DoF

moving-platform displaced by $m = 8$ cables. It is worth nothing that all the UPS kinematic chains within each $dist_j$ module are connected in parallel with each other, while $dist_j$ is linked in series with $prox_j$. As a result, a general kinematic architecture of a MCDPR can be illustrated as in Fig. 5.1b.

5.1.1 Kinematics of the Distal Module

A classical CDPR is referred to as the distal modules in a MCDPR. Let $\mathbf{t}_{MP}^{dist}$ represent the twist generated by the distal modules onto the moving-platform which is expressed as [RGL98, GDM]:

$$\mathbf{A}\ {}^{0}\mathbf{t}_{MP}^{dist} = \dot{\mathbf{l}}, \tag{5.1}$$

where $\mathbf{A}$ is the $(m \times n)$ parallel Jacobian matrix, containing the actuation wrenches due to the cables on the moving-platform. For classical CDPRs, this Jacobin matrix only depends on the pose of the moving-platform. Moreover, from the well-known kineto-statics duality, the wrench matrix $\mathbf{W}$ is closely related to the pose-dependent kinematic Jacobian of the CDPR, namely,

$$\mathbf{A} = -\mathbf{W}^T, \tag{5.2}$$

where $\mathbf{W}$ is a wrench matrix defined by Eq. (3.4). $\dot{\mathbf{l}}$ is a m-dimensional cable velocity vector. Based on the MCDPR parameterization, Eq. (5.1) can be rewritten as:

$$\begin{bmatrix} \mathbf{A}_1 \\ \mathbf{A}_2 \\ \vdots \\ \mathbf{A}_j \\ \vdots \\ \mathbf{A}_p \end{bmatrix} {}^{0}\mathbf{t}_{MP}^{dist} = \begin{bmatrix} \dot{\mathbf{l}}_1 \\ \dot{\mathbf{l}}_2 \\ \vdots \\ \dot{\mathbf{l}}_j \\ \vdots \\ \dot{\mathbf{l}}_p \end{bmatrix}, \tag{5.3}$$

$\mathbf{A}_j$ contains the actuation wrenches generated by the cables carried by $\mathscr{M}_j$, expressed as:

$$\mathbf{A}_j = -\mathbf{W}_j^T, \tag{5.4}$$

and $\dot{\mathbf{l}}_j$ is m_j-dimensional vector containing the velocities of the cables mounted on $\mathscr{M}_j$:

$$\dot{\mathbf{l}}_j = \begin{bmatrix} \dot{l}_{1j} & \dot{l}_{2j} & \dots & \dot{l}_{ij} \dots & \dot{l}_{m_j j} \end{bmatrix}^T. \tag{5.5}$$

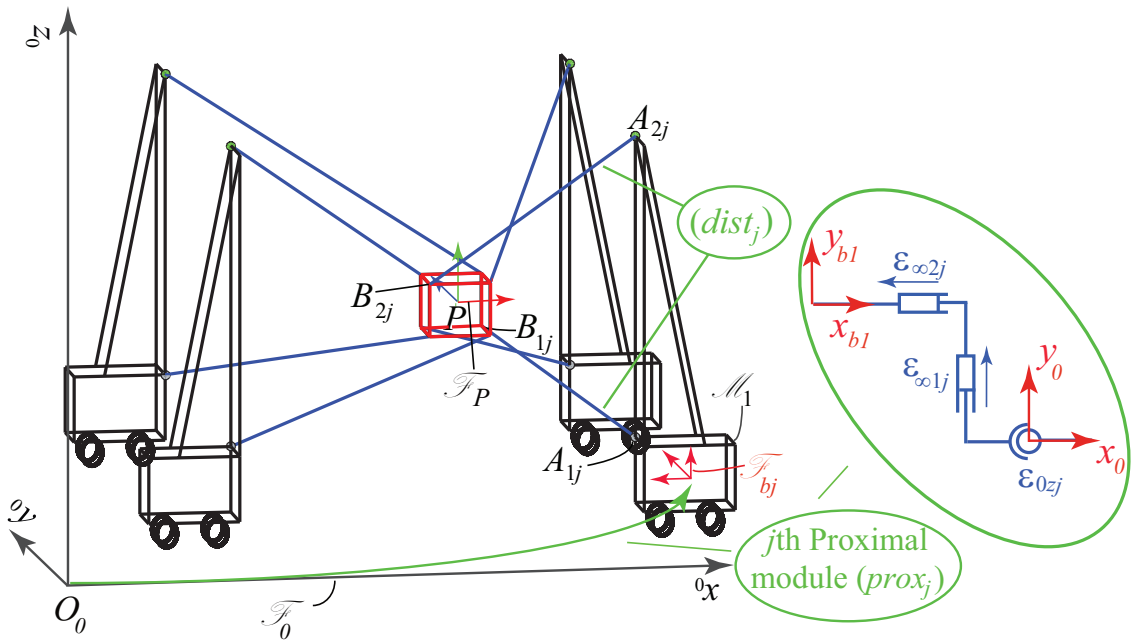

(a)

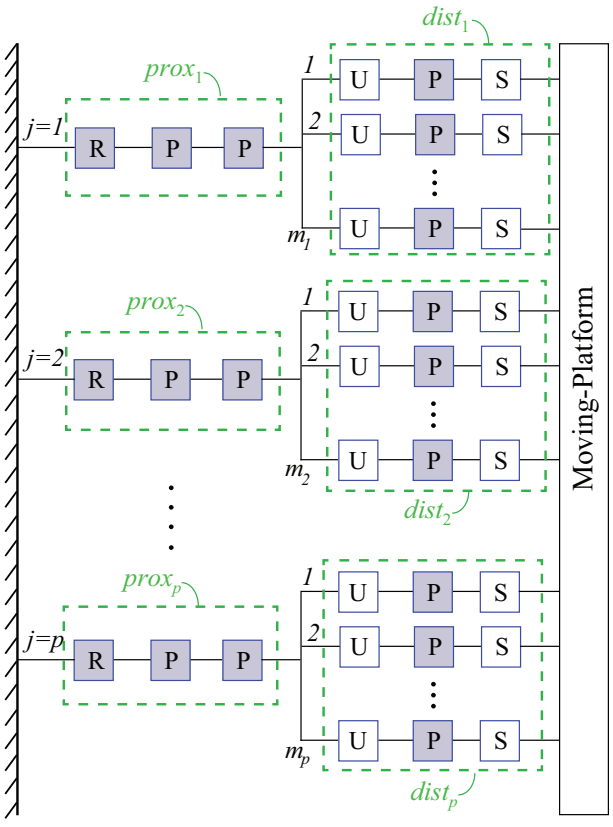

(b)

Figure 5.1: (a) MCDPR Parameterization (b) Kinematic Architecture of MCDPRs, active joints are highlighted in gray, passive joints are highlighted in white

$\dot{l}_{ij}$ corresponds to the speed of the cable $\mathscr{C}_{ij}$ that can be derived using the following relation:

$$\dot{l}_{ij} = \frac{\dot{\mathbf{l}}_{ij}}{\mathbf{u}_{ij}}, \tag{5.6}$$

where $\dot{\mathbf{l}}_{ij}$ is a cable velocity vector defined from the anchor point B_{ij} to cable exit point A_{ij} expressed as:

$$\dot{\mathbf{l}}_{ij} = \mathbf{a}_{ij} - \mathbf{b}_{ij}. \tag{5.7}$$

Note that in Eq. (5.7), the Cartesian coordinates of the anchor point B_{ij} is expressed in the base frame $\mathscr{F}_0$. In practice, $\mathbf{b}_{ij}$ is represented in moving-platform frame $\mathscr{F}_P$, denoted as ${}^P\mathbf{b}_{ij}$, which can be transformed in the base frame using the following relation:

$$\mathbf{b}_{ij} = \mathbf{p} - {}^0\mathbf{R}_P {}^P\mathbf{b}_{ij}, \tag{5.8}$$

where $\mathbf{p}$ denotes the position vector of $\mathscr{F}_P$ in $\mathscr{F}_0$. ${}^0\mathbf{R}_P$ is the rotation matrix defining the orientation of the moving-platform, *i.e.*, the orientation of the frame $\mathscr{F}_P$ expressed in $\mathscr{F}_0$.

5.1.2 Kinematic modeling of a MCDPR

Contrary to classical CDPRs, the twist generated by the proximal modules, *i.e.*, mobile bases, must be taken into account in addition of the twist generated by the distal modules on the MCDPR moving-platform. Let $\mathbf{t}_{MP}$ denotes the twist of the MCDPR moving-platform and is composed of its angular and linear velocities:

$$\mathbf{t}_{MP} = \begin{bmatrix} \boldsymbol{\omega} \\ \dot{\mathbf{p}} \end{bmatrix}, \tag{5.9}$$

where $\boldsymbol{\omega} = [\omega_x,\ \omega_y,\ \omega_z]^T$ and $\dot{\mathbf{p}} = [\dot{p}_x,\ \dot{p}_y,\ \dot{p}_z]^T$ are the vectors of the moving-platform angular and linear velocities expressed in $\mathscr{F}_0$.

In order to derive the first-order kinematic model of a MCDPR, firstly it is essential to formulate the twist generated by its jth PD module. Let ${}^0\mathbf{t}^j_{MP}$ be the twist of the moving-platform due to pd_j expressed in $\mathscr{F}_0$. ${}^0\mathbf{t}^j_{MP}$ can be computed by adding the twists generated by each of the individual module of pd_j, *i.e.*, $prox_j$ and $dist_j$:

$${}^0\mathbf{t}^j_{MP} = {}^0\mathbf{t}^{prox_j}_{MP} + {}^0\mathbf{t}^{dist_j}_{MP} \tag{5.10}$$

where ${}^{0}\mathbf{t}_{MP}^{prox_j}$ (${}^{0}\mathbf{t}_{MP}^{dist_j}$, resp.) is the twist of the moving-platform due to the motion of the proximal (distal, resp.) module of pd_j expressed in $\mathscr{F}_0$.

In practice, the twist generated by $prox_j$ is expressed in the base frame $\mathscr{F}_0$ with respect to the frame $\mathscr{F}_{bj}$ denoted as ${}^{0}\mathbf{t}_{bj}^{prox_j}$. As the proximal modules are being modeled as a virtual RPP limb, ${}^{0}\mathbf{t}_{bj}^{prox_j}$ can be written as:

$$ {}^{0}\mathbf{t}_{bj}^{prox_j} \;=\; \mathbf{J}_{bj}\;\dot{\mathbf{q}}_{bj} \tag{5.11} $$

where $\mathbf{J}_{bj}$ is a (6×3) serial Jacobian matrix of $prox_j$ and $\dot{\mathbf{q}}_{bj} = [\dot{\theta}_j \;\; \dot{\rho}_{1j} \;\; \dot{\rho}_{2j}]^T$ is the virtual joint velocities of the RPP kinematic chain, namely,

$$ {}^{0}\mathbf{t}_{bj}^{prox_j} = \begin{bmatrix} \epsilon_{0zj} & \epsilon_{\infty 1j} & \epsilon_{\infty 2j} \end{bmatrix} \begin{bmatrix} \dot{\theta}_j \\ \dot{\rho}_{1j} \\ \dot{\rho}_{2j} \end{bmatrix} \tag{5.12} $$

where ϵ_{0zj} represent the zero-pitch screw about z-axis, while $\epsilon_{\infty 1j}$ and $\epsilon_{\infty 2j}$ represent the infinite-pitch screws of the jth virtual leg in xy plane, all expressed in $\mathscr{F}_0$ (see Fig. 5.1a). These screws can be defined as:

$$ \epsilon_{0zj} = \begin{bmatrix} {}^{0}\mathbf{k} \\ {}^{0}\mathbf{k}\times\mathbf{p} \end{bmatrix}, \quad \epsilon_{\infty 1j} = \begin{bmatrix} \mathbf{0}_3 \\ {}^{0}\mathbf{R}_{bj}\,{}^{0}\mathbf{i} \end{bmatrix}, \quad \epsilon_{\infty 2j} = \begin{bmatrix} \mathbf{0}_3 \\ {}^{0}\mathbf{R}_{bj}\,{}^{0}\mathbf{j} \end{bmatrix} \tag{5.13} $$

where ${}^{0}\mathbf{i}$, ${}^{0}\mathbf{j}$ and ${}^{0}\mathbf{k}$ denotes the unit vector along the axes ${}^{0}x$, ${}^{0}y$ and ${}^{0}z$ of the global frame $\mathscr{F}_0$. To construct the twist of $prox_j$ in $\mathscr{F}_P$, ${}^{0}\mathbf{t}_{bj}^{prox_j}$ can be transformed into the moving-platform frame using the following relation:

$$ {}^{0}\mathbf{t}_{MP}^{prox_j} \;=\; {}^{bj}\mathbf{A}d_P\;{}^{0}\mathbf{t}_{bj}^{prox_j} \tag{5.14} $$

where ${}^{bj}\mathbf{A}d_P$ is called the adjoint matrix, which represents the transformation matrix between twists expressed in $\mathscr{F}_{bj}$ and twist expressed in $\mathscr{F}_P$,

$$ {}^{bj}\mathbf{A}d_P = \begin{bmatrix} \mathbf{I}_3 & 0_3 \\ -{}^{bj}\hat{\mathbf{r}}_P & \mathbf{I}_3 \end{bmatrix} \tag{5.15} $$

where ${}^{bj}\hat{\mathbf{r}}_P$ is the cross-product matrix of vector $\overrightarrow{0_{bj}P}$ expressed in $\mathscr{F}_0$. ${}^{bj}\mathbf{t}_{MP}^{dist_j}$ is the moving-platform twist due to $dist_j$ expressed in $\mathscr{F}_{bj}$.

Similarly, the twist generated by the distal modules are also needed to be formulated in $\mathscr{F}_0$. For MCDPRs, by construction $dist_j$ is carried by $prox_j$; hence, the twist due to the $dist_j$ is normally expressed in the frame of attached to $prox_j$,

i.e., in $\mathscr{F}_{bj}$, denoted as ${}^{bj}\mathbf{t}_{MP}^{dist}$. From Eq. (5.10), ${}^{0}\mathbf{t}_{MP}^{dist}$ is expressed as:

$$ {}^{0}\mathbf{t}_{MP}^{dist_j} = {}^{0}\overline{\mathbf{R}}_{bj}\ {}^{bj}\mathbf{t}_{MP}^{dist_j}, \tag{5.16} $$

Where ${}^{0}\overline{\mathbf{R}}_{bj}$ is the augmented rotation matrix which is used to express ${}^{bj}\mathbf{t}_{MP}^{dist_j}$ in $\mathscr{F}_0$:

$$ {}^{0}\overline{\mathbf{R}}_{bj} = \begin{bmatrix} {}^{0}\mathbf{R}_{bj} & 0_3 \\ 0_3 & {}^{0}\mathbf{R}_{bj} \end{bmatrix}, \tag{5.17} $$

where ${}^{0}\mathbf{R}_{bj}$ is the rotation matrix between frames $\mathscr{F}_{bj}$ and $\mathscr{F}_0$.

Substituting Eqs. (5.14) and (5.16) in Eq. (5.10), the twist of the moving-platform generated by pd_j takes the form:

$$ {}^{0}\mathbf{t}_{MP}^{j} = {}^{bj}\mathbf{A}d_P\ {}^{0}\mathbf{t}_{bj}^{prox_j} + {}^{0}\overline{\mathbf{R}}_{bj}\ {}^{bj}\mathbf{t}_{P}^{dist_j} \tag{5.18} $$

Upon multiplication of Eq. (5.18) with $\mathbf{A}_j$:

$$ \mathbf{A}_j\,{}^{0}\mathbf{t}_{MP}^{j} = \mathbf{A}_j\,{}^{bj}\mathbf{A}d_P\ \mathbf{J}_{bj}\ \dot{\mathbf{q}}_{bj} + \mathbf{A}_j\,{}^{0}\overline{\mathbf{R}}_{bj}\ {}^{bj}\mathbf{t}_{MP}^{dist_j}. \tag{5.19} $$

$\mathbf{A}_j\,{}^{0}\overline{\mathbf{R}}_{bj}\ {}^{bj}\mathbf{t}_{MP}^{dist_j}$ represents the cable velocities of $dist_j$ (see Eq. (5.3)).

$$ \mathbf{A}_j\,{}^{0}\mathbf{t}_{MP}^{j} = \mathbf{A}_j\,{}^{bj}\mathbf{A}d_P\ \mathbf{J}_{bj}\ \dot{\mathbf{q}}_{bj} + \dot{\mathbf{l}}_j. \tag{5.20} $$

The twist of the moving-platform $\mathbf{t}_{MP}$ and the twists generated by the limbs are the same, namely,

$$ {}^{0}\mathbf{t}_{MP}^{1} = {}^{0}\mathbf{t}_{MP}^{2} = {}^{0}\mathbf{t}_{MP}^{3} \ \ldots = {}^{0}\mathbf{t}_{MP}^{j} \ \ldots = {}^{0}\mathbf{t}_{MP}^{p} = \mathbf{t}_{MP} \tag{5.21} $$

Thus, the twist of the moving-platform in terms of all the p number of limbs can be expressed as:

$$ \begin{bmatrix} \mathbf{A}_1 \\ \mathbf{A}_2 \\ \vdots \\ \mathbf{A}_p \end{bmatrix} \mathbf{t}_{MP} = \begin{bmatrix} \mathbf{A}_1\,{}^{b1}\mathbf{A}d_P\ \mathbf{J}_{b1} & \mathbf{0} & \mathbf{0} & \cdots & \mathbf{0} \\ \mathbf{0} & \mathbf{A}_2\,{}^{b2}\mathbf{A}d_P\ \mathbf{J}_{b2} & \mathbf{0} & \cdots & \mathbf{0} \\ \vdots & \vdots & \vdots & & \vdots \\ \mathbf{0} & \mathbf{0} & \mathbf{0} & \cdots & \mathbf{A}_p\,{}^{bp}\mathbf{A}d_P\ \mathbf{J}_{bp} \end{bmatrix} \dot{\mathbf{q}}_b + \dot{\mathbf{l}} \tag{5.22} $$

where $\dot{\mathbf{q}}_b = [\dot{\mathbf{q}}_{b1}, \dot{\mathbf{q}}_{b2}, \ldots, \dot{\mathbf{q}}_{bp}]^T$ and $\dot{\mathbf{l}} = [\dot{\mathbf{l}}_1, \dot{\mathbf{l}}_2, \ldots, \dot{\mathbf{l}}_p]^T$. Equation (5.22) can be expressed in the matrix form as:

$$ \mathbf{A}\mathbf{t}_{MP} = \mathbf{B}_b\dot{\mathbf{q}}_b + \dot{\mathbf{l}} \tag{5.23} $$

$$\mathbf{A}\mathbf{t}_{MP} = \mathbf{B}\dot{\mathbf{q}} \tag{5.24}$$

where $\mathbf{B} = [\mathbf{B}_b \;\; \mathbf{I}_m]$ is a $(m \times (3p+m))$-matrix while $\dot{\mathbf{q}} = [\dot{\mathbf{q}}_b \;\; \dot{\mathbf{l}}]^T$ is a $(3p+m)$-dimensional vector containing all joint velocities. Equation (5.24) represents the first order kinematic model of MCDPRs.

Comparing the kinematic model of a MCDPR (Eq. (5.1)) with a classical CDPR (Eq. (5.23)), it can be observed that the former contains an additional term ($\mathbf{B}_b\dot{\mathbf{q}}_b$) representing the twist generated by the mobile bases. This additional twist is more than strictly necessary to control all the DoF of a MCDPR moving-platform. Thus, this additional twist is refereed to as the kinematic redundancy in MCDPRs. In general, the degree of kinematic redundancy depends on the total number of active actuators in $\dot{\mathbf{q}}_b$.

5.2 Available Twist Set of MCDPRs

The first-order kinematic model of a manipulator can be used to determine the set of available twists that can be achieved by its moving-platform. As discussed earlier, for a classical CDPR, the set of twist feasible poses of its moving platform are known as Available Twist Set (ATS). A CDPR posture is called twist-feasible if all the twists within a given set, can be produced at the platform, while respecting given joint velocity limits [LGCC18]. According to [LGCC18], ATS of a CDPR corresponds to a convex polytope that can be represented as the intersection of the half-spaces bounded by its hyperplanes. Such convex polytopes can be determined using the classcial Hyperplane Shifting Method (HSM) discussed in Chapter 4. Although HSM can also be utilized to determine the ATS of MCDPRs, the approach in [LGCC18] is not directly applicable due to the difference in the kinematic models of CDPR (Eq. 5.1) and MCDPR (Eq. 5.24) as matrix $\mathbf{B} \neq \mathbf{I}$.

The solution to Eq. (5.24) determines the ATS of the MCDPR moving-platform. There exist two possible scenarios to determine the solution of the Eq. (5.24). First, if the number of cables are equal to the DoF of the moving-platform, *i.e.,* $m = n$. In this case, $\mathbf{A}$ is a square matrix and Eq. (5.24) can be expressed as:

$$\mathbf{t}_{MP} = \mathbf{A}^{-1}\mathbf{B}\,\dot{\mathbf{q}} \implies \mathbf{t}_{MP} = \mathbf{J}\,\dot{\mathbf{q}} \tag{5.25}$$

where $\mathbf{J}$ is a Jacobian matrix mapping the joint velocities onto the moving-platform twist. The ATS will correspond to a single convex polytope, constructed under the mapping of Jacobian $\mathbf{J}$.

Secondly, if $m \neq n$, matrix $\mathbf{A}$ is not square, and there exists in total C_m^n $(n \times n)$

square sub-matrices of matrix $\mathbf{A}$, denoted by $\mathbf{A}^s$, $s = 1, \ldots, C_m^n$, obtained by removing $m - n$ rows from $\mathbf{A}$. For each sub-matrix we can write:

$$\hat{\mathbf{t}}_{MP}^s = (\mathbf{A}^s)^{-1}\mathbf{B}^s \implies \hat{\mathbf{t}}_{MP}^s = \mathbf{J}^s \dot{\mathbf{q}}, \qquad s = 1, \ldots, C_m^n \tag{5.26}$$

where $\hat{\mathbf{t}}_{MP}^s$ is the twist generated by the sth sub-matrix $\mathbf{A}^s$ out of C_m^n $(n \times n)$ square sub-matrices of matrix $\mathbf{A}$. $\mathbf{B}^s$ is a sub matrix of $\mathbf{B}$ using corresponding rows that are chosen in $\mathbf{A}^s$ from $\mathbf{A}$.

In both cases, the classical HSM presented in [BGM10, GK10] is directly applicable to compute all the hyperplanes of the ATS knowing the minimum and maximum joint velocity limits. For the first scenario, ATS corresponds to a single convex polytope, while for the second scenario, ATS is the region bounded by C_m^n convex polytopes.

Similar to the AWS, the ATS of MCDPRs is also a convex polytope, which strictly depends on the robot configuration and the joint velocity limits, *i.e.* velocity limits for the cables and mobile bases. Therefore, similar to Eq. (4.31), the Capacity Margin index can be used to determine if the given pose is twist feasible by using the facets of ATS and the vertices of RTS, expressed by ν:

$$\nu = \min \left(\min \nu_{x,y} \right) \tag{5.27}$$

where $\nu_{x,y}$ is the signed distance from xth vertex of the RTS to the yth face of the ATS. ν is positive as long as the platform have the ability to generate the RTS.

5.3 Results

The twist feasibility of two different case studies will be investigated. From the ATS acquired using the kinematic model of a given MCDPR configuration, we study the difference in the moving platform twist considering fixed and moving mobile bases of the MCDPRs under study.

5.3.1 Case study: $p = 2$, $m = 4$ and $n = 2$ DoF MCDPR

The first case study is a planar MCDPR with a point mass end-effector shown in Fig. 5.2a. Each mobile base has only one degree of redundancy along ${}^0\mathbf{i}$. The joint velocity limits are defined as:

$$-0.8 \text{ m.s}^{-1} \leq \dot{\rho}_{1j} \leq 0.8 \text{m.s}^{-1}, i = 1, 2, \quad j = 1, 2, \tag{5.28a}$$

$$-2 \text{m.s}^{-1} \leq \dot{l}_{ij} \leq 2 \text{m.s}^{-1}, i = 1, 2, \quad j = 1, 2, \tag{5.28b}$$

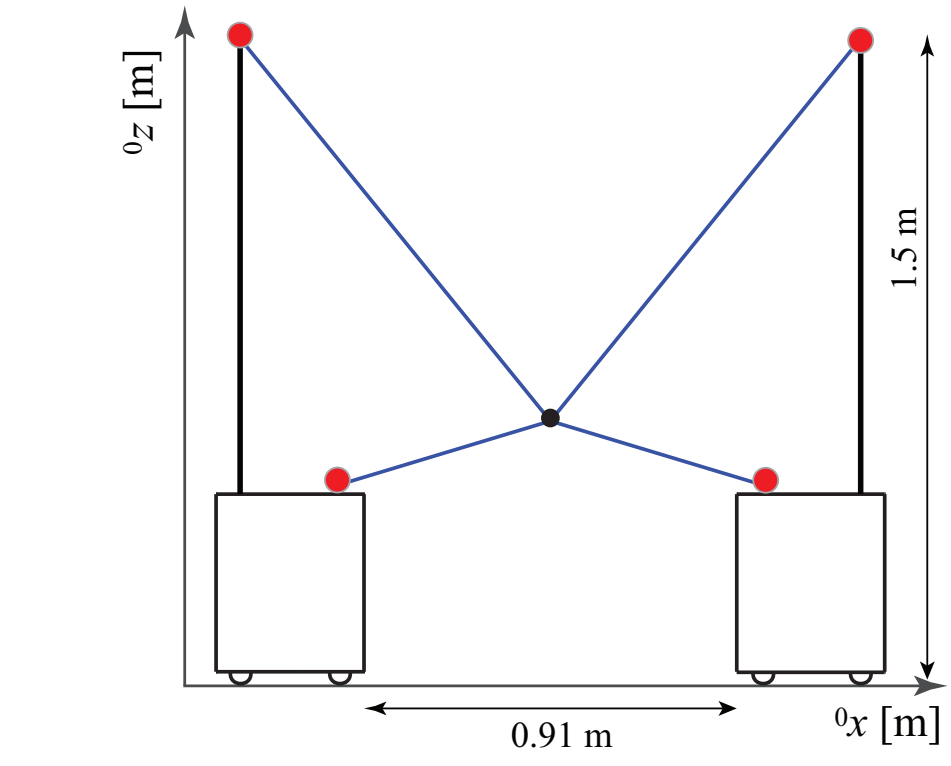

(a)

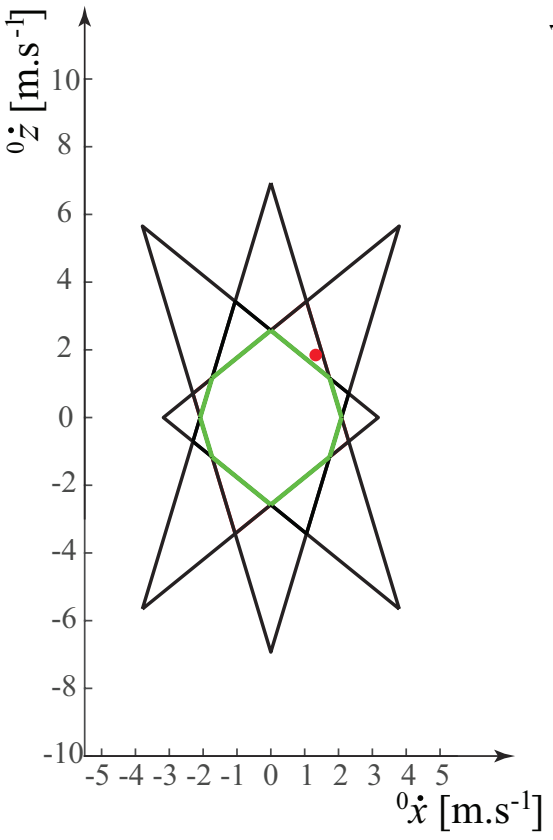

(b)

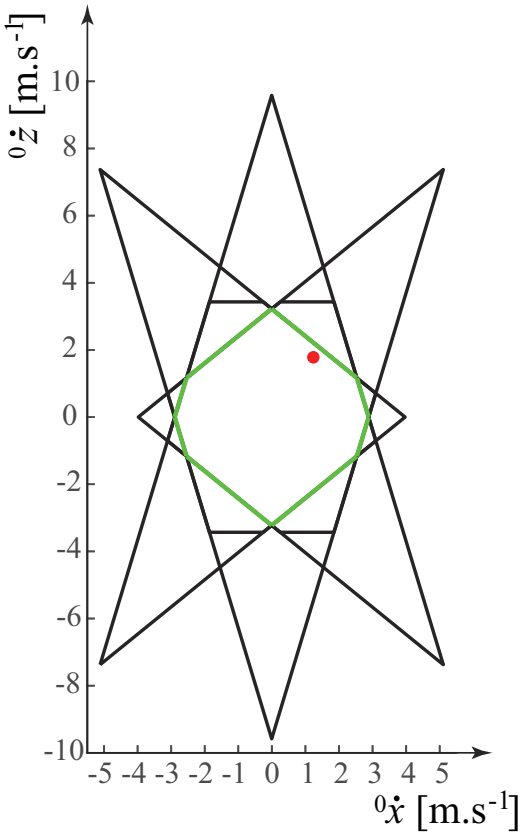

(c)

Figure 5.2: (a) Configuration under study of $p = 2$, $m = 4$ and $n = 2$ MCDPR (b) ATS in green for fixed mobile bases (c) ATS in green for moving mobile bases

Matrix $\mathbf{A}$ has six 2×2 sub-matrices Thus, ATS is the region bounded by the hyperplanes formed by these six convex polytopes. The difference of ATS between fixed (correspond to a classical CDPR) and moving mobile bases can be observed in Figs. 5.2b and 5.2c. To illustrate the difference, a RTS equal to $[1.15\ \text{m.s}^{-1}, 1.675\ \text{m.s}^{-1}]^T$ is considered, depicted by a red point in Figs. 5.2b and 5.2c. For fixed mobile bases, it should be noted that RTS is outside the ATS. In contrast, RTS is within the ATS when the motion of the mobile bases is considered.

5.3.2 Case study: $p = 2$, $m = 8$ and $n = 6$ DoF MCDPR

The Available Twist Set is also used to characterize the twist capabilities of the FASTKIT moving-platform. The ATS of FASTKIT is obtained from its joint velocity limits and first-order kinematic model. The joint velocity limits of the active mobile base ($\mathscr{M}_2$) are the following:

$$-0.2\ \text{rad.s}^{-1} \leq \dot{\theta}_2 \leq 0.2\ \text{rad.s}^{-1} \tag{5.29}$$

$$-0.2\ \text{m.s}^{-1} \leq \dot{\rho}_{12} \leq 0.2\ \text{m.s}^{-1} \tag{5.30}$$

$$-0.2\ \text{m.s}^{-1} \leq \dot{\rho}_{22} \leq 0.2\ \text{m.s}^{-1} \tag{5.31}$$

Once FASTKIT is deployed, its passive trailer ($\mathscr{M}_1$) is stabilized and does not move. Therefore, its linear and angular velocities are null, i.e.,

$$\dot{\theta}_1 = 0\ \text{rad.s}^{-1} \tag{5.32}$$

$$\dot{\rho}_{11} = 0\ \text{m.s}^{-1} \tag{5.33}$$

$$\dot{\rho}_{21} = 0\ \text{m.s}^{-1} \tag{5.34}$$

The cable velocity limits of the FASTKIT prototype are the following:

$$-2\ \text{m.s}^{-1} \leq \dot{l}_{11},\ \dot{l}_{21},\ \dot{l}_{31},\ \dot{l}_{41},\ \dot{l}_{12},\ \dot{l}_{22},\ \dot{l}_{32},\ \dot{l}_{42} \leq\ 2\ \text{m.s}^{-1} \tag{5.35}$$

From the ATS of FASTKIT in the configuration shown in Fig. 5.3a, the maximum angular (linear, resp.) velocities of the moving-platform about (along, resp.) x, y and z axes are shown in Fig. 5.3b. It can be observed the twist capacity of the moving-platform is increased when mobile bases are moving compared to the twist capability for a classical CDPR configuration of FASTKIT with fixed bases.

5.4 Conclusion

This chapter dealt with the kinematic modeling of MCDPRs necessary to analyze its kinematic performance. Each cable of the manipulator is modeled as a Universal-Prismatic-Spherical kinematic chain. Furthermore, as mobile bases are planar robots

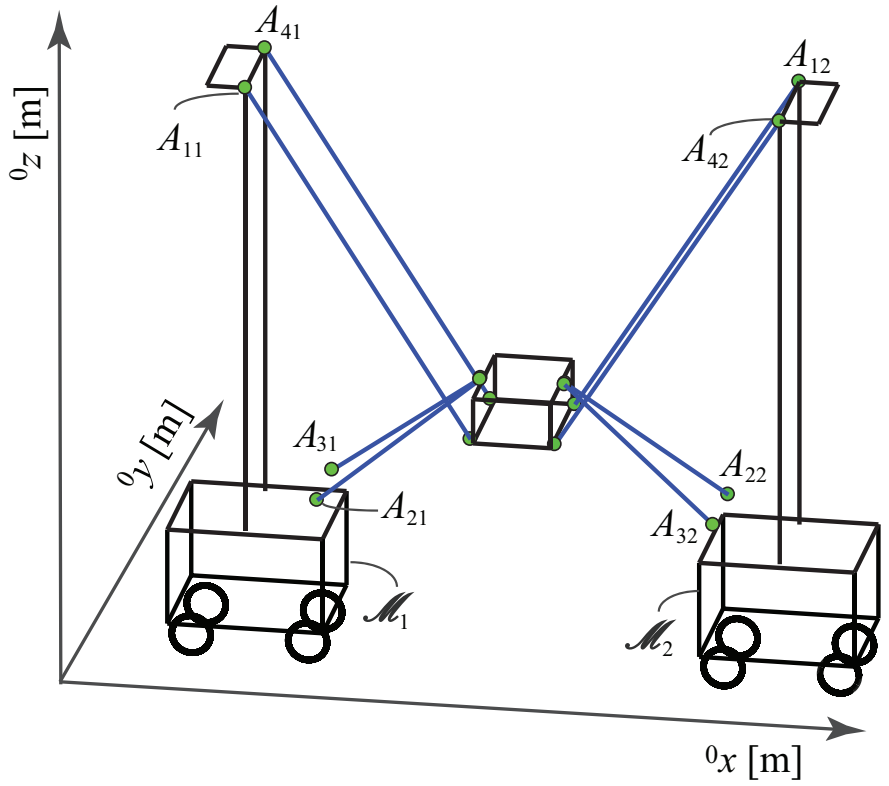

(a)

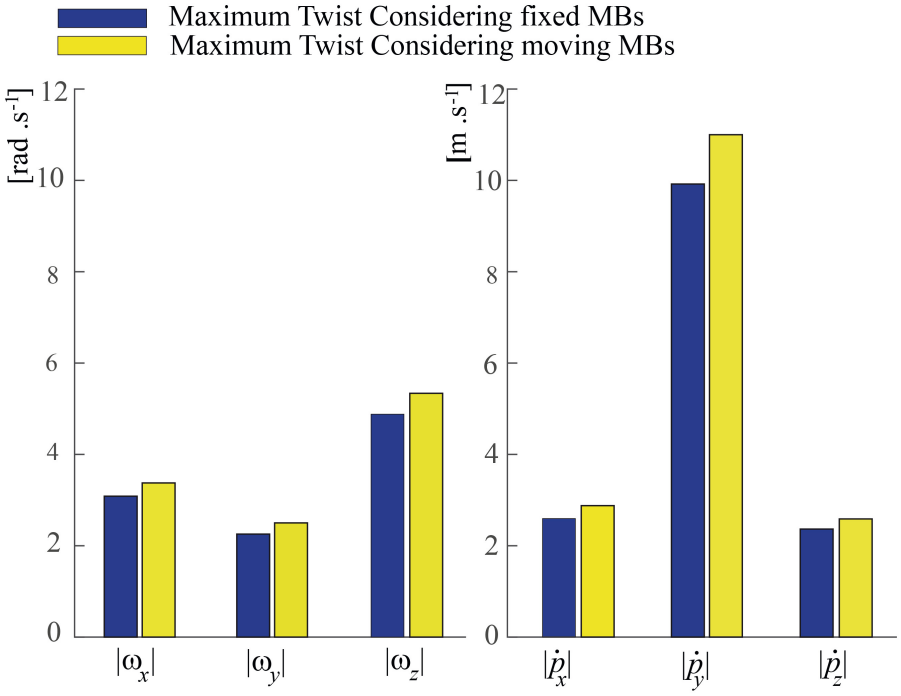

(b)

Figure 5.3: (a) A FASTKIT configuration under study (b) Maximum absolute twist and wrenches that FASTKIT platform can generate about each Cartesian direction

with two-DoF translational motions and one-DoF rotational motion; thus, they may be modeled as a Revolute-Prismatic-Prismatic kinematic chains. A general kinematic architecture is developed for MCDPRs which treats the system as a hybrid mechanism with the mobile base in series with a set of parallel cables (see. Fig. 5.1b).

The developed kinematic model was used to determine the Available Twist Set of MCDPRs by considering the joint velocity limits for the cables and the mobile bases. If the number of cables are equal to the Degree-of-Freedom of the moving-platform, the Available Twist Set corresponds to a single convex polytope. However, if number of cables and the Degree-of-Freedom of the moving-platform are not equal, the Available Twist Set is the region bounded by C_m^n convex polytopes. Once the Available Twist Set is computed, the twist capacities of the moving-platform can be determined.

Two case studies have been investigated in order to illustrate the effect of the moving mobile bases onto the platform twist. It is observed that the twist capacity of the moving-platform is higher when the mobile bases are moving compared to when the latter are fixed. This additional mobility generated by the motion of the mobile bases is refereed to as the kinematic redundancy in MCDPRs. The degree of kinematic redundancy depends on the total number of active actuators in the Revolute-Prismatic-Prismatic kinematic chains. Kinematic redundancy is advantageous as the supplementary DoF can be used to optimize a secondary criterion for instance energy minimization or joint limit avoidance. Chapter 6 presents multiple path planning strategies while addressing the issue of the kinematic redundancy for MCDPRs.

6

Path Planning of MCDPRs

Contents

6.1 Introduction

One of the main advantages of a MCDPR is the ability to deploy a fast pick-and-place manipulator throughout a factory or warehouse. To do so, the system must be able to generate safe trajectories through potentially cluttered environments. While investigating the kinematic performances of MCDPRs in Chapter 5, it has been observed that such systems are kinematically redundant due to the added mobility of the mobile bases, *i.e.,* MCDPR possesses more DoFs than the mobility of the moving-platform. As a consequence, there exist multiple paths for the MCDPR mobile bases to displace the moving-platform from one pose to another and to perform the desired task. Therefore, MCDPRs must be characterized not only based on their actuation redundancy with respect to the DoF of their moving-platform, but also by considering the kinematic redundancy due to the moving mobile bases.

While searching for a feasible MCDPR path, kinematic redundancy is viewed as a reconfiguration of the CDPR geometric architecture caused by the motion of the mobile bases. As a result, the additional DoF allow the system to modify the cable layout in order to increase the accessible workspace by enhancing the wrench capabilities of the system. However, the reconfiguration strategies must take into account the collisions with the obstacles in the surrounding environment. For this purpose, kinematic redundancy in MCDPRs can be exploited to optimize several performance criteria while respecting kinematic and environmental constraints simultaneously. Accordingly, this chapter presents path planning strategies for kinematically redundant MCDPRs.

Proposed path planning Strategies for MCDPRs

In this thesis, we examine multiple path planning strategies for MCDPRs based on the techniques mentioned in Sec. 2.3.3. However, due to the large number of constraints associated with MCDPRs, the application of these techniques is not trivial and the implementation is rather challenging. For FASTKIT, we propose an optimization based path planning approach. As discussed earlier, during the navigation mode (see Fig. 1.11a), both mobile bases of FASTKIT are coupled together and act as a single working unit while the moving-platform relative location is fixed. Therefore, the twist of the moving-platform and the passive mobile base is equal to the twist generated by the active mobile base. As a result, during the navigation mode, FASTKIT has neither kinematic nor actuation redundancy. During the task

mode, the passive mobile base remains static while the motion of the cables and the active mobile base is used to deploy the complete system (see Figs. 1.11b and 1.11c). Due to structural constraints, the system can only be deployed in a plane parallel to the shelf and thus constraining the motion of the active mobile bases along a single axis *i.e.,* leading to a system with one degree of kinematic redundancy. Therefore, Sec. 6.2 presents an optimal kinematic redundancy scheme for MCDPRs with one degree of kinematic redundancy. As a case study, FASTKIT will be used with a desired pick-and-place operation.

In contrast to FASTKIT, MoPICK is composed of four active mobile bases. As discussed earlier, the CDPR carried by MoPICK is designed such that its exit points A_{ij} lie on the axis of ${}^{bj}z$, preventing changes in the directional vector $\mathbf{u}_{ij}$ of the cable $\mathscr{C}_{ij}$ due to rotational motion of $\mathscr{M}_j$. Thus, for a given pose of the moving-platform, pure rotation of a mobile base will not cause any modification in the CDPR architecture. As a result, each mobile base only produces two degrees of kinematic redundancy *i.e,* along ${}^{0}x$ and ${}^{0}y$. Consequently, in total with four mobile bases, MoPICK has eight degrees of kinematic redundancy.

Two different path planning strategies are developed for MoPICK. The first approach presented in Sec. 6.3 is a sampling based iterative path planning algorithm aiming at optimizing the wrench capabilities of its moving-platform. The algorithm searches for a feasible and continuous path of its mobile bases between the initial and desired pose of the moving-platform by making a locally optimal choice at each step. Thus the system's kinodynamic constraints can be enforced at each instant of the path. The algorithm decomposes the problem in two parts. The first part obtains a feasible, continuous and collision free path for the mobile bases. A path is generated using an iterative procedure by generating a sequence of straight line paths. The paths are then smoothed using B-Splines. The second part of the algorithm takes as input the smoothed B-Splines and locally optimizes the moving-platform wrench capability.

The second approach detailed in Sec. 6.4, uses the direct transcription optimization method to obtain a feasible path for MoPICK. This optimization based approach allows us to embed the numerous constraints associated with CDPRs into the planning problem, while the direct transcription eases the reliance on the initial guess. The resulting path from direct transcription is transformed into a continuous motion profile using cubic splines. The results are simulated on the dynamic model of MoPICK developed using the V-REP environment [RSF13] on two different scenarios. Additionally, the second scenario is experimentally validated using the MoPICK prototype.

6.2 Redundancy planning for one degree of Kinematically redundant MCDPRs

This section presents an optimal path planning scheme for MCDPRs with one degree of kinematic redundancy. As a case study, the task mode of FASTKIT is investigated. As detailed earlier, during its task mode, the translational motion of the moving-platform is constrained to a plane as shown in Figs. 6.1 and 6.2. For ease of analysis, the task mode is studied in ${}^0x{}^0z$ plane, *i.e.*, the active mobile base is only capable of generating a single DoF transnational motion along ${}^0x$. The passive mobile base is denoted as $\mathscr{M}_1$, while active mobile base is denoted as $\mathscr{M}_2$. The position of $\mathscr{M}_1$ ($\mathscr{M}_2$, resp.) along ${}^0x$ is defined by ρ_1 (ρ_2 resp.) with respect to the frame $\mathscr{F}_{b1}$ ($\mathscr{F}_{b2}$, resp.) attached to it.

As a test scenario we define a pick and place operation, which requires feasible kinematic redundancy planning of its active mobile base *i.e.*, evolution of ρ_2, which in turn ensures that the moving platforms' task becomes feasible. In order to do that, a bi-objective optimization problem is formulated that corresponds to minimization of the total time to complete the desired operation while maximization of the robot average robustness index throughout the task.

6.2.1 Optimum Kinematic Redundancy Scheme

This section deals with a methodology that aims to determine the best ρ_2 for the pick-and-place trajectory shown in Fig. 6.2. The methodology is highlighted by defining a wrench quality criterion and the formulation of a bi-objective optimization problem, explained in the following sections.

6.2.1.1 Objective Function

The adopted path is composed of two segments, *i.e.* picking segment discretized into k_1 points and placing segment discretized into $k_2 - k_1$ points shown in Fig. 6.2. Thus the complete path is discretized into k_2 points with each point denoted by k_0 such that, $k_0 = 1, \ldots, k_1, k_1 + 1, \ldots, k_2$. Let t_1 (m_1, resp.) and t_2 (m_2, resp.) be the trajectory time (total moving mass, resp.) for the first and second segments of pick-and-place operation. It should be noted that the adopted trajectory is linear and does not require any rotational motion of the moving-platform.

For a fast pick-and-place trajectory operation, it makes sense to minimize the total trajectory time, thus the first objective function can be expressed as:

$$\text{Minimize} \quad f_1 = t_1 + t_2. \tag{6.1}$$

The second objective function aims at maximizing the robustness index of the moving-platform for the complete path, thus the second objective function can be

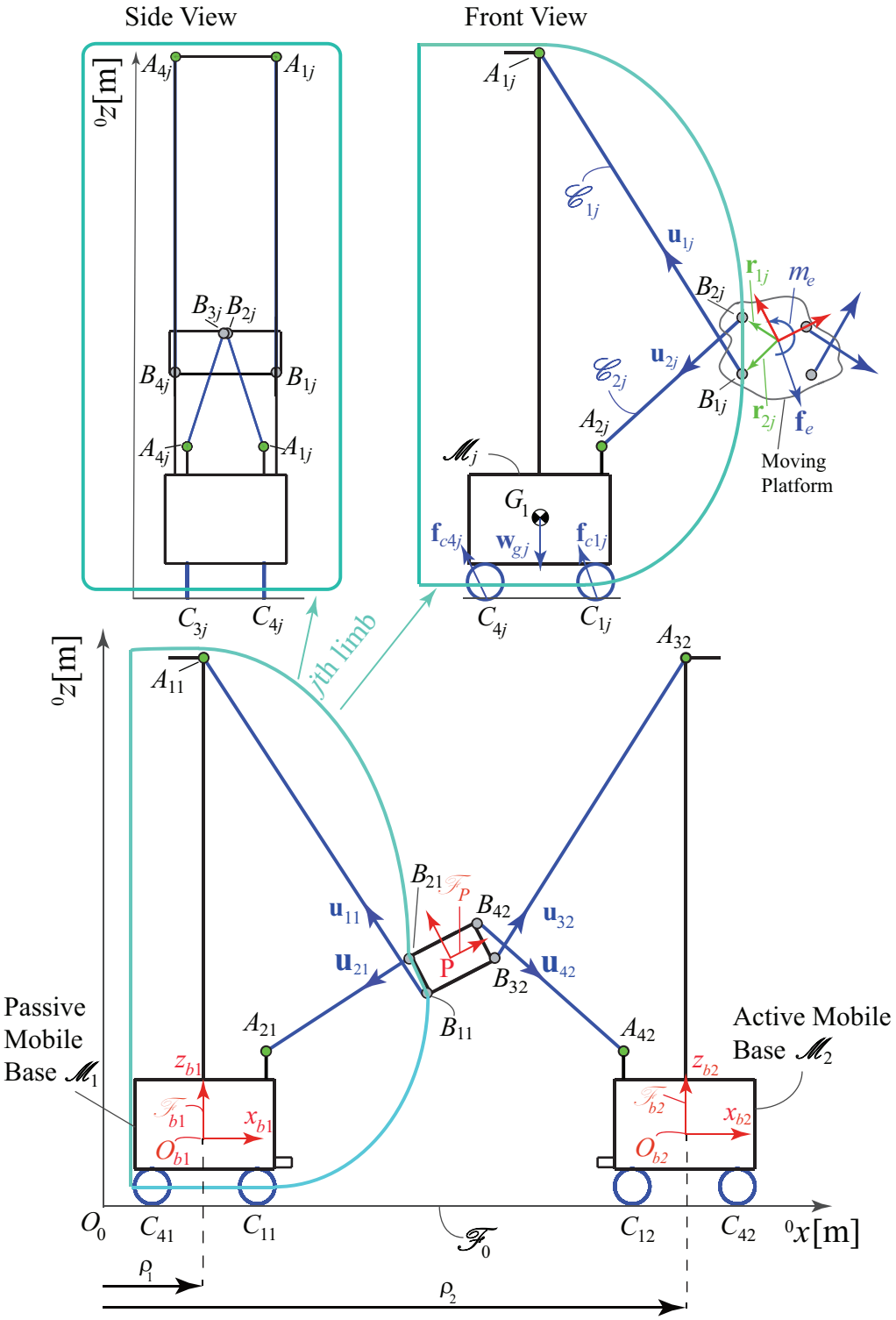

Figure 6.1: Parameterization of FASTKIT

expressed as:

$$\text{Maximize} \quad f_2 = \frac{m_1}{k_1} \sum_{k_0=1}^{k_1} \mu_{k_0} + \frac{m_2}{k_2 - k_1} \sum_{k_0=k_1+1}^{k_2} \mu_{k_0}. \tag{6.2}$$

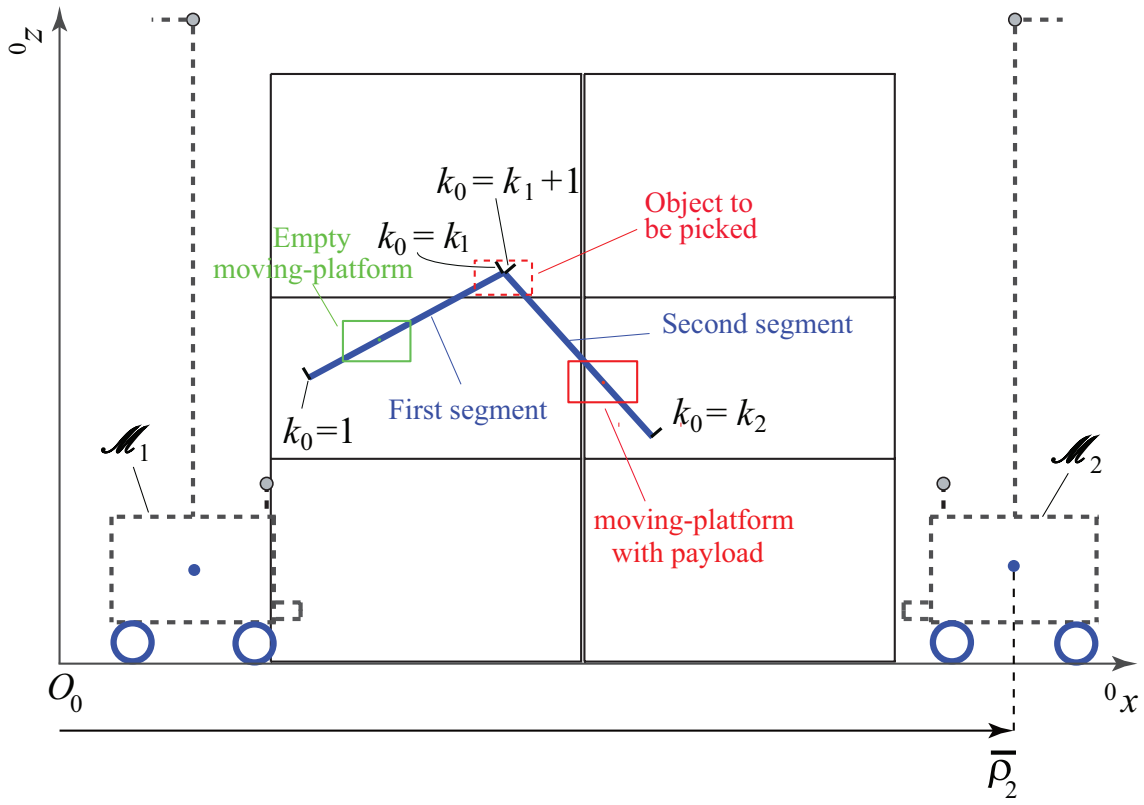

Figure 6.2: Adopted pick-and-place Path

μ_{k_0} being the capacity margin defined in Eq. (4.31) and assessed at the k_0th point of the piecewise path. The average robustness index for each segment of the path in Eq. (6.2) takes into account the mass of the moving-platform as well to have an equal ratio between the indices as it tends to decrease with the increase in the moving-platform mass and vice versa.

6.2.1.2 Decision Variables

The decision variable vector of the optimization problem contains the trajectory time of both the segments (t_1, t_2) and redundancy planning scheme. Let ρ_{2k_0} denote the position of $\mathscr{M}_2$ at k_0th point of the path. Let β denote the redundancy planning scheme containing the position of $\mathscr{M}_2$ for each k_0th discretized point such that:

$$\beta = \begin{bmatrix} \rho_{21} & \rho_{22} & \dots & \rho_{2k_1} & \dots & \rho_{2k_2} \end{bmatrix}^T, \tag{6.3}$$

with $\underline{\rho}_2 \leq \beta_{k_0} \leq \overline{\rho}_2$, $k_0 = 1, \dots, k_1, k_1 + 1, \dots, k_2$, where β_{k_0} denotes the k_0th index of β. $\underline{\rho}_2$ and $\overline{\rho}_2$ denote the lower and upper bounds on ρ_2.

6.2.1.3 Constraints

Six types of constraints are considered in the optimization problem:

1. As the passive mobile base is fixed, the velocity of $\mathscr{M}_1$ is zero,

$$\dot{\rho}_1 = 0. \tag{6.4}$$

2. The moving-platform pose must be capable of generating the RWS and RTS along the trajectory. RWS depends on the mass and the acceleration of the moving-platform. RTS is equal to the required twist of the moving-platform. Thus for each k_0th trajectory point, the indices μ_{k_0} and ν_{k_0} from Eqs. (4.31) and (5.27) must be positive, namely,

$$\mu_{k_0} \geq 0, \tag{6.5a}$$
$$\nu_{k_0} \geq 0. \tag{6.5b}$$

   Equation (6.5a) ensures that the moving-platform has the ability to generate the RWS while respecting the cable tension tension limits and the SE constraints associated with the mobile bases. Equation (6.5b) ensures that the moving-platform can generate the RTS while respecting the joint velocity limits.
3. ρ_2 is bounded between its lower bound $\underline{\rho}_2$ and its upper bound $\overline{\rho}_2$ at each k_0th trajectory point, namely,

$$\underline{\rho}_2 \;\leq\; \rho_{2k_0} \;\leq\; \overline{\rho}_2. \tag{6.6}$$

4. $\dot{\rho}_2$ is also bounded between its lower bound $\underline{\dot{\rho}}_2$ and its upper bound $\dot{\overline{\rho}}_2$ at each k_0th trajectory point, namely,

$$\underline{\dot{\rho}}_2 \;\leq\; \dot{\rho}_{2k_0} \;\leq\; \dot{\overline{\rho}}_2. \tag{6.7}$$

5. The path starts at $k_0 = 1$ with the MCDPR in a stowed undeployed configuration. Thus,

$$\rho_{21} = \underline{\rho}_2. \tag{6.8}$$

6. The search for an optimal trajectory time of bounded as:

$$0 \leq t_1 \leq \overline{t}_1, \tag{6.9a}$$
$$0 \leq t_2 \leq \overline{t}_2, \tag{6.9b}$$

where $\overline{t}_1$ and $\overline{t}_2$ are the maximum trajectory times for the first and second segments of the path.

6.2.1.4 Formulation of the optimization problem

In order to find the optimal kinematic redundancy scheme, the optimization problem formulated from Eqs. (6.1) to (6.9) is expressed as follows:

$$
\begin{aligned}
\text{Minimize} \quad & f_1(\mathbf{x}) = t_1 + t_2, \\
\text{Maximize} \quad & f_2(\mathbf{x}) = \frac{m_1}{k_1} \sum_{k_0=1}^{k_1} \mu_{k_0} + \frac{m_2}{k_2 - k_1} \sum_{k_0=k_1+1}^{k_2} \mu_{k_0}, \\
\text{over} \quad & \mathbf{x} = [\ \beta \ \ t_1 \ \ t_2\ ], \\
\text{subject to} \quad & \dot{\rho}_1 = 0, \\
& \rho_{21} = \underline{\rho}_2, \\
& \underline{\rho}_2 \ \leq \ \rho_{2k_0} \ \leq \ \overline{\rho}_2, \\
& \underline{\dot{\rho}}_2 \ \leq \ \dot{\rho}_{2k_0} \ \leq \ \overline{\dot{\rho}}_2, \\
& \mu_{k_0} \geq 0, \\
& \nu_{k_0} \geq 0, \\
& 0 \leq t_1 \leq \bar{t}_1, \\
& 0 \leq t_2 \leq \bar{t}_2, \\
& k_0 = 1, \ldots, k_1, k_1 + 1, \ldots, k_2.
\end{aligned}
\tag{6.10}
$$

The optimization problem formulated in Eq. (6.10) attempts to obtain the trajectory time for each segment and evolution of the active mobile base that minimize the total trajectory time (f_1) and maximize the criterion f_2 defined in Eq. (6.2) while respecting the set of constraints. The optimization problem is solved for the following case study of FASTKIT.

6.2.2 Case Study

In this section, all the parameters required to acquire and analyze the results for the path planning problem are presented. Segments of the pick-and-place path are discretized such that $k_2 = 2k_1 = 100$. The maximum trajectory time of each segment is defined as:

$$\bar{t}_1 = \bar{t}_2 = 10\text{s}. \tag{6.11a}$$

The mass of the moving-platform is taken as:

$$m_1 = 1\text{kg}, \quad m_2 = 2.5\text{kg}. \tag{6.12}$$

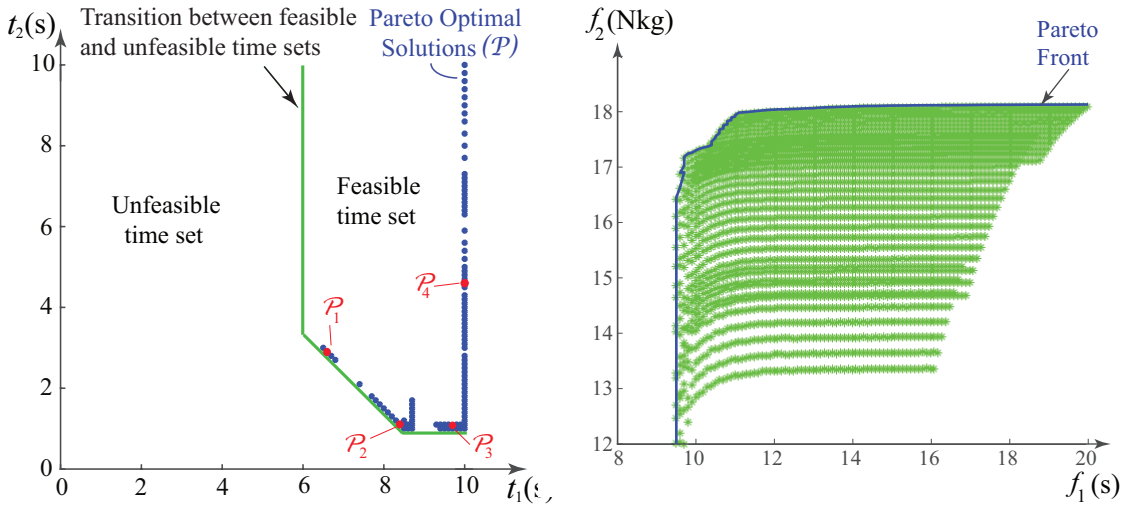

Figure 6.3: (a) Feasible and unfeasible time sets (b) All feasible solutions (green), Pareto front (blue) and four pareto-optimal solutions (red) in the Performance Function space

Each mobile base of FASTKIT is 150 kg. The joint velocity limits *i.e.* velocity limits of the cables and mobile bases are defined as:

$$\underline{\dot{\rho}}_2 = -0.2\text{m.s}^{-1}, \quad \overline{\dot{\rho}}_2 = 0.2\text{m.s}^{-1}, \tag{6.13}$$

$$-2\text{m.s}^{-1} \leq \dot{l}_{ij} \leq 2\text{m.s}^{-1}, \quad i = \{1,2\},\ j = \{1,2\}. \tag{6.14}$$

Based on the hardware specifications of FASTKIT, the lower and upper bounds on the cable tension limits are set to 0 N and 45 N, respectively. The bounds on the position of $\mathscr{M}_2$ are defined as:

$$\underline{\rho}_2 = 1.1\text{m}, \quad \overline{\rho}_2 = 4\text{m}. \tag{6.15}$$

which means that the robot can be deployed up to a maximum of $\overline{\rho}_2 - \underline{\rho}_2 = 2.9$ m.

6.2.3 Result Analysis

The only decision variables that are considered to solve the proposed optimization problem are t_1 and t_2, respectively. The vector β is searched at each iteration and is obtained in such a way that it minimizes the objective function f_1, maximizes the objective function f_2 and leads to a continuous solution for ρ_2 along the trajectory. The feasible solutions in decision space are illustrated in Fig. 6.3a. On the left side of the transition curve, there exists no solution between t_1 and t_2 that respect all the constraints defined in Eq. (6.10) referred to as unfeasible time set. On the right

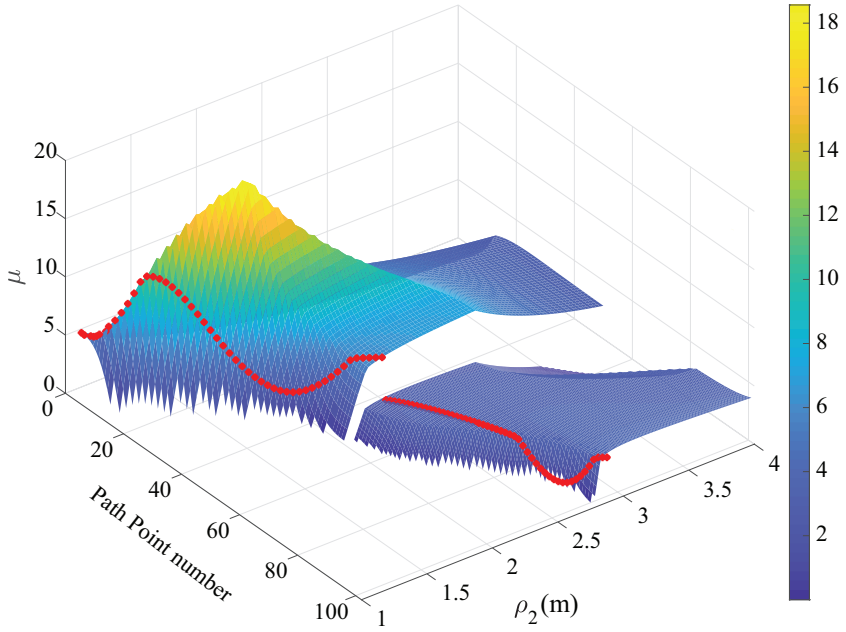

Figure 6.4: μ as a function of path point number and ρ_2 for pareto-optimal solution $\mathcal{P}_1$, *i.e.*, $t_1 = 6.6$ s and $t_2 = 2.9$ s. The red curve highlights optimum redundancy scheme

side of the transition curve, each combination between t_1 and t_2 satisfies all the constraints of the proposed optimization problem (6.10) and are referred to as the feasible time set.

The optimization problem in Eq. (6.10) has more than one optimal solution. These optimal solutions are defined as Pareto-optimal solutions, which cannot be dominated by any other feasible solution [BABB12, LW09]. The set of all Pareto-optimal solutions is called as Pareto optimal set, denoted by $\mathcal{P}$, illustrated in Fig. 6.3a. The Pareto-optimal solutions lie on a boundary in the Performance Function Space between the two objective functions called Pareto front [WCB+15] shown in Fig. 6.3b. It can be observed in Fig. 6.3a that most of the Pareto-optimal solution requires the largest t_1. This behavior can be explained from the definition of the adopted pick-and-place path.

During the first segment of the path (see Fig. 6.2), the platform height is increased that reduces the AWS along ${}^0z$. The RWS due to the acceleration of the moving-platform tends to decrease with the increase in t_1, which results in higher f_2 along the first segment. The situation is opposite for the second segment of the adopted path as AWS tends to increase along ${}^0z$ with the decrease in the platform height. A similar phenomenon can be observed in Fig. 6.3a through transition curve where the minimum time that is required to find a feasible solution for first segment is equal to 6 s while it is equal to 1 s only for the second segment. It should be noted that at $t_1 = \bar{t}_1$, changing t_2 does not produce any prominent change in f_2 (see Figs. 6.3a and 6.3b). Thus, it can be concluded that the transition curve *i.e.* the feasible and

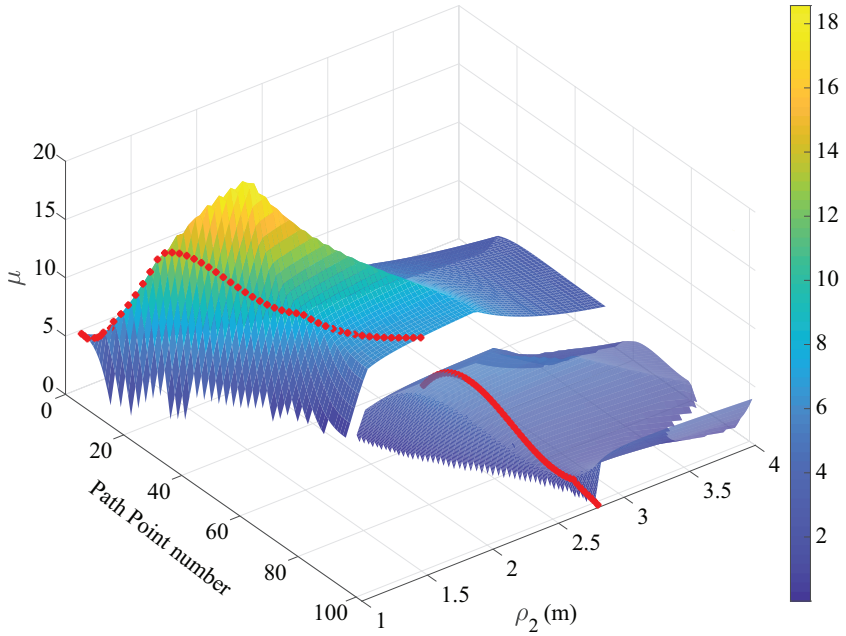

Figure 6.5: μ as a function of path point number and ρ_2 for pareto-optimal solution $\mathcal{P}_2$, *i.e.*, $t_1 = 8.4$ s and $t_2 = 1.1$ s. The red curve highlights optimum redundancy scheme

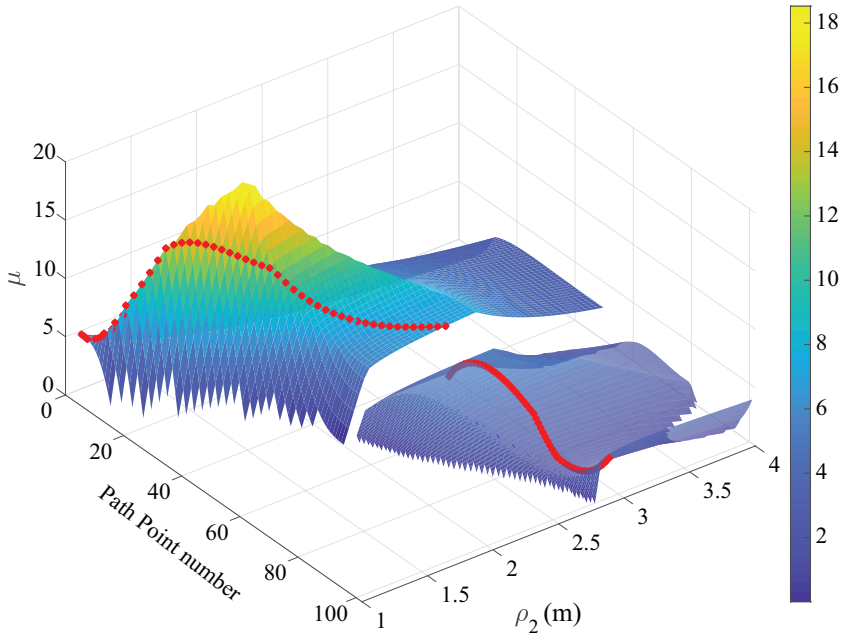

Figure 6.6: μ as a function of path point number and ρ_2 for pareto-optimal solution $\mathcal{P}_3$, *i.e.*, $t_1 = 9.7$ s and $t_2 = 1.1$ s. The red curve highlights optimum redundancy scheme

unfeasible time set is highly dependent of the adopted path.

To illustrate an optimal redundancy scheme, four different Pareto-optimal solutions, *i.e.* $\mathcal{P}_1, \mathcal{P}_2, \mathcal{P}_3$ and $\mathcal{P}_4$ have been selected in Fig. 6.3. Figures 6.4 to 6.7 show the index μ as a function of the path point number and ρ_2 for the chosen Pareto-optimal solutions $\mathcal{P}_1$, $\mathcal{P}_2$, $\mathcal{P}_3$ and $\mathcal{P}_4$ known as efficiency maps [CDGF13, CGF+14]. The red

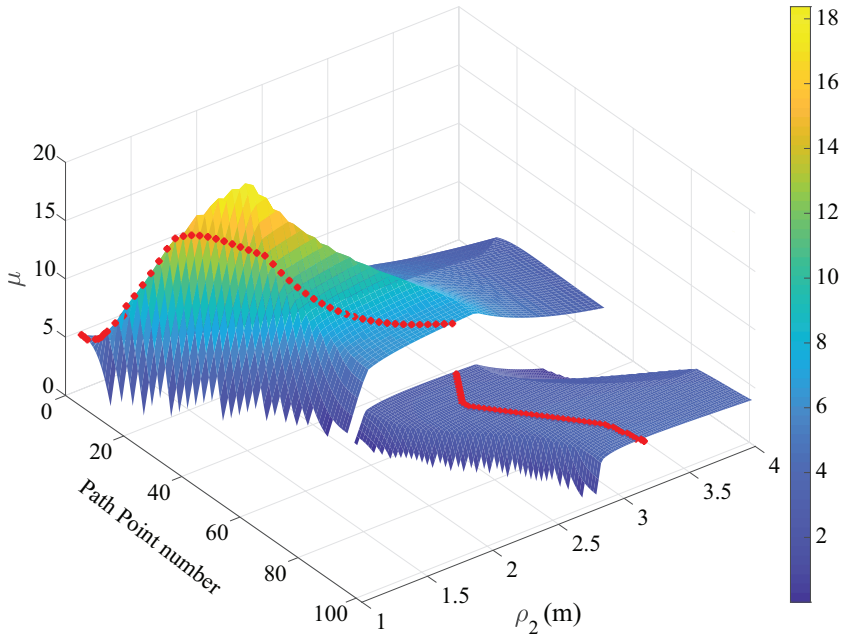

Figure 6.7: μ as a function of path point number and ρ_2 for pareto-optimal solution $\mathcal{P}_4$, *i.e.*, $t_1 = 10$ s and $t_2 = 4.6$ s. The red curve highlights optimum redundancy scheme

curve in the efficiency maps highlights the optimum redundancy scheme. The white areas in the map corresponds to the region where the constraints of the proposed optimization problem are not satisfied. It can be observed that there is a sudden change in μ at $k_0 = \frac{k_2}{2}$. It is due to the fact that the weight of the moving-platform is changed at the end of the first segment of pick-and-place operation. Due to this following reason, the mass of the moving-platform is taken into account in the definition of the second objective function f_2, which is expressed in Eq. (6.2). The simulation videos for corresponding pick-and-place operation for all the four Pareto-optimal solutions $\mathcal{P}_1, \mathcal{P}_2$, $\mathcal{P}_3$ and $\mathcal{P}_4$ can be downloaded at [1].

The presented approach gives satisfactory results for determining the optimal kinematic redundancy planning; however, is only useful for systems with one degree of redundancy. Indeed, for MCDPRs with higher degrees of kinematic redundancy, the analysis of the formulated optimization problem becomes complex. As a consequence, an optimization based direct transcription method is presented in Sec. 6.4 for highly redundant manipulators, *e.g.*, MoPICK prototype. Additionally, a sampling based iterative path planning algorithm is developed detailed in Sec. 6.3.

6.3 Iterative Path Planning Algorithm for MCDPRs

This section presents a sampling based iterative algorithm for highly redundant MCDPRs. MoPICK prototype is investigated as a case study, with its parameter-

[1] https://drive.google.com/open?id=18PWHVjZw1ZmYhuV7L5T2EwY5waI2lgNL

ization depicted in Fig. 6.8. The algorithm searches for a feasible and continuous path of its mobile bases between the initial and desired pose of the moving-platform by making a locally optimal choice at each step. Thus the system's kinodynamic constraints are enforced at each instant of the path. The algorithm decomposes the problem in two parts. The first part aims to find a feasible, continuous and collision free path for the mobile bases. A path is generated using an iterative procedure by generating a sequence of straight line paths. The paths are then smoothed using B-Splines. The second part of the algorithm takes as input the smoothed B-Splines and locally optimizes the moving-platform's wrench capability.

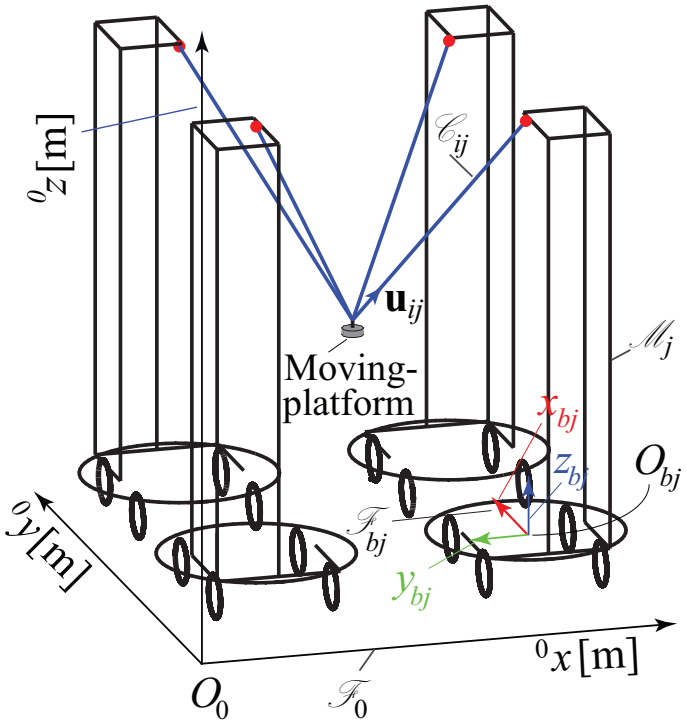

Figure 6.8: MoPICK Parameterization

6.3.1 Task Formulation

For MoPICK, the task is defined as displacing the moving-platform from an initial position $\overline{P}_1$ to a desired position $\overline{P}_f$ while ensuring that the moving-platform passes through a set of way-points. The task is performed in a constrained environment having numerous tables and obstacles in it. The way-points on the tables require a task action, for example grasping and/or releasing an object. Some intermediate way-points are placed in order to guide the system to navigate between the two consecutive task locations. These intermediate way-points are interpolated between the two task locations while maximizing the distance from the nearest obstacle.

Let $\underline{l}$ be the total number of way-points. Each way-point is denoted as $\overline{P}_{\underline{i}}$,

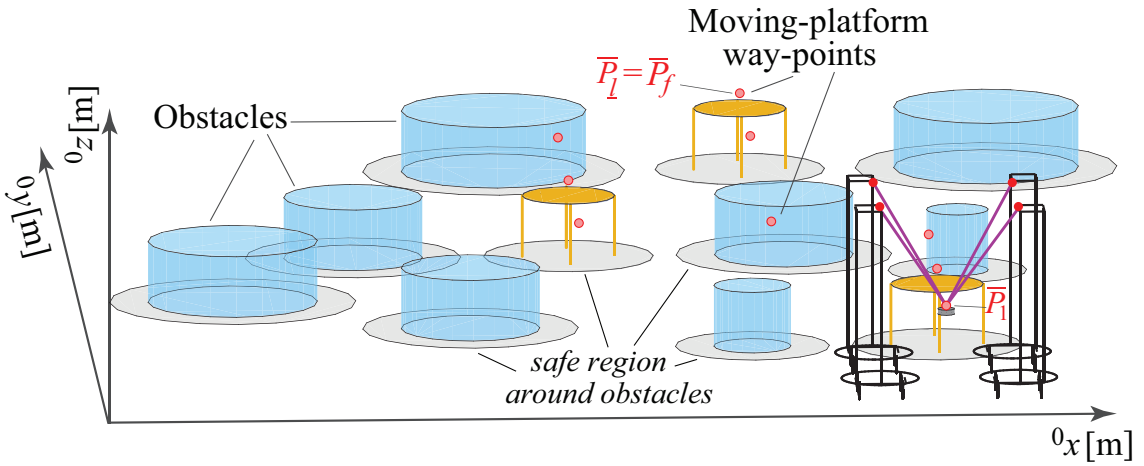

Figure 6.9: Case Scenario and illustrated environment for iterative path planning algorithm

$\underline{i} = 1, \ldots, \underline{l}$. The Cartesian coordinate vector of the $\underline{i}$th way-point is denoted as $\mathbf{p}_{\underline{i}}$. The obstacles are defined as cylinders. As discussed earlier, MoPICK mobile bases are also designed as cylindrical shape with radius of 0.25 m. To avoid collision between the obstacles and a mobile base, a common practice [CE07] is to inflate the obstacles by at least the radius of mobile bases in $^0x^0y$ plane, denoted as *safe region around obstacles*, as illustrated in Fig. 6.9. As a consequence, the mobile bases may be treated as single points, reducing the complexity of the planning problem.

In order to perform the desired task, a feasible and collision free path of the mobile bases is required. Accordingly, the path of the moving-platform is also required to displace it from $\overline{P}_1$ to $\overline{P}_f$ by sequentially following the intermediate way-points $\overline{P}_{\underline{i}}$, $\underline{i} = 1, \ldots, \underline{l}$. The following section addresses the aforementioned problem and presents a sampling based iterative path planning approach for the manipulator under study.

6.3.2 Iterative path planning Algorithm

In order to find a path between $\underline{i}$th and $(\underline{i}+1)$th way-points, the following steps are taken. First, let's assume that a feasible solution has been obtained for the mobile bases with moving-platform located at $\overline{P}_{\underline{i}}$. The wrench capability of the system is calculated when the moving-platform is located at $\overline{P}_{\underline{i}+1}$ while the mobile bases are still located at the solution of *previous* way-point ($\overline{P}_{\underline{i}}$). The mobile bases are then iteratively displaced from $\overline{P}_{\underline{i}}$ to $\overline{P}_{\underline{i}+1}$ such that each displacement maximizes the wrench capability while avoiding collisions. This results in a feasible path for the mobile bases. Given this feasible path for the mobile bases, the path of the moving-platform is optimized to further increase the wrench capability during the transition.

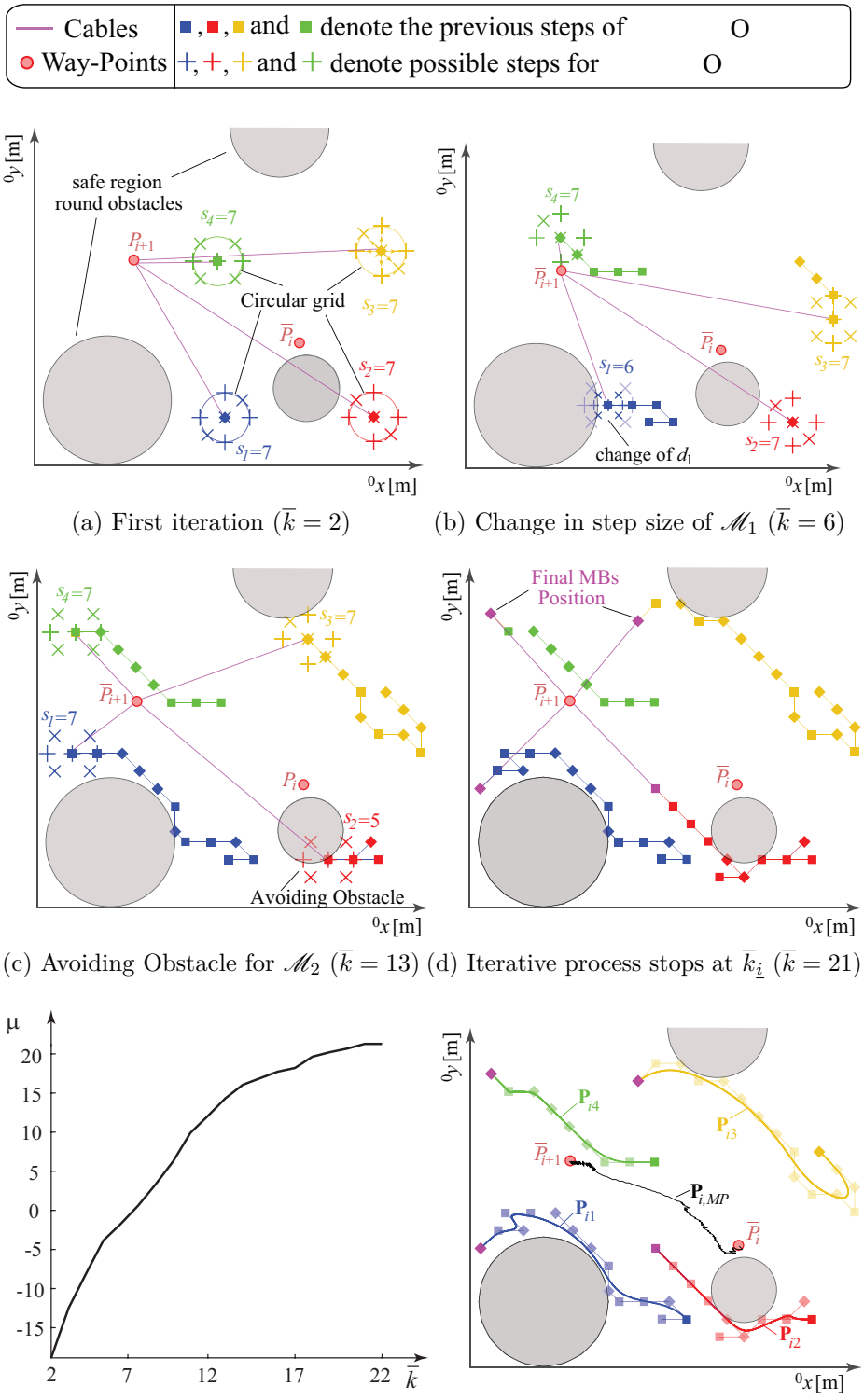

(a) First iteration ($\bar{k} = 2$) (b) Change in step size of $\mathscr{M}_1$ ($\bar{k} = 6$)

(c) Avoiding Obstacle for $\mathscr{M}_2$ ($\bar{k} = 13$) (d) Iterative process stops at $\bar{k}_{\underline{i}}$ ($\bar{k} = 21$)

(e) μ as a function of iteration number (f) Paths of the mobile bases and the moving-platform

Figure 6.10: Illustration of MCDPR iterative based path planning

6.3.2.1 Generation of feasible path for mobile bases

The first phase of the algorithm iteratively searches for a collision free continuous path for the mobile bases between any two way-points of the moving-platform. As

an illustrative example, we will show how the algorithm evolves and calculates a continuous path for $\mathscr{M}_j, j = 1, \ldots, 4$, between $\underline{i}$th and $(\underline{i}+1)$th way-points shown in Fig. 6.10a. Let $\overline{k}$ represents an iteration. Let $\mathbf{M}_{\underline{i}j}$ be a matrix whose $\overline{k}$th column contains the Cartesian coordinate vector of $\mathscr{M}_j$ in ${}^0x^0y$ plane at the $\overline{k}$th iteration of the algorithm.

From the initial configuration of the mobile bases at $\overline{k} = 1$, the iterative process starts at $\overline{k} = 2$ by displacing the moving-platform at $\overline{P}_{\underline{i}+1}$. This results in the drastic decrease of the moving-platform wrench capabilities (μ). At each $\overline{k}$th iteration, the algorithm searches for the best step of $\mathscr{M}_j$ on a circular grid with a step size d_j. On the corresponding search grid, $\mathscr{M}_j$ can either retain its current position or due to the non-holonomic constraints, can move in the forward, backward, or diagonal directions, all denoted by '+' in Figs. 6.10a, 6.10b and 6.10c. Let $\mathscr{M}_j$ have s_j possibilities of collision free steps. There exists $s_1 \times s_2 \times s_3 \times s_4$ combinations for four mobile bases. The algorithm chooses the combination that results in the maximum increase in μ. The matrix $\mathbf{M}_{\underline{i}j}$ is updated with the Cartesian coordinates of the new step taken by $\mathscr{M}_j$ and a line segment is created between its locations at $\overline{k}$th and $(\overline{k}-1)$th iteration. If there are no feasible steps for $\mathscr{M}_j$ due the blockage around any obstacle, the step size (d_j) is reduced and the search is repeated until a feasible step is obtained as illustrated in Fig. 6.10b. The procedure stops at $\overline{k} = \overline{k}_{\underline{i}}$ when μ does not increase any further (see Fig. 6.10d). For the illustrative example, the evaluation of μ as a function of iteration number is shown in Fig. 6.10e.

The next phase is to smooth the sequence of straight line segments generated between the Cartesian coordinates of $\mathscr{M}_j$ during the iterative process using B-Splines [PLH02]. The following function in MATLAB *bspline_footpoint*[2] is used which requires the two parameters *knot sequence* and *control points* to be tuned. It takes $\overline{k}_{\underline{i}}$ Cartesian coordinates of $\mathscr{M}_j$ in $\mathbf{M}_{\underline{i}j}$ as input, and generates ten times the smooth sequence of Cartesian coordinates, denoted as $\mathbf{P}_{\underline{i}j}$, as depicted in Fig. 6.10f.

The above procedure is repeated to find a collision free continuous path for the mobile bases between all the way-points of the moving-platform. It is noteworthy to mention that location of $\mathscr{M}_j$ at $\overline{k}_{\underline{i}}$th iteration is used as an initial configuration to compute $\mathbf{P}_{(\underline{i}+1)j}$, *i.e.* path of $\mathscr{M}_j$ between $(\underline{i}+1)$th and $(\underline{i}+2)$th way-points. The Pseudo-code for generating the path of mobile bases is presented in Algorithm. 1.

6.3.2.2 Generation of the moving-platform optimal path

The second phase of the path planning algorithm generates an optimal path of the moving-platform, denoted as $\mathbf{P}_{\underline{i},MP}$ between $\underline{i}$th and $(\underline{i}+1)$th way-points. Similar to the first phase, the second phase of the algorithm is also an iterative process which computes an optimal moving-platform pose for each location of the mobile

[2] https://www.mathworks.com/matlabcentral/fileexchange/27374-b-splines

Algorithm 1: Generation of mobile bases feasible path between two way-points

Input : A matrix with initial Cartesian coordinates of mobile bases $\mathbf{M}_{\underline{i}j}(1)$
Maximum number of iterations $\overline{k}_{max}$
Cartesian coordinates of the moving-platform at $(\underline{i}+1)$th way-point $\mathbf{p}_{\underline{i}+1}$

Output : Feasible Path of mobile bases $\mathbf{P}_{\underline{i}j}$

Notations : j represents the mobile base number $j = 1, \ldots, 4$
Cartesian Coordinates of $\mathscr{M}_j$ at the $\overline{k}$th iteration $\mathbf{M}_{\underline{i}j}(\overline{k})$
A vector with Wrench Capability (μ) of the moving-platform at the kth iteration $\overline{\mu}(\overline{k})$

Invoked functions : Determine smooth path of $\mathscr{M}_j$ $BSpline(\mathbf{M}_{\underline{i}j})$

$\overline{k} = 1$; // iteration initialization $\overline{\mu}(1)$ = Determine μ with $\mathscr{M}_j$ at $\mathbf{M}_{\underline{i}j}(1)$ and moving-platform at $\mathbf{p}_{\underline{i}+1}$ `// Section 4.2`

repeat
  $\overline{k} = \overline{k} + 1$;
  Determine the new step of $\mathscr{M}_j$ `// Section 6.3.2.1`
  $\mathbf{M}_{\underline{i}j}(\overline{k})$ = Cartesian coordinates for the new location of $\mathscr{M}_j$
  $\overline{\mu}(\overline{k})$ = Determine μ with $\mathscr{M}_j$ at $\mathbf{M}_{\underline{i}j}(\overline{k})$ and moving-platform at $\mathbf{p}_{\underline{i}+1}$
until $(\overline{\mu}(\overline{k}) = \overline{\mu}(\overline{k}-1)$ or $\overline{k} > \overline{k}_{max})$;
$\mathbf{P}_{\underline{i}j} = BSpline(\mathbf{M}_{\underline{i}j})$
return $(\mathbf{P}_{\underline{i}j})$

Algorithm 2: Generation of the moving-platform optimal path

Input : Path of mobile bases $\mathbf{P}_{\underline{i}j}$
Cartesian coordinates of the moving-platform at the $\underline{i}$th way-point $\mathbf{p}_{\underline{i}}$

Output : Optimal path of moving-platform $\mathbf{P}_{\underline{i},MP}$

Notations : j denotes number of mobile bases $j = 1, \ldots, 4$
Cartesian Coordinates of $\mathscr{M}_j$ at $\underline{r}$th iteration $\mathbf{P}_{\underline{i}j}(\underline{r})$
Optimal moving-platform pose at $\underline{r}$th iteration $\mathbf{P}_{\underline{i},MP}(\underline{r})$

Invoked functions : Determine the number of Cartesian coordinates of $\mathscr{M}_j$ in $\mathbf{P}_{\underline{i}j}$ $size(\mathbf{P}_{\underline{i}j})$

$\mathbf{P}_{\underline{i},MP}(1) = \mathbf{p}_{\underline{i}}$;
for $\underline{r} = 2 : size\ (\mathbf{P}_{\underline{i}1})$ **do**
  $\mathbf{P}_{\underline{i},MP}(\underline{r})$ = Compute optimal moving-platform pose with $\mathscr{M}_j$ at $\mathbf{P}_{\underline{i}j}(\underline{r})$
    `// see Section 6.3.2.2`
end

bases in $\mathbf{P}_{\underline{i}j}, j = 1, \ldots, 4$. Let $\underline{r}$ represents an iteration. Total number of iterations are fixed for the second phase *i.e.* equal to the number of Cartesian coordinates of $\mathscr{M}_j$ in $\mathbf{P}_{\underline{i}j}$. Given the initial $(\mathbf{p}_{\underline{i}})$ moving-platform pose at $\underline{r} = 1$, the iterative

process begins at $\underline{r} = 2$. It builds $\mathbf{P}_{\underline{i},MP}$ by searching for the best pose of the moving-platform on a circular grid with a step size d_{MP}. In contrast to mobile bases, the moving-platform can either retain its previous pose or take a step in all the neighboring eight directions *i.e.*, forward, back, left, right and diagonals. The algorithm chooses a step with a maximum μ among all the possible steps. For the illustrative example, $\mathbf{P}_{\underline{i},MP}$ is shown in Fig. 6.10f. The above process is repeated to find an optimal moving-platform path between all the way-points. The Pseudo-code used to generate the moving-platform path is presented in Algorithm. 2.

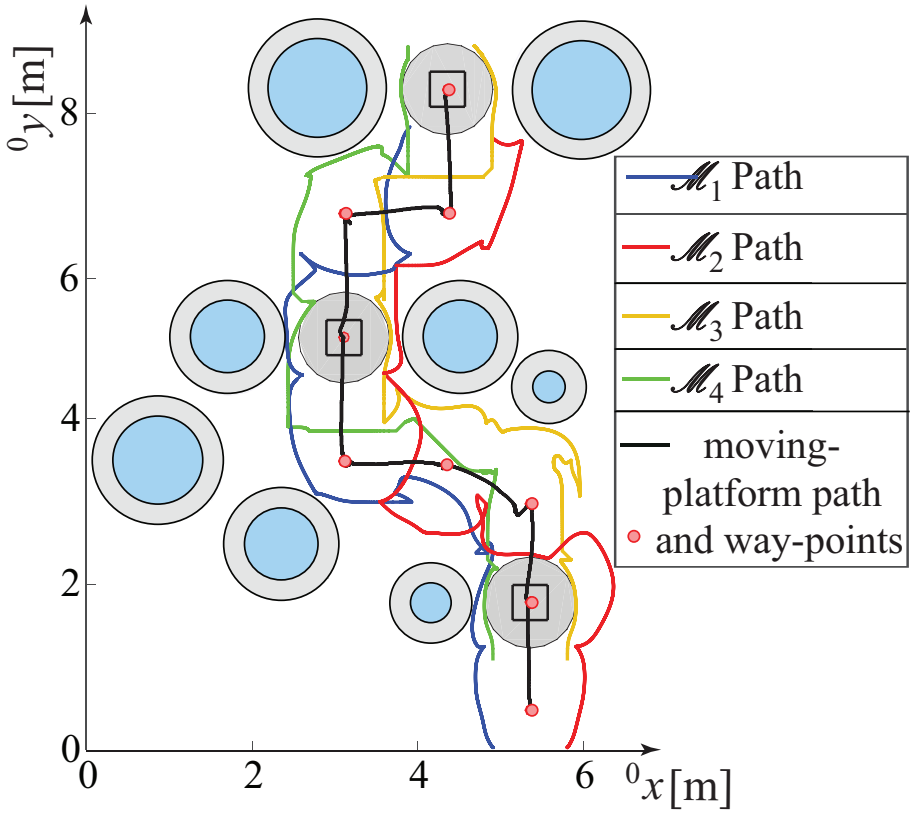

Figure 6.11: Path of MoPICK for the required task

6.3.3 Results and Discussion

As discussed in Section 6.3.1, the required task is to displace the MoPICK moving-platform from point $\overline{P}_1$ to P_f by sequentially following the intermediate way-points as depicted in Fig. 6.9. In order to perform the desired task, the output of the proposed path planning algorithm is illustrated in Fig. 6.11. The simulation showing the complete process of comprising the feasible path search and optimal path generation can be seen at[3]. The video shows the resultant motion of the complete system along with the pick-and-place operations performed at the task locations.

[3] https://youtu.be/0wrdLBvM9-s

The tunning parameters for the proposed MCDPR algorithm are the step sizes of the search grids, $d_j, j = 1 \ldots, 4$ and d_{MP}. It is important to tune these parameters in order to obtain a feasible path of the MCDPR mobile bases and the moving-platform. For example, during the first phase of the algorithm, the step size d_j must remain smaller than the diameter of the smallest obstacle in the environment in order to detect its collision with the mobile bases. However, reducing d_j increases the computation time for calculating the feasible paths. During the second phase of the algorithm, a very small step size d_{MP} may result in not achieving the desired moving-platform position due to limited number of discrete points between the two way-points while a big d_{MP} can generate large discontinuities in the moving-platform path.

The main drawback of this algorithm is the requirement of a good initial solution in the form of moving platform way-points. Moreover, the resulting path quality is often of poor quality with loops and edges that increase the distance traveled. However, the iterative algorithm is useful if the system needs to be guided through a cluttered region.

6.4 Optimization based Trajectory Planning of MCDPRs

The second path planning approach developed for highly redundant systems is based on direct transcription optimization method. As discussed earlier, this optimization based approach allows us to embed the numerous constraints associated with CDPRs into the planning problem, while the direct transcription eases the reliance on the initial guess. The method is based on discretizing the path into N number of points, and then searching for an optimal MCDPR pose at each point that maximize the wrench capability of the moving-platform while minimizing the total distance traveled. Thus, the solution to the optimization problem is in the form of discrete set of optimal MCDPR poses that are later exploited to generate the continuous motion profiles. A similar environment is considered as presented in the previous section (see Fig. 6.9); however, in this case the intermediate way-points are not required. The way-points are only positioned on the tables requiring a task action. Figure 6.12 shows the task designed for the direct transcription method, where the goal is to displace the moving-platform from an initial position $\overline{P}_1$ to a desired position $\overline{P}_4$ while passing through the defined way-points denoted as $\overline{P}_2$ and $\overline{P}_3$. Lets $\underline{s}$ denotes the total number of obstacles in the environment. Similar to the previous approach, the $\underline{q}$th obstacle is inflated, $\underline{q} =, 1, \ldots, \underline{s}$, and mobile bases are treated as single points.

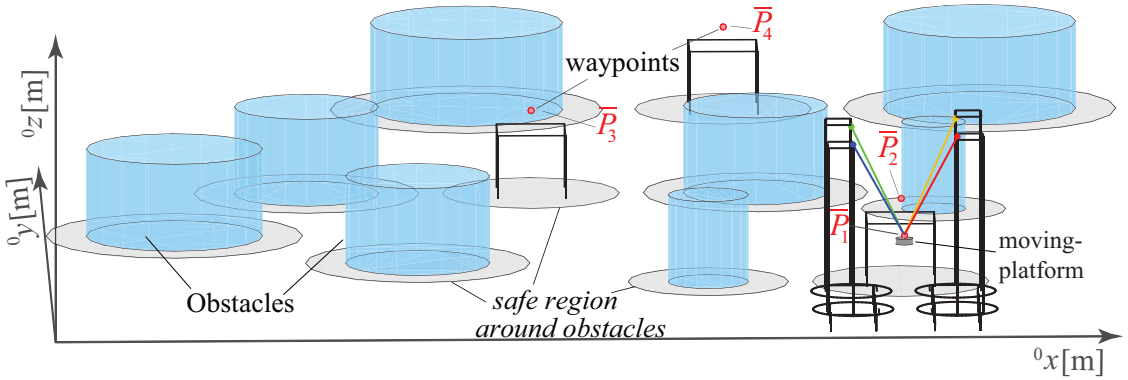

Figure 6.12: Test scenario and illustrated environment for direct transcription method

6.4.1 Trajectory Planning

In this section, a two-step trajectory planning method is presented for MCDPRs. First, direct transcription method is used for the path planning of the robot, which searches for an optimal geometric path from an initial to a final point. The output of the direct transcription method is in the form of a discrete set of poses achieved by minimizing the given criterion while respecting the set of constraints. The second step is the trajectory planning which uses the set of poses to generate a continuous motion profile of the robot.

6.4.1.1 Path Planning using Direct Transcription Optimization

In general, the dynamics of a system can be defined by the set of differential equations,

$$\dot{x} = f(x, u). \tag{6.16}$$

where x and u represent the states of the system and the control input. $f(\cdot)$ denotes the evolution of the system dynamics in time t. Trajectory optimization aims at finding a control trajectory that minimizes a given criterion subject to the dynamics constraints in Eq. (6.16). In direct transcription methods, this continuous optimal control problem is transcribed into a finite-dimensional optimization problem by discretizing the trajectories over N time steps and solved for states and controls simultaneously.

State transition between time-steps

The MCDPR is characterized by the position of its mobile bases and its moving platform. Let $\mathbf{p}_e$ be a three dimensional vector containing the Cartesian coordinates of the point-mass moving platform P in $\mathscr{F}_0$ at the eth step of the trajectory, $e = 2, \ldots, N$. Accordingly, let the two-dimensional Cartesian coordinate vector of $\mathscr{M}_j$ in ^0x ^0y plane be denoted as $\mathbf{m}_{j,e}$ at the eth time step. It should be noted that

the $e = 1$ represents the given initial configuration of MoPICK. The state of the MoPICK at the eth time step, is denoted by eleven-dimensional vector $\mathbf{x}_e$, expressed as,

$$\mathbf{x}_e = \begin{bmatrix} \mathbf{p}_e^T & \mathbf{m}_{1,e}^T & \mathbf{m}_{2,e}^T & \mathbf{m}_{3,e}^T & \mathbf{m}_{4,e}^T \end{bmatrix}^T, \tag{6.17}$$

In the direct method rather than simulating the continuous evolution of the system the states at all way-points are optimized simultaneously. To do so, $\mathbf{x}_{e+1}$ is obtained from the previous states by forward integration of the velocities. In order to do that, we use a simple Euler integration of the form:

$$\mathbf{x}_{e+1} = \mathbf{x}_e + \dot{\mathbf{x}}_{e+1}\ \Delta t. \tag{6.18}$$

The product of Δt and $\dot{\mathbf{x}}_{e+1}$ defines the maximum change in the state variables for a given time step. Typically in cluttered environments, this should be relatively small to prevent the optimizer finding solutions that *jump* over objects. Thus, the state variables for the optimization problem are defined as $\mathbf{x}$ and $\dot{\mathbf{x}}$ both $11(N-1)-$dimensional vectors containing the position and velocity of the platform and the mobile bases at each time step, namely,

$$\mathbf{x} = \begin{bmatrix} \mathbf{x}_2^T & \mathbf{x}_3^T & \dots & \mathbf{x}_N^T \end{bmatrix}^T, \tag{6.19a}$$

$$\dot{\mathbf{x}} = \begin{bmatrix} \dot{\mathbf{x}}_2^T & \dot{\mathbf{x}}_3^T & \dots & \dot{\mathbf{x}}_N^T \end{bmatrix}^T. \tag{6.19b}$$

For an initial state value denoted $\mathbf{x}_{init}$ and assuming an initial static condition, Eq. (6.18) can be extended to:

$$\begin{aligned} \mathbf{x}_2 &= \mathbf{x}_{init} + \dot{\mathbf{x}}_2\ \Delta t, \\ \mathbf{x}_3 &= \mathbf{x}_2 + \dot{\mathbf{x}}_3\ \Delta t, \\ &\vdots \\ \mathbf{x}_N &= \mathbf{x}_{N-1} + \dot{\mathbf{x}}_N\ \Delta t. \end{aligned} \tag{6.20}$$

By re-arranging the above expression into matrix form and gathering all the state variables to one side a system of linear equality constraints governing the transition of the system from one time step to the next can be written in terms of the state variables as follows:

$$\overline{\mathbf{A}} \begin{bmatrix} \mathbf{x} \\ \dot{\mathbf{x}} \end{bmatrix} = \mathbf{b}. \tag{6.21}$$

$\overline{\mathbf{A}}$ is a $22(N-1)$-dimensional sparse square matrix and $\mathbf{b}$ is a $22(N-1)$-dimensional sparse vector containing the system initial conditions.

Optimization Procedure

At each step, the MCDPR pose must be wrench feasible with respect to the RWS (only considering the weight of the moving platform). Additionally, we are interested in finding a shortest collision free path for the moving platform. Hence, the objective function of the problem is formulated as follows,

$$\underset{\mathbf{x}_{2,\dots,N},\dot{\mathbf{x}}_{2,\dots,N}}{\text{minimize}} \quad -k_3\sum_{e=2}^{N}\mu_k + k_4\sum_{e=2}^{N}\sum_{j=1}^{4}\|\mathbf{m}_{j,i}-\mathbf{m}_{j,e-1}\|^2. \tag{6.22}$$

The first cost term in Eq. (6.22), aims to maximize the capacity margin of the RWS at each time step while the second term attempts to minimize the total path length of the mobile bases. The cost weights are tuned as $k_3 = 0.4$, $k_4 = 0.6$.

The system is subject to a set of global equality constraints defined as follows:

$$\mathbf{p}_{N_1} = \overline{\mathbf{p}}_2, \tag{6.23}$$

$$\mathbf{p}_{N_2} = \overline{\mathbf{p}}_3, \tag{6.24}$$

$$\mathbf{p}_{N} = \overline{\mathbf{p}}_4, \tag{6.25}$$

$$\overline{\mathbf{A}}\begin{bmatrix}\mathbf{x}\\ \dot{\mathbf{x}}\end{bmatrix} = \mathbf{b}, \tag{6.26}$$

where N_1 and N_2 represent the time steps at the way-points of the moving platform $\overline{P}_1$ and $\overline{P}_2$, respectively. The desired poses and way-points are imposed using equality constraints Eq. (6.23) to Eq. (6.25), while as explained above the system velocities are constrained by the state transition matrix Eq. (6.26). Furthermore at any time-step $e = 1,\dots,N$ the following inequality constraints are imposed for jth, $j = 1,\dots,4$, mobile base:

$$l_{min} \leq \|\begin{bmatrix}\mathbf{m}_{j,e}^T & 1.2\end{bmatrix}^T - \mathbf{p}_e\| \leq l_{max}, \tag{6.27a}$$

$$\|\mathbf{m}_{\underline{h},e} - \mathbf{m}_{j,e}\| \geq d_{min}, \text{ for } \underline{h} = 1,\dots,4, \ \underline{h} \neq j, \tag{6.27b}$$

$$\|\mathbf{m}_{j,i} - \mathbf{o}_{\underline{q}}\|^2 - r_{\underline{q}} \geq 0, \text{ for } \underline{q} = 1,\dots,\underline{s}. \tag{6.27c}$$

Equation (6.27a) bounds the cable length between a minimum and maximum length denoted as l_{min} and l_{max}, where 1.2 m is the constant height of the exit points expressed in $\mathscr{F}_0$. Equation (6.27b) ensures the mobile bases do not collide with each other by defining d_{min} as a minimum relative distance. Equation (6.27c) ensures that the distance between the $\underline{q}$th augmented obstacle, whose position is defined by $\mathbf{o}_{\underline{q}}$ and radius is $r_{\underline{q}}$, and the mobile base is always greater than 0. Finally, Eq. (6.28b) enforces bounds on the state variables, *i.e.,*

$$\mathbf{x}_L \leq \mathbf{x}_e \leq \mathbf{x}_U, \tag{6.28a}$$

$$\dot{\mathbf{x}}_L \leq \dot{\mathbf{x}}_e \leq \dot{\mathbf{x}}_U. \tag{6.28b}$$

where $\mathbf{x}_L$, $\mathbf{x}_U$, $\dot{\mathbf{x}}_L$ and $\dot{\mathbf{x}}_U$ represents the lower and upper bounds on $\mathbf{x}_e$ and $\dot{\mathbf{x}}_e$, $e = 2, \ldots, N$, respectively.

6.4.1.2 Generation of Motion Profiles

In this section, the cubic splines approach [AA02] is adopted to obtain a trajectory profile for the robot. The objective is to generate a continuous trajectory that passes through the N discrete points obtained from the direct transcription method. To do so, a single cubic spline $\overline{s}(t)$ is defined as a function of time t and is composed of $N-1$ cubic polynomials connecting N supporting points. The hth cubic polynomial, $h = 1, \ldots, N-1$, connecting the two consecutive supporting points is expressed as,

$$\overline{s}_h(t) = a_h(t - t_h)^3 + b_h(t - t_h)^2 + c_h(t - t_h) + d_h, \tag{6.29}$$

where $t_h \leq t \leq t_{h+1}$. t_h represents the time at the hth supporting point. To completely characterize the spline $\overline{s}(t)$, the coefficients a_h, b_h, c_h, and d_h, $h = 1, \ldots, N-1$ must be determined while imposing the continuity conditions at first and second derivative with respect to t at the supporting points. The first and second derivative of the hth cubic polynomial is given as:

$$\dot{\overline{s}}_h(t) = 3a_h(t - t_h)^2 + 2b_h(t - t_h) + c_h, \tag{6.30}$$

$$\ddot{\overline{s}}_h(t) = 6a_h(t - t_h) + 2b_h. \tag{6.31}$$

The coefficient d_h can be obtained from Eq. (6.29) at $t = t_h$,

$$d_h = \overline{s}_h(t_h). \tag{6.32}$$

b_h and a_h can be achieved from Eq. (6.31) at $t = t_h$ and $t = t_{h+1}$,

$$\ddot{\bar{s}}_h(t_h) = 2b_h \implies b_h = \frac{\ddot{\bar{s}}_h(t_h)}{2}, \tag{6.33a}$$

$$\ddot{\bar{s}}_h(t_{h+1}) = 6a_h(t_{h+1} - t_h) + 2b_h. \tag{6.33b}$$

Substituting b_h from Eq. (6.33a) into the Eq. (6.33b) yields

$$a_h = \frac{\ddot{\bar{s}}_h(t_{h+1}) - \ddot{\bar{s}}_h(t_h)}{6(t_{h+1} - t_h)}. \tag{6.34}$$

Furthermore, c_h can be obtained by substituting a_h, b_h and d_h in Eq. (6.29) at $t = t_h$,

$$c_h = \frac{\Delta\bar{s}_h}{\Delta t_h} - \frac{\Delta t_h(\ddot{\bar{s}}_h(t_{h+1}) + 2\ddot{\bar{s}}_h(t_h))}{6} \tag{6.35}$$

where

$$\Delta\bar{s}_h = \bar{s}_h(t_{h+1}) - \bar{s}_h(t_h), \qquad \Delta t_h = t_{h+1} - t_h. \tag{6.36}$$

In order to compute the coefficients of the cubic polynomials, the first order continuity conditions are imposed on the values of $\bar{s}_h$, $h = 1, \ldots, N-1$ at the supporting points. The first order derivatives of the two polynomials $\bar{s}_{h-1}$ and $\bar{s}_h$ joining at t_h are expressed as

$$\dot{\bar{s}}_{h-1}(t_h) = 3a_{h-1}(\Delta t_{h-1})^2 + 2b_{h-1}(\Delta t_{h-1}) + c_{h-1}, \tag{6.37a}$$

$$\dot{\bar{s}}_h(t_h) = c_{h-1}. \tag{6.37b}$$

For the first order continuity of $\bar{s}(t)$ at t_h, Eqs. (6.37a) and (6.37b) should be equal. Equating these equations and substituting the corresponding coefficients yields,

$$\Delta t_{h-1}\ddot{\bar{s}}_h(t_{h+1}) + 2(\Delta t_h + \Delta t_{h-1}) + (\Delta t_{h-1})\ddot{\bar{s}}_h(t_{h-1}) = 6\Big(\frac{\Delta\bar{s}_h}{\Delta t_h} - \frac{\Delta\bar{s}_{h-1}}{\Delta t_{h-1}}\Big). \tag{6.38}$$

Finally, we need to impose the boundary conditions *i.e.,* the first order derivative at initial and final supporting points should be equal to zero, namely,

$$\dot{\bar{s}}_1(t_1) = 0, \qquad \dot{\bar{s}}_{N-1}(t_N) = 0 \tag{6.39}$$

Substituting the corresponding coefficients from Eqs. (6.32), (6.33a), (6.34) and

(6.35) into the (6.39) yields,

$$2\Delta t_1 \ddot{\bar{s}}_1(t_1) + \Delta t_1 \ddot{\bar{s}}_1(t_2) = 6\frac{\Delta \bar{s}_1}{\Delta t_1}, \tag{6.40a}$$

$$\Delta t_{N-1} \ddot{\bar{s}}_{N-1}(t_{N-1}) + 2\Delta t_{N-1} \ddot{\bar{s}}_{N-1}(t_N) = -6\frac{\Delta \bar{s}_{N-1}}{\Delta t_{N-1}}. \tag{6.40b}$$

Furthermore, let $\bar{\mathbf{s}}$ ($\ddot{\bar{\mathbf{s}}}$, resp.) be a N-dimensional vector containing the values of the cubic spline $\bar{s}(t)$ (second derivative of $\bar{s}(t)$, resp.) at each supporting point, expressed as:

$$\bar{\mathbf{s}} = \begin{bmatrix} \bar{s}(t_1) \\ \bar{s}(t_2) \\ \vdots \\ \bar{s}(t_{N-1}) \\ \bar{s}(t_N) \end{bmatrix}, \quad \ddot{\bar{\mathbf{s}}} = \begin{bmatrix} \ddot{\bar{s}}(t_1) \\ \ddot{\bar{s}}(t_2) \\ \vdots \\ \ddot{\bar{s}}(t_{N-1}) \\ \ddot{\bar{s}}(t_N) \end{bmatrix}. \tag{6.41}$$

From the conditions defined in Eqs. (6.38) and (6.40), the relation between $\bar{\mathbf{s}}$ and $\ddot{\bar{\mathbf{s}}}$ can be expressed as,

$$\mathbf{B}\ddot{\bar{\mathbf{s}}} = 6\mathbf{C}\bar{\mathbf{s}}, \tag{6.42}$$

where $\mathbf{B}$ and $\mathbf{C}$ are $N \times N$ matrices expressed as,

$$\mathbf{B} = \begin{bmatrix} 2\alpha_1 & \alpha_1 & 0 & 0 & \dots & 0 & 0 & 0 \\ \alpha_1 & 2\alpha_1\alpha_2 & \alpha_2 & 0 & \dots & 0 & 0 & 0 \\ 0 & \alpha_2 & 2\alpha_2\alpha_3 & \alpha_3 & \dots & 0 & 0 & 0 \\ \vdots & \vdots & \ddots & \ddots & \ddots & \ddots & \vdots & \vdots \\ 0 & 0 & 0 & 0 & \dots & \alpha_{N-2} & 2\alpha_{N-2}\alpha_{N-1} & \alpha_{N-1} \\ 0 & 0 & 0 & 0 & \dots & 0 & \alpha_{N-1} & 2\alpha_{N-1} \end{bmatrix} \tag{6.43a}$$

$$\mathbf{C} = \begin{bmatrix} -\beta_1 & \beta_1 & 0 & 0 & \dots & 0 & 0 & 0 \\ \beta_1 & -\beta_1\beta_2 & \beta_2 & 0 & \dots & 0 & 0 & 0 \\ 0 & \beta_2 & -\beta_2\beta_3 & \beta_3 & \dots & 0 & 0 & 0 \\ \vdots & \vdots & \ddots & \ddots & \ddots & \ddots & \vdots & \vdots \\ 0 & 0 & 0 & 0 & \dots & \beta_{N-2} & -\beta_{N-2}\beta_{N-1} & \beta_{N-1} \\ 0 & 0 & 0 & 0 & \dots & 0 & \beta_{N-1} & -\beta_{N-1} \end{bmatrix} \tag{6.43b}$$

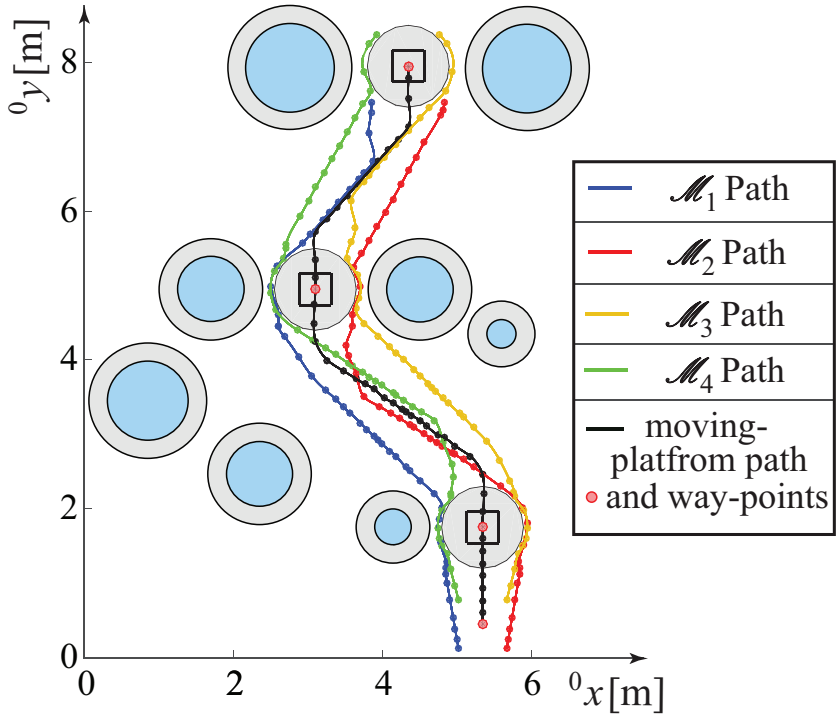

Figure 6.13: MoPICK path from direct transcription method using test scenario

where

$$\alpha_h = \Delta t_h, \qquad \beta_h = \frac{1}{\Delta t_h}, \qquad h = 1, \ldots, N-1 \tag{6.44}$$

The first and the last row of the above matrices impose the boundary conditions while the intermediate $N-2$ rows impose the first order continuity conditions. By solving Eq. (6.42) for $\ddot{\bar{\mathbf{s}}}$, the coefficients of the polynomials $\bar{s}_h,\ h = 1, \ldots, N-1$ are determined.

6.4.2 Experiments

As discussed in Sec. 1.3.3, mobile bases of MoPICK are controlled by sending rotational velocity commands to its motarized wheels. Therefore, their continuous trajectories in $\mathscr{F}_0$, obtained from the cubic splines, are transformed into the wheels rotational velocity using the system's kinematic model [MM14]. Evidently, wheels rotational velocities are also continuous. The continuous trajectories do not include any sharp turns and edges and thus gives an exemption for including the non-holonomic constraints into the planning problem.

The optimization problem defined by Eqs. (6.22) to (6.28b) is solved using the © MATLAB function *fmincon*. It took 36 minutes and 14 seconds of CPU[4] time to compute the solution of the aforementioned optimization problem with the following

[4] i7-5500U CPU@2.40GHz

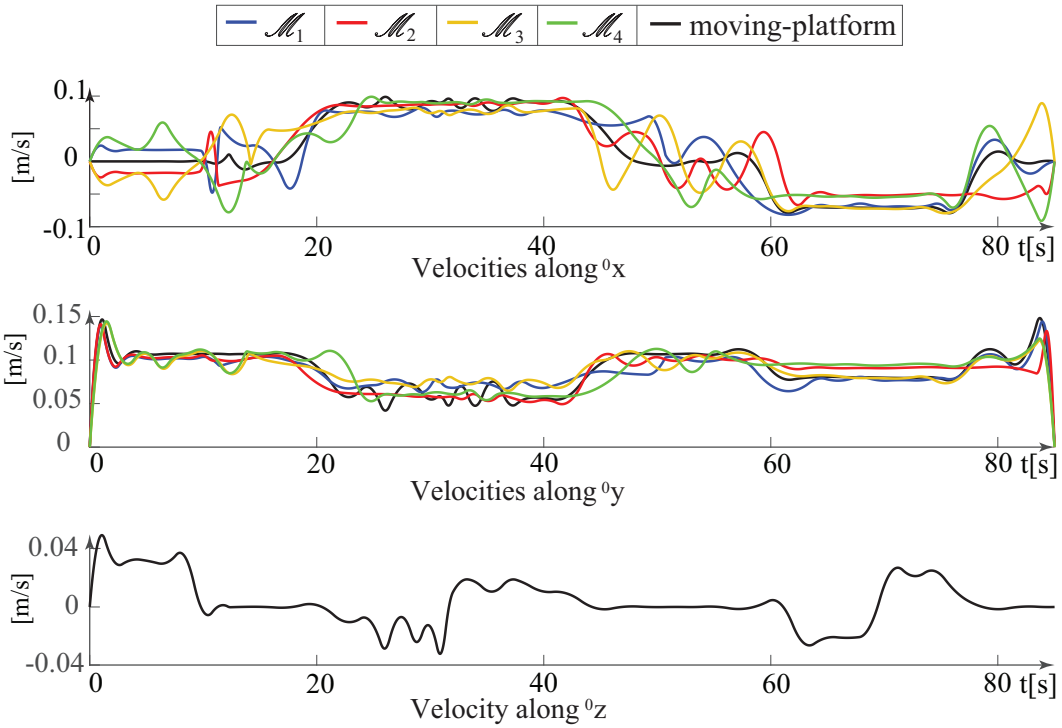

Figure 6.14: MoPICK velocity profiles for a test scenario

parameters:

$$N_1 = 8, \quad N_2 = 32, \quad N = 47, \quad \Delta t = 0.75 \ s. \tag{6.45}$$

The total trajectory time is set to 85 seconds. Figure 6.13 illustrates the N number of path points generated using the Direct Transcription method. It should be noted that a single cubic spline is required for each independent state of the manipulator defined in Eq. (6.17). Therefore 11 cubic splines are used to generate a continuous path depicted in Fig. 6.13. Accordingly, the velocity profiles of the moving-platform and the mobile bases are shown in Fig. 6.14. A simulation video showing the output of the proposed method can be seen at[5].

6.4.3 Comparison with the iterative path planning algorithm

The direct transcription method is compared with a path planning algorithm for MCDPRs presented in Sec. 6.3, which iteratively searches for a feasible and collision free path by making a locally optimal choice at each step. The comparison between the lengths of the MCDPR path acquired from the iterative algorithm (see Fig. 6.11) and direct transcription (see Fig. 6.13) is shown in Fig. 6.15. The proposed approach of direct transcription generates a more continuous path with better performance in

[5] https://youtu.be/kK714kDWUaA, from 0:29 to 0:47

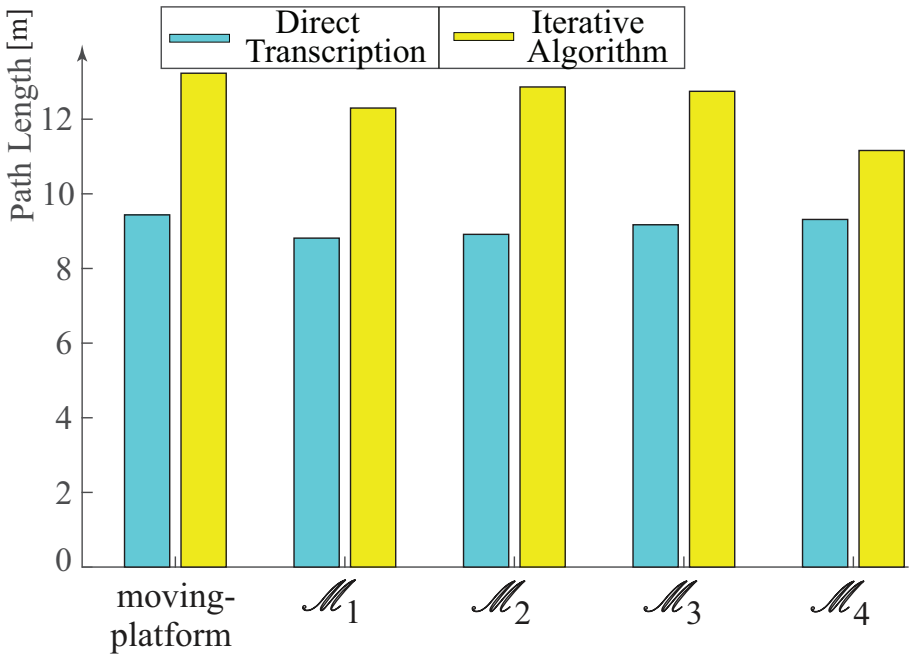

Figure 6.15: Comparison of the path length between direct transcription and iterative algorithm

terms of total distance traveled. In spite of the better quality in resulting trajectories, the direct transcription method has several limitations. First the number of decision variables may become computationally more expensive with high DoF MCDPRs, however this is somewhat mitigated by the sparsity of the state transition matrix. Secondly, the weights of the costs need to tuned, a time consuming task, to acquire a feasible trajectory of the system. Finally, as the path is obtained in terms of discrete points, the approximation between the two consecutive nodes performed by the cubic splines might not respect all constraints, *e.g.*, collisions with obstacles. This problem may be resolved by either increasing the safety distance to obstacles or increasing N, albeit with added computational cost. Alternatively, the shooting method could be employed which would used the output of this algorithm as an initial solution.

6.4.4 MoPICK Simulation in V-REP

As explained earlier, a dynamic model of the MoPick is developed using the simulation environment V-REP [RSF13], to facilitate testing and debugging before hardware deployment. The V-REP simulation of the resulting trajectory, obtained from the proposed method, can be seen in this video[6]. The results may be evaluated by analyzing the moving platform's path. Figure 6.16 shows the error between the desired and actual position of the moving platform in V-REP. It should be noted that the proposed trajectory is feasible and the moving platform achieves the desired

[6] https://youtu.be/kK714kDWUaA, from 0:47 to 0:57

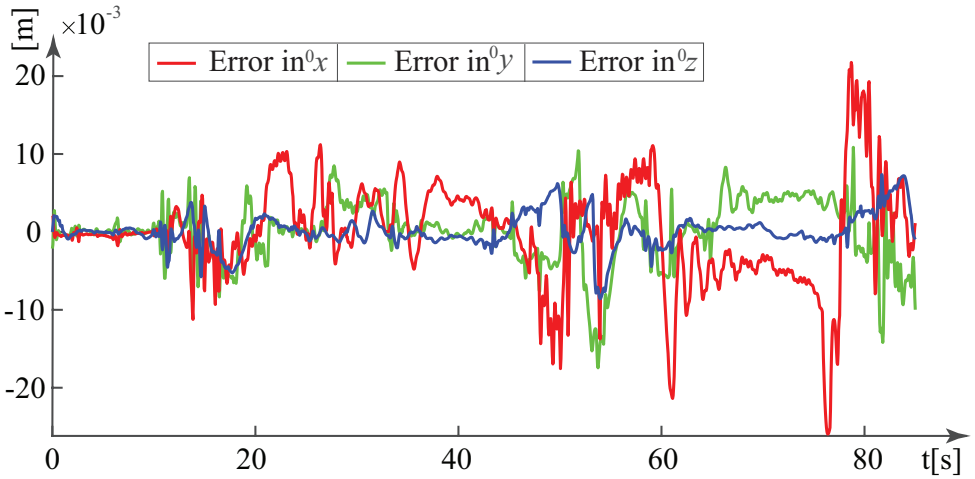

Figure 6.16: Error between the actual and the desired moving platform position

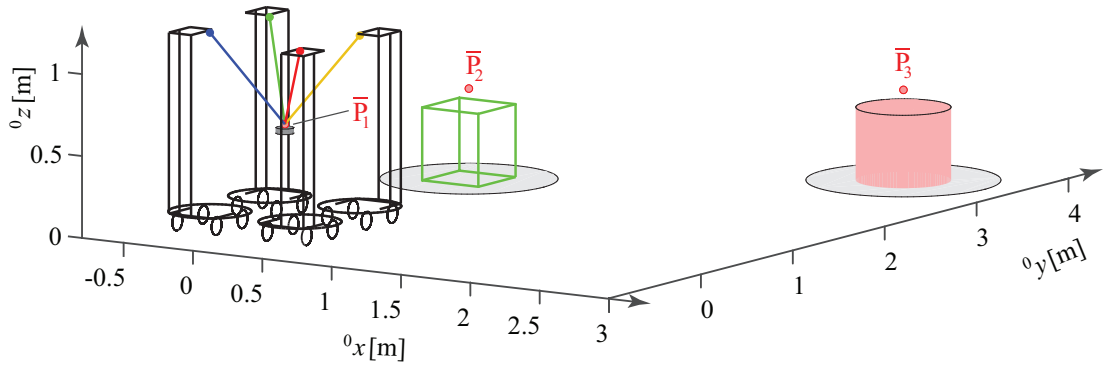

Figure 6.17: Experimental scenario

path within an acceptable range of errors.

6.4.5 Experimental Validation

The proposed approach is validated experimentally on MoPICK, using an experimental scenario with two way-points as shown in Figs. 6.17 and 6.18. The parameters of the direct transcription method are selected as $N = 2N_1 = 26$, $\Delta t = 0.5\ s$. The solution to the optimization problem is obtained in 10 minutes and 36 seconds of CPU[7] time by *fmincon*. The total trajectory time is set to 40 s for computing motion profiles using cubic splines. The resultant continuous path is depicted in Fig. 6.19. Accordingly, the velocity profiles of the moving-platform and the mobile bases are shown in Fig.6.20. The simulation showing the complete process of searching for a discrete path and generation of the continuous motion profile along with the simulation and experimental validation can be seen in[8]. From the results, it is evident that the output trajectory is continuous, safe and feasible to be implemented

[7] i7-5500U CPU@2.40GHz

[8] https://youtu.be/kK714kDWUaA, from 0:03 to 0:29

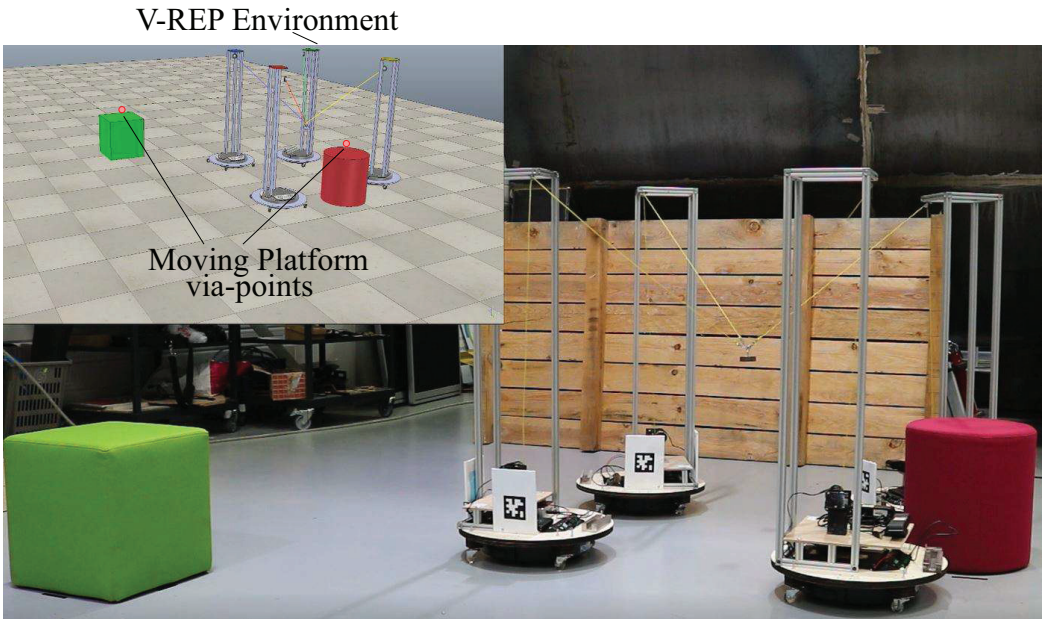

Figure 6.18: Experimental setup

on the robot.

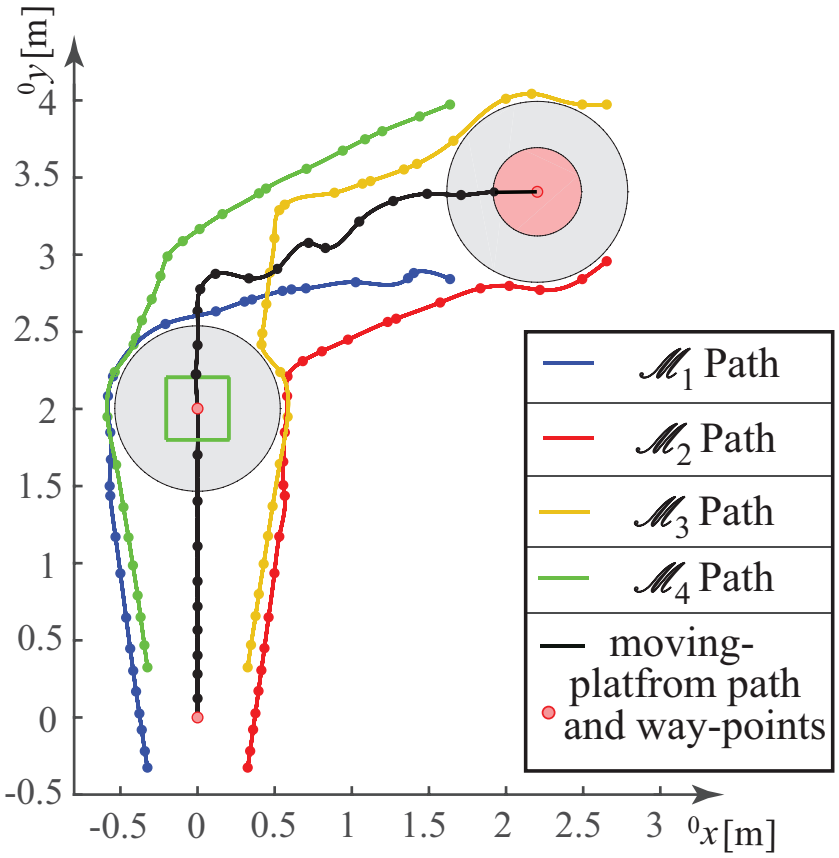

Figure 6.19: MoPICK path from direct transcription method using the experimental scenario

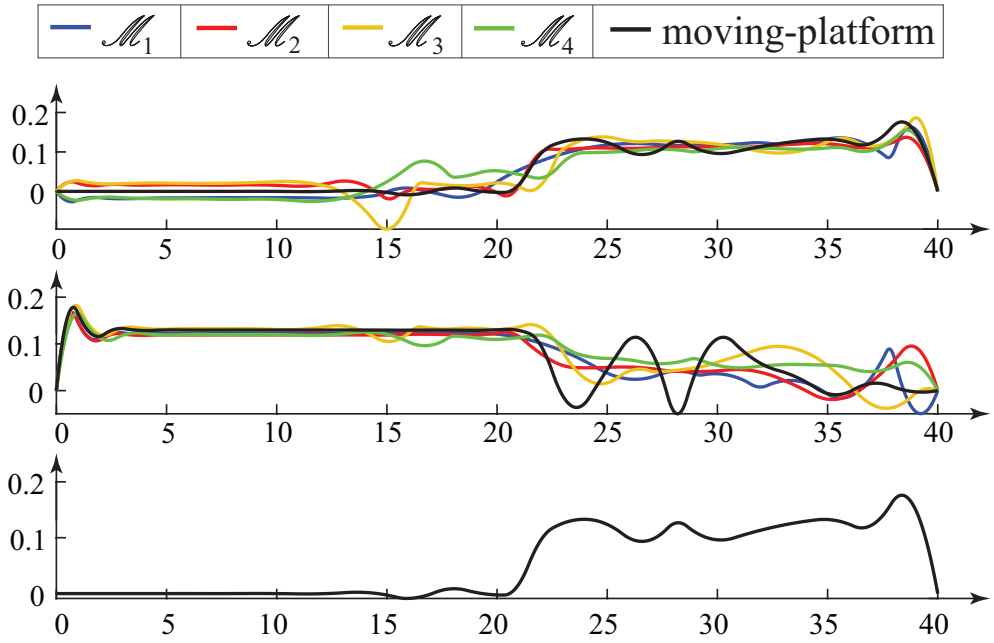

Figure 6.20: MoPICK velocity profiles for an experimental scenario

6.5 Conclusion

It has been observed that MCDPRs are kinematically redundant due to the additional mobility of the mobile bases. As a consequence, there exist multiple paths for the MCDPR mobile bases to displace the moving-platform from one pose to another and to perform a desired task. Therefore, this chapter focused on the path planning of MCDPRs.

The first part of the chapter addressed the problem of determining an optimal path also referred to as a redundancy planning for MCDPRs with one degree of kinematic redundancy. The path planning problem is formulated as a bi-objective optimization problem that corresponds to minimization of the total trajectory time and maximization of the robot average robustness index throughout the trajectory. FASTKIT is used as a case study with a desired pick-and-place operation.

In contrast to FASTKIT, MoPICK prototype has eight degrees of kinematic redundancy, thus the second part of the chapter described two different path planning strategies for highly redundant manipulators. The first approach is a sampling based iterative path planning algorithm, which plans the manipulator's path in two subsequent stages. In the first stage, the algorithm searches for a feasible and collision free path of mobile bases. The second stage generates an optimal path of the moving-platform to reach the desired pose. Although the obtained path between the initial and final poses may not be the shortest one, it leads to a feasible path, when it exists.

The second approach dealt with the path planning of MoPICK using direct

transcription optimization method. It is an optimization based approach where the continuous path planning problem is transcribed into a discrete optimization problem with N steps. The goal of the optimization problem is to maximize the wrench capability of the robot at each step while minimizing the total path length. The desired pose and intermediate way-points are enforced using a set of equality constraints. In the direct transcription method, rather than simulating the continuous evolution of the system, the states at all way-points are optimized simultaneously. The resulting discrete path is transformed into a continuous motion profile in time using cubic splines. The proposed approach is validated through simulation and experimentally on MoPICK. Additionally, the direct transcription approach produces better quality paths in comparison to iterative path planning algorithm.

7

General Conclusion and Perspectives

Contents

7.1 Summary of the Work

During the last decades, several research studies have been performed in the field of Cable-Driven Parallel Robots (CDPRs). CDPRs provide several advantages, including a wide workspace and a high payload to weight ratio. However, when the working environment is cluttered, CDPR cannot be used to accomplish complicated tasks. The focus of this work was to develop mobile, deployable and autonomous CDPRs, that can be adapted based on the desired task. As a result, a novel concept

of Mobile Cable-Driven Parallel Robot (MCDPR) has been introduced in this thesis using combination of mobile robots and a CDPR.

The contributions of this thesis are about different research aspects of MCDPRs. The research work has been validated using simulations and when possible using experiments. Furthermore, two MCDPR prototypes have been developed during the course of this thesis and are named FASTKIT and MoPICK. In the following, a description of the contributions of each chapter is briefly discussed.

Chapter 3 presented a real-time Tension Distribution Algorithm for MCDPRs. The work presented in this chapter has led to the publication of one paper presented at the international conference [RLMGC18d]. The contributions of this chapter are divided into two parts.

The first part focused on deriving the MCDPR's static equilibrium conditions. Classical CDPR connected to fixed base considers only the static equilibrium of their moving-platform while respecting the bounds on the cable tensions. In contrast, as a MCDPR possesses moving bases, additional constraints are generated, which are associated with stability of the mobile bases. Thus, these stability conditions must be taken into consideration to ensure the complete equilibrium of a MCDPR. The stability of a mobile base is characterized by its tipping and sliding conditions. The tipping conditions depend on the moment generated at the boundaries of the mobile base footprint. These tipping conditions uniquely depend on the weight of the mobile base and the tension in the cables attached to it. Likewise, the sliding conditions also depend on the weight of the mobile base and those cable tensions. However, the sliding conditions are represented in the form of a friction cone. For ease of analysis, the non-linear sliding conditions are linearized and the friction cone is transformed into a four-sided friction pyramid.

Using the aforementioned static equilibrium conditions, the second part of the chapter presented a Tension Distribution Algorithm for the real-time control of MCDPRs cables. The algorithm forms a Feasible Cable Tension Domain representing the set of feasible tensions based on the cable tension limits and the conditions associated with the static equilibrium of the mobile bases. This Feasible Cable Tension Domain takes the form of a $(m-n)$-dimensional convex polytope. The presented Tension Distribution Algorithm finds the vertices of the feasible polygon or proves that it is null. If the feasible polygon exists and is determined, then the centroid of the polygon is calculated which is a solution furthest from all constraints. The coordinates of the centroid are used to compute the feasible distribution of the cable tensions. The proposed algorithm is investigated on multiple case studies including FASTKIT and MoPICK. The obtained results show that the new set of constraints developed for MCDPRs are sufficient to compute feasible cable tensions such that they stay within the required set of limits while ensuring the stability of all

the mobile bases. The algorithm is relevant for real-time implementations, however, it has only been validated for MCDPRs up to two degrees of actuation redundancy.

Chapter 4 introduced a methodology to determine the Available Wrench Set of MCDPRs. Similar to the Tension Distribution Algorithm, the workspace also depends, not only on the static equilibrium of the moving-platform, but on the static equilibrium of the mobile bases as well. Wrench-Feasible Workspace is traced using Available Wrench Set which defines the set of wrenches the moving-platform can generate. Available Wrench Set of MCDPRs takes the form of a n-dimensional convex polytope. The Available Wrench Set is constructed using two different approaches, *i.e.*, convex hull and the Hyperplane Shifting Method. The convex-hull approach uses the vertices of the cable tension space to determine the vertices of Available Wrench Set and forms the boundary of the convex polytope. The Hyperplane Shifting Method allows us to determine the Available Wrench Set geometrically by characterizing the facets of the polytope. The equivalence between both the approaches is also presented. Multiple case studies are investigated in order to show that the approach is applicable to both planar and spatial MCDPRs. The approach was experimentally validated on a MCDPR with a point-mass end-effector and two mobile bases. The work presented in this chapter has led to the publication of one conference paper [RLMGC18a] and one journal paper [RLC19].

Chapter 5 dealt with the kinematic modeling and twist capabilities of MCDPRs. To derive the MCDPRs kinematic model, each cable of the manipulator is modeled as a Universal-Prismatic-Spherical kinematic chain. Furthermore, as mobile bases are only capable of generating two-DoF translational motions and one-DoF rotational motion in a plane, they are modeled as a Revolute-Prismatic-Prismatic kinematic chains. By integrating the aforementioned chains, a general kinematic architecture is developed for MCDPRs, where the cables carried by the jth mobile base are connected in parallel with each other, while the jth mobile base is linked in series with the aforementioned parallel architecture of the cables mounted on it. The first-order kinematic model is used to determine the Available Twist Set (ATS) of MCDPRs by considering the joint velocity limits for the cables and the mobile bases. If $m = n$, ATS corresponds to a single convex polytope. However, if $m > n$, ATS is the region bounded by C_m^n convex polytopes. Finally, ATS is used to determine the twist capacities of the moving-platform. The work presented in this chapter has led to the publication of one conference paper [RLMGC18b]. The hardware design and software architecture of FASTKIT along with the manipulator's wrench and twist analyses are published in the ECHORD++ book [PRMG+20].

Chapter 6 presented multiple path planning strategies for MCDPRs. The work presented in this chapter has led to the publication of three papers presented at international conferences [RLMGC18c, RLMGC19, RLSRC19]. The contributions

of this chapter are divided into two parts.

At first, the problem of determining an optimal path for MCDPRs with one degree of kinematic redundancy is addressed. The problem to the path planning is formulated as a bi-objective optimization problem that corresponds to minimization of the total trajectory time and maximization of the robot wrench feasibility throughout the trajectory. FASTKIT is used as a case study with a desired pick-and-place operation.

In the second part of the chapter, two different path planning strategies are presented for highly redundant manipulators. The first approach is a sampling based iterative path planning algorithm which plans the manipulator's path in two subsequent stages. In the first stage, the algorithm searches for a feasible and collision free path of mobile bases. The second stage generates an optimal path of the moving-platform to reach at the desired pose. The second approach dealt with the path planning of highly redundant MCDPRs using direct transcription optimization method. It is an optimization based approach where the continuous path planning problem is transcribed into a discrete optimization problem of N steps, with the goal to maximize the wrench capability of the robot at each step while minimizing the total path length. The desired moving-platform poses are enforced using a set of equality constraints. In the direct transcription method rather than simulating the continuous evolution of the system, the states at all way-points are optimized simultaneously. The resulting discrete path is transformed into a continuous motion profile in time using cubic splines. The proposed approach is validated through simulation and experimentally on MoPICK.

7.2 Future Work

This thesis could be considered as a first step towards a new topic in robotics, which indeed requires further studies and investigations to be matured. The foundations of the topic have been introduced during the course of this thesis together with preliminary studies and results. Here, we end this thesis by outlining the main aspects of prospective theoretical and technical research issues and challenges that can be conducted on MCDPRs in the future. There are several possible avenues for research stemming from this thesis, proposed thereafter:

7.2.1 Multi-SLAM approach for a MCDPR

The pose of the CDPR moving-platform is completely determined by the location of the cables exit and anchor points. In contrast to classical CDPRs, the exit points of MCDPRs are mobile and thus required continuous localization system. Hence, future work should focus on developing a methodology for localizing all the MCDPR mobile

bases which are carrying the exit points of the CDPR. As discussed in sec. 1.3.2, FASTKIT uses a single Simultaneous Localization and Mapping (SLAM) approach to localize and navigate its mobile bases (during the navigation mode) in a simplified manner. For highly redundant manipulators such as MoPICK, a single SLAM system is not enough to completely localize all the mobile bases.

A possible solution would be to use multiple SLAM systems on the MCDPR mobile bases and to fuse them in order to localize all the mobile bases in the task space. It must be noted that classical SLAM approach performs three function simultaneously, *i.e.,* mapping, localization, path planning. However, the classical global planners in SLAM must be replaced with the planning approaches presented in Chapter 6.

For fully characterizing the location of the mobiles bases with SLAM, the local planners must also be developed for the dynamic path planning of the manipulator. In classical SLAM approach, the local planner is only responsible for detecting the nearby obstacles (either static of dynamic) and creating a trajectory to avoid collisions. However, the local planning problem for MCDPRs must consider the additional constraints associated with the CDPRs.

7.2.2 Moving-platform position accuracy

In addition to the cable exit points, the accurate information about the position of the anchor points is also desired in order to determine the actual pose of the moving-platform. Generally, the initial position of the anchor points is determined using some calibration strategies and later continuous localization is done through the feedback of encoders (a sensor attached to the motors of the cables) and the geometric model of the manipulator. During this thesis, cables have been assumed to be always straight and massless, however in reality it is not the case. The accuracy of the moving-platform can be substantially improved by considering more complex CDPR models [Sch17]. For example, in order to describe the small displacement of the moving-platform due to the non-rigid nature of the cables, elasto-static models of the cables should be considered. Furthermore, cable sagging is another issue that should be taken into account in order to improve the moving-platform positioning accuracy.

Additional approaches such as force sensors to measure cable tensions [PCCP18]; angular position sensors to measure cable angle position [FCCCL16] and exteroceptive sensors, such as cameras, to measure where the moving-platform is with respect to its environment [DGA+12, RCM14] could be used. Visual servoying is becoming a more and more popular technique in order to reduce the uncertainties in the pose of the MCDPR moving-platform [ZCPC19]. The fusing between the two locomotion systems, *i.e.,* the visual servoying locomotion system for the moving-platform and previously

mentioned Multi-SLAM locomotion system for mobile bases, is an interesting avenue to improve the MCDPR accuracy and kinematic performance.

7.2.3 MCDPR dynamics and control

It is essential to develop the dynamic model of MCDPRs for comprehensively analyzing various aspects and characteristics of the system. Moreover, these models will be very useful to improve the control laws for MCDPRs.

For example, in Chapter 6.4, the approach of direct transcription optimization is used for the path planning of highly redundant MCDPRs. It is noteworthy that direct transcription is generally used to compute dynamically-feasible trajectories. For this purpose, the aforementioned technique of trajectory design is investigated for MCDPRs. However, the work presented in this thesis is a first step to develop and validate the approach by considering only the kinematic constraints. Future work should focus on the extension of the proposed method for online trajectory planning of MCDPRs by considering a dynamic environment. Consequently, the system dynamic parameters should be considered in the state transition equations. For this purpose, the first step will be to develop a complete dynamic model of MCDPRs in closed form, which will help us analyze the dynamic behavior of the manipulator.

Once the motion is planned, a robust control scheme is desired in order to follow the desired trajectories and to perform the required task precisely and accurately. Multiple control strategies [FFT+04, LNC07, VAT10, LG13b, PCPC18] have been developed for classical CDPRs in order to derive the moving-platform considering the limits on the cable tensions. To apply such control schemes to MCDPRs, the constraints associated with the mobile bases should be additionally considered. The extensions of these control schemes to MCDPRs will be a very interesting, but challenging issue that can be addressed in the future.

7.2.4 MCDPR Extension

A possible extension is to embarked a serial robotic arm on the MCDRP moving-platform. This type of robot will aim to combine the advantages of three types of robots, *i.e.,* the ability to reach large spaces of a cable-driven robot, the dexterity/range of large orientation of a serial arm and the autonomous reconfiguration of the cables using mobile bases. In this case, the robotic arm will generate additional external wrenches onto both the moving platform and the mobile bases. These wrenches are generated by the motion of the robotic arm and the action performed by its end-effector. Accordingly, the stability of the moving-platform and the mobile bases can be influenced. Further research works should be dedicated to the analysis of such a system.

A control strategy should be developed specifically for this kind of systems. The control strategy should integrate the motion planning which can be done using the direct transcription method. In this case, the degree of kinematic redundancy of the system will be increased and consequently the number of states. Additional constraints for avoiding any interference between the cables and the arm should also be considered.

7.2.5 MCDPR Applications

MCDPRs can be used in multiple applications. Some of the proposed applications of MCDPRs in the future can be:

- building construction
- pick-and-place operations of large and heavy parts in large and industrial environment
- agriculture
- logistics
- inspection and scanning of large indoor/outdoor environments

Nomenclature

Abbreviations

CDPRs : Cable-Driven Parallel Robots.
DoF : Degree-of-Freedom.
RCDPRs :Reconfigurable Cable-Driven Parallel Robots.
MCDPRs : Mobile Cable-Driven Parallel Robots.
ROS : Robot Operating System.
SLAM : Simultaneous Localization and Mapping.
TDA : Tension Distribution Algorithm.
FCDT : Feasible Cable Tension Domain.
WFW : Wrench Feasible Workspace.
AWS : Available Wrench Set.
HSM : Hyperplane Shifting Method.
ATS : Available Twist Set.
ZMP : Zero-Moment Point.
WCW : Wrench Closure Workspace.
RWS : Required Wrench Set.
RTS : Required Twist Set.
UPS : Universal-Prismatic-Spherical.
RPP : Revolute-Prismatic-Prismatic.
pd_j : jth proximal-distal module of a MCDPR.

General Notation

$\mathscr{F}_0(O_0, x_0, y_0, z_0)$: base frame centered at O_0.
$\mathscr{F}_{bj}(O_{bj}, x_{bj}, y_{bj}, z_{bj})$: coordinate frame attached to the jth Mobile Base.
$\mathscr{F}_P(O_P, x_p, y_p, z_p)$: coordinate frame attached to the moving-platform.
m : total number of cables carried by the MCDPR.

m_j : number of cables attached to the jth mobile base.
n : degree-of-freedom of the moving-platform.
p : total number of mobile bases.
$\mathscr{M}_j$: jth Mobile base.
$\mathscr{C}_{ij}$: ith cable connected to the jth mobile base.
$A_{ij},\ B_{ij}$: cable $\mathscr{C}_{ij}$ exit and anchor points depicted in Fig. 1.4a.
$\mathbf{u}_{ij}$: directional vector of cable $\mathscr{C}_{ij}$.
t_{ij} : tension in the cable $\mathscr{C}_{ij}$
$\mathbf{t}_j$: cable tension vector associated to the cables carried by $\mathscr{M}_j$.
C_{kj} : kth wheel contact point of the jth mobile base.
c_j : number of wheels of the jth mobile base.

Chapter 3

$\mathbf{f} = [f^x,\ f^y,\ f^z]^T$: forces applied by the cables onto the moving-platform.
$\mathbf{m} = [m^x,\ m^y,\ m^z]^T$: moments applied by the cables onto the moving-platform.
$\mathbf{c}_{rij}$: direction of the actuation moment applied by the cable $\mathscr{C}_{ij}$ onto the moving-platform.
$\mathbf{r}_{ij}$: vector pointing from point O_P to point B_{ij}.
$\mathbf{w}_{ij} = [\mathbf{u}_{ij}^T,\ \mathbf{c}_{rij}^T]^T$: actuation wrench generated by the cable $\mathscr{C}_{ij}$
$\mathbf{a}_{ij}$: Cartesian coordinate vector of the cable exit point A_{ij}
$\mathbf{b}_{ij}$: Cartesian coordinate vector of the platform attachment point B_{ij}
$\mathbf{W}_j$: actuation wrenches exerted by the cables attached to $\mathscr{M}_j$ onto the moving-platform.
$\mathbf{W} = [\mathbf{W}_1\ \mathbf{W}_2\ \ldots, \mathbf{W}_p]$: Wrench matrix mapping the cable tension vector onto the wrenches applied by the cables onto the moving-platform.
$\mathbf{w}$: wrenches applied by the cables onto the moving-platform.
$\mathbf{c}_{kj}$: Cartesian coordinate vector of point C_{kj}.
$\mathbf{f}_{c_{kj}} = [f_{c_{kj}}^x,\ f_{c_{kj}}^y,\ f_{c_{kj}}^z]$: ground contact force at point C_{kj}.
$\mathscr{L}_{C_{kj}}$: boundary of the jth mobile base footprint between C_{kj} and C_{k+1j}.
$\mathbf{u}_{C_{kj}}$: directional vector of line $\mathscr{L}_{C_{kj}}$ (see Fig.3.1).
$m_{C_{kj}}$: moment generated about $\mathscr{L}_{C_{kj}}$.
$\mathbf{g}_j$: Cartesian coordinate vector of the jth mobile base center of gravity.
$\mathbf{w}_{gj}$: weight of $\mathscr{M}_j$.
${}^{bj}\mathbf{f}_{c_{zj}}, {}^0\mathbf{f}_{c_{zj}}$: denotes the ground contact forces at ZMP expressed in the frame $\mathscr{F}_{bj}$ and $\mathscr{F}_0$
$\mathbf{E}_f$: Four sides of the friction pyramid
${}^0\mathbf{R}_{bj}$: Rotation matrix from $\mathscr{F}_0$ to $\mathscr{F}_{bj}$.
$\underline{\mathbf{t}}$, $\overline{\mathbf{t}}$: m-dimensional vectors containing the minimum and maximum limits on the cable tensions.

$\mathbf{t}_P$: Particular solution of the cable tensions

$\mathbf{t}_N$: Homogeneous solution of the cable tensions

$\mathbf{N}$: Null space projector of the wrench matrix

$\mathbf{n}_{ij}$: component of $\mathbf{N}$ associated with the ith cable of the jth mobile base.

λ : $(m-n)$ dimensional arbitrary vector.

$\overline{M}_{C_{kj}}$: Moment of $\mathscr{M}_j$ about $\mathscr{L}_{C_{kj}}$ due to its weight and the particular solution of t_{ij}.

$\mathbf{n}_{C_{kj}}$: Moment of $\mathscr{M}_j$ about $\mathscr{L}_{C_{kj}}$ due to the homogeneous solution of t_{ij}.

$\underline{\mathbf{m}}$: lower limit on the tipping moments of a MCDPR in the λ-space

$\overline{\mathbf{m}}$: upper limit on the tipping moments of a MCDPR in the λ-space

$\mathbf{N}_C$: tipping moment due to the homogeneous solution of all the MCDPR cables.

$\overline{F}_{gj}$: sliding of $\mathscr{M}_j$ due to its weight and the gth side of the friction pyramid, $g = 1, \ldots, 4$.

$\mathbf{n}_{Fgj}$: sliding of $\mathscr{M}_j$ due to the homogeneous solution of t_{ij}.

$\underline{\mathbf{f}}$: lower limit on the sliding conditions of a MCDPR in the λ-space

$\overline{\mathbf{f}}$: upper limit on the sliding conditions of a MCDPR in the λ-space

$\mathbf{N}_f$: sliding of a MCDPR due to the homogeneous solution of all the cables mounted on it.

$\mathcal{A}_{CDPR}$: Feasible Cable Tension Domain of a Cable-Driven Parallel Robot.

$\mathcal{A}$: Feasible Cable Tension Domain of a Mobile Cable-Driven Parallel Robot.

$L_{ij,min}$: constraint line in the λ-space due to the minimum limit on the cable tension t_{ij}.

$L_{ij,max}$: constraint line in the λ-space due to the maximum limit on the cable tension t_{ij}.

L_{Ckj} : constraint line in the λ-space due to the tipping moment on the jth mobile base about $\mathscr{L}_{C_{kj}}$

L_{fgj} : constraint line in the λ-space due to the gth side of the friction pyramid, $g = 1, \ldots, 4$.

Chapter 4

$\mathscr{A}_{CDPR}$: Available Wrench Set of a Cable-Driven Parallel Robot.

$\mathscr{A}$: Available Wrench Set of a Mobile Cable-Driven Parallel Robot.

$\mathscr{R}$: Required Wrench Set.

$\mathscr{T}_j$: Tension Space formed by the cables mounted on $\mathscr{M}_j$.

$\mathbf{V}_j = [\mathbf{v}_{1j}\ \mathbf{v}_{2j} \ldots \mathbf{v}_{dj} \ldots \mathbf{v}_{v_j}]$: coordinates of the vertices of $\mathscr{T}_j$.

$\mathbf{v}_{dj}$: coordinate vector of the dth vertex of $\mathscr{T}_j$.

$\mathscr{T}$: MCDPR cable Tension Space.

$\mathbf{V} = [\mathbf{v}_1\ \mathbf{v}_2\ \mathbf{v}_l \ldots . \mathbf{v}_v]$: coordinates of the vertices of the MCDPR cable Tension Space.

$\mathbf{v}_l$: coordinates of the lth vertex of the MCDPR cable tension space.

v : total number of vertices formed by the m cables.

$\mathscr{H}_q^+, \mathscr{H}_q^-$: qth pair of hyperplanes associated with the cable tension limits.

${}^a\mathbf{W}^s$: sth $n \times n$ sub-matrix of the wrench matrix $\mathbf{W}$, $s = 1, \ldots, C_n^m$.

${}^b\mathbf{W}^s$: those $m - n$ columns of $\mathbf{W}$ not located in ${}^a\mathbf{W}^s$.

${}^a\mathbf{t}^s$, ${}^b\mathbf{t}^s$: cable tensions associated with the actuation wrenches of ${}^a\mathbf{W}^s$, ${}^b\mathbf{W}^s$.

${}^a\mathbf{V}^s$, ${}^b\mathbf{V}^s$: coordinates of the tension space vertices of ${}^a\mathbf{t}^s$, ${}^b\mathbf{t}^s$.

${}^a\mathbf{v}_l^s$, ${}^b\mathbf{v}_l^s$: lth column of ${}^a\mathbf{V}^s$, ${}^b\mathbf{V}^s$.

$\mathbf{t}_j^s = [{}^a\mathbf{t}_j^{sT},\ {}^b\mathbf{t}_j^{sT}]^T$: sth division of the cable tensions $\mathbf{t}_j$ into ${}^a\mathbf{t}_j^s$ and ${}^b\mathbf{t}_j^s$.

${}^at_{oj}^s$: oth component of ${}^a\mathbf{t}_j^s$.

${}^bt_{rj}^s$: rth component of ${}^b\mathbf{t}_j^s$.

${}^a\mathbf{u}_{oj}^s$, ${}^b\mathbf{u}_{rj}^s$: unit vectors of cables whose tension magnitudes are ${}^at_{oj}^s$, ${}^bt_{rj}^s$.

${}^a\mathbf{b}_{oj}^s$, ${}^b\mathbf{b}_{rj}^s$: Coordinate vectors of the anchor points to which the cables of tensions ${}^at_{oj}^s$, ${}^bt_{rj}^s$ are attached.

${}^a\mathbf{w}_{oj}^s$, ${}^b\mathbf{w}_{rj}^s$: actuation wrenches associated with the cable tensions ${}^at_{oj}^s$, ${}^bt_{rj}^s$.

$\mathscr{H}_{tkj}^s$: sth hyperplane associated with the tipping of $\mathscr{M}_j$ about $\mathscr{L}_{C_{kj}}$.

$\mathscr{H}_{fgj}^s$: sth hyperplane associated with the sliding of $\mathscr{M}_j$ in the direction normal to the gth friction pyramid.

$\mathbf{e}_{tkj}^s$, $\mathbf{e}_{fgj}^s$: unit vector orthogonal to its hyperplane $\mathscr{H}_{tkj}^s$, $\mathscr{H}_{fgj}^s$.

d_{tkj}^s, d_{fgj}^s : shifting distances from the origin to the hyperplanes $\mathscr{H}_{tkj}^s$, $\mathscr{H}_{fgj}^s$, respectively.

μ : capacity margin index determines the wrench-feasibility of the moving-platform pose.

Chapter 5

$\mathbf{A}$: $(m \times n)$ parallel Jacobian matrix containing the actuation wrenches due to the cables on the moving-platform.

$\mathbf{A}_j$: actuation wrenches generated by the cables carried by jth mobile base.

$\dot{\mathbf{l}}_j$: Velocities of the cables mounted on the jth mobile base.

$\dot{l}_{ij}$: velocity of the cable $\mathscr{C}_{ij}$.

$\mathbf{t}_{MP}$: twist of the MCDPR moving-platform

${}^0\mathbf{t}_{MP}^j$: twist of the MCDPR moving-platform due to jth proximal-distal module expressed in $\mathscr{F}_0$

${}^0\mathbf{t}_{MP}^{prox_j}$: twist of the MCDPR moving-platform due to jth proximal module expressed in $\mathscr{F}_0$

${}^0\mathbf{t}_{MP}^{dist_j}$: twist of the MCDPR moving-platform due to jth distal module expressed in $\mathscr{F}_0$

$\boldsymbol{\omega} = [\omega_x,\ \omega_y,\ \omega_z]^T$: moving-platform angular velocity vector expressed in $\mathscr{F}_0$

$\dot{\mathbf{p}} = [\dot{p}_x,\ \dot{p}_y,\ \dot{p}_z]^T$: moving-platform linear velocity vector expressed in $\mathscr{F}_0$

$\mathbf{J}_{bj}$: serial Jacobian matrix of $prox_j$

$\dot{\mathbf{q}}_{bj} = [\dot{\theta}_j \ \dot{\rho}_{1j} \ \dot{\rho}_{2j}]^T$: virtual joint velocities of the RPP kinematic chain

${}^{bj}\mathbf{A}d_P$: adjoint matrix representing the transformation matrix between the twists expressed in $\mathscr{F}_{bj}$ and twist expressed in $\mathscr{F}_P$

${}^0\overline{\mathbf{R}}_{bj}$: augmented rotation matrix.

$\dot{\mathbf{q}} = [\dot{\mathbf{q}}_b \ \ \dot{\mathbf{l}}]^T$: joint velocity vector

$\dot{\mathbf{q}}_b$: joint velocity vector of all the RPP kinematic chains

$\hat{\mathbf{t}}^s_{MP}$: twist generated by the sth sub-matrix $\mathbf{A}^s$ out of C^n_m $(n \times n)$ square sub-matrices of matrix $\mathbf{A}$, $s = 1, \ldots, C^n_m$

ν : capacity margin index determines the twist-feasibility of the moving-platform.

Chapter 6

t_1, t_2 : trajectory time for the first and second segments of pick-and-place operation

m_1, m_2 : total mass of the moving-platform for the first and second segments of pick-and-place operation

k_1, k_2 : discretization of the path. Picking segment discretized into k_1 points and placing segment discretized into $k_2 - k_1$ points.

β : redundancy planning scheme

ρ_{2k_0} : position of $\mathscr{M}_2$ at k_0th point of the path

$\underline{\rho}_2$, $\overline{\rho}_2$: lower and upper bounds on ρ_2

$\mathcal{P}_1, \mathcal{P}_2, \mathcal{P}_3, \mathcal{P}_4$: chosen Pareto-optimal solutions for the analysis as shown in Fig 6.3.

$\overline{P}_{\underline{i}}$: $\underline{i}$ way-point, $\underline{i} = 1, \ldots, \underline{l}$, where $\underline{l}$ denotes total number of way-points.

$\mathbf{p}_{\underline{i}}$: Cartesian coordinate vector of the $\underline{i}$th way-point.

$\overline{k}$: represents an iteration in the first phase of the iterative algorithm.

$\mathbf{M}_{\underline{i}j}$: A matrix whose $\overline{k}$th column contains the Cartesian coordinate vector of the jth mobile base at the $\overline{k}$th iteration of the algorithm.

s_j = number of possible collision free steps of the jth mobile base.

d_j = step size for searching the next step of the jth mobile base.

$\mathbf{P}_{\underline{i}j}$: feasible path of mobile bases.

$\underline{r}$: represents an iteration in the second phase of the iterative algorithm.

$\mathbf{P}_{\underline{i},MP}$: optimal path of moving-platform.

d_{MP} : step size for searching the best pose of the moving-platform.

$\underline{s}$: total number of obstacles in the environment.

$\mathbf{o}_{\underline{q}}$: position of the $\underline{q}$ obstacle, $\underline{q} =, 1, \ldots, \underline{s}$.

$r_{\underline{q}}$: radius of the $\underline{q}$ obstacle, $\underline{q} =, 1, \ldots, \underline{s}$.

N : total number of time steps.

N_1, N_2 : the time steps at the desired way-points of the moving platform

$\mathbf{p}_e$: Cartesian coordinates of the moving platform at the eth step of the trajectory, $e = 2, \ldots, N$

$\mathbf{m}_{j,e}$: Cartesian coordinate vector of $\mathscr{M}_j$ in ${}^0x$ ${}^0y$ plane at the eth step of the trajectory, $e = 2, \ldots, N$

$\mathbf{x}_e$: state of a MCDPR at the eth time step of the trajectory.

$\overline{\mathbf{A}}$: Sparse square matrix

$\mathbf{b}$: sparse vector containing the system initial conditions

d_{min} : minimum relative distance between the mobile bases to avoid collisions

$\overline{s}(t)$: a cubic spline composed of $N-1$ cubic polynomials connecting N supporting points.

$\overline{s}_h$: hth cubic polynomial, $h = 1, \ldots, N-1$, connecting the two consecutive supporting points.

Appendix A

This appendix presents Gaussian Elimination algorithm, which solves the system of n linear equations for n-dimensional vector noted as $\mathbf{x}$ expressed as:

$$\mathbf{A}\mathbf{x} = \mathbf{b} \tag{A.1}$$

The algorithm consists of two steps. The first step is to create an upper triangular matrix of $\mathbf{A}$ denoted as $\mathbf{A}_u$.

Step 1: Create an upper triangular matrix of A

```
1  i = 0;  A_u = A;  b_u = b
2  for k = 1 : n − 1 do
3      if A_u(k, k) == 0 then
4          j = k;
5          for j = j + 1 : n do
6              if A_u(j, k) == 0 then
7                  continue
8              end
9              break
10         end
11         B = A_u(k, :);  C = b_u(k);  A_u(k, :) = A(j, :);
12         b_u(k) = b(j);  A_u(j, :) = B;  b_u(j) = C;
13     end
14     for l = 1 + i : n − 1 do
15         L = A_u(l + 1, k)/A_u^(k, k)
16         A_u(l + 1, :) = A_u(l + 1, :) − L ∗ A_u(k, :)
17         b_u(l + 1) = b_u(l + 1) − L ∗ b_u(k)
18     end
19     i = i + 1;
20 end
```

The second step is to use the substitutions from $\mathbf{A}_u$ to obtain the unknowns *i.e.* the components of $\mathbf{x}$.

Step 2: Obtain the unknown x

```
1 x(n) = b_u(n)A_u(n, n);
2 for i = n − 1 : −1 : 1 do
3 |   sum = 0;
4 |   for j = i + 1 : n do
5 |   |   sum = sum + A_u(i, j) ∗ x(j);
6 |   end
7 |   x(i) = (A_u(i, i)) ∗ (b_u(i) − sum);
8 end
```

Appendix B

This appendix presents the output of the Gaussian Elimination Algorithm for the MCDPR understudy in Fig. 1.4a composed of four mobile bases carrying eight cables named as $\mathscr{C}_{11}$, $\mathscr{C}_{21}$, $\mathscr{C}_{12}$, $\mathscr{C}_{22}$, $\mathscr{C}_{13}$, $\mathscr{C}_{23}$, $\mathscr{C}_{14}$ and $\mathscr{C}_{24}$ connected to a six DOF moving platform. Let for $s = 1$, the wrench matrix $\mathbf{W}$ and the cable tension vector $\mathbf{t}$ are split as,

$$ {}^{a}\mathbf{t}^{1} = \begin{bmatrix} {}^{a}t^{1}_{11} \\ {}^{a}t^{1}_{21} \\ {}^{a}t^{1}_{12} \\ {}^{a}t^{1}_{22} \\ {}^{a}t^{1}_{13} \\ {}^{a}t^{1}_{23} \end{bmatrix}, {}^{b}\mathbf{t}^{1} = \begin{bmatrix} {}^{b}t^{1}_{14} \\ {}^{b}t^{1}_{24} \end{bmatrix}, \tag{B.1} $$

$$ {}^{a}\mathbf{W}^{1} = \begin{bmatrix} \mathbf{u}_{11} & \mathbf{u}_{21} & \mathbf{u}_{12} & \mathbf{u}_{22} & \mathbf{u}_{13} & \mathbf{u}_{23} \\ \mathbf{c}_{r11} & \mathbf{c}_{r21} & \mathbf{c}_{r12} & \mathbf{c}_{r22} & \mathbf{c}_{r13} & \mathbf{c}_{r23} \end{bmatrix}, {}^{b}\mathbf{W}^{1} = \begin{bmatrix} \mathbf{u}_{14} & \mathbf{u}_{24} \\ \mathbf{c}_{r14} & \mathbf{c}_{r24} \end{bmatrix}. \tag{B.2} $$

Using GEA to solve for ${}^{\mathbf{a}}\mathbf{t}^{1}$, its components are expressed as

$$ {}^{a}t^{1}_{11} = \frac{\alpha^{1}_{11}(\mathbf{w} - {}^{b}\mathbf{W}^{s}\ {}^{b}\mathbf{t}^{s})}{\alpha^{1}_{11}\begin{bmatrix}\mathbf{u}^{T}_{11} & \mathbf{c}^{T}_{r11}\end{bmatrix}^{T}}, \qquad {}^{a}t^{1}_{21} = \frac{\alpha^{1}_{21}(\mathbf{w} - {}^{b}\mathbf{W}^{s}\ {}^{b}\mathbf{t}^{s})}{\alpha^{1}_{21}\begin{bmatrix}\mathbf{u}^{T}_{21} & \mathbf{c}^{T}_{r21}\end{bmatrix}^{T}}, \tag{B.3a} $$

$$ {}^{a}t^{1}_{12} = \frac{\alpha^{1}_{12}(\mathbf{w} - {}^{b}\mathbf{W}^{s}\ {}^{b}\mathbf{t}^{s})}{\alpha^{1}_{12}\begin{bmatrix}\mathbf{u}^{T}_{12} & \mathbf{c}^{T}_{r12}\end{bmatrix}^{T}}, \qquad {}^{a}t^{1}_{22} = \frac{\alpha^{1}_{22}(\mathbf{w} - {}^{b}\mathbf{W}^{s}\ {}^{b}\mathbf{t}^{s})}{\alpha^{1}_{22}\begin{bmatrix}\mathbf{u}^{T}_{22} & \mathbf{c}^{T}_{r22}\end{bmatrix}^{T}}, \tag{B.3b} $$

$$ {}^{a}t_{13}^{1} = \frac{\alpha_{13}^{1}(\mathbf{w} - {}^{b}\mathbf{W}^{s}\ {}^{b}\mathbf{t}^{s})}{\alpha_{13}^{1}\begin{bmatrix}\mathbf{u}_{13}^{T} & \mathbf{c}_{r13}^{T}\end{bmatrix}^{T}}, \qquad {}^{a}t_{23}^{1} = \frac{\alpha_{23}^{1}(\mathbf{w} - {}^{b}\mathbf{W}^{s}\ {}^{b}\mathbf{t}^{s})}{\alpha_{23}^{1}\begin{bmatrix}\mathbf{u}_{23}^{T} & \mathbf{c}_{r23}^{T}\end{bmatrix}^{T}}, \tag{B.3c} $$

where

$$ \alpha_{11}^{1} = \begin{bmatrix} [((\mathbf{c}_{r13}\times\mathbf{c}_{r23})^{T}\mathbf{c}_{r22})(\mathbf{u}_{21}\times\mathbf{u}_{12})^{+} & [-((\mathbf{u}_{21}\times\mathbf{u}_{12})^{T}\mathbf{u}_{22})(\mathbf{c}_{r13}\times\mathbf{c}_{r23})- \\ ((\mathbf{c}_{r12}\times\mathbf{c}_{r23})^{T}\mathbf{c}_{r13}(\mathbf{u}_{21}\times\mathbf{u}_{22})+ & ((\mathbf{u}_{21}\times\mathbf{u}_{22})^{T}\mathbf{u}_{13})(\mathbf{c}_{r12}\times\mathbf{c}_{r23})- \\ ((\mathbf{c}_{r12}\times\mathbf{c}_{r22})^{T}\mathbf{c}_{r23})(\mathbf{u}_{21}\times\mathbf{u}_{13})+ & ((\mathbf{u}_{21}\times\mathbf{u}_{13})^{T}\mathbf{u}_{23})(\mathbf{c}_{r12}\times\mathbf{c}_{r22})- \\ ((\mathbf{c}_{r12}\times\mathbf{c}_{r13})^{T}\mathbf{c}_{r22})(\mathbf{u}_{21}\times\mathbf{u}_{23})+ & ((\mathbf{u}_{21}\times\mathbf{u}_{23})^{T}\mathbf{u}_{22})(\mathbf{c}_{r12}\times\mathbf{c}_{r13})- \\ ((\mathbf{c}_{r21}\times\mathbf{c}_{r23})^{T}\mathbf{c}_{r13})(\mathbf{u}_{12}\times\mathbf{u}_{22})+ & ((\mathbf{u}_{12}\times\mathbf{u}_{22})^{T}\mathbf{u}_{13})(\mathbf{c}_{r21}\times\mathbf{c}_{r23})- \\ ((\mathbf{c}_{r23}\times\mathbf{c}_{r22})^{T}\mathbf{c}_{r21})(\mathbf{u}_{12}\times\mathbf{u}_{13})+ & ((\mathbf{u}_{12}\times\mathbf{u}_{13})^{T}\mathbf{u}_{21})(\mathbf{c}_{r23}\times\mathbf{c}_{r22})- \\ ((\mathbf{c}_{r22}\times\mathbf{c}_{r13})^{T}\mathbf{c}_{r21})(\mathbf{u}_{12}\times\mathbf{u}_{23})+ & ((\mathbf{u}_{12}\times\mathbf{u}_{23})^{T}\mathbf{u}_{21})(\mathbf{c}_{r22}\times\mathbf{c}_{r13})- \\ ((\mathbf{c}_{r21}\times\mathbf{c}_{r12})^{T}\mathbf{c}_{r23})(\mathbf{u}_{22}\times\mathbf{u}_{13})+ & ((\mathbf{u}_{22}\times\mathbf{u}_{13})^{T}\mathbf{u}_{23})(\mathbf{c}_{r21}\times\mathbf{c}_{r12})- \\ ((\mathbf{c}_{r21}\times\mathbf{c}_{r13})^{T}\mathbf{c}_{r12})(\mathbf{u}_{22}\times\mathbf{u}_{23})+ & ((\mathbf{u}_{22}\times\mathbf{u}_{23})^{T}\mathbf{u}_{12})(\mathbf{c}_{r21}\times\mathbf{c}_{r13})- \\ ((\mathbf{c}_{r22}\times\mathbf{c}_{r21})^{T}\mathbf{c}_{r12})(\mathbf{u}_{13}\times\mathbf{u}_{23})]^{T} & ((\mathbf{u}_{13}\times\mathbf{u}_{23})^{T}\mathbf{u}_{12})(\mathbf{c}_{r22}\times\mathbf{c}_{r21})]^{T} \end{bmatrix} \tag{B.4} $$

$$ \alpha_{21}^{1} = \begin{bmatrix} [((\mathbf{c}_{r13}\times\mathbf{c}_{r23})^{T}\mathbf{c}_{r22})(\mathbf{u}_{11}\times\mathbf{u}_{12})+ & [-((\mathbf{u}_{11}\times\mathbf{u}_{12})^{T}\mathbf{u}_{22})(\mathbf{c}_{r13}\times\mathbf{c}_{r23})- \\ ((\mathbf{c}_{r12}\times\mathbf{c}_{r23})^{T}\mathbf{c}_{r13})(\mathbf{u}_{11}\times\mathbf{u}_{22})+ & ((\mathbf{u}_{11}\times\mathbf{u}_{22})^{T}\mathbf{u}_{13})(\mathbf{c}_{r12}\times\mathbf{c}_{r23})^{-} \\ ((\mathbf{c}_{r12}\times\mathbf{c}_{r22})^{T}\mathbf{c}_{r23})(\mathbf{u}_{11}\times\mathbf{u}_{13})+ & ((\mathbf{u}_{11}\times\mathbf{u}_{13})^{T}\mathbf{u}_{23})(\mathbf{c}_{r12}\times\mathbf{c}_{r22})- \\ ((\mathbf{c}_{r12}\times\mathbf{c}_{r13})^{T}\mathbf{c}_{r22})(\mathbf{u}_{11}\times\mathbf{u}_{23})+ & ((\mathbf{u}_{11}\times\mathbf{u}_{23})^{T}\mathbf{u}_{22})(\mathbf{c}_{r12}\times\mathbf{c}_{r13})- \\ ((\mathbf{c}_{r11}\times\mathbf{c}_{r23})^{T}\mathbf{c}_{r13})(\mathbf{u}_{12}\times\mathbf{u}_{22})+ & ((\mathbf{u}_{12}\times\mathbf{u}_{22})^{T}\mathbf{u}_{13})(\mathbf{c}_{r11}\times\mathbf{c}_{r23})- \\ ((\mathbf{c}_{r23}\times\mathbf{c}_{r22})^{T}\mathbf{c}_{r11})(\mathbf{u}_{12}\times\mathbf{u}_{13})+ & ((\mathbf{u}_{12}\times\mathbf{u}_{13})^{T}\mathbf{u}_{11})(\mathbf{c}_{r23}\times\mathbf{c}_{r22})- \\ ((\mathbf{c}_{r22}\times\mathbf{c}_{r13})^{T}\mathbf{c}_{r11})(\mathbf{u}_{12}\times\mathbf{u}_{23})+ & ((\mathbf{u}_{12}\times\mathbf{u}_{23})^{T}\mathbf{u}_{11})(\mathbf{c}_{r22}\times\mathbf{c}_{r13})- \\ ((\mathbf{c}_{r11}\times\mathbf{c}_{r12})^{T}\mathbf{c}_{r23})(\mathbf{u}_{22}\times\mathbf{u}_{13})+ & ((\mathbf{u}_{22}\times\mathbf{u}_{13})^{T}\mathbf{u}_{23})(\mathbf{c}_{r11}\times\mathbf{c}_{r12})- \\ ((\mathbf{c}_{r11}\times\mathbf{c}_{r13})^{T}\mathbf{c}_{r12})(\mathbf{u}_{22}\times\mathbf{u}_{23})+ & ((\mathbf{u}_{22}\times\mathbf{u}_{23})^{T}\mathbf{u}_{12})(\mathbf{c}_{r11}\times\mathbf{c}_{r13})- \\ ((\mathbf{c}_{r22}\times\mathbf{c}_{r11})^{T}\mathbf{c}_{r12})(\mathbf{u}_{13}\times\mathbf{u}_{23})]^{T} & ((\mathbf{u}_{13}\times\mathbf{u}_{23})^{T}\mathbf{u}_{12})(\mathbf{c}_{r22}\times\mathbf{c}_{r11})]^{T} \end{bmatrix} \tag{B.5} $$

$$\alpha_{12}^{1} = \begin{bmatrix} [((\mathbf{c}_{r13} \times \mathbf{c}_{r23})^T \mathbf{c}_{r22})(\mathbf{u}_{11} \times \mathbf{u}_{21}) + & [-((\mathbf{u}_{11} \times \mathbf{u}_{21})^T \mathbf{u}_{22})(\mathbf{c}_{r13} \times \mathbf{c}_{r23}) - \\ ((\mathbf{c}_{r21} \times \mathbf{c}_{r23})^T \mathbf{c}_{r13})(\mathbf{u}_{11} \times \mathbf{u}_{22}) + & ((\mathbf{u}_{11} \times \mathbf{u}_{22})^T \mathbf{u}_{13})(\mathbf{c}_{r21} \times \mathbf{c}_{r23}) - \\ ((\mathbf{c}_{r21} \times \mathbf{c}_{r22})^T \mathbf{c}_{r23})(\mathbf{u}_{11} \times \mathbf{u}_{13}) + & ((\mathbf{u}_{11} \times \mathbf{u}_{13})^T \mathbf{u}_{23})(\mathbf{c}_{r21} \times \mathbf{c}_{r22}) - \\ ((\mathbf{c}_{r21} \times \mathbf{c}_{r13})^T \mathbf{c}_{r22})(\mathbf{u}_{11} \times \mathbf{u}_{23}) + & ((\mathbf{u}_{11} \times \mathbf{u}_{23})^T \mathbf{u}_{22})(\mathbf{c}_{r21} \times \mathbf{c}_{r13}) - \\ ((\mathbf{c}_{r11} \times \mathbf{c}_{r23})^T \mathbf{c}_{r13})(\mathbf{u}_{21} \times \mathbf{u}_{22}) + & ((\mathbf{u}_{21} \times \mathbf{u}_{22})^T \mathbf{u}_{13})(\mathbf{c}_{r11} \times \mathbf{c}_{r23}) - \\ ((\mathbf{c}_{r23} \times \mathbf{c}_{r22})^T \mathbf{c}_{r11})(\mathbf{u}_{21} \times \mathbf{u}_{13}) + & ((\mathbf{u}_{21} \times \mathbf{u}_{13})^T \mathbf{u}_{11})(\mathbf{c}_{r23} \times \mathbf{c}_{r22}) - \\ ((\mathbf{c}_{r22} \times \mathbf{c}_{r13})^T \mathbf{c}_{r11})(\mathbf{u}_{21} \times \mathbf{u}_{23}) + & ((\mathbf{u}_{21} \times \mathbf{u}_{23})^T \mathbf{u}_{11})(\mathbf{c}_{r22} \times \mathbf{c}_{r13}) - \\ ((\mathbf{c}_{r11} \times \mathbf{c}_{r21})^T \mathbf{c}_{r23})(\mathbf{u}_{22} \times \mathbf{u}_{13}) + & ((\mathbf{u}_{22} \times \mathbf{u}_{13})^T \mathbf{u}_{23})(\mathbf{c}_{r11} \times \mathbf{c}_{r21}) - \\ ((\mathbf{c}_{r11} \times \mathbf{c}_{r13})^T \mathbf{c}_{r21})(\mathbf{u}_{22} \times \mathbf{u}_{23}) + & ((\mathbf{u}_{22} \times \mathbf{u}_{23})^T \mathbf{u}_{21})(\mathbf{c}_{r11} \times \mathbf{c}_{r13}) - \\ ((\mathbf{c}_{r22} \times \mathbf{c}_{r11})^T \mathbf{c}_{r21})(\mathbf{u}_{13} \times \mathbf{u}_{23})]^T & ((\mathbf{u}_{13} \times \mathbf{u}_{23})^T \mathbf{u}_{21})(\mathbf{c}_{r22} \times \mathbf{c}_{r11})]^T \end{bmatrix} \tag{B.6}$$

$$\alpha_{22}^{1} = \begin{bmatrix} [((\mathbf{c}_{r13} \times \mathbf{c}_{r23})^T \mathbf{c}_{r12})(\mathbf{u}_{11} \times \mathbf{u}_{21}) + & [-((\mathbf{u}_{11} \times \mathbf{u}_{21})^T \mathbf{u}_{12})(\mathbf{c}_{r13} \times \mathbf{c}_{r23}) - \\ ((\mathbf{c}_{r21} \times \mathbf{c}_{r23})^T \mathbf{c}_{r13})(\mathbf{u}_{11} \times \mathbf{u}_{12}) + & ((\mathbf{u}_{11} \times \mathbf{u}_{12})^T \mathbf{u}_{13})(\mathbf{c}_{r21} \times \mathbf{c}_{r23}) - \\ ((\mathbf{c}_{r21} \times \mathbf{c}_{r12})^T \mathbf{c}_{r23})(\mathbf{u}_{11} \times \mathbf{u}_{13}) + & ((\mathbf{u}_{11} \times \mathbf{u}_{13})^T \mathbf{u}_{23})(\mathbf{c}_{r21} \times \mathbf{c}_{r12}) - \\ ((\mathbf{c}_{r21} \times \mathbf{c}_{r13})^T \mathbf{c}_{r12})(\mathbf{u}_{11} \times \mathbf{u}_{23}) + & ((\mathbf{u}_{11} \times \mathbf{u}_{23})^T \mathbf{u}_{12})(\mathbf{c}_{r21} \times \mathbf{c}_{r13}) - \\ ((\mathbf{c}_{r11} \times \mathbf{c}_{r23})^T \mathbf{c}_{r13})(\mathbf{u}_{21} \times \mathbf{u}_{12}) + & ((\mathbf{u}_{21} \times \mathbf{u}_{12})^T \mathbf{u}_{13})(\mathbf{c}_{r11} \times \mathbf{c}_{r23}) - \\ ((\mathbf{c}_{r23} \times \mathbf{c}_{r12})^T \mathbf{c}_{r11})(\mathbf{u}_{21} \times \mathbf{u}_{13}) + & ((\mathbf{u}_{21} \times \mathbf{u}_{13})^T \mathbf{u}_{11})(\mathbf{c}_{r23} \times \mathbf{c}_{r12}) - \\ ((\mathbf{c}_{r12} \times \mathbf{c}_{r13})^T \mathbf{c}_{r11})(\mathbf{u}_{21} \times \mathbf{u}_{23}) + & ((\mathbf{u}_{21} \times \mathbf{u}_{23})^T \mathbf{u}_{11})(\mathbf{c}_{r12} \times \mathbf{c}_{r13}) - \\ ((\mathbf{c}_{r11} \times \mathbf{c}_{r21})^T \mathbf{c}_{r23})(\mathbf{u}_{12} \times \mathbf{u}_{13}) + & ((\mathbf{u}_{12} \times \mathbf{u}_{13})^T \mathbf{u}_{23})(\mathbf{c}_{r11} \times \mathbf{c}_{r21}) - \\ ((\mathbf{c}_{r11} \times \mathbf{c}_{r13})^T \mathbf{c}_{r21})(\mathbf{u}_{12} \times \mathbf{u}_{23}) + & ((\mathbf{u}_{12} \times \mathbf{u}_{23})^T \mathbf{u}_{21})(\mathbf{c}_{r11} \times \mathbf{c}_{r13}) - \\ ((\mathbf{c}_{r12} \times \mathbf{c}_{r11})^T \mathbf{c}_{r21})(\mathbf{u}_{13} \times \mathbf{u}_{23})]^T & ((\mathbf{u}_{13} \times \mathbf{u}_{23})^T \mathbf{u}_{21})(\mathbf{c}_{r12} \times \mathbf{c}_{r11})]^T \end{bmatrix} \tag{B.7}$$

$$\alpha_{13}^{1} = \begin{bmatrix} [((\mathbf{c}_{r22} \times \mathbf{c}_{r23})^T \mathbf{c}_{r12})(\mathbf{u}_{11} \times \mathbf{u}_{21}) + & [-((\mathbf{u}_{11} \times \mathbf{u}_{21})^T \mathbf{u}_{12})(\mathbf{c}_{r22} \times \mathbf{c}_{r23}) - \\ ((\mathbf{c}_{r21} \times \mathbf{c}_{r23})^T \mathbf{c}_{r22})(\mathbf{u}_{11} \times \mathbf{u}_{12}) + & ((\mathbf{u}_{11} \times \mathbf{u}_{12})^T \mathbf{u}_{22})(\mathbf{c}_{r21} \times \mathbf{c}_{r23}) - \\ ((\mathbf{c}_{r21} \times \mathbf{c}_{r12})^T \mathbf{c}_{r23})(\mathbf{u}_{11} \times \mathbf{u}_{22}) + & ((\mathbf{u}_{11} \times \mathbf{u}_{22})^T \mathbf{u}_{23})(\mathbf{c}_{r21} \times \mathbf{c}_{r12}) - \\ ((\mathbf{c}_{r21} \times \mathbf{c}_{r22})^T \mathbf{c}_{r12})(\mathbf{u}_{11} \times \mathbf{u}_{23}) + & ((\mathbf{u}_{11} \times \mathbf{u}_{23})^T \mathbf{u}_{12})(\mathbf{c}_{r21} \times \mathbf{c}_{r22}) - \\ ((\mathbf{c}_{r11} \times \mathbf{c}_{r23})^T \mathbf{c}_{r22})(\mathbf{u}_{21} \times \mathbf{u}_{12}) + & ((\mathbf{u}_{21} \times \mathbf{u}_{12})^T \mathbf{u}_{22})(\mathbf{c}_{r11} \times \mathbf{c}_{r23}) - \\ ((\mathbf{c}_{r23} \times \mathbf{c}_{r12})^T \mathbf{c}_{r11})(\mathbf{u}_{21} \times \mathbf{u}_{22}) + & ((\mathbf{u}_{21} \times \mathbf{u}_{22})^T \mathbf{u}_{11})(\mathbf{c}_{r23} \times \mathbf{c}_{r12}) - \\ ((\mathbf{c}_{r12} \times \mathbf{c}_{r22})^T \mathbf{c}_{r11})(\mathbf{u}_{21} \times \mathbf{u}_{23}) + & ((\mathbf{u}_{21} \times \mathbf{u}_{23})^T \mathbf{u}_{11})(\mathbf{c}_{r12} \times \mathbf{c}_{r22}) - \\ ((\mathbf{c}_{r11} \times \mathbf{c}_{r21})^T \mathbf{c}_{r23})(\mathbf{u}_{12} \times \mathbf{u}_{22}) + & ((\mathbf{u}_{12} \times \mathbf{u}_{22})^T \mathbf{u}_{23})(\mathbf{c}_{r11} \times \mathbf{c}_{r21}) - \\ ((\mathbf{c}_{r11} \times \mathbf{c}_{r22})^T \mathbf{c}_{r21})(\mathbf{u}_{12} \times \mathbf{u}_{23}) + & ((\mathbf{u}_{12} \times \mathbf{u}_{23})^T \mathbf{u}_{21})(\mathbf{c}_{r11} \times \mathbf{c}_{r22}) - \\ ((\mathbf{c}_{r12} \times \mathbf{c}_{r11})^T \mathbf{c}_{r21})(\mathbf{u}_{22} \times \mathbf{u}_{23})]^T & ((\mathbf{u}_{22} \times \mathbf{u}_{23})^T \mathbf{u}_{21})(\mathbf{c}_{r12} \times \mathbf{c}_{r11})]^T \end{bmatrix} \tag{B.8}$$

$$\alpha_{23}^{1} = \begin{bmatrix} [((\mathbf{c}_{r22} \times \mathbf{c}_{r13})^T \mathbf{c}_{r12})(\mathbf{u}_{11} \times \mathbf{u}_{21}) + & [-((\mathbf{u}_{11} \times \mathbf{u}_{21})^T \mathbf{u}_{12})(\mathbf{c}_{r22} \times \mathbf{c}_{r13}) - \\ ((\mathbf{c}_{r21} \times \mathbf{c}_{r13})^T \mathbf{c}_{r22})(\mathbf{u}_{11} \times \mathbf{u}_{12}) + & ((\mathbf{u}_{11} \times \mathbf{u}_{12})^T \mathbf{u}_{22})(\mathbf{c}_{r21} \times \mathbf{c}_{r13}) - \\ ((\mathbf{c}_{r21} \times \mathbf{c}_{r12})^T \mathbf{c}_{r13})(\mathbf{u}_{11} \times \mathbf{u}_{22}) + & ((\mathbf{u}_{11} \times \mathbf{u}_{22})^T \mathbf{u}_{13})(\mathbf{c}_{r21} \times \mathbf{c}_{r12}) - \\ ((\mathbf{c}_{r21} \times \mathbf{c}_{r22})^T \mathbf{c}_{r12})(\mathbf{u}_{11} \times \mathbf{u}_{13}) + & ((\mathbf{u}_{11} \times \mathbf{u}_{13})^T \mathbf{u}_{12})(\mathbf{c}_{r21} \times \mathbf{c}_{r22}) - \\ ((\mathbf{c}_{r11} \times \mathbf{c}_{r13})^T \mathbf{c}_{r22})(\mathbf{u}_{21} \times \mathbf{u}_{12}) + & ((\mathbf{u}_{21} \times \mathbf{u}_{12})^T \mathbf{u}_{22})(\mathbf{c}_{r11} \times \mathbf{c}_{r13}) - \\ ((\mathbf{c}_{r13} \times \mathbf{c}_{r12})^T \mathbf{c}_{r11})(\mathbf{u}_{21} \times \mathbf{u}_{22}) + & ((\mathbf{u}_{21} \times \mathbf{u}_{22})^T \mathbf{u}_{11})(\mathbf{c}_{r13} \times \mathbf{c}_{r12}) - \\ ((\mathbf{c}_{r12} \times \mathbf{c}_{r22})^T \mathbf{c}_{r11})(\mathbf{u}_{21} \times \mathbf{u}_{13}) + & ((\mathbf{u}_{21} \times \mathbf{u}_{13})^T \mathbf{u}_{11})(\mathbf{c}_{r12} \times \mathbf{c}_{r22}) - \\ ((\mathbf{c}_{r11} \times \mathbf{c}_{r21})^T \mathbf{c}_{r13})(\mathbf{u}_{12} \times \mathbf{u}_{22}) + & ((\mathbf{u}_{12} \times \mathbf{u}_{22})^T \mathbf{u}_{13})(\mathbf{c}_{r11} \times \mathbf{c}_{r21}) - \\ ((\mathbf{c}_{r11} \times \mathbf{c}_{r22})^T \mathbf{c}_{r21})(\mathbf{u}_{12} \times \mathbf{u}_{13}) + & ((\mathbf{u}_{12} \times \mathbf{u}_{13})^T \mathbf{u}_{21})(\mathbf{c}_{r11} \times \mathbf{c}_{r22}) - \\ ((\mathbf{c}_{r12} \times \mathbf{c}_{r11})^T \mathbf{c}_{r21})(\mathbf{u}_{22} \times \mathbf{u}_{13})]^T & ((\mathbf{u}_{22} \times \mathbf{u}_{13})^T \mathbf{u}_{21})(\mathbf{c}_{r12} \times \mathbf{c}_{r11})]^T \end{bmatrix} \tag{B.9}$$

Similarly using GEA, ${}^{a}\mathbf{t}^{s}$ is solved and can be expressed similarly to Eq. (B.3) for any $s = 1, \ldots, C_6^8$ combination.

Bibliography

[AA02] Jorge Angeles and J Angeles. *Fundamentals of robotic mechanical systems*, volume 2. Springer, 2002.

[AAK17] Michael Anson, Aliakbar Alamdari, and Venkat Krovi. Orientation workspace and stiffness optimization of cable-driven parallel manipulators with base mobility. *ASME J Mech Robot*, 9(3):031011, 2017.

[ABD93] James Albus, Roger Bostelman, and Nicholas Dagalakis. "The NIST robocrane". *Journal of Field Robotics*, 10(5):709–724, 1993.

[AGV+14] Rachid Alami, Mamoun Gharbi, Benjamin Vadant, Raphaël Lallement, and Adolfo Suarez. "On human-aware task and motion planning abilities for a teammate robot". 2014.

[BABB12] Lam T Bui, Hussein A Abbass, Michael Barlow, and Axel Bender. "Robustness against the decision-maker's attitude to risk in problems with conflicting objectives". *IEEE Transactions on Evolutionary Computation*, 16(1):1–19, 2012.

[BADJ96] Roger BostelMan, James Albus, Nicholas Dagalakis, and Adam Jacoff. Robocrane [r] project: An advanced concept for large scale manufacturing. In *AUVSI-PROCEEDINGS-*, pages 509–522, 1996.

[BDH96] C Bradford Barber, David P Dobkin, and Hannu Huhdanpaa. "The quickhull algorithm for convex hulls". *ACM Transactions on Mathematical Software (TOMS)*, 22(4):469–483, 1996.

[Bet98] John T Betts. "Survey of numerical methods for trajectory optimization". *Journal of guidance, control, and dynamics*, 21(2):193–207, 1998.

[BEU04] Paul Bosscher and Imme Ebert-Uphoff. "Wrench-based analysis of cable-driven robots". In *IEEE International Conference on Robotics*

and Automation, 2004. Proceedings. ICRA'04. 2004, volume 5, pages 4950–4955. IEEE, 2004.

[BG05] Guillaume Barrette and Clément Gosselin. "Determination of the dynamic workspace of cable-driven planar parallel mechanisms". *ASME J. of Mech. Design*, 127(2):242–248, 2005.

[BGM10] Samuel Bouchard, Clément Gosselin, and Brian Moore. "On the ability of a cable-driven robot to generate a prescribed set of wrenches". *Journal of Mechanisms and Robotics*, 2(1):011010, 2010.

[BHJ+82] Michael Brady, John M Hollerbach, Timothy L Johnson, Tomás Lozano-Pérez, Matthew T Mason, Daniel G Bobrow, Patrick Henry Winston, and Randall Davis. *Robot motion: Planning and control*. MIT press, 1982.

[BJP+00] Roger Bostelman, Adam Jacoff, Fred Proctor, Tom Kramer, and Albert Wavering. "Cable-based reconfigurable machines for large scale manufacturing". In *Proceedings of the 2000 Japan-USA Symposium on Flexible Automation*, pages 23–26, 2000.

[BJS+09] Per Henrik Borgstrom, Brett L Jordan, Gaurav S Sukhatme, Maxim A Batalin, and William J Kaiser. "Rapid computation of optimally safe tension distributions for parallel cable-driven robots". *IEEE Transactions on Robotics*, 25(6):1271–1281, 2009.

[BKMO11] Markus Bernard, Konstantin Kondak, Ivan Maza, and Anibal Ollero. Autonomous transportation and deployment with aerial robots for search and rescue missions. *Journal of Field Robotics*, 28(6):914–931, 2011.

[BL89] Jerome Barraquand and J-C Latombe. "On nonholonomic mobile robots and optimal maneuvering". In *Proceedings. IEEE International Symposium on Intelligent Control 1989*, pages 340–347. IEEE, 1989.

[Bla15] Laurent Blanchet. *Contribution à la modélisation de robots à câbles pour leur commande et leur conception*. PhD thesis, Université Nice Sophia Antipolis, Français. NNT:2015NICE4021. tel-01169741, 2015.

[BLNS12] Tobias Bruckmann, Wildan Lalo, Khoa Nguyen, and Bashir Salah. "Development of a storage retrieval machine for high racks using a wire robot". In *ASME 2012 International Design Engineering Technical Conferences and Computers and Information in Engineering*

Conference, pages 771–780. American Society of Mechanical Engineers, 2012.

[BLS+13] Tobias Bruckmann, Wildan Lalo, Christian Sturm, Dieter Schramm, and Manfred Hiller. "Design and realization of a high rack storage and retrieval machine based on wire robot technology". *DINAME*, 2013.

[BPH06] Tobias Bruckmann, Andreas Pott, and Manfred Hiller. "Calculating force distributions for redundantly actuated tendon-based Stewart platforms". In *Advances in Robot Kinematics*, pages 403–412. Springer, 2006.

[BREU06] Paul Bosscher, Andrew T Riechel, and Imme Ebert-Uphoff. "Wrench-feasible workspace generation for cable-driven robots". *IEEE Transactions on Robotics*, 22(5):890–902, 2006.

[BRO85] G BROWN. "Skycam: An Aerial Robotic Camera System". *BYTE*, page 122, 1985.

[CCL10] Benjamin J Cohen, Sachin Chitta, and Maxim Likhachev. "Search-based planning for manipulation with motion primitives". In *2010 IEEE International Conference on Robotics and Automation*, pages 2902–2908. IEEE, 2010.

[CDGF13] Stéphane Caro, Claire Dumas, Sébastien Garnier, and Benoît Furet. "Workpiece placement optimization for machining operations with a KUKA KR270-2 robot". In *2013 IEEE International Conference on Robotics and Automation*, pages 2921–2926. IEEE, 2013.

[CE07] John Connors and Gabriel Elkaim. "Analysis of a spline based, obstacle avoiding path planning algorithm". In *2007 IEEE 65th Vehicular Technology Conference-VTC2007-Spring*, pages 2565–2569. IEEE, 2007.

[CGF+14] Stephane Caro, Sebastien Garnier, Benoit Furet, Alexandr Klimchik, and Anatol Pashkevich. "Workpiece placement optimization for machining operations with industrial robots". In *Advanced Intelligent Mechatronics (AIM), 2014*, pages 1716–1721. IEEE, 2014.

[CHL+05] Howie M Choset, Seth Hutchinson, Kevin M Lynch, George Kantor, Wolfram Burgard, Lydia E Kavraki, and Sebastian Thrun. *Principles*

of robot motion: theory, algorithms, and implementation. MIT press, 2005.

[Cla90] Reymond Clavel. "Device for the Movement and Positioning of an Element in Space", December 11 1990. US Patent 4,976,582.

[CoG08] Project ANR CoGiRo. http://www.lirmm.fr/cogiro/, 2008.

[CPN17] Stéphane Caron, Quang-Cuong Pham, and Yoshihiko Nakamura. "Zmp support areas for multicontact mobility under frictional constraints". *IEEE Transactions on Robotics*, 33(1):67–80, 2017.

[CW03] Damien Chablat and Philippe Wenger. "Architecture optimization of a 3-DOF translational parallel mechanism for machining applications, the Orthoglide". *IEEE Transactions on Robotics and Automation*, 19(3):403–410, 2003.

[DBDW06] Moritz Diehl, Hans Georg Bock, Holger Diedam, and P-B Wieber. "Fast direct multiple shooting algorithms for optimal robot control". In *Fast motions in biomechanics and robotics*, pages 65–93. Springer, 2006.

[DGA+12] Tej Dallej, Marc Gouttefarde, Nicolas Andreff, Redwan Dahmouche, and Philippe Martinet. "Vision-based modeling and control of large-dimension cable-driven parallel robots". In *2012 IEEE/RSJ International Conference on Intelligent Robots and Systems*, pages 1581–1586. IEEE, 2012.

[Dij59] Edsger W Dijkstra. "A note on two problems in connexion with graphs". *Numerische mathematik*, 1(1):269–271, 1959.

[ECC19] Julian Erskine, Abdelhamid Chriette, and Stéphane Caro. Wrench analysis of cable-suspended parallel robots actuated by quadrotor unmanned aerial vehicles. *Journal of Mechanisms and Robotics*, 11(2):020909, 2019.

[Esk12] Azim Eskandarian. *Handbook of intelligent vehicles*, volume 2. Springer, 2012.

[EUV04] Imme Ebert-Uphoff and Philip A Voglewede. "On the connections between cable-driven robots, parallel manipulators and grasping". In *IEEE International Conference on Robotics and Automation, 2004. Proceedings. ICRA'04. 2004*, volume 5, pages 4521–4526. IEEE, 2004.

[FCCCL16] Alexis Fortin-Côté, Philippe Cardou, and Alexandre Campeau-Lecours. "Improving cable driven parallel robot accuracy through angular position sensors". In *2016 IEEE/RSJ International Conference on Intelligent Robots and Systems (IROS)*, pages 4350–4355. IEEE, 2016.

[FCCG14] Alexis Fortin-Côté, Philippe Cardou, and Clément Gosselin. "An admittance control scheme for haptic interfaces based on cable-driven parallel mechanisms". In *2014 IEEE International Conference on Robotics and Automation (ICRA)*, pages 819–825. IEEE, 2014.

[FFT+04] Shiqing Fang, Daniel Franitza, Marc Torlo, Frank Bekes, and Manfred Hiller. "Motion control of a tendon-based parallel manipulator using optimal tension distribution". *IEEE/ASME Transactions On Mechatronics*, 9(3):561–568, 2004.

[GASM08] Florian Gosselin, Claude Andriot, Joan Savall, and Javier Martín. "Large workspace haptic devices for human-scale interaction: A survey". In *International Conference on Human Haptic Sensing and Touch Enabled Computer Applications*, pages 523–528. Springer, 2008.

[GCCRC14] François Guay, Philippe Cardou, Ana Lucia Cruz-Ruiz, and Stéphane Caro. "Measuring how well a structure supports varying external wrenches". In *New Advances in Mechanisms, Transmissions and Applications*, pages 385–392. Springer, 2014.

[GCG15] Lorenzo Gagliardini, Stéphane Caro, and Marc Gouttefarde. "Dimensioning of cable-driven parallel robot actuators, gearboxes and winches according to the twist feasible workspace". In *2015 IEEE International Conference on Automation Science and Engineering (CASE)*, pages 99–105. IEEE, 2015.

[GCGG15] Lorenzo Gagliardini, Stéphane Caro, Marc Gouttefarde, and Alexis Girin. "A reconfiguration strategy for Reconfigurable Cable-Driven Parallel Robots". In *IEEE International Conference on Robotics and Automation (ICRA)*, pages 1613–1620. IEEE, 2015.

[GCGG16] Lorenzo Gagliardini, Stéphane Caro, Marc Gouttefarde, and Alexis Girin. "Discrete reconfiguration planning for cable-driven parallel robots". *Mechanism and Machine Theory*, 100:313–337, 2016.

[GCRB12] Marc Gouttefarde, Jean-François Collard, Nicolas Riehl, and Cédric Baradat. "Simplified static analysis of large-dimension parallel cable-driven robots". In *2012 IEEE International Conference on Robotics and Automation*, pages 2299–2305. IEEE, 2012.

[GCRB15] Marc Gouttefarde, Jean-François Collard, Nicolas Riehl, and Cédric Baradat. "Geometry selection of a redundantly actuated cable-suspended parallel robot". *IEEE Transactions on Robotics*, 31(2):501–510, 2015.

[GDM] Marc Gouttefarde, David Daney, and Jean-Pierre Merlet. "Interval-analysis-based determination of the wrench-feasible workspace of parallel cable-driven robots". *2011 IEEE Transactions on Robotics*, 27(1):1–13.

[GG05] Marc Gouttefarde and Clément M Gosselin. "Wrench-closure workspace of six-dof parallel mechanisms driven by 7 cables". *Transactions of the canadian society for mechanical engineering*, 29(4):541–552, 2005.

[GG06] Marc Gouttefarde and Clément M Gosselin. "Analysis of the wrench-closure workspace of planar parallel cable-driven mechanisms". *IEEE Transactions on Robotics*, 22(3):434–445, 2006.

[GGC] Lorenzo Gagliardini, Marc Gouttefarde, and Stephane Caro. "Determination of a dynamic feasible workspace for cable-driven parallel robots". In *Lenarcic J., Merlet JP. (eds) Advances in Robot Kinematics 2016. Springer Proceedings in Advanced Robotics*, volume 4, pages 361–370. Springer, Cham.

[GK10] Marc Gouttefarde and Sébastien Krut. "Characterization of parallel manipulator available wrench set facets". In *Advances in robot kinematics: motion in man and machine*, pages 475–482. Springer, 2010.

[GKP+08] Marc Gouttefarde, Sébastien Krut, François Pierrot, Nacim Ramdani, et al. "On the design of fully constrained parallel cable-driven robots". In *Advances in Robot Kinematics: Analysis and Design*, pages 71–78. Springer, 2008.

[GLRB15] Marc Gouttefarde, Johann Lamaury, Christopher Reichert, and Tobias Bruckmann. "A Versatile Tension Distribution Algorithm for-DOF

Parallel Robots Driven by Cables". *IEEE Transactions on Robotics*, 31(6):1444–1457, 2015.

[GMD06] Marc Gouttefarde, J-P Merlet, and David Daney. "Determination of the wrench-closure workspace of 6-DOF parallel cable-driven mechanisms". In *Advances in Robot Kinematics*, pages 315–322. Springer, 2006.

[GMS05] Philip E Gill, Walter Murray, and Michael A Saunders. "SNOPT: An SQP algorithm for large-scale constrained optimization". *SIAM review*, 47(1):99–131, 2005.

[GRR01] Paolo Gallina, Giulio Rosati, and Aldo Rossi. "3-dof wire driven planar haptic interface". *Journal of Intelligent and Robotic Systems*, 32(1):23–36, 2001.

[Grü03] Branko Grünbaum. "Convex Polytopes. 2003". *Grad. Texts in Math*, 2003.

[HAC+09] Paul TP Ho, Pablo Altamirano, Chia-Hao Chang, Shu-Hao Chang, Su-Wei Chang, Chung-Cheng Chen, Ke-Jung Chen, Ming-Tang Chen, Chih-Chiang Han, West M Ho, et al. "The yuan-tseh lee array for microwave background anisotropy". *The Astrophysical Journal*, 694(2):1610, 2009.

[HC04] Carl S Holland and David J Cannon. "Cable array robot for material handling", November 30 2004. US Patent 6,826,452.

[HFM+05a] Manfred Hiller, Shiqing Fang, Sonja Mielczarek, Richard Verhoeven, and Daniel Franitza. "Design, analysis and realization of tendon-based parallel manipulators". *Mechanism and Machine Theory*, 40(4):429–445, 2005.

[HFM+05b] Manfred Hiller, Shiqing Fang, Sonja Mielczarek, Richard Verhoeven, and Daniel Franitza. "Design, analysis and realization of tendon-based parallel manipulators". *Mechanism and Machine Theory*, 40(4):429–445, 2005.

[HK07] Mahir Hassan and Amir Khajepour. "Minimum-norm solution for the actuator forces in cable-based parallel manipulators based on convex optimization". In *Proceedings 2007 IEEE International Conference on Robotics and Automation*, pages 1498–1503. IEEE, 2007.

[HKMP15] Wei Yang Ho, Werner Kraus, Alexander Mangold, and Andreas Pott. "Haptic interaction with a cable-driven parallel robot using admittance control". In *Cable-Driven Parallel Robots*, pages 201–212. Springer, 2015.

[Hub14] Christian Michael Hubicki. *"From running birds to walking robots: optimization as a unifying framework for dynamic bipedal locomotion"*. PhD thesis, Oregon State University, 2014.

[IGM+13] Jean-Baptiste Izard, Marc Gouttefarde, Micaël Michelin, Olivier Tempier, and Cedric Baradat. "A reconfigurable robot for cable-driven parallel robotic research and industrial scenario proofing". In *Cable-driven parallel robots*, pages 135–148. Springer, 2013.

[KBA17] Alan Kuntz, Chris Bowen, and Ron Alterovitz. "Fast Anytime Motion Planning in Point Clouds by Interleaving Sampling and Interior Point Optimization". *ISRR, 2017*, 2017.

[KCTK97] Sadao Kawamura, Won Choe, Satoshi Tanaka, and Hitoshi Kino. "Development of an ultrahigh speed robot FALCON using parallel wire drive systems". *Journal of the Robotics Society of Japan*, 15(1):82–89, 1997.

[Kel17] Matthew Kelly. "An introduction to trajectory optimization: how to do your own direct collocation". *SIAM Review*, 59(4):849–904, 2017.

[KF11] Sertac Karaman and Emilio Frazzoli. "Sampling-based algorithms for optimal motion planning". *The international journal of robotics research*, 30(7):846–894, 2011.

[KI93] Sadao Kawamura and Ken Ito. "A new type of master robot for teleoperation using a radial wire drive system". In *Proceedings IEEE/RSJ Intelligent Robots and System (IROS)*, volume 1, pages 55–60. IEEE, 1993.

[KSJ+16] Anis Koubâa, Mohamed-Foued Sriti, Yasir Javed, Maram Alajlan, Basit Qureshi, Fatma Ellouze, and Abdelrahman Mahmoud. "Turtlebot at office: A service-oriented software architecture for personal assistant robots using ros". In *2016 International Conference on Autonomous Robot Systems and Competitions (ICARSC)*, pages 270–276. IEEE, 2016.

[KSLO96] Lydia E Kavraki, Petr Svestka, J-C Latombe, and Mark H Overmars. "Probabilistic roadmaps for path planning in high-dimensional configuration spaces". *IEEE transactions on Robotics and Automation*, 12(4):566–580, 1996.

[LaV06] Steven M LaValle. *Planning algorithms*. Cambridge university press, 2006.

[LB01] Yan Li and Gary M Bone. "Are parallel manipulators more energy efficient?". In *Proceedings 2001 IEEE International Symposium on Computational Intelligence in Robotics and Automation (Cat. No. 01EX515)*, pages 41–46. IEEE, 2001.

[LCC18] Saman Lessanibahri, Philippe Cardou, and Stéphane Caro. "Kinetostatic analysis of a simple cable-driven parallel crane". In *ASME 2018 International Design Engineering Technical Conferences and Computers and Information in Engineering Conference*, pages V05AT07A049–V05AT07A049. American Society of Mechanical Engineers, 2018.

[LG13a] Johann Lamaury and Marc Gouttefarde. "A tension distribution method with improved computational efficiency". In *Cable-driven parallel robots*, pages 71–85. Springer, 2013.

[LG13b] Johann Lamaury and Marc Gouttefarde. "Control of a large redundantly actuated cable-suspended parallel robot". In *2013 IEEE International Conference on Robotics and Automation*, pages 4659–4664. IEEE, 2013.

[LGCC18] Saman Lessanibahri, Marc Gouttefarde, Stéphane Caro, and Philippe Cardou. "Twist Feasibility Analysis of Cable-Driven Parallel Robots". In *Cable-Driven Parallel Robots*, pages 128–139. Springer, 2018.

[LGCH13] Johann Lamaury, Marc Gouttefarde, Ahmed Chemori, and Pierre-Elie Hervé. "Dual-space adaptive control of redundantly actuated cable-driven parallel robots". In *IEEE/RSJ International Conference on Intelligent Robots and Systems (ICRA)*, pages 4879–4886. IEEE, 2013.

[LGW14] Jory Lafaye, David Gouaillier, and Pierre-Brice Wieber. "Linear model predictive control of the locomotion of Pepper, a humanoid robot with omnidirectional wheels". In *IEEE-RAS International Conference on Humanoid Robots*, pages 336–341. IEEE, 2014.

[LKOP19] Philip Long, Tarık Kelestemur, Aykut Ozgün Onol, and Taskın Padır. "Optimization-Based Human-in-the-Loop Manipulation Using Joint Space Polytopes". In *2019 IEEE International Conference on Robotics and Automation*. IEEE, 2019.

[LNC07] Casey Lambert, Meyer Nahon, and Dean Chalmers. "Implementation of an aerostat positioning system with cable control". *IEEE/ASME Transactions on Mechatronics*, 12(1):32–40, 2007.

[LOZ+09] Samir Lahouar, Erika Ottaviano, Said Zeghoul, Lotfi Romdhane, and Marco Ceccarelli. "Collision free path-planning for cable-driven parallel robots". *Robotics and Autonomous Systems*, 57(11):1083–1093, 2009.

[LŠP11] Tone Lerher, Matjaž Šraml, and Iztok Potrč. "Simulation analysis of mini-load multi-shuttle automated storage and retrieval systems". *The International Journal of Advanced Manufacturing Technology*, 54(1-4):337–348, 2011.

[LW09] Xiang Li and Hau-San Wong. "Logic optimality for multi-objective optimization". *Applied Mathematics and Computation*, 215(8):3045–3056, 2009.

[MD10] Jean-pierre Merlet and David Daney. "A portable, modular parallel wire crane for rescue operations". In *IEEE International Conference on Robotics and Automation (ICRA)*, pages 2834–2839. IEEE, 2010.

[Mer96] J-P Merlet. "Direct kinematics of planar parallel manipulators". In *Proceedings of IEEE international conference on robotics and automation*, volume 4, pages 3744–3749. IEEE, 1996.

[Mer98] J-P Merlet. "Efficient computation of the extremum of the articular velocities of a parallel manipulator in a translation workspace". In *IEEE International Conference on Robotics and Automation (ICRA)*, volume 3, pages 1976–1981. IEEE, 1998.

[Mer06] Jean-Pierre Merlet. *Parallel robots*, volume 128. Springer Science & Business Media, 2006.

[Mer08] Jean-Pierre Merlet. "Kinematics of the wire-driven parallel robot MARIONET using linear actuators". In *2008, IEEE International Conference on Robotics and Automation (ICRA)*, pages 3857–3862. IEEE, 2008.

[MFDRGC13] Montserrat Manubens Ferriol, Didier Devaurs, Lluís Ros Giralt, and Juan Cortés. Motion planning for 6d manipulation with aerial towed-cable systems. In *Proceedings of the IX Robotics: Science and Systems Conference (RSS)*, 2013.

[MLB+16] Philipp Miermeister, Maria Lächele, Rainer Boss, Carlo Masone, Christian Schenk, Joachim Tesch, Michael Kerger, Harald Teufel, Andreas Pott, and Heinrich H Bülthoff. "The cablerobot simulator large scale motion platform based on cable robot technology". In *IEEE/RSJ International Conference on Intelligent Robots and Systems (IROS)*, pages 3024–3029. IEEE, 2016.

[MM14] Sandeep Kumar Malu and Jharna Majumdar. "Kinematics, localization and control of differential drive mobile robots". *Global Journal of Research In Engineering*, 2014.

[Mot53] Theodore S Motzkin. "The Double Description Method, in Contributions to the Theory of Games II". *Annals of Mathematics Study*, 28, 1953.

[MSJ+11] Jim Mainprice, E Akin Sisbot, Léonard Jaillet, Juan Cortés, Rachid Alami, and Thierry Siméon. "Planning human-aware motions using a sampling-based costmap planner". In *2011 IEEE International Conference on Robotics and Automation*, pages 5012–5017. IEEE, 2011.

[MTT+99] Kiyoshi Maeda, Satoshi Tadokoro, Toshi Takamori, Manfred Hiller, and Richard Verhoeven. "On design of a redundant wire-driven parallel robot WARP manipulator". In *Robotics and Automation, 1999. Proceedings. 1999 IEEE International Conference on*, volume 2, pages 895–900. IEEE, 1999.

[OA05] So-Ryeok Oh and Sunil Kumar Agrawal. "Cable suspended planar robots with redundant cables: Controllers with positive tensions". *IEEE Transactions on Robotics*, 21(3):457–465, 2005.

[OLP18] Aykut Ozgun Onol, Philip Long, and Taskin Padlr. "A comparative analysis of contact models in trajectory optimization for manipulation". In *2018 IEEE/RSJ International Conference on Intelligent Robots and Systems (IROS)*, pages 1–9. IEEE, 2018.

[OLP19] Aykut Ozgun Onol, Philip Long, and Taskin Padir. "Contact-Implicit Trajectory Optimization Based on a Variable Smooth Contact Model

and Successive Convexification". In *2019 IEEE International Conference on Robotics and Automation*. IEEE, 2019.

[OS14] Bo Ouyang and Weiwei Shang. "Wrench-feasible workspace based optimization of the fixed and moving platforms for cable-driven parallel manipulators". *Robotics and Computer-Integrated Manufacturing*, 30(6):629–635, 2014.

[PCCP18] Etienne Picard, Stéphane Caro, Fabien Claveau, and Franck Plestan. "Pulleys and force sensors influence on payload estimation of cable-driven parallel robots". In *2018 IEEE/RSJ International Conference on Intelligent Robots and Systems (IROS)*, pages 1429–1436. IEEE, 2018.

[PCGO10] Simon Perreault, Philippe Cardou, Clément M Gosselin, and Martin J-D Otis. "Geometric determination of the interference-free constant-orientation workspace of parallel cable-driven mechanisms". *Journal of Mechanisms and Robotics*, 2(3):031016, 2010.

[PCPC18] Etienne Picard, Stéphane Caro, Franck Plestan, and Fabien Claveau. "Control Solution for a Cable-Driven Parallel Robot with Highly Variable Payload". In *the ASME 2018 International Design Engineering Technical Conferences & Computers and Information in Engineering Conference IDETC/CIE*, 2018.

[PCT14] Michael Posa, Cecilia Cantu, and Russ Tedrake. "A direct method for trajectory optimization of rigid bodies through contact". *The International Journal of Robotics Research*, 33(1):69–81, 2014.

[PFAM04] Jason Pusey, Abbas Fattah, Sunil Agrawal, and Elena Messina. "Design and workspace analysis of a 6-6 cable-suspended parallel robot". *Mechanism and machine theory*, 39(7):761–778, 2004.

[PJS06] R Philippsen, B Jensen, and R Siegwart. "Autonomous Navigation in Dynamic Environments". *Springer Tracts on Advanced Robotics*, 2006.

[PLH02] Helmut Pottmann, Stefan Leopoldseder, and Michael Hofer. "Approximation with active B-spline curves and surfaces". In *10th Pacific Conference on Computer Graphics and Applications, 2002. Proceedings.*, pages 8–25. IEEE, 2002.

[PMK+13] Andreas Pott, Hendrick Mütherich, Werner Kraus, Valentine Schmidt, Philipp Miermeister, and Alexander Verl. "IPAnema: a family of cable-driven parallel robots for industrial applications". In *Cable-Driven Parallel Robots*, pages 119–134. Springer, 2013.

[PMN+16] Diego Pardo, Lukas Möller, Michael Neunert, Alexander W Winkler, and Jonas Buchli. "Evaluating direct transcription and nonlinear optimization methods for robot motion planning". *IEEE Robotics and Automation Letters*, 1(2):946–953, 2016.

[PMV10] Andreas Pott, Christian Meyer, and Alexander Verl. "Large-scale assembly of solar power plants with parallel cable robots". In *ISR 2010 (41st International Symposium on Robotics) and ROBOTIK 2010 (6th German Conference on Robotics)*, pages 1–6. VDE, 2010.

[Poo14] David Poole. *Linear algebra: A modern introduction*. Cengage Learning, 2014.

[Pot14] Andreas Pott. "An improved force distribution algorithm for over-constrained cable-driven parallel robots". In *Computational Kinematics*, pages 139–146. Springer, 2014.

[PRF90] François Pierrot, C Reynaud, and Alain Fournier. "DELTA: a simple and efficient parallel robot". *Robotica*, 8(2):105–109, 1990.

[PRMG+20] Nicolò Pedemonte, Tahir Rasheed, David Marquez-Gamez, Philip Long, Étienne Hocquard, Francois Babin, Charlotte Fouché, Guy Caverot, Alexis Girin, and Stéphane Caro. "FASTKIT: A Mobile Cable-Driven Parallel Robot for Logistics". In *Advances in Robotics Research: From Lab to Market*, pages 141–163. Springer, 2020.

[QCG+09] Morgan Quigley, Ken Conley, Brian Gerkey, Josh Faust, Tully Foote, Jeremy Leibs, Rob Wheeler, and Andrew Y Ng. "ROS: an open-source Robot Operating System". In *ICRA workshop on open source software*, volume 3, page 5. Kobe, Japan, 2009.

[RCCG15] Ana Lucia Cruz Ruiz, Stéphane Caro, Philippe Cardou, and François Guay. "Arachnis: Analysis of robots actuated by cables with handy and neat interface software". In *Cable-Driven Parallel Robots*, pages 293–305. Springer, 2015.

[RCM14] Rémy Ramadour, François Chaumette, and Jean-Pierre Merlet. "Grasping objects with a cable-driven parallel robot designed for

transfer operation by visual servoing". In *2014 IEEE International Conference on Robotics and Automation (ICRA)*, pages 4463–4468. IEEE, 2014.

[REU04] Andrew T Riechel and Imme Ebert-Uphoff. "Force-feasible workspace analysis for underconstrained, point-mass cable robots". In *IEEE International Conference on Robotics and Automation, 2004. Proceedings. ICRA'04. 2004*, volume 5, pages 4956–4962. IEEE, 2004.

[RGL98] Rodney G Roberts, Todd Graham, and Thomas Lippitt. "On the inverse kinematics, statics, and fault tolerance of cable-suspended robots". *Journal of Field Robotics*, 15(10):581–597, 1998.

[RLC19] Tahir Rasheed, Philip Long, and Stéphane Caro. "Wrench Feasible Workspace of Mobile Cable-Driven Parallel robots". In *Journal of Mechanisms and Robotics, American Society of Mechanical Engineers*, accepted, 2019.

[RLMGC18a] Tahir Rasheed, Philip Long, David Marquez-Gamez, and Stéphane Caro. "Available Wrench Set for Planar Mobile Cable-Driven Parallel Robots". In *2018, IEEE International Conference on Robotics and Automation (ICRA)*. IEEE, 2018.

[RLMGC18b] Tahir Rasheed, Philip Long, David Marquez-Gamez, and Stéphane Caro. "Kinematic modeling and twist feasibility of mobile cable-driven parallel robots". In *Lenarcic J., Parenti-Castelli V. (eds) Advances in Robot Kinematics (ARK)*, pages 410–418. Springer, 2018.

[RLMGC18c] Tahir Rasheed, Philip Long, David Marquez-Gamez, and Stéphane Caro. "Optimal Kinematic Redundancy Planning for Planar Mobile Cable-Driven Parallel Robots". In *The ASME 2018 International Design Engineering Technical Conferences & Computers and Information in Engineering Conference IDETC/CIE 2018*, 2018.

[RLMGC18d] Tahir Rasheed, Philip Long, David Marquez-Gamez, and Stéphane Caro. "Tension Distribution Algorithm for Planar Mobile Cable-Driven Parallel Robots". In *The Third International Conference on Cable-Driven Parallel Robots (CableCon 2017)*, pages 268–279. Springer, 2018.

[RLMGC19] Tahir Rasheed, Philip Long, David Marquez-Gamez, and Stèphane Caro. "Path Planning of a Mobile Cable-Driven Parallel Robot in a

Constrained Environment". In *International Conference on Cable-Driven Parallel Robots (CableCon)*, pages 257–268. Springer, 2019.

[RLSRC19] Tahir Rasheed, Philip Long, Adolfo Suarez Roos, and Stéphane Caro. "Optimization based Trajectory Planning of Mobile Cable-Driven Parallel Robots". In *IEEE/RSJ International Conference on Intelligent Robots and Systems (IROS)*. IEEE, 2019.

[RSF13] Eric Rohmer, Surya PN Singh, and Marc Freese. "V-REP: A versatile and scalable robot simulation framework". In *2013 IEEE/RSJ International Conference on Intelligent Robots and Systems*, pages 1321–1326. IEEE, 2013.

[Rud14] Joseph Rudy. "Zero-Moment Point Walking Controller For Humanoid Walking Using Darwin-Op". *Dept. of Aerospace and Mechanical Engineering, University of Notre Dame, Indiana*, 2014.

[Sat02] Makoto Sato. "Development of string-based force display: SPIDAR". In *8th international conference on virtual systems and multimedia*. Citeseer, 2002.

[SB04] Philippe Sardain and Guy Bessonnet. "Forces acting on a biped robot center of pressure-zero moment point". *IEEE Transactions on Systems, Man, and Cybernetics-Part A: Systems and Humans*, 34(5):630–637, 2004.

[SCBK17] Vincent Samy, Stéphane Caron, Karim Bouyarmane, and Abderrahmane Kheddar. "Adaptive Compliance in Post-Impact Humanoid Falls Using Preview Control of a Reduce Model". 2017.

[Sch17] Valentin Lorenz Schmidt. *Modeling techniques and reliable real-time implementation of kinematics for cable-driven parallel robots using polymer fiber cables*. Stuttgart: Fraunhofer Verlag, 2017.

[SRB15] Dragoljub Surdilovic, Jelena Radojicic, and Nick Bremer. Efficient calibration of cable-driven parallel robots with variable structure. In *Cable-Driven Parallel Robots*, pages 113–128. Springer, 2015.

[SRK18] Javad Sovizi, Rahul Rai, and Venkat Krovi. Wrench uncertainty quantification and reconfiguration analysis in loosely interconnected cooperative systems. *ASCE-ASME Journal of Risk and Uncertainty in Engineering Systems, Part B: Mechanical Engineering*, 4(2):021002, 2018.

[VAT10] Alaleh Vafaei, Mohammad M Aref, and Hamid D Taghirad. "Integrated controller for an over-constrained cable driven parallel manipulator: KNTU CDRPM". In *2010 IEEE International Conference on Robotics and Automation*, pages 650–655. IEEE, 2010.

[VB04] Miomir Vukobratović and Branislav Borovac. "Zero-moment point-thirty five years of its life". *International journal of humanoid robotics*, 1(01):157–173, 2004.

[Veg16] Iván Fernández Vega. "Development of a programming environment for a simulated turtlebot-2 robot with a Widowx manipulator arm through the connection of V-REP and Matlab". Universidad de Málaga, June 2016.

[Ver04] Richard Verhoeven. *"Analysis of the workspace of tendon based Stewart platforms"*. PhD thesis, Verlag nicht ermittelbar, 2004.

[VH00] Richard Verhoeven and Manfred Hiller. "Estimating the controllable workspace of tendon-based Stewart platforms". In *Advances in Robot Kinematics*, pages 277–284. Springer, 2000.

[VRE] "V-REP, Designing Dynamical Simulations" http://www.coppeliarobotics.com/helpFiles/en/designingDynamicSimulations.htm.

[VS18] Vojtech Vonasek and Martin Saska. "Increasing Diversity of Solutions in Sampling-based Path Planning". In *Proceedings of the 2018 4th International Conference on Robotics and Artificial Intelligence*, pages 97–102. ACM, 2018.

[WCB+15] Weijun Wang, Stéphane Caro, Fouad Bennis, Ricardo Soto, and Broderick Crawford. "Multi-objective robust optimization using a postoptimality sensitivity analysis technique: application to a wind turbine design". *Journal of Mechanical Design*, 137(1):011403, 2015.

[WFP+17] Alexander W Winkler, Farbod Farshidian, Diego Pardo, Michael Neunert, and Jonas Buchli. "Fast trajectory optimization for legged robots using vertex-based zmp constraints". *IEEE Robotics and Automation Letters*, 2(4):2201–2208, 2017.

[Wil06] Paul Williams. Optimal terrain-following for towed-aerial-cable sensors. *Multibody System Dynamics*, 16(4):351–374, 2006.

[WS02] Manfred Weck and Dirk Staimer. “Parallel kinematic machine tools–current state and future potentials”. *CIRP Annals*, 51(2):671–683, 2002.

[WSS08] Yonatan Wischnitzer, Nir Shvalb, and Moshe Shoham. “Wire-driven parallel robot: Permitting collisions between wires”. *The International Journal of Robotics Research*, 27(9):1007–1026, 2008.

[YMQ11] Peng Yang, Li-Xin Miao, and Ming-Yao Qi. “Slotting optimization in a multi-shuttle automated storage and retrieval system”. *Computer Integrated Manufacturing Systems*, 17(5):1050–1055, 2011.

[YTWH09] Rui Yao, Xiaoqiang Tang, Jinsong Wang, and Peng Huang. “Dimensional optimization design of the four-cable-driven parallel manipulator in fast”. *IEEE/ASME Transactions On Mechatronics*, 15(6):932–941, 2009.

[ZCPC19] Zane Zake, François Chaumette, Nicolò Pedemonte, and Stéphane Caro. “Vision-Based Control and Stability Analysis of a Cable-Driven Parallel Robot”. *IEEE Robotics and Automation Letters*, 4(2):1029–1036, 2019.

Publications

Journal papers

Tahir Rasheed, Philip Long, and Stéphane Caro. "Wrench feasible workspace of mobile cable-driven parallel robots". In *Journal of Mechanisms and Robotics, American Society of Mechanical Engineers* 2019.

International conference papers

Tahir Rasheed, Philip Long, David Marquez-Gamez, and Stéphane Caro. "Tension distribution algorithm for planar mobile cable-driven parallel robots". In *the Third International Conference on Cable-Driven Parallel Robots (CableCon 2017)*, pages 268–279. Springer, 2018.

Tahir Rasheed, Philip Long, David Marquez-Gamez, and Stéphane Caro. "Available wrench set for planar mobile cable-driven parallel robots". In *2018 IEEE International conference on Robotics and Automation (ICRA)*. IEEE, 2018.

Tahir. Rasheed, Philip. Long, D M. Gamez, and Stéphane. Caro. "Kinematic modeling and twist feasibility of mobile cable-driven parallel robots". In *Lenarcic J., Parenti-Castelli V. (eds) Advances in Robot Kinematics (ARK)*, pages 410-418, 2018.

Tahir Rasheed, Philip Long, David Marquez-Gamez, and Stéphane Caro. "Optimal kinematic redundancy planning for planar mobile cable-driven parallel robots". In *The ASME 2018 International Design Engineering Technical Conferences & Computers and Information in Engineering Conference IDETC/CIE*, 2018.

Tahir Rasheed, Philip Long, David Marquez-Gamez, and Stèphane Caro. "Path planning of a mobile cable-driven parallel robot in a constrained environment". In *International Conference on Cable-Driven Parallel Robots*, pages 257–268. Springer, 2019.

Tahir Rasheed, Philip Long, Adolfo Suarez Roos, and Stéphane Caro. "Optimization based trajectory planning of mobile cable-driven parallel robots". In *IEEE/RSJ International Conference on Intelligent Robots and Systems (IROS)*, IEEE, 2019.

Book chapters

Nicolò Pedemonte, Tahir Rasheed, David Marquez-Gamez, Philip Long, Étienne Hocquard, Francois Babin, Charlotte Fouché, Guy Caverot, Alexis Girin, and Stéphane Caro. 2020, "FASTKIT : A Mobile Cable-Driven Parallel Robot for Logistics.", In *Grau A., Morel Y., Puig-Pey A., Cecchi F. (eds) Advances in Robotics Research : From Lab to Market. Springer Tracts in Advanced Robotics*, vol 132. Springer, Cham, pp. 141–163.

UNIVERSITE BRETAGNE SCIENCES LOIRE POUR L'INGENIEUR

CENTRALE NANTES

Titre : Collaborative Robot parallèle à câble mobile

Mots clés : Robotique Collaborative, Robot parallèle à câble mobile, Planification de trajectoire, Analyse de l'espace de travail, Algorithme de distribution de tension

Résumé: Cette thèse présente un nouveau concept de robots parallèles à câble mobile (RPCM) comme un nouveau système robotique. RPCM est composé d'un robot parallèle à câble (RPC) classique monté sur plusieurs bases mobiles. Les RPCMs combinent l'autonomie des robots mobiles avec les avantages des RPCs, à savoir un grand espace de travail, un rapport charge utile/poids élevé, une faible inertie de l'effecteur final, une capacité de déploiement et une reconfigurabilité. De plus, les RPCMs présentent une nouvelle innovation technique qui pourrait contribuer à apporter plus de flexibilité et de polyvalence par rapport aux solutions robotiques industrielles existantes.

Deux prototypes de RPCMs appelés FASTKIT et MoPICK ont été développés au cours de cette thèse. FASTKIT est composé de deux bases mobiles portant une plate-forme mobile à six degrés de liberté, tirée par huit câbles, dans le but de fournir une solution robotique économique et polyvalente pour la logistique.

MoPICK est composé d'une plate-forme mobile à trois degrés de liberté tirée par quatre câbles montés sur quatre bases mobiles. Les applications ciblées de MoPICK sont des tâches mobiles dans un environnement contraint, par exemple un atelier ou des opérations logistiques dans un entrepôt.

Les contributions de cette thèse sont les suivantes. Tout d'abord, toutes les conditions nécessaires à l'atteinte de l'équilibre statique d'un RPCM sont étudiées. Ces conditions sont utilisées pour développer un algorithme de distribution de tension pour le contrôle en temps réel des câbles RPCM. Les conditions d'équilibre sont également utilisées pour étudier l'espace de travail clé en main des RPCMs. Ensuite, les performances cinématiques et les capacités de torsion des RPCMs sont étudiées. Enfin, la dernière partie de la thèse présente des stratégies de planification de trajectoires multiples pour les RPCMs afin de reconfigurer l'architecture géométrique du RPC pour réaliser la tâche souhaitée.

Title : Collaborative Mobile Cable-Driven Parallel Robots

Keywords : Collaborative Robotics, Mobile Cable Robots, Path Planning, Workspace analysis, Tension Distribution Algorithm

Abstract: This thesis presents a novel concept of Mobile Cable-Driven Parallel Robots (MCDPRs) as a new robotic system. MCDPR is composed of a classical Cable-Driven Parallel Robot (CDPR) mounted on multiple mobile bases. MCDPRs combines the autonomy of mobile robots with the advantages of CDPRs, namely, large workspace, high payload-to-weight ratio, low end-effector inertia, deployability and reconfigurability. Moreover, MCDPRs presents a new technical innovation that could help to bring more flexibility and versatility with respect to existing industrial robotic solutions.

Two MCDPRs prototypes named FASTKIT and MoPICK have been developed during the course of this thesis. FASTKIT is composed of two mobile bases carrying a six degrees-of-freedom moving-platform, pulled by eight cables, with a goal to provide a low cost and versatile robotic solution for logistics.

MoPICK is composed of a three degrees-of-freedom moving-platform pulled by four cables mounted on four mobile bases. The targeted applications of MoPICK are mobile tasks in a constrained environment, for example, a workshop or logistic operations in a warehouse.

The contributions of this thesis are as follows. Firstly, all the necessary conditions are studied that required to achieve the static equilibrium of a MCDPR. These conditions are used to develop a Tension Distribution Algorithm for the real time control of the MCDRP cables. The equilibrium conditions are also used to investigate the Wrench-Feasible-Workspace of MCDPRs. Afterwards, the kinematic performance and twist capabilities of the MCDPRs are investigated. Finally, the last part of the thesis presents multiple path planning strategies for MCDPRs in order to reconfigure the CDPR's geometric architecture for performing the desired task.